

**Design and Construction of a Double-Layer PVDF  
Wearable Ultrasonic Sensor for the Quantitative  
Assessment of Muscle Contractile Properties**

by

**Ibrahim AlMohimeed**

A thesis submitted to the Faculty of Graduate and Postdoctoral Affairs in  
partial fulfillment of the requirements  
for the degree of

**Doctor of Philosophy**

in

Ottawa-Carleton Institute for Electrical and Computer Engineering  
Department of Systems and Computer Engineering  
Carleton University  
Ottawa, Ontario, Canada

© 2020

Ibrahim AlMohimeed

# Abstract

Assessment of the skeletal muscle contractile properties provides valuable information for various medical applications. This thesis presents the development of a wearable ultrasonic sensor (WUS) and a method to measure the skeletal muscle contractile parameters. The proposed WUS was made of flexible polyvinylidene fluoride (PVDF) piezoelectric polymer film. A double-layer PVDF configuration was proposed to improve ultrasonic performance such as ultrasound signal strength. In order to study the double-layer PVDF WUS performance for its design consideration, a formulation of a numerical simulation model for the double-layer PVDF WUS was derived, based on Mason's equivalent circuit model of piezoelectric resonators. The double-layer PVDF configuration and the effects of non-piezoelectric layers on ultrasonic performance, such as backing, bonding, and electrode layers, were studied in detail using the simulation model developed to obtain a guideline for the design and construction of double-layer PVDF WUS. The construction procedure of the proposed design of the double-layer PVDF WUS was simple and relatively low-cost. The experimental evaluation showed the improved ultrasound performance of the developed double-layer PVDF WUS. The flexibility, lightweight, thinness, and small size of the double-layer PVDF WUS enable a steady attachment to the skin surface without affecting the underlying tissue motion in the area of interest. Such features could reduce the motion artifacts in the ultrasound measurement of tissue thickness. The developed double-layer PVDF WUS was tested for *in vivo* measurements of the skeletal muscle contractile parameters. Comparative measurements of the electrically-evoked static contractions of a skeletal muscle

were performed by the developed double-layer PVDF WUS and the laser displacement sensor (LDS). The double-layer PVDF WUS demonstrated less variability in the extracted contractile parameters than the LDS. In addition, it was verified that the double-layer PVDF WUS was less susceptible to the motion artifacts induced by the body/limb motion than the LDS. The contractile parameters were successfully extracted from the tissue thickness changes measured by the double-layer PVDF WUS during voluntary and tetanic contractions. Furthermore, the muscle tetanic progression level was quantitatively assessed using the fusion index (FI) parameter obtained.

# Acknowledgments

I would like to express my sincere gratitude and appreciation to my supervisor Prof. Yuu Ono, for his time, patience, and guidance throughout my time at Carleton University. This thesis work would not have been accomplished without his encouragement and support. Also, I extend my thanks to my thesis committee, Prof. Victor Frenkel, Prof. Jiyong Zhao, Prof. Tong Xu, Prof. Chris Joslin, and Prof. Paul Van Geel for their constructive comments.

I also like to acknowledge Carleton University for the opportunity, Natural Sciences and Engineering Research Council of Canada for the research funding, and Majmaah University represented by the Saudi Arabian Cultural Bureau (SACB) for the scholarship and the financial support.

Many thanks to Dr. Zhen Qu, Dr. Bruno Trindade, Dr. Shermeen Nizami, Dr. Fatemeh Zabihollahy, Andy Huang, Elliot Yeung, Kevin Dick, and Mohamed Abdelaziz for their heartfelt thoughts and help. They always generously shared their valuable knowledge and experience. I also extend my thanks and appreciation to Nagui Mikhail for his assistance and lab equipment.

I am grateful to my siblings and friends for their encouragement, prayers, and persistent support throughout my life. I owe particular thanks to Marwan and Shady.

Lastly, I am immensely thankful to my parents, Norah and Rasheed, for making every possible effort to get me to where I am today; to my beloved wife, Manal, for helping me during my research by taking care of everything else; to my children, Firas, Elaf, and Yusuf for a consistent source of love. This would not have been possible without you.

# Table of Contents

<b>Abstract</b>	<b>i</b>
<b>Acknowledgments</b>	<b>iii</b>
<b>Table of Contents</b>	<b>iv</b>
<b>List of Abbreviations</b>	<b>xxvii</b>
<b>List of Symbols</b>	<b>xxxi</b>
<b>1 Introduction</b>	<b>1</b>
1.1 Overview . . . . .	1
1.2 Problem Statements . . . . .	5
1.3 Objectives . . . . .	6
1.4 Contributions . . . . .	8
1.5 Thesis Structure . . . . .	11
<b>2 Literature Review of Muscle Monitoring</b>	<b>13</b>
2.1 Skeletal Muscle Function Assessment . . . . .	14
2.1.1 Human Muscle Physiology . . . . .	14
2.1.2 Medical Applications . . . . .	18

2.2	Common Measurement Methods and Limitations . . . . .	22
2.2.1	Surface Electrocardiography (SEMG) . . . . .	22
2.2.2	Mechanomyography (MMG) . . . . .	23
2.2.3	Ultrasound Imaging . . . . .	25
2.3	Wearable Ultrasonic Transducers . . . . .	27
2.4	Other Wearable Sensors . . . . .	38
<b>3</b>	<b>Numerical Simulation Model for the Double-Layer PVDF WUS</b>	<b>49</b>
3.1	Review of Piezoelectric Simulation Models . . . . .	50
3.2	Modeling of Single-Layer PVDF Piezoelectric . . . . .	54
3.3	Modeling of Multiple-Layer PVDF Arrangement . . . . .	57
3.3.1	Series Electrically Connected . . . . .	59
3.3.2	Parallel Electrically Connected . . . . .	62
3.4	Modeling of Non-Piezoelectric Layers . . . . .	68
3.5	Equivalent Circuit Model of Double-Layer PVDF WUS . . . . .	70
<b>4</b>	<b>Numerical Study and Design Considerations of the Double-Layer PVDF WUS</b>	<b>77</b>
4.1	Choosing the PVDF Piezoelectric Film . . . . .	78
4.2	Numerical Study of Double-Layer PVDF WUS . . . . .	80
4.2.1	PVDF Layer Thickness and Ultrasound Sensing Area . . . . .	80
4.2.2	Double-Layer PVDF Configuration . . . . .	83
4.2.3	Effect of Backing . . . . .	90
4.2.4	Effect of Electrode Layers . . . . .	98
4.2.5	Effect of Bonding Layer . . . . .	110
4.3	Design Considerations of Double-Layer PVDF WUS . . . . .	116
4.3.1	Double-Layer PVDF Arrangement Considerations . . . . .	116

4.3.2	PVDF Film Thickness and Active Ultrasound Area Selection . . . . .	117
4.3.3	Electrode and Electrical Connection Considerations . . . . .	119
4.3.4	Bonding of the Two PVDF Layers Considerations . . . . .	120
4.3.5	Acoustic Insulation and Packaging Considerations . . . . .	121
4.4	Double-Layer PVDF WUS Design . . . . .	123
<b>5</b>	<b>Construction and Experimental Performance Evaluation of the Double-Layer PVDF WUS</b>	<b>126</b>
5.1	Construction Procedure of Double-Layer PVDF WUS . . . . .	127
5.1.1	PVDF Layers Preparation . . . . .	127
5.1.2	Bonding the Two PVDF Layers . . . . .	129
5.1.3	Attachment of Electrical Wire . . . . .	134
5.1.4	Creation of Acoustic Insulator Layer . . . . .	136
5.1.5	Complete Construction With Packaging . . . . .	137
5.2	Performance Evaluation of Double-Layer PVDF WUS . . . . .	141
5.2.1	Operating Ultrasound Frequency . . . . .	141
5.2.2	Ultrasonic Signal Strength . . . . .	147
5.2.3	Noise Interference Reduction . . . . .	148
<b>6</b>	<b><i>In Vivo</i> Experimental Evaluation of the Double-Layer PVDF WUS for the measurement of Skeletal Muscle Contractile Parameters</b>	<b>151</b>
6.1	Double-Layer PVDF WUS Measurement Methodology . . . . .	152
6.1.1	Ultrasonic Soft Tissue Thickness Measurement Methods . . . . .	153
6.1.2	<i>In Vivo</i> Measurement Configuration . . . . .	154
6.1.3	Muscle Contractile Parameters Extraction . . . . .	157
6.2	Performance Evaluation . . . . .	160

6.2.1	Comparative Study of Double-Layer PVDF WUS and LDS . . . . .	160
6.2.2	Influence of Motion Artifact on Measurement Variability . . . . .	171
6.3	<i>In Vivo</i> Demonstration . . . . .	176
6.3.1	Skeletal Muscle Tetanic Contraction Progression . . . . .	176
6.3.2	Dynamic Voluntary Contraction . . . . .	185
6.4	Discussion . . . . .	189
6.4.1	Comparison Between the Double-Layer PVDF WUS and LDS . . .	189
6.4.2	Double-layer PVDF WUS and Motion Artifact . . . . .	191
6.4.3	Assessment of Muscle Contractile Properties . . . . .	191
6.5	Limitations . . . . .	194
6.5.1	Assumed Sound Velocity . . . . .	194
6.5.2	Alignment of an Ultrasonic Beam . . . . .	196
6.5.3	Ultrasonic PE and TT Modes . . . . .	197
<b>7</b>	<b>Conclusions and Future Research</b>	<b>199</b>
7.1	Summary of Thesis Research . . . . .	199
7.1.1	Numerical Simulation Model . . . . .	199
7.1.2	Numerical Study and Design Considerations . . . . .	200
7.1.3	Construction and Experimental Evaluation . . . . .	201
7.1.4	<i>In Vivo</i> Performance Evaluation and Experimental Demonstration .	202
7.2	Scope and Limitation . . . . .	203
7.3	Future Research . . . . .	204
	<b>Appendix A In Vivo Measurement of Cardiac Muscle Motion</b>	<b>208</b>
	<b>References</b>	<b>211</b>

# List of Figures

<b>Figure 2.1</b>	Internal structural layers of muscle tissue. Adapted from OpenStax, Wikimedia (CC BY 4.0 license) . . . . .	15
<b>Figure 2.2</b>	A muscle fiber composed of myofibril bundles. Each myofibril is divided into segments of sarcomere. Adapted from OpenStax, Wikimedia (CC BY 4.0 license). . . . .	16
<b>Figure 2.3</b>	The sliding of sarcomere filaments. Contraction occurs as a result of the overlap of thin and thick filaments. Adapted from OpenStax, Wikimedia (CC BY 4.0 license). . . . .	16
<b>Figure 2.4</b>	Typical twitch response of a skeletal muscle. . . . .	17
<b>Figure 2.5</b>	A conventional hand-held ultrasound probe. Reproduced from from Drickey at English Wikipedia (CC BY-SA 2.5) . . . . .	26
<b>Figure 2.6</b>	A basic structure of an ultrasound probe. . . . .	27

- Figure 2.7** Photos of single-element UTs for muscle activity monitoring. A photo of the single-element UT for A-mode measurement of tissue thickness changes during the skeletal muscle contraction by [1] (a), photos of the single-element UT attachment using armband for muscle fatigue assessment by [2] (b), a photo of the four single-element UTs attachment using armband for muscle force estimation by [3] (c), a photo of the four single-element UTs for finger motion prediction by [4] (d), a photo of the single-element UT attachment for finger motion prediction with voluntary and electrically evoked muscle contraction by [5] (e), and photos of the single-element UT mounted on flexible printed circuit board (PCB) for tracking diaphragm wall motion by [6] (f). . . . . 29
- Figure 2.8** Flexible PMUT arrays by mounting diced PZT piezoceramic into patterned cavities on a flexible polyimide film. The photos of the PMUT array fabricated by [7] (a) and a schematic drawing and a photo of the PMUT array fabricated by [8] (b). . . . . 31
- Figure 2.9** Flexible PMUT arrays by embedding aluminum nitride (AlN) piezoelectric onto a flexible polyimide substrate. A photo of the AlN flexible PMUT array fabricated by [9] (a), and a photo and a schematic drawing of the flexible PMUT array fabricated by [10] (b). 32
- Figure 2.10** Flexible PMUT arrays using island-bridge technique. Photos of the flexible PMUT arrays by [11] (a), photos of the flexible PMUT arrays fabricated by [12] (b), and photos of the stretchable PMUT arrays fabricated by [13]. . . . . 33

<b>Figure 2.11</b>	A flexible CMUT array using a concave bottom electrode. Schematic drawings of the flexible CMUT fabricated by [14] (a), and a photo of the flexible PMUT arrays fabricated by [15] (b). . . . .	34
<b>Figure 2.12</b>	<i>In-vivo</i> demonstration of the flexible UT in the measurement of tissue thickness changes on human subjects. A photo of the PVDF UT integrated into a belt and wrapped around the chest for the heart wall motion monitoring by [16] (a), and schematic drawings of the stretchable PMUT attachment on the skin surface above the carotid and radial arteries for the estimation of the blood pressure by [17] (b). . . . .	35
<b>Figure 2.13</b>	Wearable strain sensors. A photo of the wearable polymeric strain sensor by [18] (a), photos of the wearable CNT strain sensor by [19] (b), photos of the wearable silver nanoparticles and nanowires strain sensor by [20] (c), and photos of the wearable piezoresistive silicon-based strain sensor by [21] (d). . . . .	41
<b>Figure 2.14</b>	The flexible sensing belt by [22]: structure of the sensing belt (a), and a Photo of the sensing belt mounted on the subject right upper arm (b). . . . .	42
<b>Figure 2.15</b>	The wearable pressure mapping system embedded in pants by [23].	42
<b>Figure 2.16</b>	The wearable MMG taped to a subject's leg for rhythmic auditory cueing by [24] (a), and SEMG electrodes attached to skin surface of the upper arm for localized muscle fatigue detection by [25] (b).	44

<b>Figure 2.17</b>	The wearable microphone and the inertial measurement unit embedded in an armband by [26] (a), the muscle activity recognition system (MARS) based on wearable sensor nodes by [27] (b), the SEMG-MMG hybrid system for upper-extremity prosthetic control by [28] (c), and the wearable gesture detection system of multiple sensor types by [29] (d). . . . .	46
<b>Figure 3.1</b>	Three-port network representation of Mason's model consists of a single-layer piezoelectric material operating in thickness mode. The force and particle velocity entities of the acoustic ports acting on the top and bottom surfaces are denoted by $F^+$ , $F^-$ , $U^+$ , and $U^-$ , respectively. The voltage and current entities of the electrical port acting across the thickness of the piezoelectric material are denoted by $V$ and $I$ , respectively. . . . .	55
<b>Figure 3.2</b>	Representation of the mechanical and electrical quantities acting on each PVDF layer in the double-layer PVDF arrangement. . . . .	59
<b>Figure 3.3</b>	General representation of series electrically connected multiple-layer PVDF. . . . .	60
<b>Figure 3.4</b>	General representation of parallel electrically connected multiple-layer PVDF. . . . .	62
<b>Figure 3.5</b>	General representation of interchange electrode connections in parallel electrically connected multiple-layer PVDF case: even-numbered (a) and odd-numbered (b) PVDF layers. . . . .	66
<b>Figure 3.6</b>	Representation of common electrical connections to electrodes between the bonding layer . . . . .	70

<b>Figure 3.7</b>	Acting quantities on each individual layer of double-layer PVDF WUS. Reversal voltage orientation is assumed. . . . .	72
<b>Figure 3.8</b>	Equivalent circuit of double-layer PVDF ultrasonic sensor as a two-port network for transmitting and receiving modes. . . . .	73
<b>Figure 4.1</b>	The PVDF layer resonance frequencies. The PVDF acoustic power is computed as a function of frequency to illustrate the fundamental and harmonic frequencies of single-layer 52 $\mu\text{m}$ -thick PVDF. The structural configuration of the simulation (a) and the resonance frequencies (b) are shown. Input voltage =1V is assumed. . . . .	82
<b>Figure 4.2</b>	The PVDF thickness layer effect on the operating frequency. The operating frequencies are computed as a function of the single-layer PVDF layer thickness, $d$ , in a range of 10 – 250 $\mu\text{m}$ . The structural configuration of the simulation (a) and the operating frequency (b) are shown. . . . .	83
<b>Figure 4.3</b>	The effect of the active ultrasound area of PVDF layer on the acoustic output power. The acoustic output powers at the operating frequency of single-layer 104- $\mu\text{m}$ -thick PVDF are computed as a function of the area range of 0.1 – 8.0 $\text{cm}^2$ . The Structural configuration of the simulation (a) and the acoustic power at the operating frequency (b) are shown. Input voltage =1 V is assumed.	84
<b>Figure 4.4</b>	Representation of the parallel electrically connected double-layer PVDF (a) and a single-layer PVDF of an equivalent total thickness (b). . . . .	85

- Figure 4.5** Four cases of PVDF layer configurations: single-layer 52- $\mu\text{m}$ -thick PVDF, single-layer 104- $\mu\text{m}$ -thick PVDF, double-layer 52- $\mu\text{m}$ -thick PVDF in the parallel polarization direction, and double-layer 52- $\mu\text{m}$ -thick PVDF in the antiparallel polarization direction (a) are simulated. The calculated electrical input impedance (b), acoustic output power (c), and conversion loss (d) are shown. Surface area = 4 cm<sup>2</sup> and input voltage = 1 V are assumed. . . . . 88
- Figure 4.6** Polarization directions in double-layer PVDF configuration: parallel (a) and antiparallel (b). . . . . 89
- Figure 4.7** Double-layer PVDF with reversal voltage orientation and antiparallel polarization directions (a) behaves equivalently to the double-layer PVDF of parallel polarization directions (b). . . . . 89
- Figure 4.8** Standing waves representations of the half-wavelength (a) and quarter-wavelength resonating (b) modes of PVDF. . . . . 91
- Figure 4.9** The effect of the backing acoustic impedance on the ultrasonic performance of the double-layer PVDF sensor. The CL parameter of the double-layer 52- $\mu\text{m}$ -thick PVDF sensor is computed as a function of the backing acoustic impedance of 0 – 30 MRayls. The structural configuration of the simulation (a) and the operating frequency (b), operating frequency bandwidth (c), and CL value at the operating frequency (d) are shown. . . . . 93

- Figure 4.10** The effect of the backing acoustic impedance on the transmitted ultrasound of the double-layer 52- $\mu\text{m}$ -thick PVDF. The acoustic output power and CL are computed for four types of backing: air (427 Rayls), Spurr's epoxy (2.3 MRayls), PVDF (4.02 MRayls), and aluminum (17 MRayls). The structural configuration of the simulations (a), the acoustic output power (b), and CL (c) are shown.  $Z_B$  is the acoustic impedance of the backing (MRayls). Surface area = 4  $\text{cm}^2$  and input voltage = 1 V are assumed. . . . . 95
- Figure 4.11** The effect of the packaging on the ultrasonic performance of the double-layer PVDF. The acoustic output power and CL are calculated for the double-layer 52- $\mu\text{m}$ -thick PVDF with and without the packaging layers of a 13- $\mu\text{m}$ -thick polyimide layer and a 25- $\mu\text{m}$ -thick silicone adhesive layer on the back side. The structural configuration of the simulation (a), the acoustic power (b), and CL (c) are shown. Active ultrasound area = 4  $\text{cm}^2$  and input voltage = 1 V are assumed. . . . . 99

- Figure 4.12** The isolation of the packaging effect on the ultrasonic performance of the double-layer PVDF by creating an air gap. The acoustic power and CL are calculated for double-layer 52- $\mu\text{m}$ -thick PVDF with 1  $\mu\text{m}$  air gap on the back side between the PVDF layers and the packaging layers of polyimide and silicone adhesive (13- $\mu\text{m}$ -thick polyimide layer and 25- $\mu\text{m}$ -thick silicon adhesive layer), and, for comparison, the double-layer 52- $\mu\text{m}$ -thick PVDF only. The structural configuration of the simulation (a), the acoustic power (b), and the CL (c) are shown. Active ultrasound area = 4  $\text{cm}^2$  and input voltage = 1 V are assumed. . . . . 100
- Figure 4.13** Illustration of the inner and outer electrode layers of the double-layer PVDF. . . . . 101
- Figure 4.14** The effect of the inner electrode layer acoustic impedance on the ultrasonic performance of the double-layer PVDF sensor. The acoustic power and CL are calculated for the double-layer 52- $\mu\text{m}$ -thick PVDF with a 10- $\mu\text{m}$ -thick inner electrode layer each for three silver electrode materials: 5.15 MRayls (silver epoxy), 12.24 MRayls (silver ink), 38.16 MRayls (pure silver). The structural configuration of the simulation (a), the acoustic power (b), and the CL (c) are shown. Active ultrasound area = 4  $\text{cm}^2$  and input voltage = 1 V are assumed. . . . . 102

- Figure 4.15** The effect of the inner electrode layers thickness on the ultrasonic performance of the double-layer PVDF. The operating frequency, bandwidth, acoustic power, and CL are computed for the double-layer 52- $\mu\text{m}$ -thick PVDF as a function of the individual layer thickness (0 – 25  $\mu\text{m}$ ) of silver ink (12.24 MRayls) inner electrode. The structural configuration of the simulation (a), operating frequency (b), frequency bandwidth (c), maximum acoustic power (d), and minimum CL (e) are shown. Active ultrasound area = 4  $\text{cm}^2$  and input voltage = 1 V are assumed. . . . . 104
- Figure 4.16** The effect of the outer electrode layers on the ultrasonic performance of the double-layer PVDF sensor. The acoustic power and CL are calculated for the double-layer 52- $\mu\text{m}$ -thick PVDF with a 10- $\mu\text{m}$ -thick outer electrode layer each for three silver electrode materials: 5.15 MRayls (silver epoxy), 12.24 MRayls (silver ink), 38.16 MRayls (silver). The structural configuration of the simulation (a), the acoustic power (b), and the CL (c) are shown. Active ultrasound area = 4  $\text{cm}^2$  and input voltage = 1 V are assumed. . . . 107
- Figure 4.17** The effect of the outer electrode layers thickness on the ultrasonic performance of the double-layer PVDF sensor. The parameters are computed for the double-layer 52- $\mu\text{m}$ -thick PVDF as a function of the individual layer thickness (0 – 25  $\mu\text{m}$ ) of silver ink (12.24 MRayls) outer electrode. The structural configuration of the simulation (a), operating frequency (b), frequency bandwidth (c), maximum acoustic power (d), and minimum CL (e) are shown. Active ultrasound area = 4  $\text{cm}^2$  and input voltage = 1 V are assumed. 108

- Figure 4.18** The effect of the inner and outer electrode layers thickness on the ultrasonic performance of the double-layer PVDF sensor. The parameters are computed for the double-layer 52- $\mu\text{m}$ -thick PVDF as a function of the thickness of each electrode layer (0 – 25  $\mu\text{m}$ ). It is calculated for electrode materials of 5.15 MRayls (silver epoxy), 12.24 MRayls (silver ink), 38.16 MRayls (silver). The structural configuration of the simulation (a), operating frequency (b), frequency bandwidth (c), maximum acoustic power (d), and minimum CL (e) are shown. Active ultrasound area = 4  $\text{cm}^2$  and input voltage = 1 V are assumed. . . . . 109
- Figure 4.19** The effect of the acoustic impedance of the bonding layer on the ultrasonic performance of the double-layer PVDF sensor. The acoustic power and CL are calculated for the double-layer 52- $\mu\text{m}$ -thick PVDF with a 7.5- $\mu\text{m}$ -thick bonding layer of five types of adhesive materials: 1.07-MRayls Sylgard, 2.4-MRayls Spurr's epoxy, 3.04-MRayls Araldite 10phe, 6.18-MRayls Araldite 50phe, and 11.7-MRayls Ecosorb. The structural configuration of the simulation (a), the acoustic power (b), and the CL (c) are shown. Active ultrasound area = 4  $\text{cm}^2$  and input voltage = 1 V are assumed. 113

<b>Figure 4.20</b>	The effect of the bonding layer thickness on the double-layer PVDF. The operating frequency, bandwidth, acoustic power, and CL are calculated for the double-layer 52- $\mu\text{m}$ PVDF as a function of the thickness of the bonding layer. Five types of adhesive materials are assumed: 1.07-MRayls Sylgard, 2.4-MRayls Spurr's epoxy, 3.04-MRayls Araldite 10phe, 6.18-MRayls Araldite 50phe, and 11.7-MRayls Ecosorb. The structural configuration of the simulation (a), operating frequency (b), frequency bandwidth (c), maximum acoustic power (d), and minimum CL (e) are shown. Active ultrasound area = 4 $\text{cm}^2$ and input voltage = 1 V are assumed.	115
<b>Figure 4.21</b>	A schematic of the active ultrasonic area and interconnection area of a single PVDF layer. . . . .	120
<b>Figure 4.22</b>	A schematic design of the double-layer PVDF WUS . . . . .	125
<b>Figure 5.1</b>	PVDF layers preparation. A schematic of the single PVDF layer with electrodes (a) and a photo of the PVDF layer at the bottom view (b). . . . .	128
<b>Figure 5.2</b>	Experimental configuration of the ultrasonic signal strength evaluation of the bonded double-layer PVDF. . . . .	131
<b>Figure 5.3</b>	Photos of the bonded double-layer PVDF attachment to clamp jaws: directly (a) and sandwiched between two PMMA plates (b). . . . .	132
<b>Figure 5.4</b>	A schematic of the electrical wire attachment to the inner and outer electrode layers using conductive adhesive tapes. . . . .	137
<b>Figure 5.5</b>	A photo of the removal of the protection layer from the ultrasonic sensing area. . . . .	138

- 
- Figure 5.6** Photos of the constructed double-layer PVDF WUS. . . . . 139
- Figure 5.7** Measured (dotted line) and calculated (solid lines) electrical input impedance of an air-loaded single-layer PVDF with an electrode layer on the top and bottom surfaces. The structural configuration (a) and electrical impedance (b) of the single-layer 52- $\mu\text{m}$ -thick PVDF, and the structural configuration (c) and impedance (d) of the single-layer 110- $\mu\text{m}$ -thick PVDF. The active ultrasound area is 4  $\text{cm}^2$ . . . . . 144
- Figure 5.8** The operating frequencies obtained from the measured and calculated impedance for the air-loaded (air/air): single-layer 52  $\mu\text{m}$ -thick PVDF WUS, single-layer 110  $\mu\text{m}$ -thick PVDF WUS, double-layer 52  $\mu\text{m}$ -thick PVDF WUS, and double-layer 110  $\mu\text{m}$ -thick PVDF WUS. . . . . 145
- Figure 5.9** Calculated electrical input impedance for the air-loaded double-layer PVDF only, double-layer PVDF with bonding layer only, double-layer PVDF with electrode layers only, and the full structure of constructed double-layer PVDF WUS to illustrates the loading effect of the electrode and bonding layers that led to the operating frequency of double-layer 52  $\mu\text{m}$ -thick PVDF WUS. The structural configurations of the simulations (a) and the input impedance magnitude and phase (b) are shown. Active ultrasound area is 4  $\text{cm}^2$ . 146
- Figure 5.10** Experimental evaluation of signal strength. The structural configuration of double-layer 52- $\mu\text{m}$  PVDF WUS and single-layer 110- $\mu\text{m}$  PVDF WUS (a) and the Ultrasonic RF signals obtained in pulse-echo mode (b). . . . . 149

- Figure 5.11** Noise reduction with the electromagnetic shielding layer. The received ultrasonic signals were acquired from *in vivo* measurements to compare between a double-layer PVDF WUS before and after applying the EM shielding layer. The received ultrasonic RF signals using the double-layer PVDF WUS before applying the EM shield layer (a) and after applying the EM shielding layer (b). 150
- Figure 6.1** Schematic diagram of *in vivo* measurement configuration using double-layer PVDF WUS in ultrasonic pulse-echo (PE) mode (a) and through-transmission (TT) mode (b). . . . . 155
- Figure 6.2** Examples of the received ultrasonic RF signals using the developed double-layer PVDF WUS in the PE mode (a) and TT mode (b). The dashed lines indicate a relaxed state of the measured skeletal muscle contraction, where the solid lines indicate a contracted state. 157
- Figure 6.3** Photos of the tensiomyography (TMG) [30] (a) and laser displacement sensor (LDS) [31] (b) measurement methods. . . . . 158
- Figure 6.4** Example of the thickness changes/time curve of a single contraction twitch obtained by double-layer PVDF WUS and the contractile parameters. . . . . 159
- Figure 6.5** Photo of the experimental setup for monitoring the electrically-evoked contractions of the biceps muscle using the LDS and the double-layer PVDF WUS in ultrasonic PE mode. The double-layer PVDF WUS and electrical muscle stimulator (EMS) electrodes were attached to the skin surface of the upper arm while the LDS was placed on a support fixture. . . . . 162

- Figure 6.6** Tissue thickness changes, measured by the LDS and double-layer PVDF WUS (in PE mode), due to the electrically-evoked contraction of the biceps muscle at EMS frequencies of 2 Hz (a). The comparison of the thickness changes between the LDS and double-layer PVDF WUS measurements with indications of the stimulation and rest intervals (b). . . . . 163
- Figure 6.7** Contractile parameter of  $Th$  extracted from the individual twitch using the thickness changes measured by the LDS and double-layer PVDF WUS in S1 (a), S2 (b), S3 (c), and S4 (d). The 0%, 10%, 50%, 90%, and 100% of  $Th$  were indicated. . . . . 164
- Figure 6.8**  $Th$  variation plots for comparison between the double-layer PVDF WUS and LDS obtained from the multiple contraction twitches of the S1 (a), S2 (b), S3 (c), and S4 (d) intervals. Line graphs of mean  $\pm$  SD  $Th$  values for each interval (e). . . . . 167
- Figure 6.9**  $Tc$  variation plots of comparison between the double-layer PVDF WUS and LDS obtained from the multiple contraction twitches of the S1 (a), S2 (b), S3 (c), and S4 (d) intervals. Line graphs of mean  $\pm$  SD  $Tc$  values for each interval (e). . . . . 168
- Figure 6.10**  $Ts$  variation plots for comparison between the double-layer PVDF WUS and LDS obtained from the multiple contraction twitches of the S1 (a), S2 (b), S3 (c), and S4 (d) intervals. Line graphs of mean  $\pm$  SD  $Ts$  values for each interval (e). . . . . 169

- Figure 6.11** *Tr* variation plots for comparison between the double-layer PVDF WUS and LDS obtained from the multiple contraction twitches of the S1 (a), S2 (b), S3 (c), and S4 (d) intervals. Line graphs of mean  $\pm$  SD *Tr* values for each interval (e). . . . . 170
- Figure 6.12** *Vc* variation plots for comparison between the double-layer PVDF WUS and LDS obtained from the multiple contraction twitches of the S1 (a), S2 (b), S3 (c), and S4 (d) intervals. Line graphs of mean  $\pm$  SD *Vc* values for each interval (e). . . . . 171
- Figure 6.13** Tissue thickness changes, measured by the LDS and double-layer PVDF WUS (PE mode), due to the electrically-evoked contraction of the biceps muscle at EMS frequency of 2 Hz during an induced motion artifact (a). The comparison of the thickness changes between LDS and double-layer PVDF WUS measurements (b). . . 173
- Figure 6.14** Contractile parameter of *Th* extracted from the individual twitch using the thickness changes measured by the LDS and double-layer PVDF WUS with the induced motion artifact in **Figure 6.13** measured . The 0%, 10%, 50%, 90%, and 100% of *Th* were indicated. . . . . 174
- Figure 6.15** Contractile parameters variation plots for comparison between the double-layer PVDF WUS and LDS obtained from the multiple contraction twitches of the electrically-evoked biceps muscle contraction with induced motion artifact . . . . . 175

- Figure 6.16** Photos of the experimental setup for monitoring the tetanic contractions of the gastrocnemius (GC) muscle in the TT mode. The two double-layer PVDF WUSs (transmitter and receiver) and EMS electrodes were attached to the skin surface of a lower leg. . . . . 178
- Figure 6.17** A schematic of the measurement configuration of GC muscle contractions in the lower leg. The muscle contraction was evoked by EMS, and the tissue thickness were measured using two developed WUSs in the TT mode. . . . . 179
- Figure 6.18** Tissue thickness changes, measured by the WUSs, due to the electrically evoked contraction of GC muscle at EMS frequencies of: 2 Hz (a), 4 Hz (b), 6 Hz (c), 8 Hz (d), 10 Hz (e), 12 Hz (f), and 30 Hz (g). . . . . 180
- Figure 6.19** Definition of fusion index (FI) quantifying the tetanic contraction progression level [32–34]. . . . . 181
- Figure 6.20** FI value (cross mark) with the standard deviation (error bar) at each EMS frequency, obtained from the results shown in **Figure 6.18**. The FI-EMS frequency curve denoted by the solid line was obtained by curve fitting of a sigmoid function. . . . . 182
- Figure 6.21** Extracted contractile parameters from a chosen single contraction twitch of the GC muscle evoked at EMS frequencies of: 2 Hz (a), 4 Hz (b), 6 Hz (c), 8 Hz (d), and 10 Hz (e). . . . . 183
- Figure 6.22** The average contractile parameters of  $Tc$ ,  $Ts$ , and  $Tr$  of the monitored muscle contractions with respect to the EMS frequencies. The error bar indicates the standard deviation. . . . . 185

- 
- Figure 6.23** Photos of double-layer PVDF WUS attachment to skin surface for monitoring the voluntary dynamic contraction of biceps muscle in PE mode. . . . . 187
- Figure 6.24** Monitored tissue thickness changes during the dynamic contraction of the biceps muscle performed by the voluntary flexion and extension of the forearm and measured by the double-layer PVDF WUS in the PE mode. . . . . 188
- Figure 6.25** Extracted contractile parameters from a chosen single contracting-relaxing cycle of the voluntary biceps muscle. . . . . 188
- Figure 6.26** M-mode ultrasonic measurement of the biceps voluntary contraction in pulse-echo mode to illustrate local motion of soft tissue boundaries at the depth of 5 – 7 mm, 18 – 20 mm, and 31 – 35 mm. 198
- Figure A.1** Photo of double-layer PVDF WUS and ECG electrodes attachment to skin surface for the ultrasonic monitoring of cardiac tissue motion in pulse-echo mode. . . . . 209
- Figure A.2** Monitored cardiac tissue motion. ECG signal (top) and M-mode ultrasonic measurement of cardiac muscle motion (bottom). . . . 210

# List of Tables

<b>Table 2.1</b>	An overview of wearable ultrasonic transducers (UT) and their medical applications. . . . .	36
<b>Table 2.2</b>	An overview of recent wearable sensors for the muscle mechanical activity measurement. . . . .	47
<b>Table 4.1</b>	Typical properties of piezoelectric materials of interest. . . . .	79
<b>Table 4.2</b>	Acoustic properties of the materials used in the numerical simulations.	81
<b>Table 5.1</b>	Typical viscosity of epoxy resins and common Fluids . . . . .	135
<b>Table 6.1</b>	Definition of contractile parameters. . . . .	159
<b>Table 6.2</b>	Mean values $\pm$ standard deviation (SD) and coefficient of variation (CV) of the contractile parameters from the monitored electrically-evoked contractions of the biceps muscle using the LDS and double-layer PVDF WUS showed in <b>Figure 6.7</b> . . . . .	165
<b>Table 6.3</b>	Mean values $\pm$ SD (CV) of the contractile parameters obtained from the monitored electrically-evoked contractions of biceps muscle with induced motion artifact using the double-layer PVDF WUS and LDS showed in <b>Figure 6.14</b> . . . . .	176

---

<b>Table 6.4</b>	CV values of the contractile parameters from the monitored electrically-evoked contractions of biceps muscle with and without induced motion artifact using the double-layer PVDF WUS and LDS. . . . .	177
<b>Table 6.5</b>	Average values $\pm$ SD and CV of the contractile parameters from the monitored tetanic contraction of GC muscle at the EMS frequencies in <b>Figure 6.18</b> . . . . .	184
<b>Table 6.6</b>	Extracted contractile parameters from the monitored dynamic contraction of the biceps muscle in <b>Figure 6.24</b> . . . . .	189
<b>Table 6.7</b>	Typical sound velocity values in body tissues [35–37]. . . . .	195

# List of Abbreviations

Acronym	Definition
A-mode	Amplitude mode
ACL	Anterior cruciate ligament
AlN	Aluminium nitride
B-mode	Brightness mode
CMUT	Capacitive micromachined ultrasound transducer
CNT	Carbon nanotube
COPD	Chronic obstructive pulmonary disease
CP	Cerebral palsy
CTT <sub>1/2</sub>	Contraction time to half tetanic
CV	Coefficient of variation
DAQ	Data Acquisition
ECG	Electrocardiography
EM	Electromagnetic
EMG	Electromyography
EMD <sub>c</sub>	Electromechanical delay of contraction

Continued on next page

## – Continue

Acronym	Definition
EMDr	Electromechanical delay of relaxation
EMS	Electrical muscle stimulator
FEA	Finite element analysis
FES	Function electrical stimulation
FFR	Force-frequency relationship
FI	Fusion index
FSS	Fabric strain sensor
FWHM	Full width at half maximum
GC	Gastrocnemius
IMU	Inertial measurement unit
LDS	Laser displacement sensor
M-mode	Motion mode
MARS	Muscle activity recognition system
MEMS	Microelectromechanical systems
MMG	Mechanomyography
MRI	Magnetic resonance imaging
MRS	Muscle relax state
MU	Motor unit
MVC	Maximal voluntary contraction
PC	Personal computer

Continued on next page

## – Continue

Acronym	Definition
PE	Pulse-echo
PMMA	Polymethyl methacrylate
PRR	Pulse repetition rate
PMUT	Piezoelectric micromachined ultrasound transducer
PVDF	Polyvinylidene fluoride
P(VDF-TrFE)	Poly(vinylidene fluoride-trifluoroethylene)
PZT	Lead zirconate titanate
RF	Radio frequency
RMS	Root mean square
SD	Standard deviation
SEMG	Surface electromyography
SCI	Spinal cord injury
SNR	Signal-to-noise ratio
TMG	Tensiomyography
TOF	Time-of-flight
TT	Through-transmission
UT	Ultrasonic transducer
VO <sub>2</sub>	Oxygen consumption rate
WURMADS	Wearable ultrasound radial muscle activity detection system

Continued on next page

---

**– Continue**

---

Acronym	Definition
WUS	Wearable ultrasonic sensor

---

# List of Symbols

Symbol	Definition
$A, B, C, D$	Elements of the compact $2 \times 2$ -matrix expression for the equivalent circuit of the double-layer PVDF WUS
$A_S$	Area
$\beta$	Complex acoustic impedance for a given area
$C$	Clamped bulk capacitance
$CL$	Conversion loss
$c^D$	Elastic stiffness constant
$c^*$	Complex elastic stiffness constant
$d$	Thickness
$e$	Piezoelectric constant
$\epsilon_o$	Vacuum permittivity
$\epsilon^S$	Dielectric permittivity
$\epsilon^*$	Complex dielectric permittivity
$F$	Force
$F_T$	Output force of double-layer PVDF WUS

Continued on next page

## – Continue

Symbol	Definition
$f$	Resonance frequency
$\gamma$	Wave propagation constant
$h$	Transmitting constant
$I$	Electrical current
$I^+$ and $I^-$	Partial sum currents of parallel electrically connected multiple-layer PVDF
$I^+$ and $I^-$	Partial sum currents of parallel electrically connected multiple-layer PVDF with reversal voltage orientation
$j$	Unit imaginary number
$k_t$	Thickness coupling factor
$\lambda$	Wavelength
$M$	Resultant $4 \times 4$ -matrix of the double-layer PVDF WUS
$ML$	Matching loss
$\omega$	Angular frequency
$P$	$3 \times 3$ -matrix expression of parallel electrically connected multiple-layer PVDF
$P^M$	$4 \times 4$ -matrix expression of parallel electrically connected multiple-layer PVDF
$P^M$	$4 \times 4$ -matrix expression of parallel electrically connected multiple-layer PVDF with reversal voltage orientation

Continued on next page

## – Continue

Symbol	Definition
$P^{np}$	$4 \times 4$ -matrix expression of non-piezoelectric layers
$P_E$	Transmitted electrical power
$P_T$	Acoustic output power
$P_S$	Electrical power from a source
$f_{ap}$	Operating frequency of multiple-layer PVDF in case of antiparallel polarization direction
$f_p$	Operating frequency of multiple-layer PVDF in case of parallel polarization direction
$f_s$	Operating frequency of single-layer PVDF
$Re$	Real part of complex variables
$R_L$	Load impedance at electric terminal of double-layer PVDF WUS in receiving mode
$\rho$	Density
$S$	$3 \times 3$ -matrix expression of of series electrically connected multiple-layer PVDF
$S^M$	$4 \times 4$ -matrix expression of series electrically connected multiple-layer PVDF
$T$	$3 \times 3$ -matrix expression of PVDF piezoelectric
$T_c$	Contraction time
$Th$	Maximum tissue thickness change

Continued on next page

## – Continue

Symbol	Definition
$TL$	Transducer loss
$ToF_{PE}$	Time of flight in the ultrasonic pulse-echo mode
$ToF_{TT}$	Time of flight in the ultrasonic through-transmission mode
$Tr$	Half-relaxation time
$T_s$	Sustain time
$\tan \delta_e$	Dielectric loss
$\tan \delta_m$	Mechanical loss
$U$	Particle velocity
$v$	Longitudinal velocity of sound
$V$	Voltage
$V_C$	Contraction velocity
$V_L$	Output voltage of the double-layer PVDF WUS
$Z_B$	Acoustic impedance of backing medium
$Z_E$	Electrical impedance of double-layer PVDF WUS
$Z_M$	Acoustic impedance of double-layer PVDF WUS
$Z_P$	Acoustic impedance of propagation medium
$Z_S$	Electrical impedance of the power source
<b>-superscript</b>	-----
+	Top surface
–	Bottom surface

Continued on next page

## – Continue

Symbol	Definition
<b>-subscript</b>	-----
<i>B</i>	Backing medium
<i>bond</i>	Bonding layer
<i>elc</i>	Electrode layer
<i>n</i>	Number of the layer
<i>PE</i>	Pulse-echo mode
<i>P</i>	Propagation medium
<i>s</i>	Single
<i>st</i>	Soft tissue
<i>TT</i>	Through-transmission mode

# Chapter 1

## Introduction

This chapter is the introduction of the thesis topic and provides an overview of the research work. The motivation, the challenges, and the objectives are presented, followed by the contribution and the organization of the thesis.

### 1.1 Overview

The analysis of the skeletal muscle mechanical characteristics is of great interest for a wide range of medical applications. The measurement of changes in the muscle contractile properties during contractions provides valuable information. For instance, the assessment of muscle contractile properties helps in investigating muscle fatigue [38, 39], diagnosing neuromuscular diseases [40, 41], evaluating the progression of treatment and rehabilitation [42–44], evaluating the efficiency and effectiveness of physical training [43], evaluating injury risks [45, 46], and controlling prosthetic devices [47–50]. The skeletal muscle is considered as a near-constant volume system; therefore, the changes in muscle length due to contractions are paralleled by the changes in muscle thickness [46, 51]. Monitoring the change in tissue thickness during muscle contraction would be a useful tool to assess muscle contractile properties [46, 52]. From the measured tissue thickness, the contractile

parameters such as maximum thickness changes ( $Th$ ), contraction time ( $Tc$ ), sustain time ( $Ts$ ), half-relaxation time ( $Tr$ ), contraction velocity ( $Vc$ ), and tetanic fusion index (FI) can be extracted [32, 46]. Estimation of the contractile parameters provide a quantitative assessment of the muscle function such as the workload intensity, the relation of the force production in respect to the muscle contraction frequency, and the degree of force loss by the muscle fatigue [32, 46, 52–54]. Thus, the quantitative evaluation of the skeletal muscle function would be a useful tool in the diagnosis of neuromuscular diseases and investigating their progression and etiology [38–42, 55, 56]. The utilization of skeletal muscle contraction measurement helps assess the impact of the clinical interventions and the evaluation of rehabilitation and training progress. For example, evaluating the muscle contractile parameters of the lower extremity before and after an anterior cruciate ligament (ACL) reconstruction surgery would provide a quantitative assessment of the improvement of the ACL reconstruction [44]. The changes of muscle contractile parameters throughout the course of the rehabilitation therapy would provide an evaluation of the effectiveness and help to aid in the optimization of therapeutic exercises[43]. Also, the routine assessment of athletes' responses to a given training facilitates the improvement and development of the training strategy [57]. Furthermore, the recognition of body movements is another application of skeletal muscle monitoring, which could be utilized in prosthetic control [48], movement assistance to vulnerable groups [49, 58], and assistive robotic device control [50].

Various measurement techniques have been explored and employed for the assessment of muscle functions. The common non-invasive methods include surface electromyography (SEMG), mechanomyography (MMG), and ultrasound imaging. SEMG signal represents the sum of electrical activity generated by the muscular electrical activation [59] while MMG measures the muscle mechanical response on the skin surface such as oscillation and acceleration. SEMG has been used extensively as a standard clinical tool for assessing

muscle function for decades, but does not provide the direct measurement of the mechanical counterpart of the muscle function [60–62]. Among the MMG sensing methods, teniomyography (TMG) and laser displacement sensors (LDS) have gained popularity as a quantitative and consistent tool for the assessment of the muscle contractile properties in recent years [31, 46]. However, they are non-wearable and susceptible to contamination by motion artifact. Most studies of muscle contractile properties using the above mentioned methods precluded dynamic contraction, such as flexion and extension of a limb, and they are usually conducted within very restrict measurement configuration to minimize limb or body movements [63, 64]. Therefore, their practical scope is limited.

Ultrasound provides real-time dynamic images of the internal tissue structure, including skeletal muscles, non-invasively with high spatial and temporal resolutions [65]. The ultrasonic method provides a direct measurement of the internal tissue thickness changes during the muscle contraction [66, 67]. Although, the bulkiness and weight of the ultrasonic B-mode imaging clinical probe might cause its undesired displacement on the skin surface during the muscle contraction, especially when limb movement is involved. While a special zig or holder could be used to minimize the undesired displacement, this approach introduces inevitable compression to the local muscles and affect their contraction/relaxation behavior.

This thesis work proposes and develops a wearable ultrasonic sensor (WUS) and method to measure the skeletal muscle contractile parameters. The motivation behind the research presented in this thesis was driven by the ongoing need for reliable, long-term and continuous monitoring of muscle contraction for the quantitative assessment of the muscle contractile properties, especially during dynamic contractions. A flexible and lightweight WUS is needed to make the attachment of the sensor to the skin surface more secure without restricting the muscle contraction beneath the sensor in order to measure muscle contractile parameters accurately. Thus, the proposed WUS is flexible, thin, and lightweight based on

double-layer configuration of the polyvinylidene fluoride (PVDF) piezoelectric polymer. The WUS takes advantage of the A-mode ultrasound measurement as a cost-effective and relatively simple technique in contrast to B-mode. A-mode ultrasound measurement is one-dimensional along the tissue depth and capable of measuring the tissue thickness with a single piezoelectric element [68, 69]. Thus, the developed double-layer PVDF WUS could provide a practical measurement tool that requires less strict posture conditions during the skeletal muscle contraction measurement. The wearability of the developed ultrasonic sensor could have advantages over the conventional methods (TMG and LDS) for the evaluation of muscle performance and the influence of fatigue during physiotherapy and physical training. Also, the recognition of body movement for prosthetics and movement assistance control. In the previous work of this author [70], the development of a wearable ultrasonic sensor (WUS) using a single-layer PVDF piezoelectric polymer was proposed for the monitoring of muscle contraction. The ultrasonic performance improvement of the WUS would enable further research in clinical applications.

This thesis research proposes for the first time, to the best of the author's knowledge, the development of the WUS using a double-layer PVDF for the measurement of skeletal muscle contractile parameters. It first presents a comprehensive literature review that discusses the limitations of the common measurement methods and the recent development of wearable sensors for muscle contraction monitoring. Then, it discusses the details of the proposed WUS design considerations and construction approach. A numerical simulation model of the developed WUS is described and implemented to study its ultrasonic performance and validate its design. Experimental measurements are conducted to evaluate the WUS ultrasonic performance. Furthermore, *in vivo* measurements of the skeletal muscle contractions are conducted to evaluate, demonstrate, and discuss the performance of the developed double-layer PVDF WUS in the quantitative assessment of the contractile

properties.

Detailed problem statements are given in **Section 1.2**, and the thesis objectives are presented in **Section 1.3**.

## 1.2 Problem Statements

The PVDF piezoelectric polymer offers flexibility and the close matching of the PVDF acoustic impedance to the biological soft tissues that provides a good coupling efficiency without the need for intermediate matching layers. However, the PVDF has a relatively weak transmitted ultrasound and requires high driving voltage to transmit sufficient ultrasonic power for deeper tissue penetration. This causes a poor signal-to-noise ratio (SNR) of the received ultrasonic pulse signals from tissue layers. One approach to improve the SNR of the received ultrasonic signals is using the double-layer PVDF configuration to increase the generated ultrasound intensity [71].

Designing a double-layer PVDF WUS demands several considerations, including the selection of PVDF film thickness, double-layer PVDF arrangement, and sensor construction elements of non-piezoelectric materials in order to improve the ultrasonic performance. Thus, theoretical studies of the ultrasonic performance and the effects of backing, electrodes, and bonding layers require a numerical simulation model to facilitate the double-layer PVDF WUS design. Additionally, constructing a double-layer PVDF ultrasonic sensor imposes the technical challenge of bonding the two PVDF layers [72]. The bonding layer of the two PVDF layers has to be thin and uniform in order for the two PVDF layers to align parallel and improve the ultrasonic performance. Another important consideration is the acoustic loading of packaging layers, which may negatively impact the ultrasonic performance. The packaging is required to bind the WUS structure and to provide protection. Therefore, a

practical bonding technique to overcome the challenges of bonding the two PVDF layers and addressing the acoustic loading of packaging layers in the WUS design are needed.

### 1.3 Objectives

The goal of this thesis work is to design, construct, and evaluate a double-layer PVDF WUS for the quantitative assessment of the skeletal muscle contractile properties. The following are the objectives to achieve the goal of this thesis.

#### 1) **Development of a numerical simulation model for the double-layer PVDF WUS**

In order to design and construct a double-layer PVDF WUS, a study on the ultrasonic performance of double-layer PVDF WUS would be required. A numerical simulation model would provide the means to study the double-layer PVDF WUS ultrasonic performance and the effects of non-piezoelectric layers, such as electrodes, bonding, and packaging layers, on the ultrasonic performance. It would also enable the evaluation of the sensor performance under varying conditions and beyond the experimental limitations. Several studies have been published in the context of piezoelectric sensor modeling. Still, they may not be directly applicable to simulate the proposed configuration of a double-layer PVDF. Therefore, the research of this part would detail the complete derivation and the formulation of a numerical model suitable for simulating and characterizing the double-layer PVDF WUS based on Mason's equivalent circuit model [73] The **Objectives 2** and **3** would be based upon this numerical simulation model.

#### 2) **Numerical simulation study of ultrasonic performance and design considerations of the double-layer PVDF WUS**

The study of the PVDF piezoelectric performance under several conditions is an essential step toward designing the double-layer PVDF WUS. The ultrasonic properties of double-layer PVDF WUS, such as operating frequency, bandwidth, acoustic output power, and power conversion efficiency, depend not only on the piezoelectric properties of the PVDF but also on the properties of non-piezoelectric layers. Therefore, the research of this part would study the double-layer PVDF WUS performance and the effects of the non-piezoelectric layers on the ultrasonic performance, using the developed numerical simulation model to obtain some guidelines for the design of double-layer PVDF WUS. Based on the numerical study results, the design considerations of the physical structure and materials selection for the double-layer PVDF WUS could be discussed.

### **3) Construction and evaluation of the double-layer PVDF WUS**

Constructing a double-layer PVDF WUS requires special considerations to address the challenges mentioned in **Section 1.2** regarding the technique of bonding two PVDF layers and the packaging approach to improve the sensor performance and to maintain its flexibility and a thin profile. Therefore, the research of this part would discuss and explain the construction procedure and techniques of the double-layer PVDF WUS. It would also experimentally evaluate the operating ultrasound frequency, ultrasonic signal strength, and noise interference of the constructed double-layer PVDF WUS.

### **4) *In vivo* experiments and evaluation of the double-layer PVDF WUS for the measurement of muscle contractile parameters**

*In vivo* experimental evaluation and demonstration of the double-layer PVDF WUS in monitoring the tissue thickness changes due to muscle contractions and assessing the contractile parameters are an integral part of this thesis work. Thus, the research of this

part would evaluate and discuss the *In vivo* performance of the developed double-layer PVDF WUS in the measurement of muscle contractile parameters during static and dynamic contractions. The *in vivo* evaluation would include the comparative study between the double-layer PVDF WUS and LDS, as one of the MMG measurement methods, in the measurement of the muscle contractile parameters.

## 1.4 Contributions

Several academic contributions were achieved upon the accomplishment of the thesis objectives. They are summarized and listed as follows:

- 1) A numerical simulation model was developed for the numerical characterization of the double-layer PVDF configuration. A complete derivation and formulation of transfer matrix expressions of the PVDF and non-piezoelectric layers for the proposed design of the double-layer PVDF WUS based on Mason's equivalent circuit model were presented. The formulated matrix expression accounted for the voltage orientation reversal of the parallel electrically connected double-layer PVDF and the internal losses of the PVDF. Thus, the model enabled the calculation of ultrasonic performance, such as the operating frequency, frequency bandwidth, acoustic power, and conversion efficiency.
- 2) The design of a double-layer PVDF WUS was presented. The ultrasonic performance of the double-layer PVDF configuration was studied in detail under several conditions using the developed numerical simulation model. The numerical study included the effects of the non-piezoelectric layers, such as backing, bonding, and electrode layers for several materials and layer thicknesses. Afterward, the design considerations,

approaches, and material selections of the double-layer PVDF WUS were discussed based on the numerical simulation study results. The negative effect of the packaging layers on the ultrasonic performance was addressed in the presented design by using an acoustic insulator layer.

- 3) A novel double-layer PVDF WUS was constructed using two 52- $\mu\text{m}$ -thick PVDF layers with silver ink electrodes that were bonded by a thin epoxy layer. A construction procedure that addressed the practical difficulties involving the PVDF layer bonding and packaging the double-layer PVDF WUS structure was established using basic equipment and ordinary hand tools. The constructed double-layer PVDF WUS showed 1.7 times greater ultrasonic signal amplitude in comparison to a single-layer PVDF WUS of equivalent total PVDF layer thickness.
- 4) *In vivo* measurements of the skeletal muscle contractile parameters using the double-layer PVDF WUS were conducted. The double-layer PVDF WUS measurement was compared with the LDS measurement. It was verified that a proposed ultrasound measurement method with the double-layer PVDF WUS was less affected by motion artifact caused by the undesired body movement. Also, *In vivo* demonstrations of the developed double-layer PVDF WUS and ultrasound method were presented for skeletal muscle contraction monitoring. The quantitative assessment of tetanic contraction progression was successfully demonstrated.
- 5) Several academic papers were published based on the outcomes of this thesis research. Publications related to this thesis work:  
  
Journal article:
  - Ibrahim AlMohimeed and Yuu Ono. Ultrasound measurement of skeletal muscle

contractile parameters using flexible and wearable single-element ultrasonic sensor. *Sensors*, 20(13):3616, 2020. doi: 10.3390/s20133616. (Chapter 6).

Proceeding papers:

- Ibrahim AlMohimeed and Yuu Ono. Flexible and wearable ultrasonic sensor for assessment of skeletal muscle contractile properties. In *proceeding of IEEE International Conference on Flexible and Printable Sensors and Systems (FLEPS)*. IEEE, 2019. doi: 10.1109/fleps.2019.8792301. (Chapters 5 and 6)
- Ibrahim AlMohimeed, Manas Agarwal, and Yuu Ono. Wearable Ultrasonic Sensor Using Double-Layer PVDF Films for Monitoring Tissue Motion. In *proceeding of IEEE Canadian Conference on Electrical & Computer Engineering (CCECE)*, pages 1–4, 2018. doi: 10.1109/ccece.2018.8447859. (Chapters 4, 5, and 6)

Publications related but not included to this thesis:

- Elliot Yeung, Ibrahim AlMohimeed, and Yuu Ono. Ultrasonic sensor and method for monitoring of skeletal muscle contraction evoked by electromyostimulation. In *proceeding of international symposium on advanced biomedical ultrasound*, pages 1–2, 2020
- Elliot Yeung, Ibrahim AlMohimeed, and Yuu Ono. Estimation of tissue thickness changes due to electrical muscle stimulation using wearable ultrasonic sensor in pulse echo mode. In *proceeding of IEEE Sensors*, pages 1–4. IEEE, 2019. doi: 10.1109/sensors43011.2019.8956742.

## 1.5 Thesis Structure

This thesis is organized into seven chapters, briefly described as follows:

### **Chapter 1: Introduction**

This chapter is the introduction of the thesis topic. It presents an overview of the research and statements regarding the thesis research problems, objectives, and contributions, followed by the structure of the thesis.

### **Chapter 2: Literature Review of Muscle Monitoring**

This chapter provides the literature reviews of the medical applications, common measurement methods, challenges and limitations, and recent development of wearable sensors that are related to skeletal muscle monitoring.

### **Chapter 3: Numerical Simulation Model for the Double-Layer PVDF WUS**

This chapter presents the derivation and the formulation of the numerical simulation model of the double-layer PVDF WUS based on Mason's equivalent circuit model. The literature reviews of the mathematical models and formulation methods for the piezoelectric ultrasonic sensors are also presented.

### **Chapter 4: Numerical Study and Design Considerations of the Double-Layer PVDF WUS**

This chapter studies and discusses the developed double-layer PVDF WUS design based on the numerical simulation model developed in Chapter 3:. It first studies the ultrasonic performance of the double-layer PVDF WUS and the effects of the non-piezoelectric layers on ultrasonic performance using the numerical simulation

model. Then, it discusses the design considerations and challenges based on the results of the numerical study.

### **Chapter 5: Construction and Experimental Performance Evaluation of the Double-Layer PVDF WUS**

This chapter presents the construction procedure and techniques of the double-layer PVDF WUS, followed by the experimental performance evaluation of the double-layer PVDF WUS constructed.

### **Chapter 6: *In Vivo* Experimental Evaluation of the Double-Layer PVDF WUS for the Measurement of Skeletal Muscle Contractile Parameters**

This chapter presents the evaluation and demonstration of the developed double-layer PVDF WUS in in-vivo experiments for monitoring of muscle contraction. It investigates the WUS and the ultrasonic measurement method performance in monitoring the skeletal muscle contractions and the quantitative assessment of the contractile properties.

### **Chapter 7: Conclusions and Future Research**

This chapter summarizes and reviews the thesis research and provides suggestions for future research.

## Chapter 2

# Literature Review of Muscle Monitoring

This chapter provides a comprehensive review of medical applications and common non-invasive methods related to the monitoring of muscle contraction. The literature review is an integral part of the development of the wearable ultrasonic sensor and the ultrasound method introduced in this thesis work. In this review, the clinical importance of the skeletal muscle function assessment is highlighted. The challenges and limitations of the current measurement methods as well as recent developments in wearable sensors relevant to the monitoring of muscle contraction are discussed in detail.

This chapter is organized as follows: **Section 2.1** describes the importance of muscle function assessment for medical applications; **Section 2.2** discusses the common non-invasive measurement methods of muscle mechanical function and their limitations; **Section 2.3** presents the development status of wearable and flexible ultrasonic transducers; **Section 2.4** surveys the recent development of other wearable sensors for muscle monitoring.

## 2.1 Skeletal Muscle Function Assessment

### 2.1.1 Human Muscle Physiology

Muscle is a specialized tissue which converts chemical energy into mechanical energy when it is stimulated. The main properties of muscle tissue are excitability, contractility, extensibility, and elasticity. Muscles respond to stimulation either by shortening or stretching and recoil back to the original length after the stimulation [79]. Muscle tissues, in general, are composed of a firmly organized internal structure of long, cylindrical cells known as muscle fibers that are bundled together and wrapped in a connective tissue covering called the epimysium, as shown in **Figure 2.1**.

Within each muscle fiber are myofibrils which are long-cylindrical structures lying parallel to the muscle fiber. Myofibril is divided into segments of the functional unit of muscle, the contractile element, known as a sarcomere. The sarcomeres are composed of thin and thick filaments. The thin filaments are attached at one end of the sarcomere (Z-line) toward the center where the thick filaments extend along the center of the sarcomere (M-line) and overlap with the thin filaments, as shown in **Figure 2.2** [79–81]. Muscle contraction occurs as a result of the sliding of filaments. When the muscle is stimulated, the distance between the Z-line is shortened due to the sliding of the thin and thick filaments toward each other, as shown in **Figure 2.3**.

There are three types of muscular tissue: skeletal, cardiac, and smooth muscles. This thesis work focuses on the measurement of soft tissue thickness due to skeletal muscle contractions. The skeletal muscles of the human enable the body movement and the force to maintain posture. Skeletal muscles are controlled mainly voluntarily and account for nearly 40% of human body weight [82, 83]. A skeletal muscle is stimulated by an action potential,

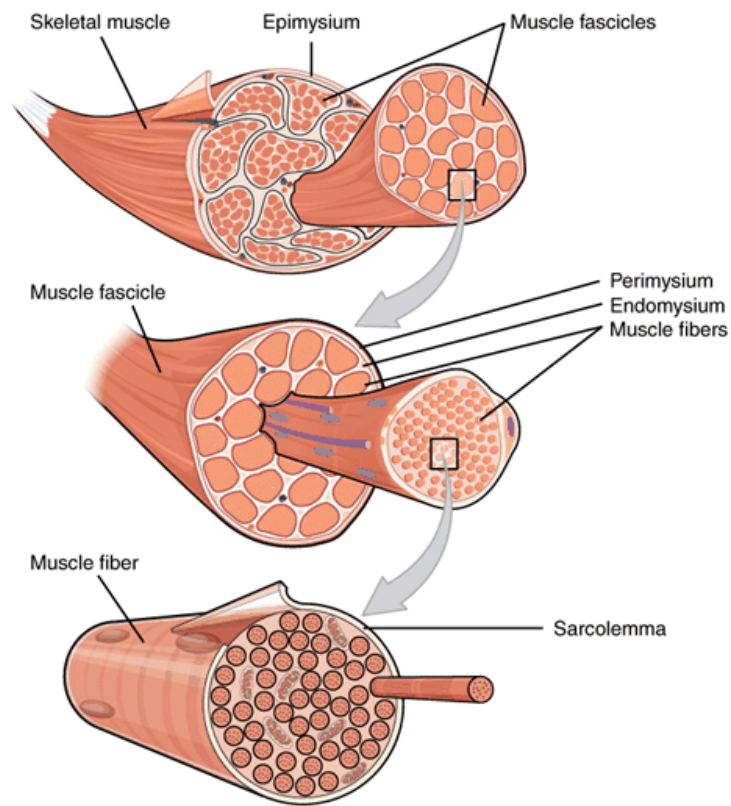


**Figure 2.1:** Internal structural layers of muscle tissue. Adapted from OpenStax, Wikimedia (CC BY 4.0 license)

a biological electrical pulse, delivered by the motor neuron at the neuromuscular junctions. Then, the stimulation spreads across the muscle fiber membrane (sarcolemma), which leads to the sliding of filaments. This series of events from nerve impulse to the contraction is known as an excitation-contraction coupling [84]. A single motor unit is connected to a group of muscle fibers. The number of muscle fibers connected to a motor unit varies from several muscle fibers to thousands of muscle fibers [80]. For example, in the muscles of a hand where fine control is needed, a motor unit is connected to a few fibers. While a stronger force is needed in the muscles of a leg, a motor unit is connected to a larger number of fibers [85]. The intensity of muscle contraction is controlled for the required force by adjusting the number of activated motor units. The process of additional activation of motor units

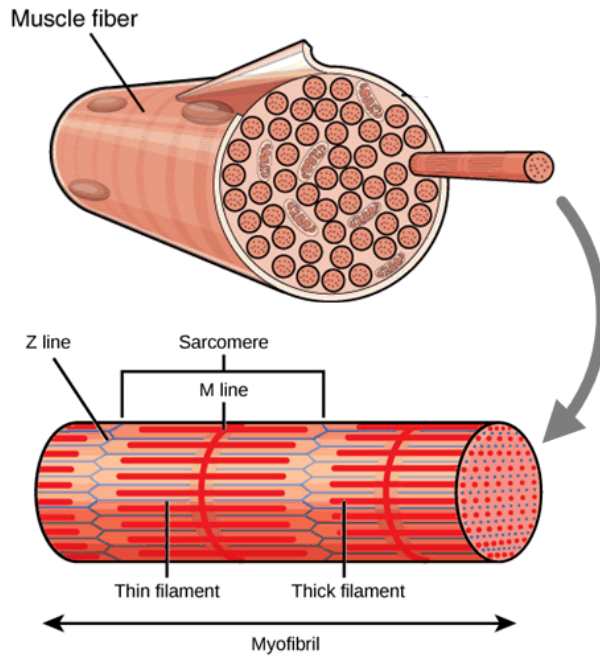


**Figure 2.2:** A muscle fiber composed of myofibril bundles. Each myofibril is divided into segments of sarcomere. Adapted from OpenStax, Wikimedia (CC BY 4.0 license).

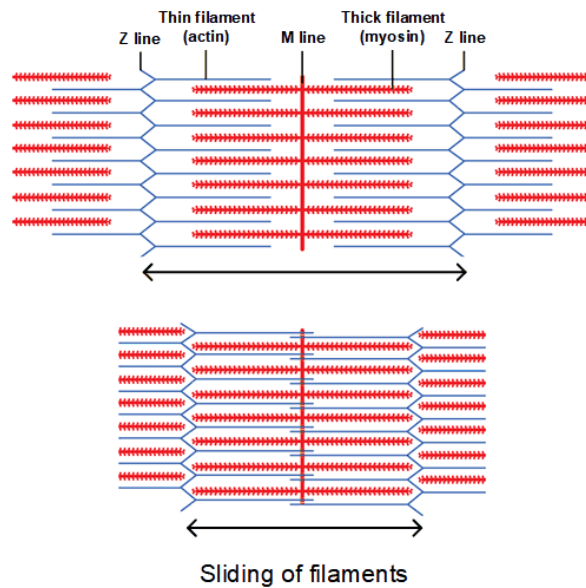


**Figure 2.3:** The sliding of sarcomere filaments. Contraction occurs as a result of the overlap of thin and thick filaments. Adapted from OpenStax, Wikimedia (CC BY 4.0 license).

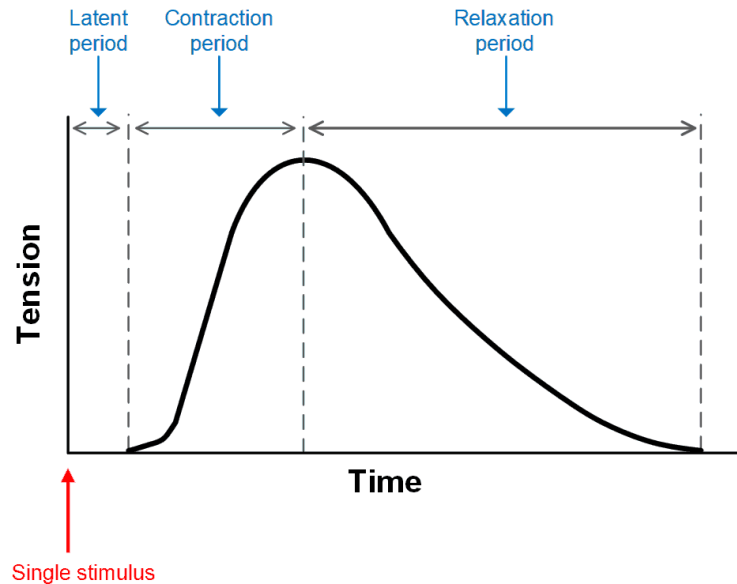


**Figure 2.4:** Typical twitch response of a skeletal muscle.

to accomplish the increase in contraction intensity is referred to as motor unit recruitment. A long period of muscle contraction is usually achieved by alternating the recruitment of motor units.

A muscle fiber responds to a single action potential of the motor unit by contraction and relaxation. A single stimulation response is known as a twitch, which begins with a latent period followed by a contraction period and then a relaxation period. The latent period is a brief delay before the beginning of the contraction, which is the time of action potential propagation along the muscle fiber length. The muscle fiber starts shortening during the contraction period and returns to its original length at the end of the relaxation period. **Figure 2.4** shows the typical twitch response of a skeletal muscle.

When the muscle fiber receives a second stimulus during the relaxation period before reaching the full relaxation state, the new contraction builds at a higher level of tension and consequently achieves higher contractile tension. The stimulation rate at which the fiber

has partial relaxation between stimuli results in a sustained but wavering contraction called unfused (incomplete) tetanus. The partial relaxation will get shorter as the stimulation rate increases up to a point where the fiber does not relax and results in constant contraction called a fused (complete) tetanus [81]. When a muscle sustains a prolonged contraction period, its contraction intensity starts to decline which results in a temporary state of fatigue. The muscle fibers are generally divided into two types: slow-twitch (type I) and fast-twitch (type II) [79]. On average, fast-twitch fibers have five to six times faster contraction time than slow twitch. However, muscle twitch time varies among muscle types and locations.

Skeletal muscles perform different types of contraction to maintain posture or to create movement. The contraction can be sorted into two groups based on whether or not a movement occurs during a contraction. These two groups are isometric and isotonic contractions [81]. In an isometric (static) contraction, the muscle contracts to resist an applied force without movement. Holding a weight in a stationary position is an example of isometric contraction. Isotonic contraction is a dynamic contraction in which the muscle produces a movement. The movement resulting from the shortening of the muscle fiber is a concentric contraction, whereas the movement resulting from the stretching of the muscle fiber is an eccentric contraction. An example of a concentric contraction is lifting a weight from the ground, whereas lowering the weight to the ground is considered an eccentric contraction.

### **2.1.2 Medical Applications**

Analysis of the mechanical characteristics of skeletal muscle is of great interest to a broad spectrum of medical applications. The measurement of changes in the physical parameters during muscle contractions provides valuable information. The skeletal muscle is considered

as a near-constant volume system; therefore, muscle length changes due to contractions are paralleled by the changes in muscle thickness [46, 51]. The skin surface fluctuations during muscle contractions are related to the dimensional changes of the active muscle fibers and possess physiological information about the muscle contractile properties [32, 86]. Thus, monitoring the change in muscle thickness during contractions would provide a wealth of information about the muscle function [46, 52]. The workload intensity and the stiffness of the muscle can be estimated by measuring the mechanical parameters of the muscle contraction [53]. The motor unit recruitment and firing rate have shown distinct patterns of activation at different work intensity levels of isometric, concentric, and eccentric contraction types [87]. The sound recording of the muscle contraction was found to resemble the output force of the contractions over the measured time [88]. The relationship between the force production of a skeletal muscle and its contraction frequency could be utilized to assess the muscle functions. For example, the observation of a thenar muscle force-frequency relationship (FFR) showed that 50% of maximum force occurs at low excitation rates of 12 Hz, and the maximum tetanic force was achieved between 30 and 100 Hz [54]. Also, the changes of FFR have been related to the degree of force loss indicated by fatigue [32]. The measurement of muscular activity by mechanomyography (MMG) and the metabolic activity through the oxygen consumption rate ( $VO_2$ ) during the incremental cycle ergometry demonstrated a close association between MMG and  $VO_2$  [89].

The quantitative evaluation of the skeletal muscle function has gradually evolved as a useful tool in clinical diagnosis. For example, the characteristic differences in contraction between Parkinson's patients and a control group were indicated. The electromechanical delay of contraction (EMDc), electromechanical delay of relaxation (EMDr), and contraction time to half tetanus (CTT1/2) were measured from the stimulated tetanic contraction at 20 Hz [41]. A substantial difference of CTTI/2 between the Parkinson's patients and the

control group was observed, which may describe the change in characteristics of muscle contraction in patients with Parkinson's disease. The muscle contraction measurement could indicate the muscle fatigue stages during electrically evoked exercises in individuals who lack voluntary muscle recruitment. The study of individuals with spinal cord injury (SCI) during electrically evoked exercises by Mohamad et al. [55] demonstrated the detection of different muscle contraction levels and fatiguing contraction by measuring the mechanical changes using tensiomyography (TMG). Ng et al. [39] also showed the ability of TMG to detect fatigue during electrically evoked contraction of an SCI patient. The assessment of muscle contraction helps to investigate the etiology of neuromuscular diseases. For instance, the deterioration in contractile properties of the measured bicep contractions in patients with spastic cerebral palsy (CP) suggested that the motor disabilities are not only due to neural impairment but also due to muscle fiber atrophy [40]. In addition, the analysis of erector spinae muscle measurements during isometric lower-back extension using surface electromyography (SEMG), microphone, and near-infrared spectroscopy indicated that the restriction of blood flow due to high intramuscular pressure is one of the most important underlying factors of lower-back muscle fatigue [38]. Furthermore, monitoring muscle contraction is valuable in detecting and evaluating the progression of some diseases such as cancer cachexia and chronic obstructive pulmonary disease (COPD) [42, 56].

The impact assessment of the clinical interventions and the evaluation of rehabilitation and training progress would benefit greatly from the utilization of skeletal muscle contraction measurement. For example, measuring the muscle contractile parameters of the lower extremity before and after an anterior cruciate ligament (ACL) reconstruction surgery would provide a quantitative assessment of the improvement of the ACL reconstruction in comparison with the uninjured leg [44]. Monitoring the changes of muscle contractile parameters throughout the course of the rehabilitation therapy would provide objective

feedback to aid in the optimization of therapeutic exercises and evaluate their effectiveness [43]. The advantage of skeletal muscle monitoring has garnered the interest of many sports medicine practitioners and conditioning coaches [46]. The routine assessment of athletes' responses to a given training facilitates the improvement and development of the training strategy [57]. For instance, the study of the effect of training between soccer player groups that endure two types of training courses by Rusu et al. [90] showed a substantial difference in the measured parameters, such as contraction time and muscle displacement, between the groups. The quantitative assessment of skeletal muscles could also be employed to assess the risk of injury to athletes and aid in the design of adequate prevention programs [45, 46]. For example, the measured parameters of the evoked hamstring and quadriceps muscles contraction on the injured leg side of soccer players with confirmed ACL tear, demonstrated substantially soccer players [45]. The measured parameters include, maximal displacement, delay time, contraction time, sustained time, and half-relaxation time.

Furthermore, the recognition of body movements is another application of skeletal muscle monitoring, which could be utilized in prosthetic control [48], movement assistance to vulnerable groups [49, 58], and assistive robotic device control [50]. For instance, the study by Ding et al. [47] demonstrated the recognition of finger gestures using the MMG measurement for prosthesis control applications.

The medical applications of muscle function assessment might be limited by the current sensing method. There is still a need for a reliable and wearable measurement method that would provide continuous monitoring with more tolerance to motion artifacts due to the limb and/or body motion. Utilizing a wearable ultrasonic method to measure muscle contractile properties could offer advantages for medical applications.

## **2.2 Common Measurement Methods and Limitations**

A variety of medical sensing methods have been employed to provide a diverse assessment of muscle functions. Generally, measurement methods can be categorized into invasive and non-invasive techniques. Invasive techniques usually require internal access to the human body via an incision, puncture needle, or surgery. In contrast, non-invasive techniques are employed by attaching sensors to the skin surface. The focus of this review is on the exploration of common, non-invasive and portable measurement methods for the assessment of muscle function. The common approaches include SEMG, MMG, and ultrasound imaging.

### **2.2.1 Surface Electromyography (SEMG)**

SEMG is a conventional modality to monitor muscle activity and has been used extensively for muscle assessment for decades [62]. The signal of SEMG represents the sum of the electrical activities generated by the muscles located near the biopotential electrodes attached to the skin surface. The increase of contraction force is a result of the increase of the motor unit recruitment and the firing frequency of activated motor units. However, the quantification of muscle mechanical activities from SEMG signals is challenging. The relationship complexity of biological electrical signal and mechanical activity of the muscles impose a limitation of the analysis of the muscle mechanical function and the variability in interpretation among researchers [61, 91, 92]. Additionally, the electrode displacement, electrical interference (cross-talk) between adjacent muscles, contact resistance, skin humidity, and surrounding electrical interference contribute to the difficulty in obtaining a reliable relation between the electrical activity and the mechanical performance of the muscle, especially in dynamic contractions [91, 93]. Thus, SEMG measures the muscle electrical activity, but might not

directly measure the muscle mechanical activity [61].

### 2.2.2 Mechanomyography (MMG)

Contrary to SEMG, MMG is the measurement of the muscle mechanical activity on the skin surface that results from the voluntary or electrically evoked contractions [61, 94, 95]. The mechanical signal measured by MMG sensors reflects the mechanical counterpart of the electrical activity of the motor units. There are several types of sensors employed in the MMG measurement method such as: piezoelectric sensor, condenser microphone, accelerometer, and laser displacement sensor (LDS) [32, 46, 95, 96].

Piezoelectric contact sensors are mechanically coupled to the skin surface near the muscle of interest, usually using an elastic band or external support to measure skin displacement [97]. Condenser microphones are usually placed on one end of a cylinder with an air chamber where the other end of the cylinder is attached to the skin surface. The air chamber converts the muscle vibration to a pressure change, which is then detected by the condenser microphone [98]. The signals of the piezoelectric contact sensor and the condenser microphone are sensitive to the contact pressure of the attachment, which contributes to a variation of the amplitude response [32]. Also, the pressure exerted by the attachment method and the mass loading of the size of the sensor might affect the skin surface dynamic during the muscle contraction. Thus, the influence of the contact pressure on the temporal and spectral response of the measurement is a major drawback.

Accelerometers detect the local motion on the skin surface due to the muscle contraction by measuring the acceleration in one or more axes of the motion directions [99]. One advantage of the accelerometer is that output signal could easily be converted to a physical unit ( $m/s^2$ ) to allow a direct comparison between the results of different experiments [100].

The low mass of accelerometers (less than 2 g) is another advantage that facilitates the simple attachment to the skin surface without interfering with muscle surface dynamic. However, the accelerometer signal is highly influenced by motion artifacts, especially during dynamic contractions [63, 98, 101].

LDSs are non-contact sensors that detect the distance between the laser-beam head and the skin surface above the muscle [32]. The laser beam measures the position changes as the skin surface moves towards or away from the laser head. This high-speed laser technology provides a high-resolution measurement (a fraction of a millimeter) of muscle thickness changes during isometric contraction [31, 102–104]. As an alternative MMG method, TMG was developed to measure muscle displacement during an electrically evoked muscle contraction [52]. The TMG method employs a high-precision displacement sensor. The displacement sensor tip is pressed onto the skin surface with a controlled pre-tension while the sensor body is attached to a fixed support [105]. TMG measures the displacement of the skin surface due to an electrically evoked muscle twitch. LDS and TMG directly measure the skin surface displacement due to muscle contraction. This advantageous feature provides further physiological information by extraction of the muscle contractile parameters from the TMG and LDS waveforms with no extensive postprocessing or filtering [31, 104–107]. In recent years, LDS and TMG methods have been favored for the assessment of the muscle contractile properties among other MMG methods [31, 46, 106–112]. However, they examine the electrically evoked contractions exclusively through static contraction [113]. During the measurement of muscle contraction using LDS or TMG, the subject is required to remain still on the examination table to minimize any limb or body movements in order to reduce the motion artifact in the measurement [31, 63, 100, 114]. The restriction of body movement limits the practicality of frequent monitoring with a more convenient measurement setup for a subject where the muscle functions in daily activities and sports

involve dynamic contraction.

In general, motion artifact is the main challenge regarding MMG measurement methods, especially during dynamic measurement, which limits their utility [61, 63, 115]. The dynamic contraction of the muscles as well as limb movements impose undesired displacement of the employed MMG sensor on the skin surface [116]. Other considerations are the degree of wearability and the uncertainty regarding the reliability of MMG methods [31]. In addition, the skinfold thickness might attenuate MMG spectral and temporal characteristics, especially in deeper muscles [117].

### 2.2.3 Ultrasound Imaging

Ultrasound could provide real-time dynamic images of the internal tissue structure, including skeletal muscles, non-invasively with high spatial and temporal resolutions [65]. The ultrasonic imaging method would allow a measurement of the internal tissue thickness for both superficial and deep-layered muscles without crosstalk from those adjacent [66, 67]. Ultrasound imaging has been used widely in the assessment of skeletal muscle function as well as tracking the muscle thickness changes during static and dynamic contractions [66, 118–132]. Many studies have demonstrated the use of ultrasound images to detect the changes of muscle thickness [133–135], pennation angle [136, 137], cross-sectional area [138], and muscle fascicle length [139].

B-mode ultrasound images are captured by a B-mode clinical ultrasound imaging system with a handheld ultrasound probe, as shown in **Figure 2.5**. The basic ultrasound probe is composed of a piezoelectric ceramic array, electrodes, backing layer, and matching layer, as shown in **Figure 2.6**. Piezoelectric ceramics are the active elements that transmit and receive ultrasound. They are used in nearly all medical ultrasound probes [140]. Electrodes are



**Figure 2.5:** A conventional hand-held ultrasound probe. Reproduced from from Drickey at English Wikipedia (CC BY-SA 2.5)

an electrically conductive material formed on the top and bottom surfaces of piezoelectric elements such as gold, silver, and copper, which are connected to cable leads. In order to dampen the internal reverberations (ringing) within the piezoelectric elements, a layer of high absorption coefficient is attached to the back side. Piezoelectric ceramics have a much higher acoustic impedance compared to soft tissues. Therefore, an acoustic impedance matching layer is bonded to the piezoelectric elements at the front side to increase the transmission of the ultrasound into the soft tissue.

The bulky size of the ultrasound probe causes an undesired displacement over the skin surface during the muscle contraction, especially where limb movement is involved [29, 120, 124, 127, 141]. Such an undesired probe displacement could cause an inaccurate estimation of the underlying tissue thickness. A special zig or holder could be used for the steady attachment of the ultrasonic probe and minimize the undesired displacement on the skin surface in order to monitor the muscle contraction accurately. However, the pressure exerted on the skin surface by the weight of the ultrasonic probe and/or the attachment method might restrict the natural motion and muscle contraction of underlying tissue [133]. Thus, the continuous monitoring of the muscle contraction may be limited by conventional ultrasonic imaging probes. In addition, the creation of the two-dimensional ultrasound

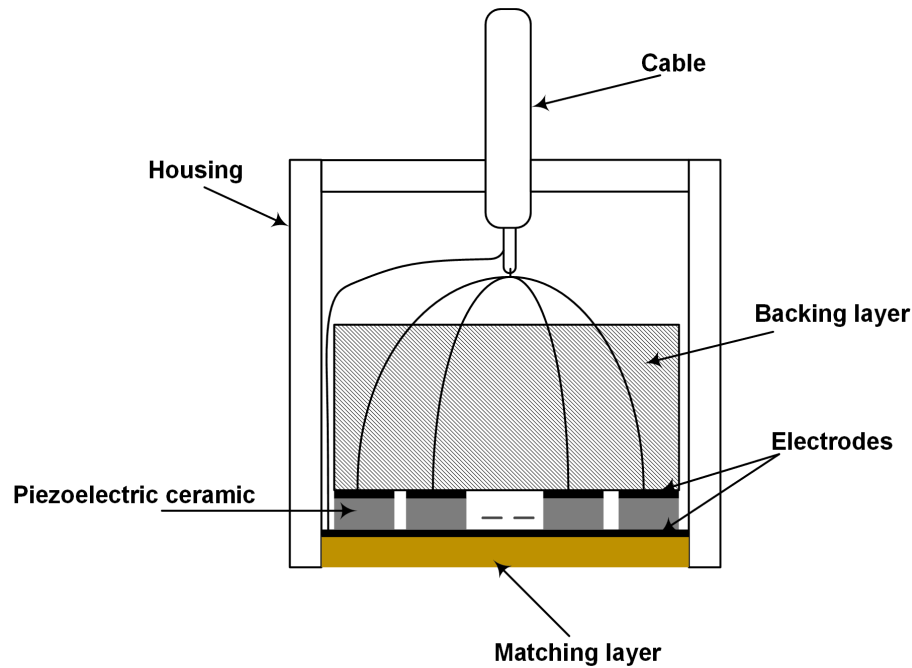


**Figure 2.6:** A basic structure of an ultrasound probe.

images require high computational power and sophisticated processing techniques.

## 2.3 Wearable Ultrasonic Transducers

A-mode ultrasound measurement has been proposed as a more wearable and cost-effective alternative for measuring muscle activities [1]. In contrast to B-mode ultrasound, A-mode ultrasound is one-dimensional along with the tissue depth that is capable of directly measuring tissue thickness changes due to muscle contraction with a single piezoelectric element [68, 69]. Thus, A-mode ultrasonic transducer (UT) can be made smaller, which might address the limitations of the bulky multiple-element B-mode ultrasonic probe. A smaller single-element UT could make the UT attachment more accessible and stable on the desired location on the skin surface.

The work of Guo et al. [1, 142] may be one of the earliest studies using a single-element

UT for tracking the thickness changes during the skeletal muscle contraction, as shown in **Figure 2.7** (a). They demonstrated the tracking of the extensor carpi radialis muscle that controls the movement of the wrist. The ultrasonic measurement in their result showed a higher accuracy of tracking the wrist extension in comparison to the SEMG measurement. The study by Sun et al. [2] showed that the single-element UT, developed by Hettiarachchi et al. [143], could effectively assess muscle fatigue from the measured muscle thickness changes, as shown in **Figure 2.7** (b). Yang et al. in [3, 4, 130] presented the estimation of muscle force and the prediction of finger motion using an A-mode ultrasound of four single-element UTs, as shown in **Figure 2.7** (c) and (d). Also, Zhou et al. [5] demonstrated an A-mode ultrasound sensing approach in the prediction of finger movement with voluntary and electrically evoked muscle contractions using a single-element UT, as shown in **Figure 2.7** (e). Furthermore, Shahshahani et al. [6, 144] introduced a respiratory detection system based on tracking the diaphragm wall motion using a single-element UT mounted on flexible printed circuit board (PCB), as shown in **Figure 2.7** (f).

The single-element UTs employed in the above-mentioned studies [1, 2, 4, 6, 130, 142, 144] were made of piezoelectric ceramic, which is a rigid and inflexible material. The piezoelectric ceramics such as lead zirconate titanate (PZT) are commonly used as a UT material due to their superior electromechanical performance. Therefore, the issue of displacement of the single-element UTs on the skin may still persist. Guo et al. [1, 142] indicated in their work that the ultrasonic tracking errors increased when the dynamic movement of the wrist joint extension increased from 20 to 50 cycle/min. Also, Shahshahani et al. [6] noted that the placement of a single-element UT posed challenges when tracking the diaphragm wall motion for respiratory activity monitoring. The single-element UT could be firmly attached to the skin surface using a body-worn band in order to minimize the undesired UT displacement during the muscle contraction. However, this approach

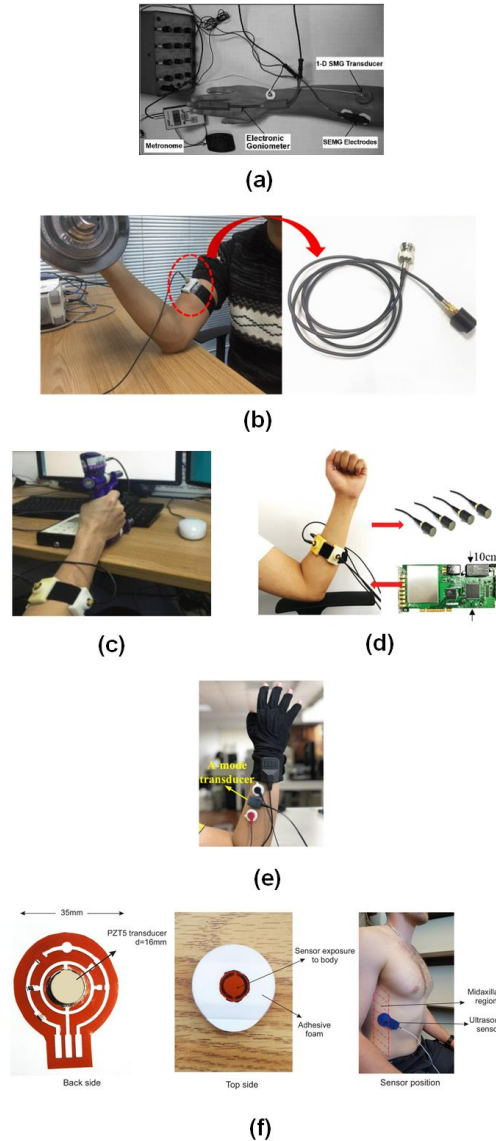


**Figure 2.7:** Photos of single-element UTs for muscle activity monitoring. A photo of the single-element UT for A-mode measurement of tissue thickness changes during the skeletal muscle contraction by [1] (a), photos of the single-element UT attachment using armband for muscle fatigue assessment by [2] (b), a photo of the four single-element UTs attachment using armband for muscle force estimation by [3] (c), a photo of the four single-element UTs for finger motion prediction by [4] (d), a photo of the single-element UT attachment for finger motion prediction with voluntary and electrically evoked muscle contraction by [5] (e), and photos of the single-element UT mounted on flexible printed circuit board (PCB) for tracking diaphragm wall motion by [6] (f).

introduces inevitable compression to the local muscles and affect their contraction/relaxation behavior, leading to inaccurate of the muscle contractile parameters.

Compared to the rigid UTs, a flexible, thin, and lightweight UT may have the advantage of steady UT attachment to the skin surface since it could be conformably attached to the curved skin surface. The MEMS technology has recently emerged for fabricating a relatively flexible miniaturized UT array for medical imaging. Yang et al. [7] and Wang et al. [8] introduced fabricated piezoelectric micromachined ultrasound transducer (PMUT) arrays by mounting diced PZT piezoceramic into patterned cavities on a flexible polyimide film, as shown in **Figure 2.8**. Similarly, Mastronardi et al. [9] and Sun et al. [10] used aluminum nitride (AlN) as a piezoelectric material instead of PZT, to be embedded onto a flexible polyimide substrate, enabling more flexible and thinner PMUT, as shown in **Figure 2.9**. Singh et al. [11], Sadeghpour et al. [12], Hu et al. [13], and Wang et al. [17] exploited the island-bridge technique by mounting small pieces of PZT elements into a microfabricated array of rigid islands that were connected with flexible polyimide joints, as shown in **Figure 2.10**. Also, Cheng et al. [14] and Chong et al. [15] fabricated flexible UT arrays based on capacitive micromachined ultrasound transducer (CMUT) using a concave bottom electrode, as shown in **Figure 2.11**. Fabrication of CMUT using polymeric materials was also described by Gerardo et al. [145] as a potential cost-effective flexible CMUT. Furthermore, Lanata et al. [16] introduced a flexible UT based on polyvinylidene fluoride (PVDF) piezoelectric polymer integrated into a textile belt that could be wrapped around the body. **Table 2.1** summarizes the wearable ultrasonic transducers and their medical applications described in the above-motioned studies in tabulated form.

A few studies examined the flexible UT for the measurement of internal tissue motion in human subjects. Lanata et al. [16] presented the heart wall motion monitoring using the flexible UT based PVDF polymer piezoelectric material. The PVDF UT was integrated into

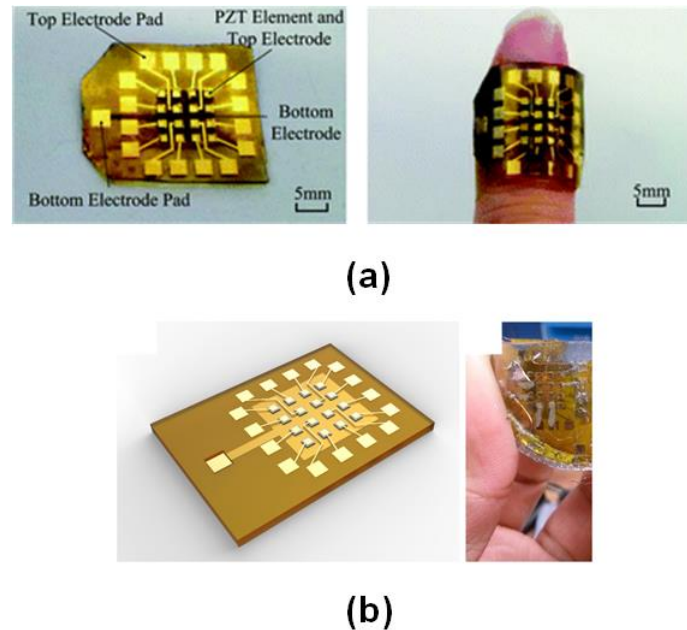


**Figure 2.8:** Flexible PMUT arrays by mounting diced PZT piezoceramic into patterned cavities on a flexible polyimide film. The photos of the PMUT array fabricated by [7] (a) and a schematic drawing and a photo of the PMUT array fabricated by [8] (b).

a belt and wrapped around the chest, as shown in **Figure 2.12** (a). Their results showed the potential for the continuous monitoring of cardiopulmonary activity. Wang et al. [17] also demonstrated the monitoring of blood pressure by measuring the arterial wall motion using a thin, stretchable PMUT, as shown in **Figure 2.12** (b). Their stretchable UT offers the capability of measuring human tissue up to a depth of 40 mm and was demonstrated in the estimation of the blood pressure at the carotid, brachial, radial, and pedal arteries using the ultrasonic wall-tracking technique. However, to the best of the author's knowledge, there is still no research focusing on the application of flexible and wearable single-element UT using the A-mode ultrasound measurement for measuring the muscle contractile parameters, especially when combined with limb or body movements. In the previous work of the author [70], a preliminary development of a wearable ultrasonic sensor (WUS) using a single-layer PVDF piezoelectric polymer was proposed for the monitoring of muscle contraction. The

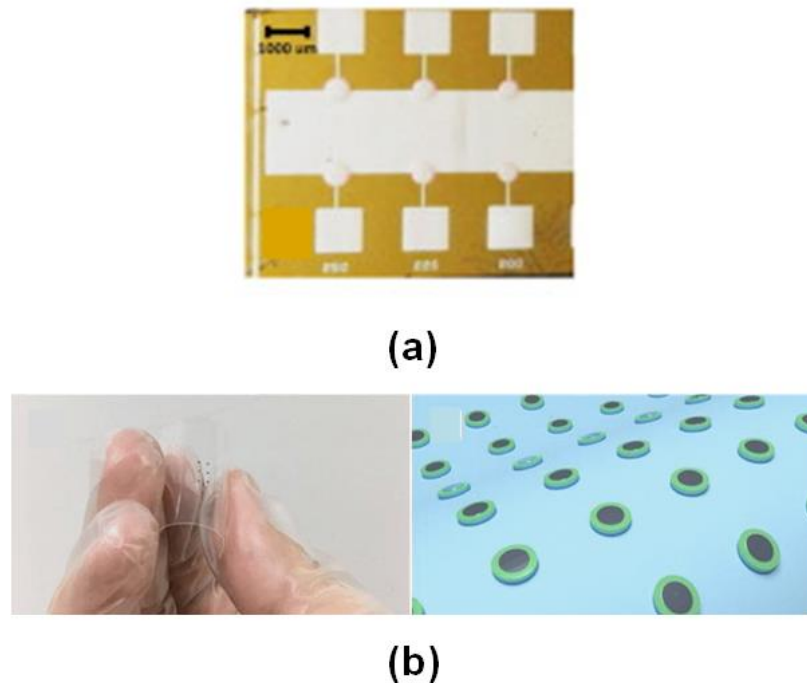


**Figure 2.9:** Flexible PMUT arrays by embedding aluminum nitride (AlN) piezoelectric onto a flexible polyimide substrate. A photo of the AlN flexible PMUT array fabricated by [9] (a), and a photo and a schematic drawing of the flexible PMUT array fabricated by [10] (b).

feasibility of the proposed WUS was demonstrated in monitoring muscle contraction up to the depth of 34 mm [70, 146, 147]. The weak ultrasonic signal strength and the dual operating frequencies of the previously developed WUS are the main issues that require further research.

The PVDF piezoelectric polymer offers advantageous features such as flexibility, thinness, and lightweight. The close matching of the PVDF acoustic impedance to the biological soft tissues provides a good coupling efficiency without the need for intermediate matching layers, which is usually required for the piezoelectric ceramic sensors. The PVDF is a flexible material that would allow the bending over the uneven and rounded nature of the human body surface. The availability of PVDF in large-area film sheets allows the ease of fabricating

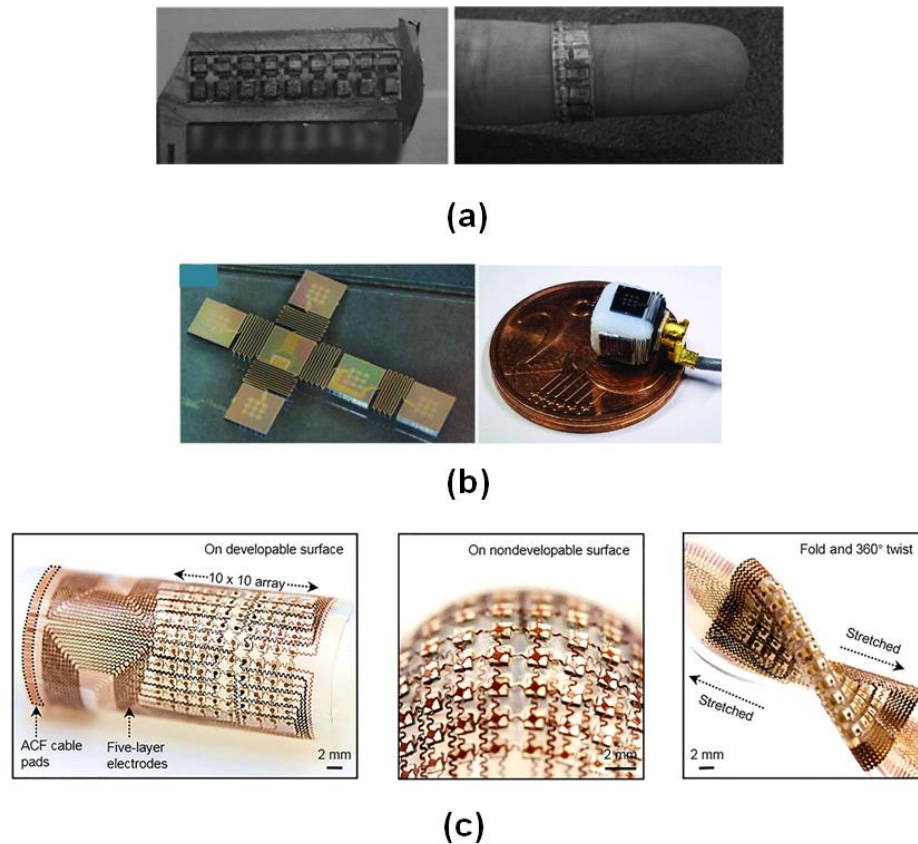


**Figure 2.10:** Flexible PMUT arrays using island-bridge technique. Photos of the flexible PMUT arrays by [11] (a), photos of the flexible PMUT arrays fabricated by [12] (b), and photos of the stretchable PMUT arrays fabricated by [13].

the ultrasonic sensor into any desired dimensions. These features make constructing a flexible, thin, lightweight, and small in size ultrasonic sensor feasible. These features of PVDF attracted the interest for several medical applications such as high-frequency medical imaging [148], photoacoustic imaging [149], and transcranial therapy monitoring [150]. However, the PVDF has less acoustic output than the piezoceramic piezoelectric due to the weak piezoelectric properties, large dielectric and elastic losses, and a low dielectric constant. Thus, designing a PVDF ultrasonic sensor requires careful considerations regarding film thickness and active area, electroding selection, backing material, construction procedure, and

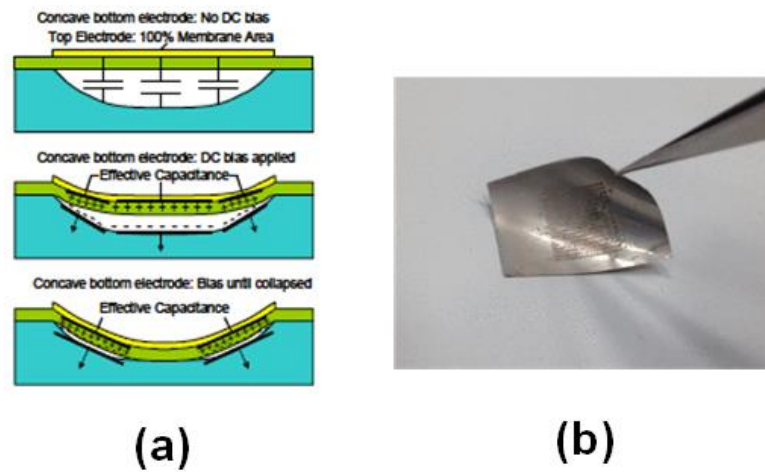


**Figure 2.11:** A flexible CMUT array using a concave bottom electrode. Schematic drawings of the flexible CMUT fabricated by [14] (a), and a photo of the flexible PMUT arrays fabricated by [15] (b).

packaging requirements to improve the ultrasound performance for the desired application and required ultrasound penetration depth [72, 151, 152].

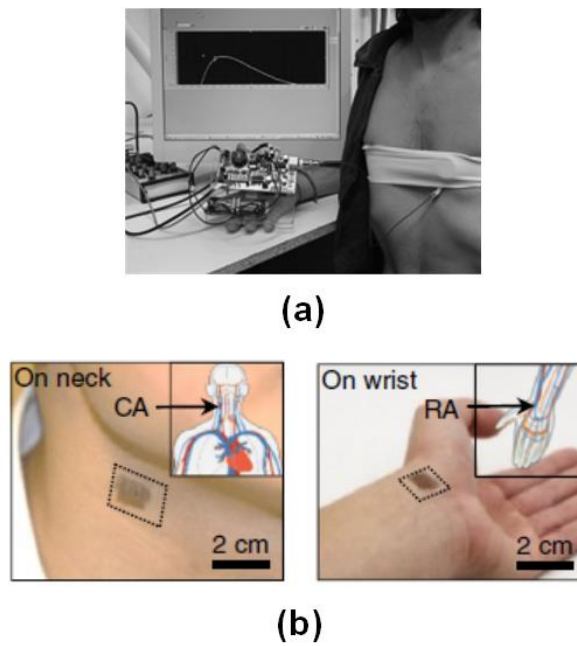


**Figure 2.12:** *In-vivo* demonstration of the flexible UT in the measurement of tissue thickness changes on human subjects. A photo of the PVDF UT integrated into a belt and wrapped around the chest for the heart wall motion monitoring by [16] (a), and schematic drawings of the stretchable PMUT attachment on the skin surface above the carotid and radial arteries for the estimation of the blood pressure by [17] (b).

**Table 2.1:** An overview of wearable ultrasonic transducers (UT) and their medical applications.

Study	UT type	Attachment method	Application
Guo et al. [1]	A Single-element piezoceramic UT inserted into silicone gel holder	Double-sided adhesive tape	Measurement of tissue thickness changes during skeletal muscle contraction
Sun et al. [2]	A single-element piezoceramic UT	Arm-band	Tissue thickness changes of skeletal muscle contraction during fatigue process
Yang et al. [3, 4, 130]	Four single-element piezoceramic UTs	Arm-band	Tissue thickness changes of skeletal muscle contraction for estimation of muscle force and the prediction of finger motion
Zhou et al. [5]	A single-element piezoceramic UT inserted into custom-designed holder	Double-sided adhesive tape	Tissue thickness changes of skeletal muscle contraction for prediction of finger movement
Shahshahani et al. [6]	A single-element PZT UT mounted on a flexible printed circuit board	Double-sided adhesive pad	Tracking diaphragm wall motion for respiratory monitoring
Yang et al. [7]	PMUT arrays by mounting PZT piezoceramic elements on polyimide film and wrapped with polydimethylsiloxane (PDMS)	—	Proposed for medical applications

Continued on next page

Table 2.1 – Continued from previous page

Study	UT type	Attachment method	Application
Wang et al. [8]	PMUT arrays by mounting PZT piezoceramic elements on polyimide film and wrapped with polydimethylsiloxane (PDMS)	—	Proposed for medical applications
Mastronardi et al. [9]	Flexible PMUT array based on aluminum nitride (AlN) piezoelectric elements embedded onto a polyimide substrate	—	—
Sun et al. [10]	Flexible PMUT array based on aluminum nitride (AlN) piezoelectric elements embedded onto a thin polyimide substrate	—	Proposed for medical application as a wearable or implantable UT for health monitoring and treatment
Singh et al. [11]	Conformal PMUT array with PZT piezoceramic elements mounted on microfabricated array of silicon islands connected by polyimide joints	—	Proposed for medical imaging
Sadeghpour et al. [12]	Flexible PMUT array with PZT piezoceramic elements mounted on microfabricated array of silicon islands connected by silicon springs	—	—

Continued on next page

Table 2.1 – Continued from previous page

Study	UT type	Attachment method	Application
Hu et al. [13]	Stretchable PMUT array with PZT piezoceramic elements bridged by stretchable multi-layer electrodes and encapsulated by thin silicone elastomers	—	Proposed for ultrasonic imaging of complex surfaces
Wang et al. [17]	Stretchable PMUT array with PZT piezoceramic elements bridged by stretchable multi-layer electrodes and encapsulated by thin silicone elastomers	—	Measurement of arterial wall motion for blood pressure monitoring
Cheng et al. [14]	Flexible CMUT with a concave bottom electrode	—	—
Chong et al. [15]	Flexible CMUT with a concave bottom electrode embedded on polymer layer	—	Proposed for high ultrasonic frequency range applications
Lanata et al. [16]	Multimodal UT based on PVDF polymer piezoelectric integrated into a textile belt	Belt	Monitoring of heart wall motion

## 2.4 Other Wearable Sensors

In recent years, the development of wearable muscle monitoring systems has garnered the interest of many researchers and clinicians. The extensive research in the field of

wearable systems is fostered by the need for continuous, long-term, real-time monitoring of muscle activities, particularly outside healthcare facilities. The advancement in the fields of sensors, electronic circuits, data analysis methodologies, communication technologies, and battery technologies have promoted the development and deployment of wearable monitoring systems. Sensors are the fundamental element of the wearable monitoring system and essential to the implementation of a body-worn measurement system. A wearable sensor should be flexible, lightweight, thin, and small in size in order to facilitate the free-hand attachment to the curved nature of the body surface. The current state of research on wearable sensors and newly developed wearable systems for skeletal muscle monitoring is presented and discussed in this section.

The incorporation of the advancements in solutions based on the nanomaterial manufacturing process via printing technologies has enabled the development of different strain sensors on various flexible substrates [153, 154]. Ferrone et al. [18] fabricated a polymeric strain sensor using a mixture of thermoplastic and nonconductive particles. The developed polymeric strain sensors were embedded in a cloth wristband to detect the movement of the hand, as shown in **Figure 2.13** (a). Similarly, Cai et al. [19] presented a super-stretchable carbon nanotube (CNT) strain sensor. The CNT sensor is a nanometer-sized fiber that exhibits good linearity and a strain range of up to 300%. They proposed the potential of the CNT sensors to be integrated into smart cloth or directly attached to the skin for human motion detection and demonstrated the integration of a CNT sensor onto a rubber glove to detect the bending movement of a finger, as shown in **Figure 2.13** (b). Additionally, Shengbo et al. [20] developed a highly sensitive and flexible strain sensor based on silver nanoparticles and nanowires. The developed silver strain sensor has demonstrated the ability to detect the motion of finger bending, wrist bending, and walking by attaching the developed sensor to the skin using adhesive tapes, as shown in **Figure 2.13** (c).

Furthermore, Takei et al. [21] developed a wearable and flexible piezoresistive silicon-based strain sensor for muscle activity measurement. The developed ultrathin piezoresistive sensor was integrated into an armband and was employed in measuring the electrically evoked biceps muscle contractions at a range of Electrical muscle stimulator (EMS) frequencies, as shown in **Figure 2.13** (d). The conducted measurements of the muscle contractions by the piezoresistive sensor demonstrated a good association with the magnitude and frequency of the EMS. In general, the calibration requirement of strain sensors should be taken into consideration as it may impose a complexity for the practical implementation in the measurement of muscle contraction.

The recent advancements in textile-based sensors enabled the integration of the sensors into wearable garments [155]. For example, the flexible sensing belt by Wang et al. [22] composed of an array of fabric strain sensors (FSS) embedded in a wearable belt, as shown in **Figure 2.14**. The FSS was developed to measure the limb circumference changes during muscle contraction. Likewise, Belbasis and Fuss [23] introduced a wearable pressure mapping system to quantify muscular exertion and loading. The pressure mapping system was based on the wearable dynamic pressure measurement device by [156]. The pressure mapping system consisted of a compression garment with six embedded piezoresistive polymer sensing nodes to measure the pressure between the compression garment and the skin above the muscle of interest, as shown in **Figure 2.15**. The system was demonstrated by providing a comparative measurement between the muscle relaxed state (MRS) and the maximal voluntary contraction (MVC).

For specialized applications, a novel wearable MMG based biofeedback system was presented by Plewa et al. [24] for rhythmic auditory cueing in movement rehabilitation. The wearable biofeedback system used two tri-axial accelerometers taped to the skin over the leg muscles, as shown in **Figure 2.16** (a). The accelerometers were wired to a portable

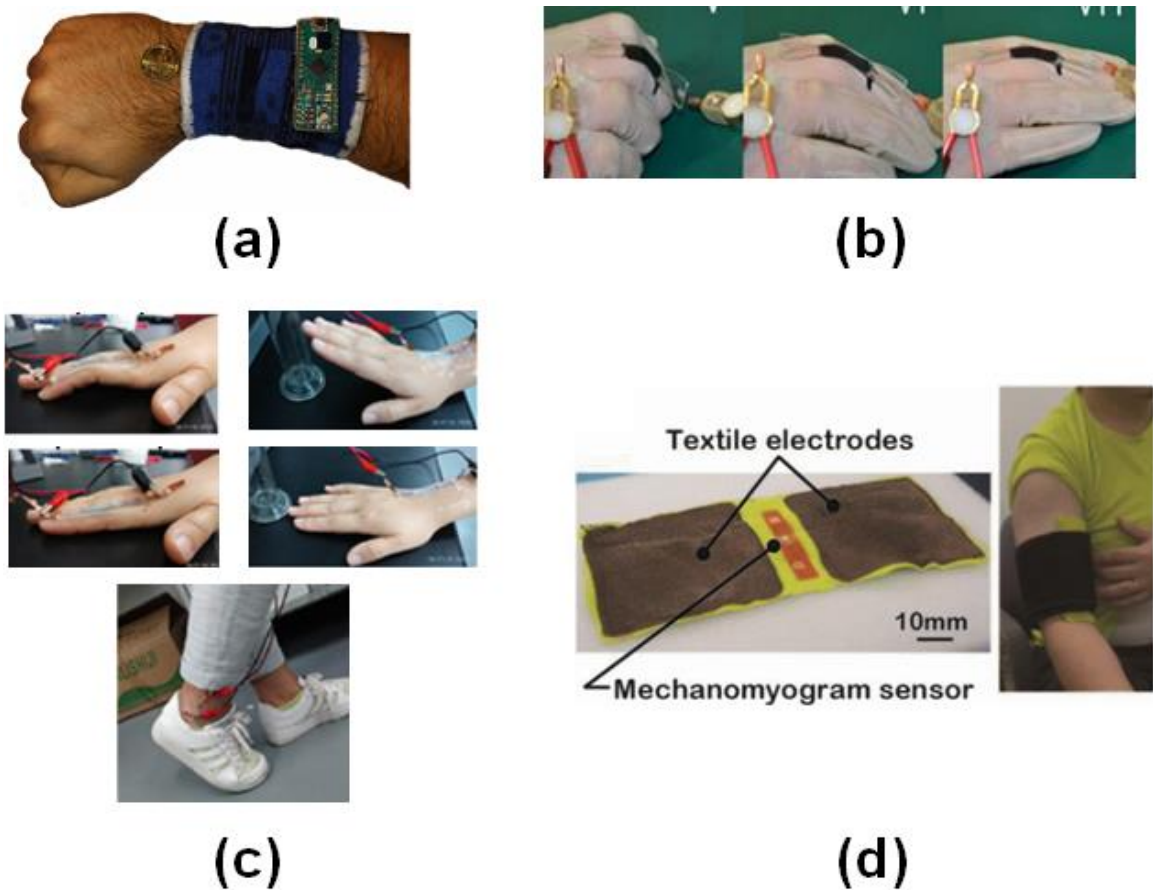


**Figure 2.13:** Wearable strain sensors. A photo of the wearable polymeric strain sensor by [18] (a), photos of the wearable CNT strain sensor by [19] (b), photos of the wearable silver nanoparticles and nanowires strain sensor by [20] (c), and photos of the wearable piezoresistive silicon-based strain sensor by [21] (d).

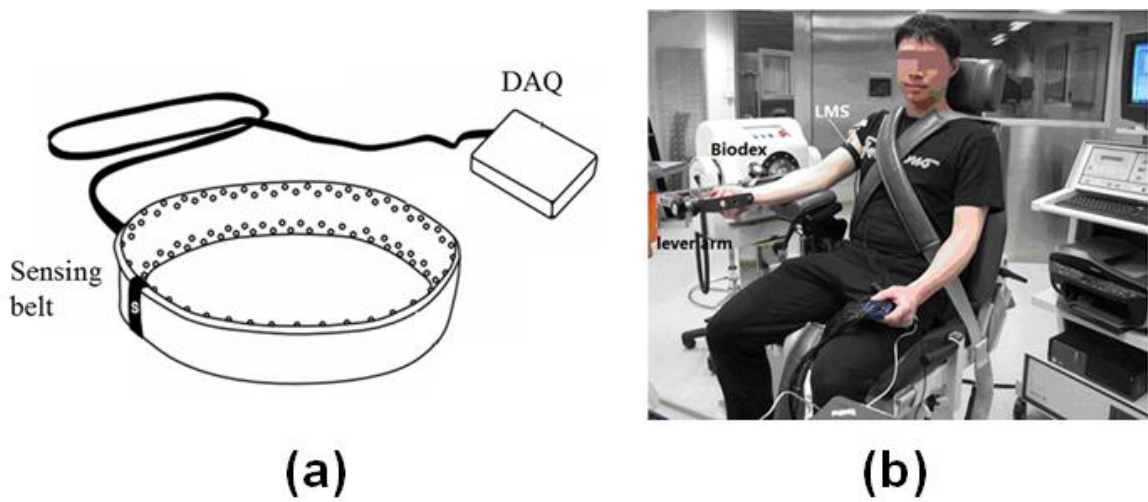


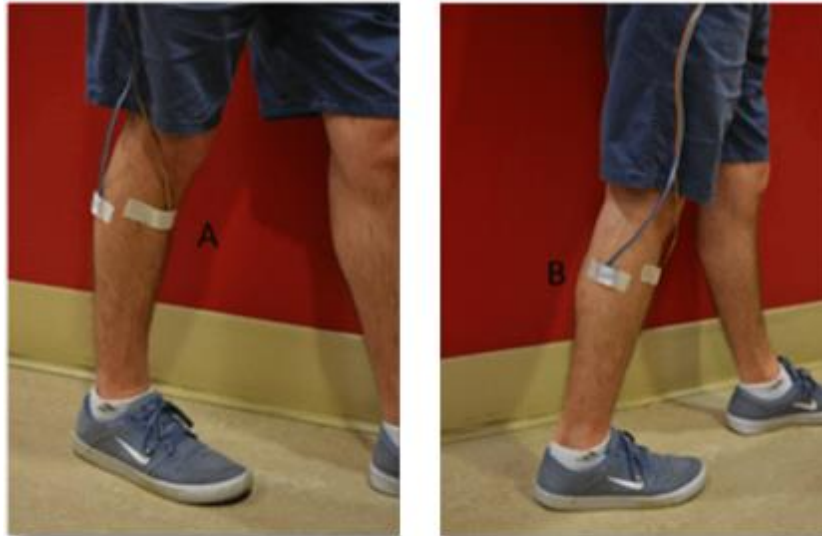
**Figure 2.14:** The flexible sensing belt by [22]: structure of the sensing belt (a), and a Photo of the sensing belt mounted on the subject right upper arm (b).



**Figure 2.15:** The wearable pressure mapping system embedded in pants by [23].

Arduino board that processes the acquired signals and transfers the data to the developed mobile application via Bluetooth. The mobile application plays real-time auditory feedback based on the detection of the gait patterns by accelerometers. Additionally, Bhat and Gupta [25] developed a localized muscle fatigue detection system based on SEMG measurement, as shown in **Figure 2.16** (b). The novelty of the muscle fatigue detection system was that the SEMG signal is sent via Bluetooth to an application on a mobile device that uses an algorithm for the detection of the localized muscle fatigue during isometric exercises.

The recent advancement in technology offers the possibility of integrating various sensors to achieve a more accurate measurement during mobility exercises. Wilson and Vaidyanathan [26] introduced the integration of a microphone and an inertial measurement unit (IMU) in a wearable system for upper limb prosthetic control. The wearable prosthetic control system consists of six microelectromechanical systems, (MEMS) based microphones and an IMU embedded in an armband. The armband also contained a module for wireless data streaming to a computer, as shown in **Figure 2.17** (a). The developed prosthetic control system demonstrated an average identification accuracy of 64% for seven hand gestures among five subjects. In a similar approach, Mokaya et al. [27, 157] presented a muscle activity recognition system (MARS) based on wearable sensor nodes for detecting and tracking muscle activity during physical exercises. The MARS consisted of a triple-axis accelerometer, a gyroscope, and magnetometer sensors embedded in a wearable garment, as shown in **Figure 2.17** (b). The impact of motion artifacts during the physical exercises was addressed by the developed motion noise mitigation algorithm. The developed algorithm uses the extreme value analysis method to model and separate motion artifacts from the recorded muscle vibration. The results of their conducted experiment showed a prediction accuracy of 97% in the low motion exercises and 90% in the high motion exercises. Utilizing the advantage of the integration of multiple data sources, Guo et al. [28] introduced an



(a)



(b)

**Figure 2.16:** The wearable MMG taped to a subject's leg for rhythmic auditory cueing by [24] (a), and SEMG electrodes attached to skin surface of the upper arm for localized muscle fatigue detection by [25] (b).

SEMG-MMG hybrid system for upper-extremity prosthetic control. A condenser microphone was placed between the SEMG electrodes on a fabricated housing of the hybrid SEMG-MMG system, as shown in **Figure 2.17** (c). The hybrid approach addresses the SEMG electrode fault by using combined SEMG-MMG features.

For a larger scale of sensor integration, Ma et al. [29] presented a wearable gesture detection system that included multiple sensor types as well as ultrasound imaging, as shown in **Figure 2.17** (d). Their wearable gesture detection system consisted of an ultrasound probe, two SEMG electrodes, three force-sensing resistors, an accelerometer, and a two-axis goniometer. The system simultaneously measures the muscle electrical activity, records the motion on the skin surface, and captures the B-mode ultrasound images by an ultrasonic probe. The wearable gesture detection system showed a moderate test-retest reliability in the gait cycle monitoring, in comparison to a commercial motion capture system. **Table 2.2** summarized the wearable sensors described in the above-motioned studies in tabulated form.

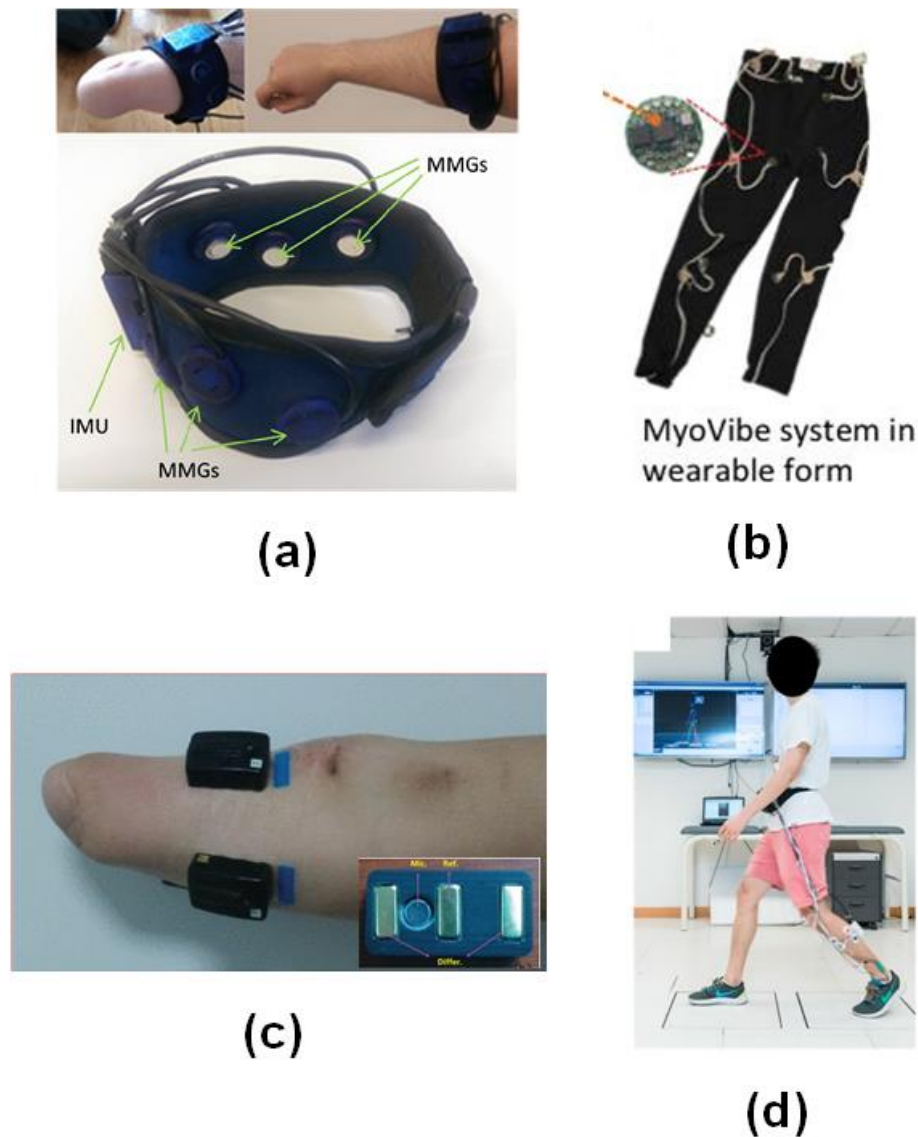


**Figure 2.17:** The wearable microphone and the inertial measurement unit embedded in an armband by [26] (a), the muscle activity recognition system (MARS) based on wearable sensor nodes by [27] (b), the SEMG-MMG hybrid system for upper-extremity prosthetic control by [28] (c), and the wearable gesture detection system of multiple sensor types by [29] (d).

**Table 2.2:** An overview of recent wearable sensors for the muscle mechanical activity measurement.

Study	Measurement technique	Sensor type	Application	Attachment method
Ferrone et al. [18]	MMG	Polymeric strain sensor	Hand gesture recognition	Wearable band
Cai et al. [19]	MMG	Carbon nanotube strain sensor	Muscle motion detection	Integrated into garment
Shengbo et al. [20]	MMG	Silver nanowires and nanoparticles strain sensor	Muscle motion detection	Adhesive tape
Takei et al. [21]	MMG	Silicon-based piezoresistive strain sensor	Muscle contraction monitoring	Integrated into garment
Seyedin et al. [155]	MMG	Fabric strain sensor	Limb circumference changes measurement	Wearable band
Belbasis and Fuss [23]	MMG	Piezoresistive polymer strain sensor	Muscle contraction monitoring	Integrated into garment
Plewa et al. [24]	MMG	Accelerometer	Rhythmic auditory cueing in movement rehabilitation	Adhesive tape
Bhat and Gupta [25]	SEMG	Surface biopotential electrode	Localized muscle fatigue detection	Adhesive tape

Continued on next page.

Table 2.2 – Continued from previous page

<b>Study</b>	<b>Measurement technique</b>	<b>Sensor type</b>	<b>Application</b>	<b>Attachment method</b>
Wilson and Vaidyanathan [26]	MMG	- MEMS based microphones - Accelerometer - Gyroscope - Magnetometer	Upper-limb prosthetic control	Wearable band
Mokaya et al. [27]	MMG	- Accelerometer - Gyroscope - Magnetometer	Muscle activation prediction in high motion	Integrated into garment
Guo et al. [28]	MMG SEMG	- Electret condenser microphone - Surface biopotential electrode	Upper-limb prostheses control	Adhesive tape
Ma et al. [29]	MMG SEMG Ultrasound	- Thin-film force sensing resistor - Accelerometer - Goniometer - Surface biopotential electrode - Ultrasonic probe	Muscle contraction monitoring during walking	Adhesive tape

## Chapter 3

# Numerical Simulation Model for the Double-Layer PVDF WUS

In this chapter the formulation and derivation of the double-layer PVDF WUS numerical simulation model is presented. To study the double-layer PVDF WUS design, theoretical simulation of the ultrasonic performance (center frequency, frequency bandwidth, and acoustic power) and the effects of non-piezoelectric layers, such as electrodes, bonding, and backing layers, would facilitate the design and construction of an ultrasonic sensor. The piezoelectric material properties, such as dielectric and mechanical coefficients and non-piezoelectric layer properties, impact the performance of the ultrasonic sensor. It is advantageous to have a numerical simulation model to predict the sensor performance considering the internal losses of PVDF piezoelectric and the effects of the structural layers beyond the experimental limitations. In particular, the center frequency, frequency bandwidth, conversion loss, and acoustic output power are the parameters of focus in studying and designing the wearable PVDF ultrasonic sensor. Several studies have been published in the context of piezoelectric sensor modeling, though they may not be directly applicable in the simulation of the proposed design of the double-layer PVDF WUS. Thus, the complete derivation and the formulation of the PVDF transfer  $3 \times 3$ -matrix expression

by [158] was expanded into  $4 \times 4$ -matrix expressions that are suitable for simulating and characterizing the proposed design of the double-layer PVDF WUS. The common formulation methods reported for multiple-layer piezoelectric sensors have been reviewed. The described numerical simulation model is implemented to study and evaluate the double-layer PVDF WUS in the following chapters (**Chapter 4** and **Chapter 5**).

In the following sections, the formulation and derivation of the double-layer PVDF WUS simulation model were described based on the reviewed simulation models and methods. **Section 3.1** reviews the piezoelectric simulation models. The basic equations and the core  $3 \times 3$ -matrix of the single-layer PVDF piezoelectric modeling are described first in **Section 3.2**. Then, the formulation method and derivation of the  $4 \times 4$ -matrix of the multiple-layer PVDF piezoelectric modeling are explained in **Section 3.3**. In order to formulate the  $4 \times 4$ -matrix for the parallel electrical connection, the core  $3 \times 3$ -matrix of the single-layer PVDF piezoelectric is formulated first to the  $4 \times 4$ -matrix for the series electrical connection in **Section 3.3.1** followed by the formulation of the parallel electrical connection in **Section 3.3.2**. Lastly, the equivalent circuit of the double-layer PVDF WUS and the definition of the calculated parameters are described in **Section 3.5**.

### 3.1 Review of Piezoelectric Simulation Models

There are two main approaches for the theoretical study of piezoelectric material-based ultrasonic sensors [152]: the finite element analysis (FEA) and the equivalent electrical circuit. In the FEA, the structure of an ultrasonic sensor is divided, in terms of geometry of the piezoelectric resonator, into a finite number of simple geometrically shaped elements. The mesh of finite elements is mathematically described by a set of linear differential equations. Thus, the finite elements allow the computation of the mechanical and electrical

behavior of a piezoelectric element [159–161]. Many simulation softwares use the FEA due to their ability to model any geometric shape of two- (2D) or three-dimensions (3D) such as COMSOL Multiphysics (COMSOL, Inc., Burlington, MA, USA), ANSYS (ANSYS, Inc., Canonsburg, PA, USA), Onscale (formally PzFlex, Onscale Inc., Redwood City, CA, USA), and open source FEM code OOFEM [7, 8, 161–170]. The FEA would provide a highly accurate simulation via the increase in the element number but requires expensive computing hardware and longer computation time, especially for high frequencies [152, 162].

In contrast, a numerical simulation based on the equivalent circuit modeling approach would provide a faster computation speed and accurate prediction with less extensive computation hardware [152, 171]. Several equivalent circuit models are proposed in literature such as the Mason's model [73, 172], Redwood's model [173], KLM model [174, 175], Rhyne's model [176], and Leach's model [177]. Mason [172] provided the fundamental model for piezoelectric material. He presented the equivalent circuit of the single piezoelectric as a three-port network that separated into one electrical port and two acoustic ports through the use of an ideal electromechanical transformer. Redwood [173] incorporated a transmission line into Mason's model to represent the time delay for a mechanical signal traveling from one side of the piezoelectric material to the other. Krimholtz et al. [174] introduced an alternative circuit, known as KLM, for the simpler representation of series cascaded piezoelectric circuits. Rhyne [176] introduced a series impedance to the mechanical side of Mason's model, accounting for mechanical losses. Leach [177] modeled the coupling between the electric and acoustic ports of Mason's model by the controlled current and voltage sources instead of transformers. The KLM and Mason models are equivalent and commonly used for modeling piezoelectric sensors [178].

The Mason's model was assumed for lossless piezoelectric material neglecting internal losses, which was a suitable assumption for the low-loss of the piezoceramics during the

time of his classical work before the discovery of the lossy piezoelectric polymer by Kawai [179]. Since the piezoelectric polymers have large electric and mechanical losses, the utilization of Mason's model without considering these losses would result in large errors in the theoretical analysis. Holland [180] and Ohigashi et al. [181] introduced a method to include the internal losses into the equivalent circuit representation of Mason's model by treating the dielectric and elastic constants of the piezoelectric material as a complex number, where the corresponding imaginary part represents the losses.

Ohigashi in [158] presented the  $3 \times 3$ -matrix expression for polymer piezoelectric materials operating in thickness mode based on the three-port Mason's model of the piezoelectric material. The  $3 \times 3$ -matrix expression by Ohigashi related the entities of the acoustic ports acting on both surfaces of the piezoelectric layer and the electric port entities acting across the film thickness. However, for multiple piezoelectric layers mechanically connected in series, the direct multiplication of  $3 \times 3$ -matrix of each piezoelectric layer would not yield the equivalent resultant matrix expression that relates the entities of the mechanical and electrical ports between the multiple piezoelectric layers. The current and voltage of the electrical port must be considered separate entities on each surface of each piezoelectric layer for the proper summation of the total current and voltage. Sittig [182] proposed a method that would be suitable for calculating the multiple piezoelectric layers' arrangement for both the series and parallel electrical connections. The work of Sittig suggested using Mason's model with the representation of the piezoelectric layer as a four-port network with two electrical ports and two acoustic ports. Thus, each piezoelectric layer in the multiple piezoelectric layer's arrangement would be expressed in a  $4 \times 4$ -matrix form that relates the partial current and voltage entities on both surfaces of each successive piezoelectric layer separately instead of expressing the current and voltage as one entity across the piezoelectric layer.

Zhang et al. [183, 184] presented the theoretical analysis of multiple-layer PVDF structures based on the method suggested by Sittig [182]. In their work, the  $4 \times 4$ -matrix was formulated for the multiple PVDF layers connected electrically in series, which could not be utilized for the parallel case. Rashidian and Rahnavard [185, 186] also presented the method of formulating the  $4 \times 4$ -matrices for the series and the parallel cases of electrical connection. However, the account of the orientation of electrical connections between piezoelectric layers was not considered in [185, 186]. Additionally, the treatment of the alternating voltage orientation and particle velocity direction in their  $4 \times 4$ -matrices of each piezoelectric layer was not clear. Bloomfield [187] realized the limitations of the previously published methods using the  $4 \times 4$ -matrix formalisms by [182–186]. He presented a general formulation method of  $4 \times 4$ -matrices for both the series and parallel cases where the voltage orientation reversals were taken into consideration. The non-piezoelectric layers, such as electrode and bonding layers, were treated as a pure mechanical layer in the  $4 \times 4$ -matrix expression in [187]. Deriving the correct  $4 \times 4$ -matrix expression of each successive piezoelectric material arranged in multiple-layer configuration, including the non-piezoelectric layers, would allow the cascade multiplication of the  $4 \times 4$ -matrices to obtain the resultant  $4 \times 4$ -matrix. Thus, the resultant  $4 \times 4$ -matrix that yields the equivalent expression of all the piezoelectric and non-piezoelectric layers could be utilized to model the ultrasonic sensor as a single device.

The ultrasonic sensor is, in effect, a box which transforms the electrical quantities (voltage and current) into the mechanical quantities (force and particle velocity) or vice versa. Therefore, the equivalent circuit of the ultrasonic sensor is modeled as a two-port network where one side represents the electrical variables, and the other side represents the mechanical variables [158, 188]. The  $2 \times 2$ -matrix expression of the two-port network model of the ultrasonic sensor is obtained by reformulating the resultant  $4 \times 4$ -matrix of the acting layers of the ultrasonic sensor into the compact  $2 \times 2$ -matrix. The ultrasonic sensor

parameters such as electrical and mechanical impedances, voltage transfer ratio, matching loss, conversion loss, and transducer loss could be calculated by relating the input and output quantities of the two-port network.

The proposed design of the double-layer PVDF WUS consists of two PVDF layers that are electrically connected in parallel with inverse voltage orientation and inverse polarization direction. Each PVDF layer has top and bottom electrode layers. The two PVDF layers are adhered to the inner electrode layers by the bonding layer. The outer electrode layers are in contact with the backing and propagation media. The research of this chapter provides the complete derivation and formulation of the double-layer PVDF WUS numerical simulation model. The introduced numerical model is based on Mason's model and the review of previously published work regarding multiple-layer piezoelectric sensors treatments. It considers the reversed voltage orientation applied in the parallel electrically connected multiple PVDF layers to yield the correct summation of electrical quantities.

## 3.2 Modeling of Single-Layer PVDF Piezoelectric

As mentioned in **Section 3.1**, Mason [172] presented the equivalent circuit of the single-layer piezoelectric material as a three-port network that divided into two acoustic ports and one electrical port. **Figure 3.1** shows the three-port network representation of the piezoelectric material operating in thickness-extension mode. The acoustic ports were represented by forces,  $F^+$  and  $F^-$ , and particle velocities,  $U^+$  and  $U^-$ , acting on the top and bottom surfaces of the piezoelectric film, respectively. The electric port was represented by voltage,  $V$ , and current,  $I$ , acting across the PVDF film thickness.

PVDF piezoelectric has large dielectric and mechanical losses compared to the ceramic piezoelectric materials. In order to include the internal losses of the PVDF piezoelectric

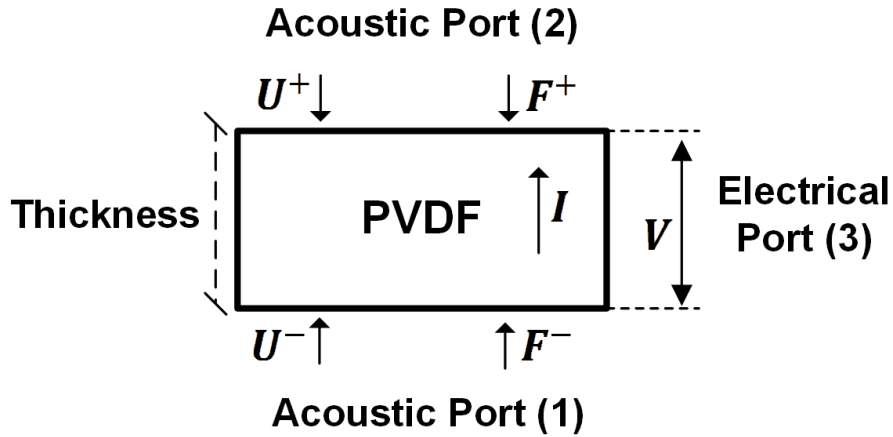


**Figure 3.1:** Three-port network representation of Mason's model consists of a single-layer piezoelectric material operating in thickness mode. The force and particle velocity entities of the acoustic ports acting on the top and bottom surfaces are denoted by  $F^+$ ,  $F^-$ ,  $U^+$ , and  $U^-$ , respectively. The voltage and current entities of the electrical port acting across the thickness of the piezoelectric material are denoted by  $V$  and  $I$ , respectively.

film, Ohigashi et al. [181] proposed the complex form of the dielectric permittivity,  $\varepsilon^*$ , and the complex elastic stiffness constant,  $c^*$ . The dielectric loss,  $\tan \delta_e$  and the mechanical loss,  $\tan \delta_m$  were added as the imaginary part to the dielectric permittivity,  $\varepsilon^S$ , and the elastic stiffness constant,  $c^D$ , respectively as:

$$\varepsilon^* = \varepsilon^S(1 - j \tan \delta_e), \quad (3.1)$$

$$c^* = c^D(1 + j \tan \delta_m). \quad (3.2)$$

The relation between the forces,  $F^-$  and  $F^+$ , particle velocities,  $U^-$  and  $U^+$ , the voltage,  $V$ ,

and the current,  $I$ , could be expressed in the form of a  $3 \times 3$  transfer matrix,  $T$ , as [158, 189]:

$$\begin{pmatrix} F^- \\ F^+ \\ V \end{pmatrix} = T \begin{pmatrix} U^- \\ U^+ \\ I \end{pmatrix}, \quad (3.3)$$

$$T = \begin{pmatrix} -j\beta \coth \gamma d & -j\beta \operatorname{csch} \gamma d & \frac{-jh}{\omega} \\ -j\beta \operatorname{csch} \gamma d & -j\beta \coth \gamma d & \frac{-jh}{\omega} \\ \frac{-jh}{\omega} & \frac{-jh}{\omega} & \frac{-j}{C\omega} \end{pmatrix} = \begin{pmatrix} T_1 & T_2 & T_3 \\ T_2 & T_1 & T_3 \\ T_3 & T_3 & T_4 \end{pmatrix}, \quad (3.4)$$

where the complex quantities of acoustic impedance for an area of the film surface,  $\beta$ , wave propagation constant,  $\gamma$ , transmitting constant,  $h$ , and clamped bulk capacitance,  $C$ , are defined as:

$$\beta = j\rho v \left(1 + \frac{j \tan \delta_m}{2}\right) A_S, \quad (3.5)$$

$$\gamma = j \left(\frac{\omega}{v}\right) \left(1 - \frac{j \tan \delta_m}{2}\right), \quad (3.6)$$

$$h = \frac{e}{\epsilon_S}, \quad (3.7)$$

$$C = \frac{\epsilon^* A_S}{d}. \quad (3.8)$$

In **Eq. 3.4 – Eq. 3.8**,  $d$  is the thickness,  $\rho$  is the density,  $v$  is the longitudinal velocity of sound,  $A_S$  is the surface area, and  $e$  is the piezoelectric constant of the PVDF layer.  $\omega$  is the angular frequency of ultrasound. The  $3 \times 3$ -matrix expression of  $T$  is suitable for the calculation of a single-layer PVDF. However, it cannot be directly applied for the cascading of multiple-layer PVDF. Therefore, the  $T$  expression will be extended to represent the multiple-layer piezoelectric arrangement in the following section.

### 3.3 Modeling of Multiple-Layer PVDF Arrangement

The  $3 \times 3$ -matrix expression of  $T$  in **Eq. 3.4**, is a mixed representation where the quantities on one surface were related to those on both surfaces. For instance,  $F^-$  on the bottom surface was related to the  $U^-$  and  $U^+$  on the bottom and top surfaces, respectively. Relating the mechanical quantities on the bottom surface to those on the top surface allows the multiplication of the transfer matrices to yield the mechanical quantities of the last layer in terms of the first layer of the multiple-layer PVDF arrangement [182, 183, 185, 187]. Therefore, the relationships were reformulated so that the  $F^-$  and  $U^-$  on the bottom surface were given in terms of  $F^+$  and  $U^+$  on the top surface as:

$$\begin{pmatrix} F^- \\ -U^- \\ V \end{pmatrix} = S \begin{pmatrix} F^+ \\ U^+ \\ I \end{pmatrix}, \quad (3.9)$$

and  $3 \times 3$ -matrix,  $S$ , is derived from **Eq. 3.4** as:

$$S = \begin{pmatrix} \frac{T_1}{T_2} & \frac{-T_1^2}{T_2} + T_2 & \frac{-T_1 T_3}{T_2} + T_3 \\ \frac{-1}{T_2} & \frac{T_1}{T_2} & \frac{T_3}{T_2} \\ \frac{T_3}{T_2} & \frac{-T_1 T_3}{T_2} + T_3 & \frac{-T_3^2}{T_2} + T_4 \end{pmatrix}. \quad (3.10)$$

After performing some algebraic manipulations on **Eq. 3.10**, the  $3 \times 3$ -matrix,  $S$ , is expressed as:

$$\begin{aligned}
S &= \begin{pmatrix} \cosh \gamma d & j\beta \sinh \gamma d & \frac{-jh(1 - \cosh \gamma d)}{\omega} \\ \frac{-j \sinh \gamma d}{\beta} & \cosh \gamma d & \frac{h \sinh \gamma d}{\beta\omega} \\ \frac{h \sinh \gamma d}{\beta\omega} & \frac{-jh(1 - \cosh \gamma d)}{\omega} & \frac{-j}{C\omega} \left(1 - \frac{h^2 C \sinh \gamma d}{\beta\omega}\right) \end{pmatrix} \\
&= \begin{pmatrix} S_{11} & S_{12} & S_{13} \\ S_{21} & S_{22} & S_{23} \\ S_{31} & S_{32} & S_{33} \end{pmatrix}.
\end{aligned} \tag{3.11}$$

The three-port network expression given by  $3 \times 3$ -matrix,  $S$ , relates the mechanical quantities ( $F^-$ ,  $U^-$ ,  $F^+$ , and  $U^+$ ) between the PVDF layer surfaces but not the electrical quantities since  $V$  and  $I$  are given across the layer thickness. In order to model the equivalent circuit of the double-layer PVDF as an ultrasonic sensor, the relationships of the mechanical and electrical quantities between the bottom surface of the first layer and top surface of the last layers have to be expressed in one equivalent matrix expression. **Figure 3.2** shows the mechanical and electrical quantities acting on each surface of the double-layer PVDF arrangement. As an example in **Figure 3.2**, the resultant equivalent matrix expression should relate the quantities on the bottom surface of PVDF 1 ( $F_1^-$ ,  $U_1^-$ , and  $V_1^-$ ) in terms of the quantities on the top surface of PVDF 2 ( $F_2^+$ ,  $U_2^+$ , and  $V_2^+$ ). Therefore, the matrix expression of the double-layer PVDF arrangement should include the representation of the electrical quantities ( $V$  and  $I$ ) on each surface of the PVDF layer. In order to include the relationships of the electrical quantities, the PVDF layer is represented as a four-port network with two pairs of mechanical and electrical quantities each [182, 185, 187]. Note that for the electrical

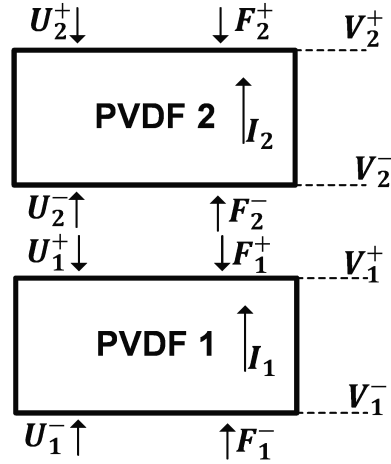


**Figure 3.2:** Representation of the mechanical and electrical quantities acting on each PVDF layer in the double-layer PVDF arrangement.

currents,  $I_1$  and  $I_2$ , through each PVDF layer should be treated to yield the sum of all currents entering and leaving every PVDF layer for both series and parallel connected multiple-layer PVDF cases. Thus, it is more convenient to formulate the  $4 \times 4$ -matrix expression for the series electrically connected multiple-layer PVDF first since the total current,  $I$ , is equal to the current through each PVDF layer ( $I = I_1 = I_2$ ). In the following subsections, the formulations of series electrically connected multiple-layer PVDF are presented first, then the parallel electrically connected case formulation. The polarization direction of the PVDF layer is indicated by the sign of  $h$ . The positive polarization direction points from the bottom (-) to the top (+) surfaces.

### 3.3.1 Series Electrically Connected

**Figure 3.3** shows the general representation of series electrically connected multiple-layer PVDF. In the series electrical connection, the same current flows through each layer

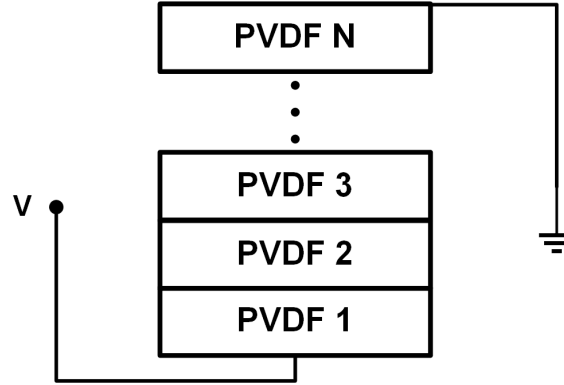


**Figure 3.3:** General representation of series electrically connected multiple-layer PVDF.

and the voltages drop across each layer. Thus, the total current and total voltage drop were defined as:

$$I = I_1 = I_2 = I_3 = \cdots = I_N, \quad (3.12)$$

$$V = V_1 + V_2 + V_3 + \cdots + V_N. \quad (3.13)$$

The relationship between the mechanical and electrical quantities on each surface of the series electrically connected multiple-layer PVDF is formulated from  $3 \times 3$ -matrix expression,  $S$ , in **Eq. 3.9** and **Eq. 3.11** by adding a new row and column. The additional row stands for the equality of the electrical current in the series electrical ports, and the additional column maintains the correct relationships between the other quantities. The positively defined voltage differences and currents were directed from the bottom (–) surface to the top (+) surface as the active voltage electrode (connected to high terminal) and grounded electrode (connected to ground terminal) were assumed on the bottom (–) of the 1<sup>st</sup> PVDF layer and the top (+) of the N<sup>th</sup> PVDF layer, respectively. Thus, the  $S^M$   $4 \times 4$ -matrix for the 1<sup>st</sup> PVDF

layer in case of the series electrical connection is expressed as:

$$\begin{pmatrix} F_1^- \\ -U_1^- \\ V_1^- \\ I_1 \end{pmatrix} = S^M \begin{pmatrix} F_1^+ \\ U_1^+ \\ V_1^+ \\ I_1 \end{pmatrix}, \quad (3.14)$$

where

$$S^M = \begin{pmatrix} \cosh \gamma d & j\beta \sinh \gamma d & 0 & \frac{-jh(1 - \cosh \gamma d)}{\omega} \\ \frac{-j \sinh \gamma}{\beta} & \cosh \gamma d & 0 & \frac{h \sinh \gamma d}{\beta\omega} \\ \frac{h \sinh \gamma d}{\beta\omega} & \frac{-jh(1 - \cosh \gamma d)}{\omega} & 1 & \frac{-j}{C\omega} \left(1 - \frac{h^2 C \sinh \gamma d}{\beta\omega}\right) \\ 0 & 0 & 0 & 1 \end{pmatrix}, \quad (3.15)$$

$$V_1 = V_1^- - V_1^+. \quad (3.16)$$

The superscript  $M$  denotes the multiple layers. The  $4 \times 4$ -matrix expression of  $S^M$ , in **Eq. 3.15** can compute the bottom (-) surface quantities from those on the top (+) surface. Thus, the multiplication of  $S^M$  matrices of  $n$  layers in the series electrically connected multiple-layer PVDF depicted in **Figure 3.3** yields the relationship between the bottom (-) surface of the 1<sup>st</sup> PVDF layer and the top (+) surface of the  $N^{\text{th}}$  PVDF layer as:

$$\begin{pmatrix} F_1^- \\ -U_1^- \\ V_1^- \\ I_1 \end{pmatrix} = S_{\{N\}}^M \begin{pmatrix} F_N^+ \\ U_N^+ \\ V_N^+ \\ I_N \end{pmatrix}, \quad (3.17)$$

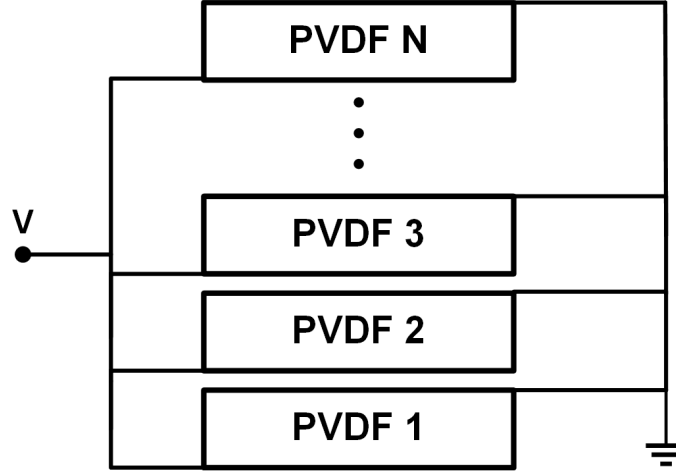


**Figure 3.4:** General representation of parallel electrically connected multiple-layer PVDF.

where

$$S_{\{N\}}^M = \prod_{k=1}^N S_k^M, \quad (3.18)$$

$$V = V_1^- - V_N^+, \quad (3.19)$$

$$I_1 = I_N \equiv I. \quad (3.20)$$

Note that multiplication of  $S_{\{N\}}^M$  in **Eq. 3.18** yields the total voltage drop across all the  $n$ -PVDF layers (between the bottom (-) surface of the 1<sup>st</sup> PVDF layer and the top (+) surface of the  $N^{\text{th}}$  PVDF layer). Since the top (+) surface of the  $N^{\text{th}}$  PVDF layer is connected to the ground, this gives  $V_N^+ = 0$  and  $V = V_1^-$ .

### 3.3.2 Parallel Electrically Connected

**Figure 3.4** shows the general representation of parallel electrically connected multiple-layer PVDF. In the parallel electrical connection, the voltage across each layer is the same, and the total current is equal to the sum of the currents flowing through each layer. Thus, the

total current and total voltage can be defined as:

$$I = I_1 + I_2 + \dots + I_N, \quad (3.21)$$

$$V = V_1 = V_2 = \dots = V_N. \quad (3.22)$$

Since the same voltage is applied to each PVDF layer, reformulating **Eq. 3.9** to represent the current on the bottom surface (–) in terms of the voltage on the top surface (+) is more convenient for the calculation of parallel electrical connection multiple-layer PVDF. Thus, the  $3 \times 3$ -matrix expression,  $P$ , is derived from  $S$  in **Eq. 3.11** as:

$$\begin{pmatrix} F^- \\ -U^- \\ I \end{pmatrix} = P \begin{pmatrix} F^+ \\ U^+ \\ V \end{pmatrix}, \quad (3.23)$$

$$P = \begin{pmatrix} S_{11} - \frac{S_{13}S_{31}}{S_{33}} & S_{12} - \frac{S_{13}S_{32}}{S_{33}} & \frac{S_{13}}{S_{33}} \\ S_{21} - \frac{S_{23}S_{31}}{S_{33}} & S_{22} - \frac{S_{23}S_{32}}{S_{33}} & \frac{S_{23}}{S_{33}} \\ \frac{-S_{31}}{S_{33}} & \frac{-S_{32}}{S_{33}} & \frac{1}{S_{33}} \end{pmatrix}. \quad (3.24)$$

After performing some algebraic manipulations on **Eq. 3.24**, the  $P$   $3 \times 3$ -matrix is expressed as:

$$P = \begin{pmatrix} \frac{\cosh \gamma d - X \sinh \gamma d}{1 - X \sinh \gamma d} & \frac{j\beta[\sinh \gamma d + 2X(1 - \cosh \gamma d)]}{1 - X \sinh \gamma d} & \frac{hC(1 - \cosh \gamma d)}{1 - X \sinh \gamma d} \\ \frac{-j \sinh \gamma d}{\beta(1 - X \sinh \gamma d)} & \frac{\cosh \gamma d - X \sinh \gamma d}{1 - X \sinh \gamma d} & \frac{jhC \sinh \gamma d}{\beta(1 - X \sinh \gamma d)} \\ \frac{-jhC \sinh \gamma d}{\beta(2 - X \sinh \gamma d)} & \frac{-hC(1 - \cosh \gamma d)}{1 - X \sinh \gamma d} & \frac{jC\omega}{1 - X \sinh \gamma d} \end{pmatrix}, \quad (3.25)$$

where

$$X = \frac{h^2 C}{\beta \omega}. \quad (3.26)$$

Now, the relationships between the mechanical and electrical quantities on each surface of the parallel electrically connected multiple-layer PVDF arrangement can be formulated from  $3 \times 3$ -matrix expression,  $P$ , in **Eq. 3.23** into a  $4 \times 4$ -matrix expression by adding a new row and column. The additional row stands for the equivalence of voltage, and the additional column maintains the correct relationship of the other quantities. Thus, the  $P^M$   $4 \times 4$ -matrix for the 1<sup>st</sup> PVDF layer in the case of parallel electrical connection is expressed as:

$$\begin{pmatrix} F_1^- \\ -U_1^- \\ V_1 \\ I_1^- \end{pmatrix} = P^M \begin{pmatrix} F_1^+ \\ U_1^+ \\ V_1 \\ I_1^+ \end{pmatrix}, \quad (3.27)$$

where

$$P^M = \begin{pmatrix} \frac{\cosh \gamma d - X \sinh \gamma d}{1 - X \sinh \gamma d} & \frac{j\beta[\sinh \gamma d + 2X(1 - \cosh \gamma d)]}{1 - X \sinh \gamma d} & \frac{hC(1 - \cosh \gamma d)}{1 - X \sinh \gamma d} & 0 \\ \frac{-j \sinh \gamma d}{\beta(1 - X \sinh \gamma d)} & \frac{\cosh \gamma d - X \sinh \gamma d}{1 - X \sinh \gamma d} & \frac{jhC \sinh \gamma d}{\beta(1 - X \sinh \gamma d)} & 0 \\ 0 & 0 & 1 & 0 \\ \frac{-jhC \sinh \gamma d}{\beta(2 - X \sinh \gamma d)} & \frac{-hC(1 - \cosh \gamma d)}{1 - X \sinh \gamma d} & \frac{jC\omega}{1 - X \sinh \gamma d} & 1 \end{pmatrix}, \quad (3.28)$$

$$I_1^- = I_1 + I_2 + \cdots + I_N, \quad (3.29)$$

$$I_1^+ = -I_2 - I_3 - \cdots - I_{N-1}. \quad (3.30)$$

The  $P^M$   $4 \times 4$ -matrix in **Eq. 3.28** can compute the bottom (−) surface quantities from those on the top (+) surface. The currents in **Eq. 3.29** and **Eq. 3.30** are treated as the partial sum current,  $I^-$  and  $I^+$ , on each surface of the PVDF layer in order to yield the correct summation of current ( $I$ ) after the multiplication of  $P^M$  matrices. Thus, the multiplication of

parallel electrically connected  $n$  PVDF layers depicted in **Figure 3.4** yields the relationships between the bottom ( $-$ ) surface of the 1<sup>st</sup> PVDF layer and the top ( $+$ ) surface of the  $N^{\text{th}}$  PVDF layer as:

$$\begin{pmatrix} F_1^- \\ -U_1^- \\ V_1 \\ I \end{pmatrix} = P_{\{N\}}^M \begin{pmatrix} F_N^+ \\ U_N^+ \\ V_N \\ 0 \end{pmatrix}, \quad (3.31)$$

where

$$P_{\{N\}}^M = \prod_{k=1}^N P_k^M, \quad (3.32)$$

$$V_1 = V_N \equiv V. \quad (3.33)$$

The partial sum currents,  $I_n^-$  and  $I_n^+$ , on each surface are defined as:

$$I_n^- = \sum_{k=n}^N I_k, \quad (3.34)$$

$$I_n^+ = \sum_{k=n}^{N-1} (-1) I_{k+1}, \quad \text{for } n \leq N-1, \quad (3.35)$$

where

$$I_N^+ = 0. \quad (3.36)$$

However, the adjacent surfaces of the parallel electrically connected multiple-layer PVDF are practically connected to a common ground terminal or a common high terminal, as shown in **Figure 3.5** (more explanation is given in **Section 4.3.3**). Hence, reversal voltage orientations are applied to successive PVDF layers, which give the definition of the total voltage and current depicted in **Figure 3.5** as:

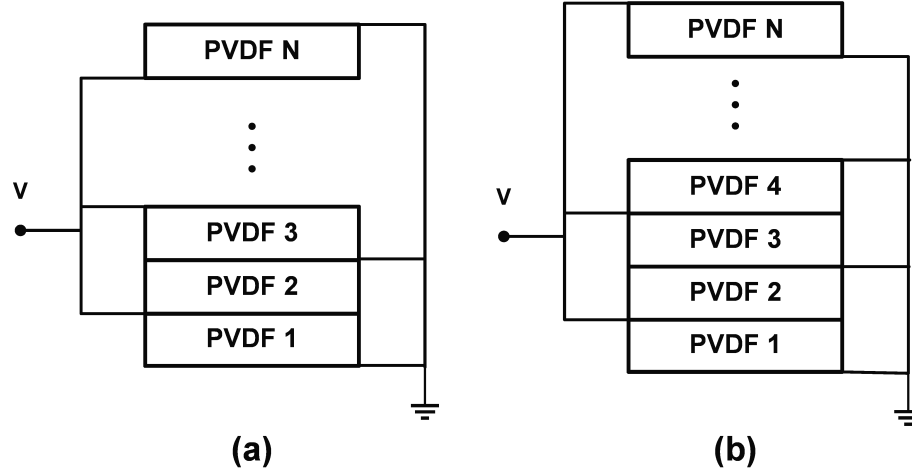


**Figure 3.5:** General representation of interchange electrode connections in parallel electrically connected multiple-layer PVDF case: even-numbered (a) and odd-numbered (b) PVDF layers.

$$I = -I_1 + I_2 + \dots + (-1)^N I_N, \quad (3.37)$$

$$V = -V_1 = V_2 = \dots = (-1)^N V_N. \quad (3.38)$$

In order to take account of the reversal in the voltage orientation and current direction, the sum of the voltage and partial currents can be formed by summing alternately signed quantities [187]. Therefore, the  $\langle 33 \rangle$  and  $\langle 44 \rangle$  elements of  $P^M$   $4 \times 4$ -matrix are given with a minus sign. To maintain the correct definition of voltages in **Eq. 3.38**, the expression of  $P^M$  is given in terms of  $-V$ . Consequently, the  $P^M$   $4 \times 4$ -matrix given in **Eq. 3.27 – Eq. 3.30** is reformulated into  $4 \times 4$ -matrix expression,  $\mathcal{P}^M$ . Thus, the  $\mathcal{P}^M$  for the 1<sup>st</sup> PVDF layer in the

case of parallel electrical connection with alternative voltage orientation is formulated as:

$$\begin{pmatrix} F_1^- \\ -U_1^- \\ V_1 \\ I_1^- \end{pmatrix} = \mathbf{P}^M \begin{pmatrix} F_1^+ \\ U_1^+ \\ -V_1 \\ I_1^+ \end{pmatrix}, \quad (3.39)$$

where

$$\mathbf{P}^M = \begin{pmatrix} \frac{\cosh \gamma d - X \sinh \gamma d}{1 - X \sinh \gamma d} & \frac{j\beta[\sinh \gamma d + 2X(1 - \cosh \gamma d)]}{1 - X \sinh \gamma d} & \frac{-hC(1 - \cosh \gamma d)}{1 - X \sinh \gamma d} & 0 \\ \frac{-j \sinh \gamma d}{\beta(1 - X \sinh \gamma d)} & \frac{\cosh \gamma d - X \sinh \gamma d}{1 - X \sinh \gamma d} & \frac{-jhC \sinh \gamma d}{\beta(1 - X \sinh \gamma d)} & 0 \\ 0 & 0 & -1 & 0 \\ \frac{-jhC \sinh \gamma d}{\beta(2 - X \sinh \gamma d)} & \frac{-hC(1 - \cosh \gamma d)}{1 - X \sinh \gamma d} & \frac{-jC\omega}{1 - X \sinh \gamma d} & -1 \end{pmatrix}, \quad (3.40)$$

$$I_1^- = \sum_{k=1}^N (-1)^{N-k} I_k, \quad (3.41)$$

$$I_1^+ = \sum_{k=1}^{N-1} (-1)^{N-k-1} I_{k+1}, \quad \text{for } n \leq N-1, \quad (3.42)$$

$$I_N^+ = 0. \quad (3.43)$$

The strikethrough symbols of  $\mathbf{P}$  and  $\mathbf{I}$  are introduced to the parallel electrical connection with alternating voltage orientation.

Now, the multiplication of  $\mathbf{P}^M$  matrices yields the sum of all currents entering and leaving all the PVDF layers that are connected electrically in parallel with alternating voltage orientation. Thus, the relationships between the bottom (-) surface of the 1<sup>st</sup> PVDF layer

and the top (+) surface of the  $N^{\text{th}}$  PVDF layer are given as:

$$\begin{pmatrix} F_1^- \\ -U_1^- \\ V_1 \\ I \end{pmatrix} = \mathcal{P}_{\{N\}}^M \begin{pmatrix} F_N^+ \\ U_N^+ \\ -V_N \\ 0 \end{pmatrix}, \quad (3.44)$$

where

$$\mathcal{P}_{\{N\}}^M = \prod_{k=1}^N \mathcal{P}_k^M, \quad (3.45)$$

$$-V_1 = (-1)^N V_N \equiv V. \quad (3.46)$$

The partial sum currents,  $I_n^-$  and  $I_n^+$ , on each surface are defined as:

$$I_n^- = \sum_{k=n}^N (-1)^{N-k} I_k, \quad (3.47)$$

$$I_n^+ = \sum_{k=n}^{N-1} (-1)^{N-k-1} I_{k+1}, \quad \text{for } n \leq N-1, \quad (3.48)$$

where

$$I_N^+ = 0. \quad (3.49)$$

### 3.4 Modeling of Non-Piezoelectric Layers

The previous section presented the formulation of multiple-layer PVDF as an active piezoelectric layer. The ultrasonic sensor is composed of piezoelectric layers and non-piezoelectric layers such as electrodes and bonding layers. The non-piezoelectric layers are mechanically in series with the PVDF layers, and their finite thickness loads the PVDF

ultrasonic response. Since electrode layers have high electrical conductivity, their electrical resistance could be neglected and assumed  $R = 0$ . In addition, the electrode layers between the bonding layer, an intervening layer that adheres to the PVDF layers, are usually connected to a common terminal, as shown in **Figure 3.6**. Therefore, it could be assumed that there is no voltage drop across the intervening bonding layers. Thus, the electrode and bonding layers are considered to be purely mechanical in which

$$h = 0, \quad 1/C = 0. \quad (3.50)$$

The inclusion of the intervening non-piezoelectric layers between the PVDF layers in the multiplication of  $4 \times 4$ -matrices of the multiple-layer PVDF arrangement requires the expression of the non-piezoelectric mechanical properties to be in  $4 \times 4$ -matrix. Hence, the  $P^M$   $4 \times 4$ -matrix expression in **Eq. 3.28** is simplified for the non-piezoelectric layer by substituting **Eq. 3.50** as:

$$P^{np} = \begin{pmatrix} \cosh \gamma d & -j\beta \sinh \gamma d & 0 & 0 \\ jB^{-1} \sinh \gamma d & \cosh \gamma d & 0 & 0 \\ 0 & 0 & 1 & 0 \\ 0 & 0 & 0 & 1 \end{pmatrix}. \quad (3.51)$$

The  $P^{np}$   $4 \times 4$ -matrices expression of non-piezoelectric layers can be directly included in the multiplication of  $4 \times 4$ -matrices of the PVDF layers while maintaining the correct relationship between the acting quantities on the bottom (–) and top (+) surfaces.

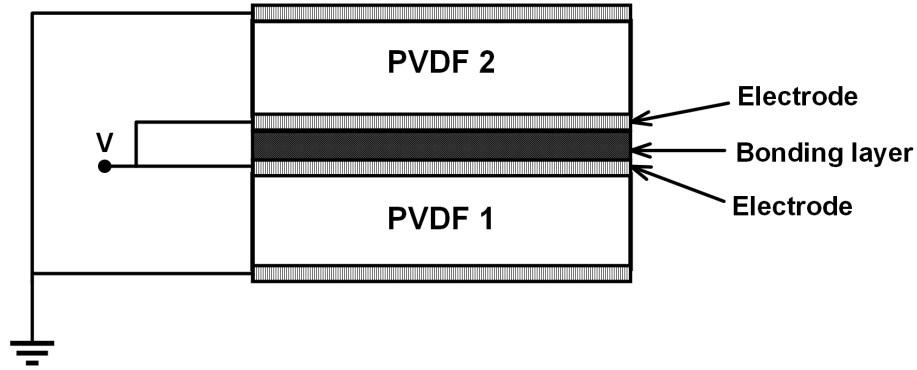


**Figure 3.6:** Representation of common electrical connections to electrodes between the bonding layer

### 3.5 Equivalent Circuit Model of Double-Layer PVDF

#### WUS

The general construction of the essential layers of a double-layer PVDF ultrasonic sensor is shown in **Figure 3.7**. The figure illustrates the mechanical and electrical quantities acting on the top and bottom surfaces of each layer. The double-layer ultrasonic sensor is composed of two PVDF layers with top and bottom electrode layers and a bonding layer between the inner electrode layers. The design of the developed double-layer PVDF WUS in this thesis is detailed in the following chapter (**Chapter 4**). The multiplication of the  $4 \times 4$  matrices sequence of the layers yields the resultant  $4 \times 4$ -matrix expression,  $M$ . The  $M$  expression relates  $F_{elc1}^-$  and  $U_{elc1}^-$  on the bottom (-) surface of the first electrode layer next to the backing medium in terms of  $F_{elc4}^+$  and  $U_{elc4}^+$  on the top (+) side of the fourth electrode layer next to the propagation medium. Also, it produces the sum of the running current,  $I$ . The polarization directions of the two PVDF layers are represented by the sign of  $h$  in **Eq. 3.40**.

Thus, the resultant matrix,  $M$ , of the double-layer PVDF ultrasonic sensor is given as:

$$\begin{pmatrix} F_{elc1}^- \\ U_{elc1}^- \\ -V \\ I \end{pmatrix} = M \begin{pmatrix} F_{elc4}^+ \\ U_{elc4}^+ \\ V \\ 0 \end{pmatrix}, \quad (3.52)$$

where

$$M = \mathbf{P}_{elc1}^{np} \mathbf{P}_{PVDF1}^M \mathbf{P}_{elc2}^{np} \mathbf{P}_{bond}^{np} \mathbf{P}_{elc3}^{np} \mathbf{P}_{PVDF2}^M \mathbf{P}_{elc4}^{np}$$

$$= \begin{pmatrix} M_{11} & M_{12} & M_{13} & M_{14} \\ M_{21} & M_{22} & M_{23} & M_{24} \\ M_{31} & M_{32} & M_{33} & M_{34} \\ M_{41} & M_{42} & M_{43} & M_{44} \end{pmatrix}. \quad (3.53)$$

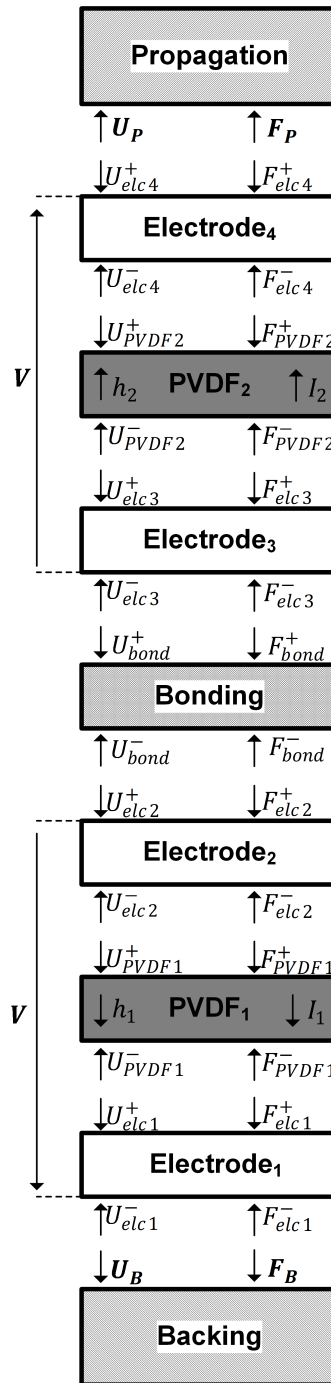


**Figure 3.7:** Acting quantities on each individual layer of double-layer PVDF WUS. Reversal voltage orientation is assumed.

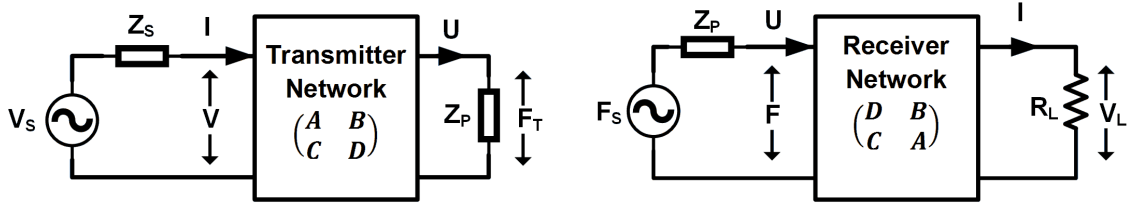


**Figure 3.8:** Equivalent circuit of double-layer PVDF ultrasonic sensor as a two-port network for transmitting and receiving modes.

The equivalent circuit of the double-layer PVDF ultrasonic sensor can be described as a two-port network that relates between the input electrical variables and output mechanical variables in transmitting mode or vice versa in the receiving mode [190], as shown in **Figure 3.8**. The compact  $2 \times 2$ -matrix expression of the two-port network representation of the double-layer ultrasonic sensor is obtained by reformulating the resultant  $4 \times 4$ -matrix,  $M$ , in **Eq. 3.53** in terms of the acoustic impedance of the backing medium,  $Z_B$ , and the propagation medium,  $Z_P$ . For the double-layer PVDF configuration in **Figure 3.7**,  $Z_B$  and  $Z_P$  are defined as:

$$Z_B = \frac{F_B}{U_B} = \frac{F_{elc(1)}^-}{-U_{elc(1)}^-}, \quad (3.54)$$

$$Z_P = \frac{F_P}{U_P} = \frac{F_{elc(4)}^+}{-U_{elc(4)}^+}. \quad (3.55)$$

Thus, the compact  $2 \times 2$ -matrix expression for the equivalent circuit of the double-layer PVDF ultrasonic sensor is obtained by substituting **Eq. 3.54** and **Eq. 3.55** in **Eq. 3.52** as:

$$\begin{pmatrix} V \\ I \end{pmatrix} = \begin{pmatrix} A & B \\ C & D \end{pmatrix} \begin{pmatrix} F_P \\ U_P \end{pmatrix}, \quad (3.56)$$

where

$$A = -M_{33} \left( \frac{M_{21}Z_B - M_{11}}{M_{23}Z_B - M_{13}} \right), \quad (3.57)$$

$$B = M_{33} \left( \frac{M_{22}Z_B - M_{12}}{M_{23}Z_B - M_{13}} \right), \quad (3.58)$$

$$C = M_{41} - M_{43} \left( \frac{M_{21}Z_B - M_{11}}{M_{23}Z_B - M_{13}} \right), \quad (3.59)$$

$$D = -M_{42} + M_{43} \left( \frac{M_{22}Z_B - M_{12}}{M_{23}Z_B - M_{13}} \right). \quad (3.60)$$

From the equivalent circuit of the double-layer PVDF sensor in the ultrasonic transmitting mode shown in **Figure 3.8**, the electrical input impedance of the double-layer ultrasonic sensor,  $Z_E$ , seen at the electrical side in the transmitting mode when the output is loaded by the acoustic impedance,  $Z_P$ , of the propagation medium defined as:

$$Z_E = \frac{AZ_P + B}{CZ_P + D}. \quad (3.61)$$

The voltage transfer ratio in the transmitting mode between the input voltage,  $V$ , and the output force,  $F_T$ , is defined as:

$$\frac{F_T}{V} = \frac{Z_P}{AZ_P + D}. \quad (3.62)$$

The acoustic input impedance,  $Z_M$ , seen at the mechanical terminal pair in the receiving mode when the output is loaded by electrical impedance,  $R_L$ , is defined as:

$$Z_M = \frac{DR_L + B}{CR_L + A}. \quad (3.63)$$

The voltage transfer ratio in the receiving mode between the input force,  $F$ , and the output

voltage,  $V_L$ , is defined as:

$$\frac{V_L}{F} = \frac{R_L}{DR_L + B}. \quad (3.64)$$

For pulsed ultrasound, there is no interference effect between the transmitted and received pulse ultrasound. Thus, the force transfer ratio between the output force,  $F_T$ , in the transmitting mode and the input force,  $F$ , in the receiving mode could be obtained by assuming the propagation medium is a loss-free as :

$$\frac{F}{F_T} = \frac{2Z_M}{Z_M + Z_P}. \quad (3.65)$$

The overall voltage transfer ratio through both the transmitting and receiving modes, neglecting the loss by the ultrasound propagation, is defined as [182]:

$$\frac{V_L}{V} = \frac{F_T}{V} \cdot \frac{F}{F_T} \cdot \frac{V_L}{F} = \frac{2R_L Z_P}{(AZ_P + B)[R_L(CZ_P + D) + (AZ_P + B)]}. \quad (3.66)$$

The acoustic output power,  $P_T$ , at the mechanical terminal in the transmitting mode can be obtained from **Eq. 3.62** in terms of the input voltage,  $V$ , as:

$$P_T = \frac{Z_P}{|AZ_P + B|^2} \cdot V^2. \quad (3.67)$$

The transmitted power at the electrical terminal in the transmitting mode,  $P_E$ , is defined as [191]:

$$P_E = \frac{V^2 \operatorname{Re}(Z_E)}{|Z_E|^2}. \quad (3.68)$$

The conversion efficiency of the transmitted power,  $P_E$ , into the acoustic power,  $P_T$ , can be

obtained from **Eq. 3.67** and **Eq. 3.68** as a conversion loss (CL) expressed in dB as:

$$CL = -10 \log \frac{P_T}{P_E} = -10 \log \frac{Z_P |Z_E|^2}{|AZ_P + B| \operatorname{Re}(Z_E)}. \quad (3.69)$$

The CL is independent of the power reflection due to the impedance mismatching between the power source and the ultrasonic sensor. The ratio of the transmitted power,  $P_E$ , to the power available,  $P_S$ , from the power source is defined by the matching loss (ML) parameter expressed in dB:

$$ML = -10 \log \frac{P_E}{P_S} = -10 \log \frac{4 \operatorname{Re}(Z_s) \operatorname{Re}(Z_E)}{|Z_S + Z_E|^2}. \quad (3.70)$$

Lastly, the ratio of the electrical power available from the source,  $P_S$ , converted into acoustic output power,  $P_T$ , is given by the transducer loss (TL) parameter expressed in dB as:

$$TL = -10 \log \frac{P_T}{P_S} = ML + CL. \quad (3.71)$$

The developed double-layer PVDF WUS performance in terms of operating frequency, frequency bandwidth, and signal strength is studied and evaluated in the following chapters (**Chapter 4** and **Chapter 5**) using the above parameters, such as  $Z_E$ ,  $P_T$ , CL. All the parameters are functions of frequency and are calculated accordingly.

# **Chapter 4**

## **Numerical Study and Design**

### **Considerations of the Double-Layer**

### **PVDF WUS**

This chapter presents the design of the double-layer PVDF WUS. It first studies the ultrasonic performance of the double-layer PVDF WUS, such as operating frequency, frequency bandwidth, acoustic power, and electromechanical conversion efficiency, under several conditions using the numerical simulation model developed in **Chapter 3**. The effects of the mass loading of the non-piezoelectric layers, such as backing, bonding, and electrode layers, on the ultrasonic performance of the double-layer PVDF WUS are also studied in detail for several materials and layer thicknesses. Then, the design considerations of the double-layer PVDF WUS are discussed based on the numerical simulation study. This chapter also addresses the challenges related to the PVDF layer thickness and sensing area selection, the double-layer PVDF arrangement, the electrical connection and lead wire attachment, the bonding of the two PVDF layers, and the packaging of the WUS structure. Lastly, the design of the double-layer PVDF WUS is described based on the results of the

numerical simulation study and the design considerations and challenges discussed.

## 4.1 Choosing the PVDF Piezoelectric Film

There are a variety of piezoelectric materials such as crystals, ceramics, polymers, and their composites. Since the discovery of piezoelectric ceramic materials during the 1940s, they have become widely used in many ultrasonic applications due to their high piezoelectric coefficient [192]. In ultrasonic medical applications, piezoceramics, such as PZT, are most commonly used [193]. Piezoceramics exhibit a very high electromechanical coupling coefficient, high dielectric constants, and low electrical and mechanical losses compared to other piezoelectric materials. The major challenges of using piezoelectric ceramics such as PZT in designing a WUS are their brittle nature, inflexibility, and high acoustic impedance mismatching to human soft tissue [194–196]. Despite the piezoceramic's superior piezoelectricity, piezoelectric polymer materials such as polyvinylidene fluoride (PVDF) offer the flexibility that could be suitable for a WUS. There are several polymeric piezoelectric materials, such as poly(vinylidene fluoride-trifluoroethylene) [P(VDF-TrFE)] copolymer [72], nylon-(5, 7, and 11) [72, 197], and polyurea [198–200]. Although there have been many piezoelectric polymers investigated, the choice of commercially available piezopolymers remains limited. PVDF and P(VDF-TrFE) are commercially available as film sheets in different thicknesses from vendors such as Measurement Specialties. However, the commercially available P(VDF-TrFE) has greater crystallinity resulting in brittleness [72]. The PVDF film offers high flexibility and thus can be firmly attached to the curved skin surface. In addition, the close matching of the PVDF acoustic impedance to that of human soft tissues provides a good ultrasonic transmission to the tissue without the requirement of acoustic matching layers. The sensor could also be easily fabricated into

**Table 4.1:** Typical properties of piezoelectric materials of interest.

Parameter	Piezopolymer				Piezoceramic
	PVDF [158]	P(VDF-TrFE) [158]	Nylon-11 [197, 203]	Polyurea [199, 200]	PZT-4 [158]
Density, $\rho$ (kg/cm <sup>2</sup> )	1780	1880	1023	1450	7500
Longitudinal sound velocity, $v$ (m/s)	2260	2400	2000	2.18	4630
Acoustic impedance, $Z$ (MRayl)	4.02	4.51	2.05	3.16	34.40
Stiffness constant, $c^D$ (10 <sup>9</sup> N/m <sup>2</sup> )	9.10	11.3	–	6.9	159
Thickness coupling factor, $k_t$	0.20	0.30	0.11	0.1	0.51
Piezoelectric constant, $e$ (C/m <sup>2</sup> )	-0.14	-0.22	–	-0.06	15.10
Transmitting constant, $h$ (10 <sup>9</sup> V/m)	-2.6	-4.7	–	-1.7	2.7
Dielectric constant, $\epsilon_S/\epsilon_o$	6.20	5.3	2.5	4.4	635
Dielectric loss tangent, $\tan \delta_e$	0.25	0.14	0.25	0.02	0.004
Mechanical loss tangent, $\tan \delta_m$	0.10	0.04	0.12	–	0.004

any desired dimensions due to the commercial availability of PVDF films in large-area sheets. Therefore, the PVDF polymer film has been chosen as a piezoelectric material to construct the WUS for this thesis research objective. **Table 4.1** shows the typical properties of common piezopolymers and a piezoceramic. The acoustic impedance ( $Z$ ) is the resistance to ultrasound propagation through the medium. The stiffness constant ( $c^D$ ) is the resistance to deformation per unit area, the thickness coupling factor ( $k_t$ ) is the conversion efficiency between electrical energy and mechanical energy. The piezoelectric constant ( $e$ ) is the electric charge generated by a piezoelectric material per unit of surface area. The dielectric constant ( $\epsilon_S/\epsilon_o$ ) is the dielectric displacement ratio relative to the vacuum permittivity. The transmitting constant ( $h$ ) is the ratio of the piezoelectric constant to the dielectric displacement with constant strain. The loss tangents ( $\tan \delta_e$  and  $\tan \delta_m$ ) are the energy dissipation within the piezoelectric material [201, 202].

## 4.2 Numerical Study of Double-Layer PVDF WUS

In this section, the PVDF ultrasonic sensor properties are studied to obtain some guidelines for the design and construction of double-layer PVDF WUS based on the numerical simulation model of the double-layer PVDF WUS introduced in **Chapter 3**. In general, the ultrasonic properties of double-layer PVDF WUS, such as operating frequency, bandwidth, acoustic output power, and power conversion efficiency, depend not only on the piezoelectric properties of the PVDF film but also on the properties of non-piezoelectric layers such as backing, electrode, and bonding layers. Therefore, the effects of each non-piezoelectric layer are studied in this section in order to design the double-layer PVDF WUS. The parameters of non-piezoelectric materials used in the numerical simulations are given in **Table 4.2**.

### 4.2.1 PVDF Layer Thickness and Ultrasound Sensing Area

The thickness and the ultrasound sensing area of the PVDF layer are important parameters for the WUS operating frequency, ultrasonic signal strength, and spatial resolution in ultrasonic measurements. The thickness of the PVDF layer determines the resonance frequency as the PVDF piezoelectric film operates in the thickness-extensional mode. When an alternating voltage at the resonant frequency of the PVDF layer is applied along its thickness direction, the thickness of the PVDF layer changes periodically, which leads to the generation of ultrasound waves and vice versa to the detection of ultrasound waves [209]. The starting point for the thickness selection of a PVDF film is the desired ultrasound frequency. The resonance frequency is when the PVDF layer converts electrical energy into acoustic energy most efficiently. Thus, the PVDF layer oscillations at the resonance

**Table 4.2:** Acoustic properties of the materials used in the numerical simulations.

Material	Longitudinal sound velocity, $v$ (m/s)	Density, $\rho$ (kg/cm <sup>3</sup> )	Acoustic impedance, $Z$ (MRayl)
Air [204]	344	1.24	0.0004
Aluminum [151, 204]	6300	2700	17
Araldite 10 phe [205]	2620	1160	3.04
Araldite 50 phe [205]	2160	2860	6.18
Ecosorb [204]	2600	4500	11.7
Polyimide [206]	2414	1421	3.43
Silicon adhesive [207]	960	1470	1.41
Silver [205]	3600	1060	38.16
Silver epoxy [205]	1900	2710	5.15
Silver ink *	3600	3400	12.24
Spurr's epoxy [151, 208]	2200	1090	2.4
Sylgard [205]	1027	1050	1.07
Water [204]	1500	1000	1.5

\* Estimated.

frequency will occur with much greater ultrasonic intensity. **Figure 4.1** shows the calculated acoustic output power,  $P_T$ , of a single-layer 52  $\mu\text{m}$ -thick PVDF as a function of frequency. The acoustic power of the PVDF is obtained by assuming the input voltage =1 V in **Eq. 3.67**. The highest acoustic power occurs at the fundamental frequency of the PVDF layer. Also, the PVDF layer has frequencies of a large amplitude of acoustic power at an odd multiple of the fundamental frequency. These are termed harmonic frequencies. In this study, the fundamental frequency of a PVDF layer is the operating frequency of interest.

To study the operating frequency of PVDF layer dependence on the thickness, the

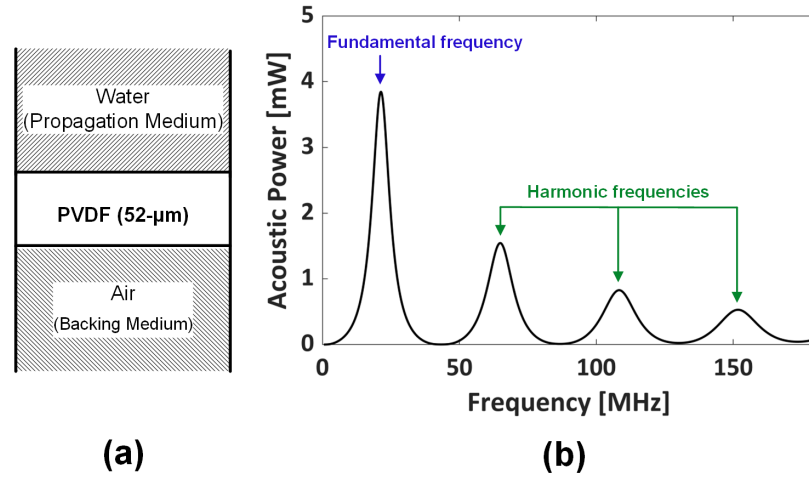


**Figure 4.1:** The PVDF layer resonance frequencies. The PVDF acoustic power is computed as a function of frequency to illustrate the fundamental and harmonic frequencies of single-layer 52  $\mu\text{m}$ -thick PVDF. The structural configuration of the simulation (a) and the resonance frequencies (b) are shown. Input voltage = 1V is assumed.

single-layer PVDF operating frequency is computed as a PVDF layer thickness function.

**Figure 4.2** (a) depicts the structural configuration of the single-layer PVDF simulation, and **Figure 4.2** (b) shows the operating frequency of the single-layer PVDF in a thickness range of 10 – 250  $\mu\text{m}$ . As the thickness,  $d$ , of the PVDF layer doubles, the operating frequency reduces nearly by half. For example, a 52  $\mu\text{m}$ -thick PVDF layer resonates at 21.3 MHz, where a 104  $\mu\text{m}$ -thick ( $52 \times 2$ ) PVDF layer resonates at 10.7 MHz ( $21.3/2$ ). Thus, the thicker the PVDF layer, the lower the resonant (operating) frequency of the ultrasonic sensor.

The active ultrasound area of the PVDF layer is related to the ultrasonic signal strength of the ultrasonic sensor. **Figure 4.3** shows the acoustic power of single-layer 104- $\mu\text{m}$ -thick PVDF at the operating frequency (10.7 MHz) for the area range of 0.1 – 8.0  $\text{cm}^2$ . The result shows that the PVDF acoustic power (ultrasonic signal strength) increases as the active ultrasound increases.

The numerical simulation study carried out in this section is mainly based on a 52

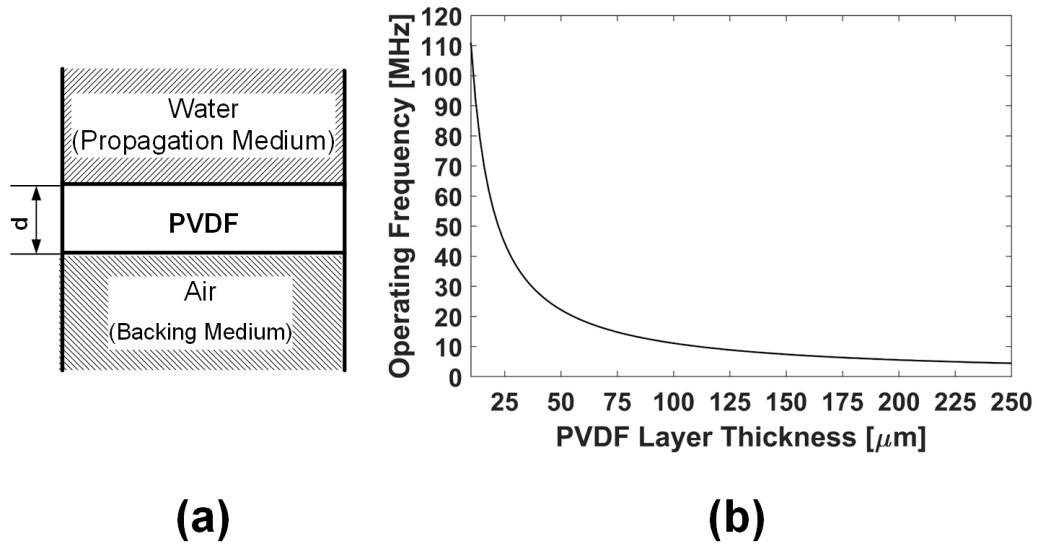


**Figure 4.2:** The PVDF thickness layer effect on the operating frequency. The operating frequencies are computed as a function of the single-layer PVDF layer thickness,  $d$ , in a range of 10 – 250  $\mu\text{m}$ . The structural configuration of the simulation (a) and the operating frequency (b) are shown.

$\mu\text{m}$ -thick PVDF layer of an active ultrasound area of  $4 \text{ cm}^2$ . The selection of the PVDF layer thickness and active ultrasound area will be discussed in the next section, **Section 4.3.2**.

#### 4.2.2 Double-Layer PVDF Configuration

The inherent properties of PVDF piezoelectric may be suitable features for a WUS to perform the continuous monitoring of muscle contraction. However, the PVDF has relatively weak piezoelectric properties and high internal losses comparing with the piezoceramic materials, as seen in **Table 4.1**. The high dielectric loss of the PVDF ( $\tan \delta_e = 0.25$ ) causes the high dissipation of power within the PVDF, and the low electromechanical coupling coefficient ( $k_t = 0.20$ ) indicates the low electric-acoustic conversion ratio. The low dielectric constant of PVDF ( $\epsilon_S/\epsilon_o = 6.20$ ) implies the high electrical input impedance, which leads to the requirement of a much higher input voltage,  $V$ . For example, the PVDF film, in general,

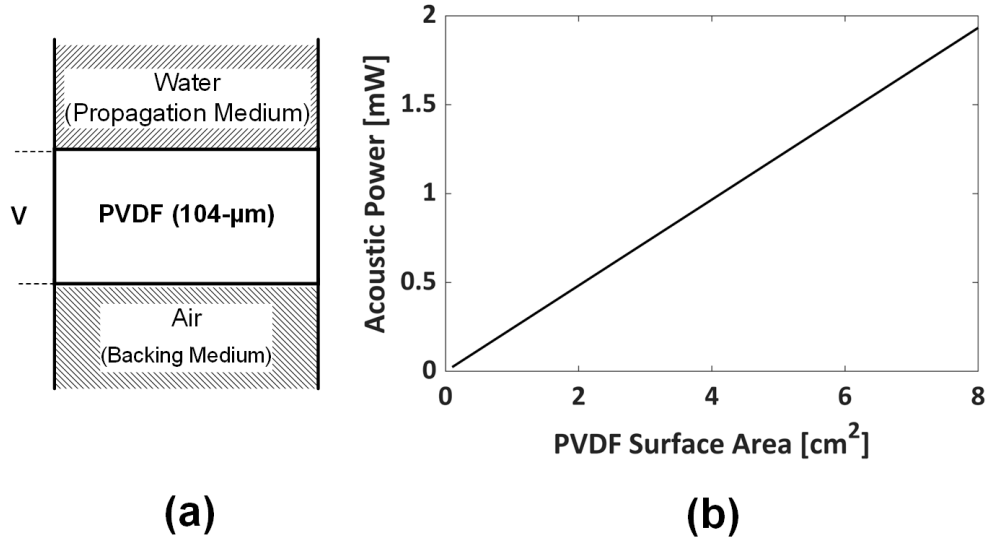


**Figure 4.3:** The effect of the active ultrasound area of PVDF layer on the acoustic output power. The acoustic output powers at the operating frequency of single-layer 104- $\mu\text{m}$ -thick PVDF are computed as a function of the area range of 0.1 – 8.0  $\text{cm}^2$ . The Structural configuration of the simulation (a) and the acoustic power at the operating frequency (b) are shown. Input voltage = 1 V is assumed.

would require a driving voltage eight times higher than the PZT to generate a comparable ultrasonic intensity [71].

One of the main considerations in designing a PVDF WUS is the signal-to-noise ratio (SNR) due to the ultrasonic transmission power limitation and the requirement of the high driving voltage. Increasing the transmitting ultrasound intensity, the transmitted acoustic power ( $P_T$ ), in the transmission mode, would increase the received/reflected ultrasound intensity. Hence, the SNR of the received ultrasound would be increased. Swartz and Plummer [71] proposed the approach of the multiple-layer PVDF configuration to increase the output power from a PVDF ultrasonic sensor from the available voltage source. The multiple-layer PVDF arranged electrically in parallel and mechanically in series would increase the ratio of the voltage to the acoustic power in the transmission mode. Thus, the same input voltage,  $V$ , for parallel electrically connected double-layer PVDF, as shown

in **Figure 4.4**, would theoretically have acoustic output power four times higher than the single-layer PVDF of an equivalent total thickness [71].

**Figure 4.5** (a) shows the four cases of PVDF layer configuration: single-layer 52- $\mu\text{m}$ -thick PVDF, single-layer 104- $\mu\text{m}$ -thick PVDF, double-layer 52- $\mu\text{m}$ -thick PVDF in parallel polarization direction, and double-layer 52- $\mu\text{m}$ -thick PVDF in antiparallel polarization direction. The parallel electrical connection of two 52- $\mu\text{m}$ -thick PVDF layers has reduced the electrical input impedance by factors of around two and four in comparison to the cases of single-layer 52- $\mu\text{m}$ -thick and 104- $\mu\text{m}$ -thick PVDF thickness, respectively, as shown in **Figure 4.5** (b).

Another aspect of the double-layer PVDF configuration is the polarization directions of the two bonded PVDF layers. In the double-layer configuration, the polarization directions of the two PVDF layers can be arranged in either parallel or antiparallel. The parallel polarization direction of the two PVDF layers points in the same direction, as shown by the thick arrows in **Figure 4.6** (a), where the antiparallel polarization of the two PVDF layers points in opposite directions, as shown by the thick arrows in **Figure 4.6** (b). The arrangement of the polarization direction determines the operating frequency of the double-layer PVDF configuration. From the calculated acoustic power and conversion loss (CL) in **Figure 4.5** (c) and (d), respectively, the operating frequency,  $f_p$ , of the double-layer 52- $\mu\text{m}$ -thick PVDF

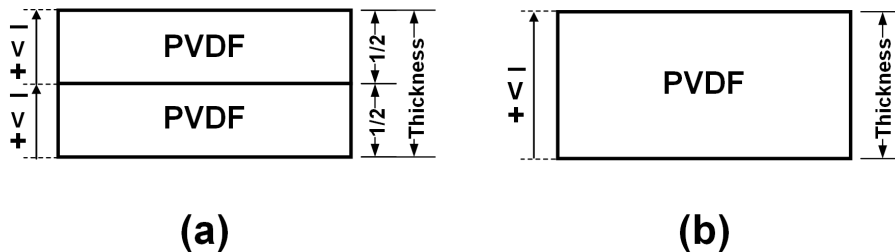


**Figure 4.4:** Representation of the parallel electrically connected double-layer PVDF (a) and a single-layer PVDF of an equivalent total thickness (b).

in parallel polarization direction is at 10.7 MHz where the operating frequency,  $f_{ap}$ , of the case of antiparallel polarization direction is at 21.3 MHz. Thus, the relation of the  $f_p$  and  $f_{ap}$  to the operating frequency of the single-layer PVDF of the same individual PVDF layer thickness (52- $\mu\text{m}$ -thick),  $f_s$ , could be expressed as:

$$f_p \propto \frac{f_s}{2}, \quad (4.1)$$

$$f_{ap} \propto f_s. \quad (4.2)$$

The main advantage of the double-layer PVDF configuration is the increase of the acoustic output power to the input voltage,  $V$ , ratio. For the same surface area and input voltage, the double-layer 52- $\mu\text{m}$ -thick PVDF in both cases of parallel and antiparallel polarization directions have four times higher acoustic power at their operating frequencies compared to the single-layer cases of 104- $\mu\text{m}$ -thick and 52- $\mu\text{m}$ -thick PVDF, respectively, as shown in **Figure 4.5** (c). In addition, the antiparallel polarization direction of the double-layer 52- $\mu\text{m}$ -thick PVDF has an acoustic power of 8.7 mW at 21.3 MHz, which is higher than the parallel polarization direction case of the double-layer 52- $\mu\text{m}$ -thick PVDF of 3.9 mW at 10.7 MHz. This is due to the decrease of electrical impedance as the operating frequency increases, as shown in **Figure 4.5** (b) of the electrical impedance curve. Similarly, the single-layer PVDF of a thicker layer would have larger impedance due to its lower operating frequency. Thus, a thicker PVDF layer requires a higher voltage to transmit a comparable ultrasound intensity to the thinner PVDF layer at their operating frequencies. However, all simulated cases in **Figure 4.4** (a) have approximately the same CL value of  $6.97 \pm 0.012$  dB at their fundamental resonance frequencies, as shown in **Figure 4.5** (d). Thus, the double-layer PVDF configuration increases the acoustic power ratio from the input voltage due to its lower electrical impedance, but would have the same electric power to acoustic power ratio

compared to that of the single-layer PVDF. For the frequency bandwidth, they would have the same full width at half maximum (FWHM) frequency bandwidth of 35% except for the antiparallel polarization direction case of the double-layer PVDF where it has a narrower FWHM bandwidth of 23.1%.

To summarize, the double-layer PVDF that is electrically connected in parallel with their polarization direction in parallel operate at the same frequency and bandwidth as the single-layer PVDF of the equivalent total PVDF layer thickness, but with four times higher acoustic output power to input voltage ratio. Thus, the double-layer PVDF configuration with parallel polarization direction would be a preferable choice for the WUS design due to the higher ultrasound signal strength at the desired frequency chosen.

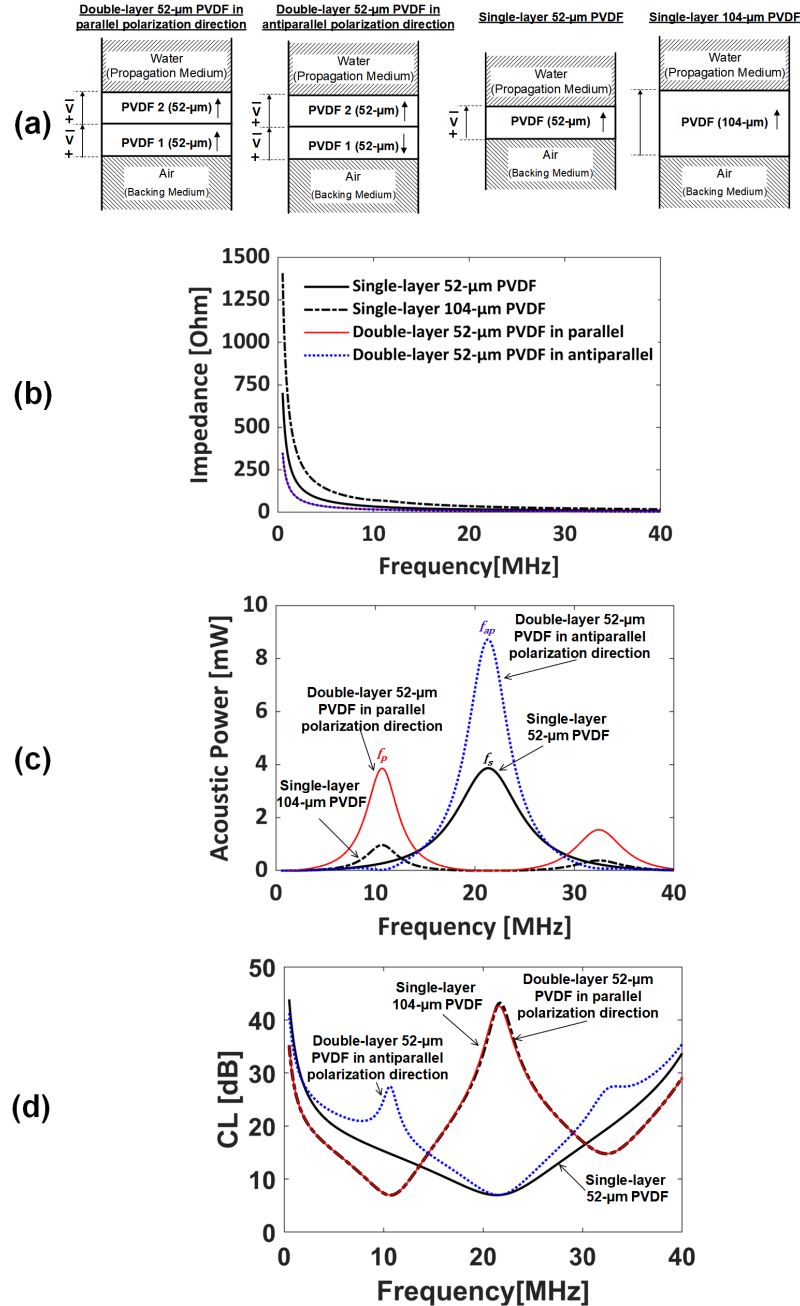


**Figure 4.5:** Four cases of PVDF layer configurations: single-layer 52- $\mu\text{m}$ -thick PVDF, single-layer 104- $\mu\text{m}$ -thick PVDF, double-layer 52- $\mu\text{m}$ -thick PVDF in the parallel polarization direction, and double-layer 52- $\mu\text{m}$ -thick PVDF in the antiparallel polarization direction (a) are simulated. The calculated electrical input impedance (b), acoustic output power (c), and conversion loss (d) are shown. Surface area = 4 cm<sup>2</sup> and input voltage = 1 V are assumed.

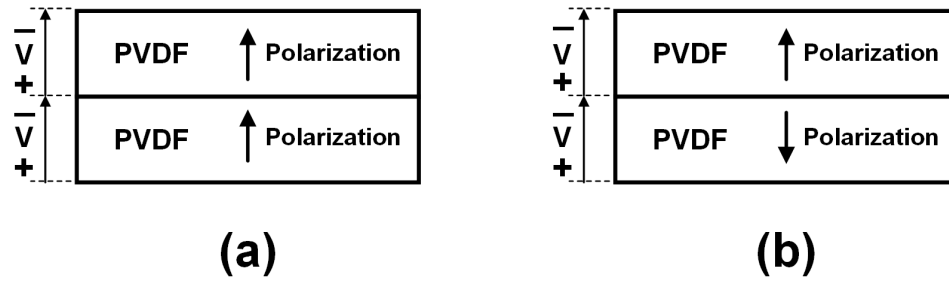


**Figure 4.6:** Polarization directions in double-layer PVDF configuration: parallel (a) and antiparallel (b).

Furthermore, it is conveniently practical to connect the inner electrode of the double-layer PVDF to a common terminal to avoid the interconnection complexity of the electrodes. The connection of the inner electrode to the common electrical terminal would result in an application of an inverted voltage orientation to the two PVDF layers. As the polarization direction is relative to the voltage orientation, the antiparallel polarization direction of the double-layer PVDF layer with inverted voltage orientation would behave as if their polarization directions were in parallel, as illustrated in **Figure 4.7**. Thus, the double-layer PVDF configuration of **Figure 4.7** (a) is employed in the double-layer PVDF WUS design. It is worth noting that the terms parallel and antiparallel polarization directions would be used as described in **Figure 4.6** despite the voltage orientation.

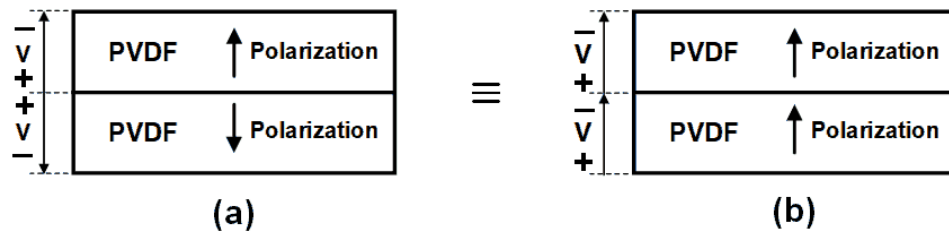


**Figure 4.7:** Double-layer PVDF with reversal voltage orientation and antiparallel polarization directions (a) behaves equivalently to the double-layer PVDF of parallel polarization directions (b).

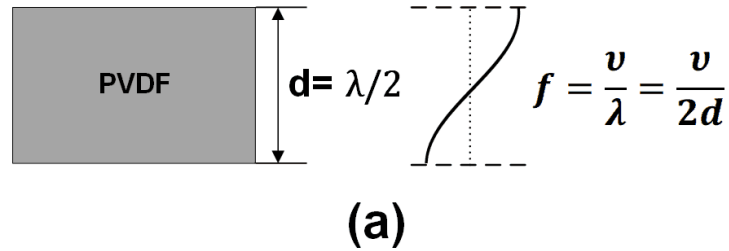
### 4.2.3 Effect of Backing

One of the important aspects in the design of an ultrasonic sensor is taking into consideration the effect of backing material on the PVDF sensor performance. In the previous section, the operating frequency and ultrasound signal strength were discussed for the double-layer PVDF configuration, where the backing and propagation media were assumed to be air and water, respectively. This section focuses on the effect of the backing medium or material on the double-layer PVDF operating frequency, bandwidth, acoustic output power, and CL.

For a PVDF piezoelectric operating in the thickness-extensional mode, the resonance frequency occurs at a wavelength twice the thickness of the PVDF film when there are no backing materials (air backing) due to an open boundary condition. Hence a half-wavelength resonance mode, as shown in **Figure 4.8** (a). If the PVDF is backed with a material of an acoustic impedance much higher than the PVDF, the resonance frequency occurs at a wavelength four times the thickness of PVDF film due to a close boundary condition of the backing. Hence a quarter-wavelength resonance frequency, as shown in **Figure 4.8** (b).

Sherar and Foster [151] and Brown [210] have shown that the operating frequency and conversion efficiency of the single-layer PVDF case depend on the acoustic impedance of the backing. For a backing with very low acoustic impedance material such as air (427 Rayls), the PVDF that is loaded at the front by water (1.5 MRayls) would resonate in the  $\lambda/2$  (half wavelength) mode at the maximum conversion efficiency and narrowest frequency bandwidth. When the PVDF is backed by a high acoustic impedance material such as aluminum (17 MRayls), the PVDF would resonate in  $\lambda/4$  mode at a lower conversion efficiency and broader frequency bandwidth. For the backing of a close acoustic impedance to that of the PVDF, the PVDF would resonate weakly in both  $\lambda/2$  and  $\lambda/4$  modes at the lowest

### A half-wavelength resonance



### A quarter-wavelength resonance

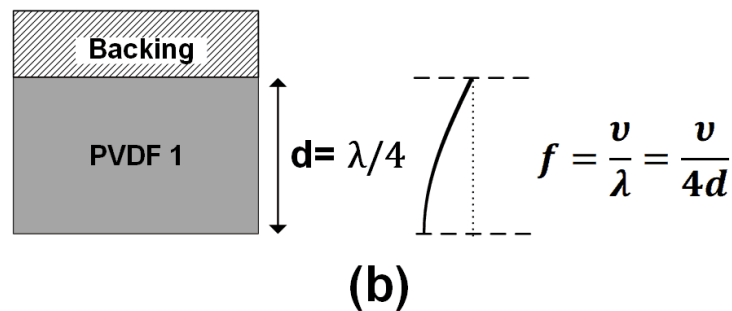


**Figure 4.8:** Standing waves representations of the half-wavelength (a) and quarter-wavelength resonating (b) modes of PVDF.

conversion efficiency and the broadest frequency bandwidth. Thus, the acoustic impedance of the backing determines whether the double-layer PVDF resonates in the half-wavelength ( $\lambda/2$ ), one-quarter wavelength ( $\lambda/4$ ) mode, or both modes.

The prior work of Sherar and Foster [151] and Brown [210] can be extended for the double-layer PVDF ultrasonic sensor attached to the human body in which the front surface of the sensor is loaded by the soft tissue (the propagation medium). The average acoustic impedance of the soft tissue (1.58 MRayls) is close to the acoustic impedance of water (1.50 MRayls); therefore, water is assumed as the propagation medium in the following numerical simulations. To investigate the dependence of the double-layer PVDF sensor performance on the acoustic impedance of the backing material, **Figure 4.9** shows the operating frequency, -3

dB frequency bandwidth at the operating frequency, and CL value at the operating frequency for the double-layer 52- $\mu\text{m}$ -thick PVDF with a backing material acoustic impedance range of 0 – 30 MRayls.

The results in **Figure 4.9** (b) show that the double-layer 52- $\mu\text{m}$ -thick PVDF with a backing impedance of less than 3.0 MRayls operates in  $\lambda/2$  mode (average of  $10.34 \pm 0.26$  MHz). As the backing impedance becomes greater than 7.0 MRayls, the double-layer 52- $\mu\text{m}$ -thick PVDF operates in  $\lambda/4$  mode (average of  $4.9 \pm 0.06$  MHz). When a backing impedance is between the two acoustic impedance values (3.0 – 7.0 MRayls), the double-layer 52- $\mu\text{m}$ -thick PVDF operates in both  $\lambda/2$  and  $\lambda/4$  modes (between 5 and 10 MHz). The backing impedance also affects the operating frequency bandwidth. **Figure 4.9** (c) shows the -3-dB bandwidth percentage of the CL at the corresponding operating frequency. The  $\lambda/2$  operating mode (with a backing of near-zero acoustic impedance) has the narrowest bandwidth of approximately 40.7%, where the  $\lambda/2$  operating mode (with a backing of very high acoustic impedance) has a broader bandwidth of approximately 85%. The operating modes in both  $\lambda/2$  and  $\lambda/4$  results in a very broad bandwidth of more than 100%. The main consideration of the operating modes is the conversion efficiency of the double-layer PVDF sensor. In **Figure 4.9** (d), the CL minima for the double-layer PVDF sensor operates in both  $\lambda/2$  and  $\lambda/4$  modes in the range of 14 dB compared to 6.97 dB for the impedance backing of near-zero (air backing). The backing of very high impedance causes the double-layer PVDF to operate at a lower frequency ( $\lambda/4$  mode) with broader frequency bandwidth; however, it would be at the cost of a larger CL at a range of 10 – 12 dB.

The effect of the backing on the double-layer PVDF is discussed by analyzing the CL parameter in **Figure 4.9**. In order to study the effect of the backing material on the operating frequency and the strength of the ultrasound signal, the acoustic output power is calculated using four different types of backing: air (427 Rayls), Spurr's epoxy (2.4 MRayls),

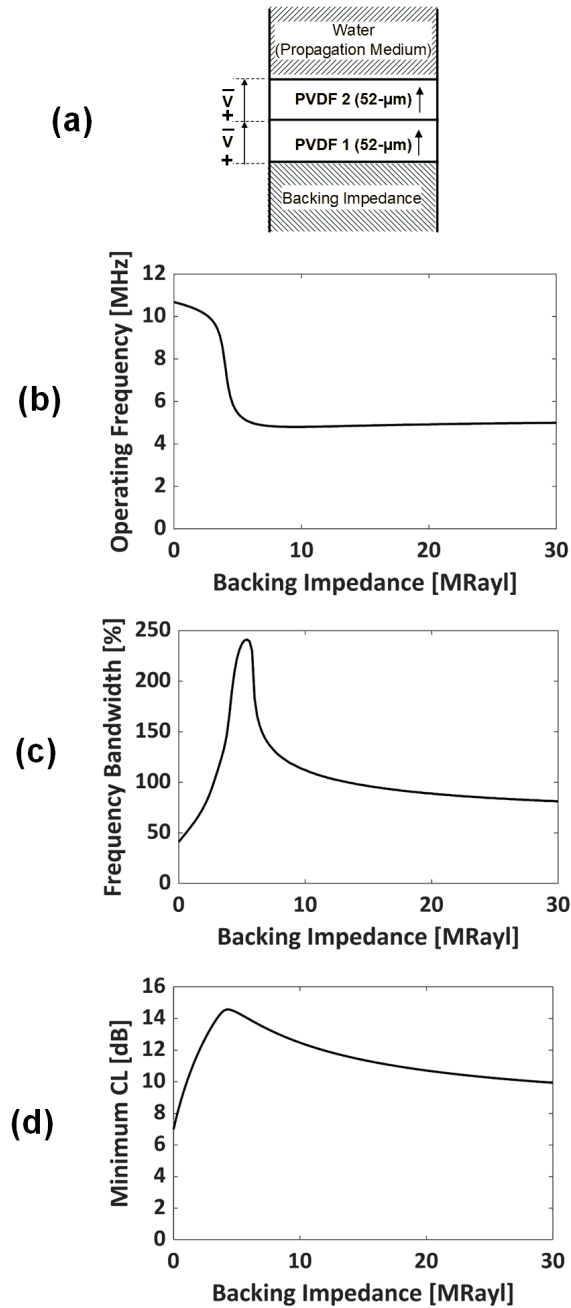


**Figure 4.9:** The effect of the backing acoustic impedance on the ultrasonic performance of the double-layer PVDF sensor. The CL parameter of the double-layer 52- $\mu\text{m}$ -thick PVDF sensor is computed as a function of the backing acoustic impedance of 0 – 30 MRayls. The structural configuration of the simulation (a) and the operating frequency (b), operating frequency bandwidth (c), and CL value at the operating frequency (d) are shown.

PVDF (4.02 MRayls), and aluminum (17 MRayls) with the sensor configuration shown in **Figure 4.10** (a). The acoustic properties of the materials used in the numerical simulations are given in **Table 4.2**. **Figure 4.10** (b) shows the acoustic power of the double-layer 52- $\mu\text{m}$ -thick PVDF using four different types of backing material where the input voltage and active ultrasound area are assumed to be 1 V and 4  $\text{cm}^2$ , respectively. The substantial reduction of the acoustic power from 3.9 mW at the operating frequency in the case of air backing to 0.93 mW and lower in the cases of Spurr's epoxy, PVDF, and aluminum backing materials is observed. The reduction of the acoustic power is due to the increase of CL, as shown in **Figure 4.10** (c), for the cases of Spurr's epoxy, PVDF, aluminum backing materials. For a backing material of the same impedance as the PVDF (4.02 MRayls), the double-layer PVDF sensor has the lowest acoustic power of 0.51 mW at the operating frequency due to the weak resonance in both  $\lambda/2$  and  $\lambda/4$  modes. This result shows that the mass-loading on the back of the double-layer PVDF substantial decreases the transmitted acoustic power. The improvement of the PVDF piezoelectric signal strength is the main objective of designing the WUS. Therefore, it would be preferable to design the double-layer PVDF WUS in an air-back configuration to achieve the maximum possible acoustic power from the applied voltage.

In the simulation of **Figure 4.9** and **Figure 4.10**, the four types of backing are assumed as a backing medium (infinite thickness). In the operational environment of the proposed double-layer PVDF WUS application, the WUS would be exposed to air at the back side. Although, the construction of the double-layer PVDF WUS requires packaging layers in order to bind and protect the WUS structure. The packaging layers would be an intervening layer between the backing medium (air) and the back side of the double-layer PVDF. Sherar and Foster [151] have noted the difficulty in constructing an air-backed PVDF sensor and suggested the use of a low acoustic impedance material such as Spurr's epoxy (2.4 MRayls)

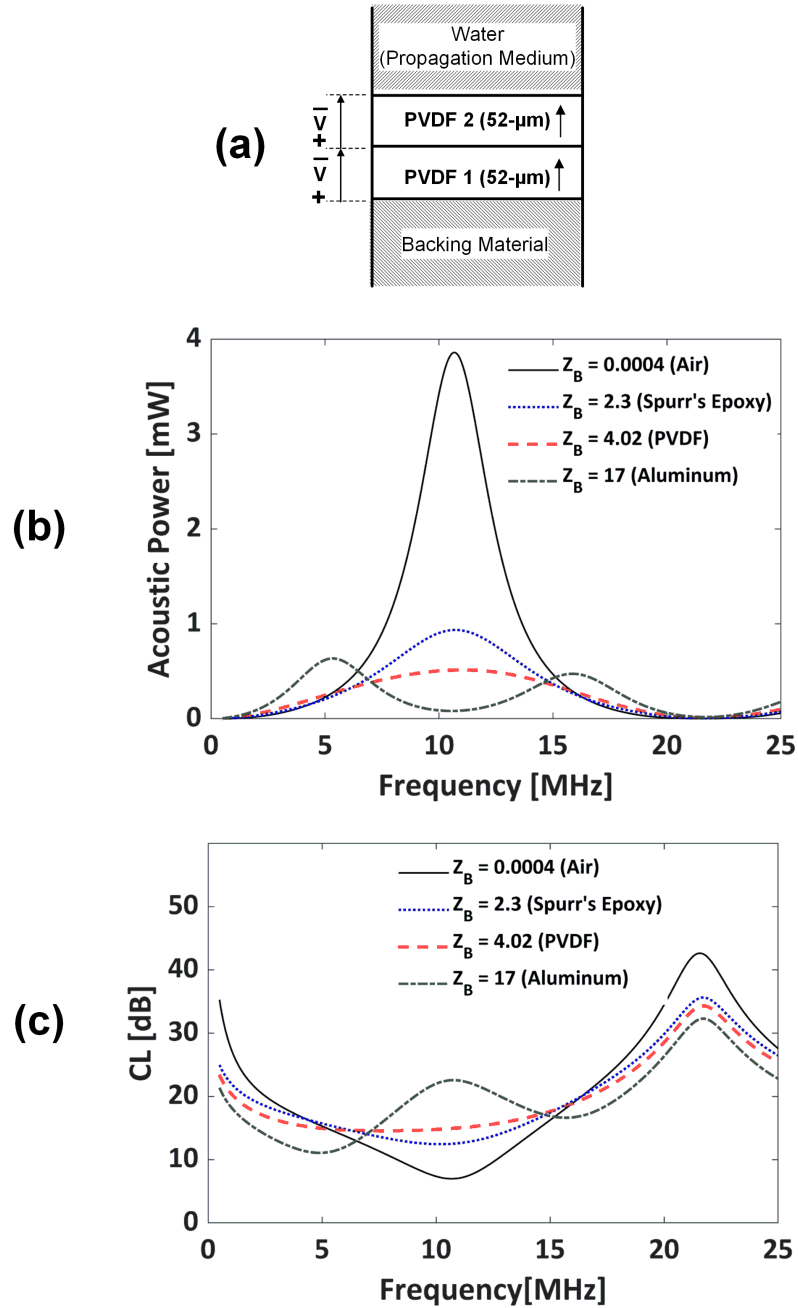


**Figure 4.10:** The effect of the backing acoustic impedance on the transmitted ultrasound of the double-layer 52- $\mu\text{m}$ -thick PVDF. The acoustic output power and CL are computed for four types of backing: air (427 Rayls), Spurr's epoxy (2.3 MRayls), PVDF (4.02 MRayls), and aluminum (17 MRayls). The structural configuration of the simulations (a), the acoustic output power (b), and CL (c) are shown.  $Z_B$  is the acoustic impedance of the backing (MRayls). Surface area = 4 cm<sup>2</sup> and input voltage = 1 V are assumed.

with sufficient thickness as an alternative approach. Even though the Spurr's epoxy has a relatively low acoustic impedance, the simulation in **Figure 4.10** (b) shows the substantial reduction of the acoustic power compared to the air backing. Also, the addition of a thick Spurr's epoxy layer might increase the thickness and decrease the flexibility of the WUS.

A packaging approach by using a polyimide film with an adhesive was found to be well suited for designing the WUS in the previous study [70]. The polyimide films with adhesive are available in relatively thin layers, such as 13- $\mu\text{m}$ -thick polyimide and 25- $\mu\text{m}$ -thick silicone adhesive layers. The selection of the polyimide film with adhesive as packaging provides a thin and flexible profile, good isolation, strong adhesion, and simplicity of construction. However, the polyimide and adhesive layers negatively affect the operating frequency and bandwidth of the double-layer PVDF WUS. **Figure 4.11** shows the simulation of an air-backed double-layer 52- $\mu\text{m}$ -thick PVDF and a double-layer 52- $\mu\text{m}$ -thick PVDF with a 13- $\mu\text{m}$ -thick polyimide layer and a 25- $\mu\text{m}$ -thick silicone adhesive layer on the back side. The polyimide and silicone adhesive layers cause the double-layer 52- $\mu\text{m}$ -thick PVDF to operate in two frequencies of 6.1 MHz and 11.4 MHz with a narrower bandwidth (FWHM) of 5.3 – 6.5 MHz (19.4%) and 10.1 – 11.4 MHz (24.1%), respectively. In comparison, the air-backed double-layer 52- $\mu\text{m}$ -thick PVDF (without the packaging layers of the polyimide and silicone adhesive) operates at a single frequency of 10.7 MHz with a bandwidth (FWHM) of 8.8 – 12.5 MHz (35%). For the WUS application of muscle contraction measurement, a single operating frequency and broader bandwidth are desirable to obtain short ultrasonic pulses.

The necessity of the packaging layers in the construction of WUS provided the impetus for finding an approach to isolate the mass-loading of the packaging layers without impeding the WUS flexibility or increasing its thickness. This thesis research proposes the approach of isolating the mass-loading effect of the packaging layers by creating an air gap between

the back side of the double-layer PVDF and the packaging layers (the polyimide adhesive tape). This approach takes advantage of the natural damping of the PVDF without the requirement of the backing layer to dampen its reverberation due to the large internal losses. While in the case of the piezoceramic materials, a backing layer is required to achieve a broadband response. Also, a minimal gap of air in the order of one micrometer would be sufficient to create a total reflection that prevents the unwanted ultrasonic reflection on the back side within the packaging layers due to the very low acoustic impedance of air (427 Rayls). **Figure 4.12** shows the calculated acoustic power and CL parameters of the double-layer 52- $\mu\text{m}$ -thick PVDF with 1  $\mu\text{m}$ -thick air gap on the back side between the PVDF layers and the packaging layers. The acoustic power and CL curves are matched to those of the double-layer 52- $\mu\text{m}$ -thick PVDF without the packaging layers. Hence, the numerical simulation showed that creating an air gap of few micrometers on the back side makes the double-layer PVDF effectively air-backed, and the packaging layers would not affect the double-layer PVDF performance, assuming that the vibration magnitude of the PVDF is less than 1  $\mu\text{m}$  in the thickness-extensional mode of ultrasound generation.

To conclude, the backing medium/material of the double-layer PVDF would cause a shift in the operating frequency to a lower range and increase the bandwidth of the operating frequency depending on the acoustic impedance of the backing medium. As the acoustic impedance of the backing becomes close to that of the PVDF, the double-layer PVDF sensor would have the largest CL and broadest frequency bandwidth due to the weak resonance in both  $\lambda/2$  and  $\lambda/4$  modes. With a backing of high acoustic impedance, the double-layer PVDF would operate in  $\lambda/4$  frequency with relatively large CL which would lead to approximately four times less acoustic output power in comparison to the air-backed double-layer PVDF ( $\lambda/2$  operating mode). The requirement of a higher electromechanical conversion efficiency and acoustic output power of the PVDF ultrasonic sensor outweighs the preference of broad

frequency bandwidth. In addition, the need for the packaging layers increases the difficulty in the construction of an air-backed PVDF ultrasonic sensor. This thesis research proposes the creation of an air gap between the packaging layers and the back side of double-layer PVDF to address the mass-loading of the packaging layers. Thus, a double-layer PVDF WUS that operates at the maximum ultrasonic intensity could be achieved.

#### 4.2.4 Effect of Electrode Layers

Electrode layers are an electrically conductive layer on both sides of each PVDF layer (top and bottom). The electrode materials generally have higher acoustic impedance compared to the PVDF. The low melting and Curie temperatures of the PVDF prevent the use of the common electroding techniques of the piezoceramics [72]. Sputtered electroding and conductive metal-based ink may be a common electroding method available for PVDF. The sputtered electroding of gold or copper-nickel offers low mass loading due to its minimal thickness ( $\sim 10 - 80$  nm). However, the brittle profile, low operating voltage, and poor adhesion to PVDF of the sputtered electrodes may limit their suitability for flexible PVDF ultrasonic sensors.

On the contrary, conductive metal-based inks, such as silver ink, would be a more suitable option for the flexible PVDF ultrasonic sensor due to their high flexibility, excellent adhesion, high conductivity, and higher operating voltage. The electroding of printed silver ink is much thicker ( $6 - 10$   $\mu\text{m}$ ), which would acoustically load the PVDF [72, 211]. Therefore, the mass-loading of a thick layer of the electrode must be characterized to understand the effect of the double-layer PVDF performance. The studies in [72, 151, 211] have discussed the effect of the electrode on the single-layer PVDF. However, to the best of the author's knowledge, the electrode layers' effect on the double-layer PVDF has not been studied yet.

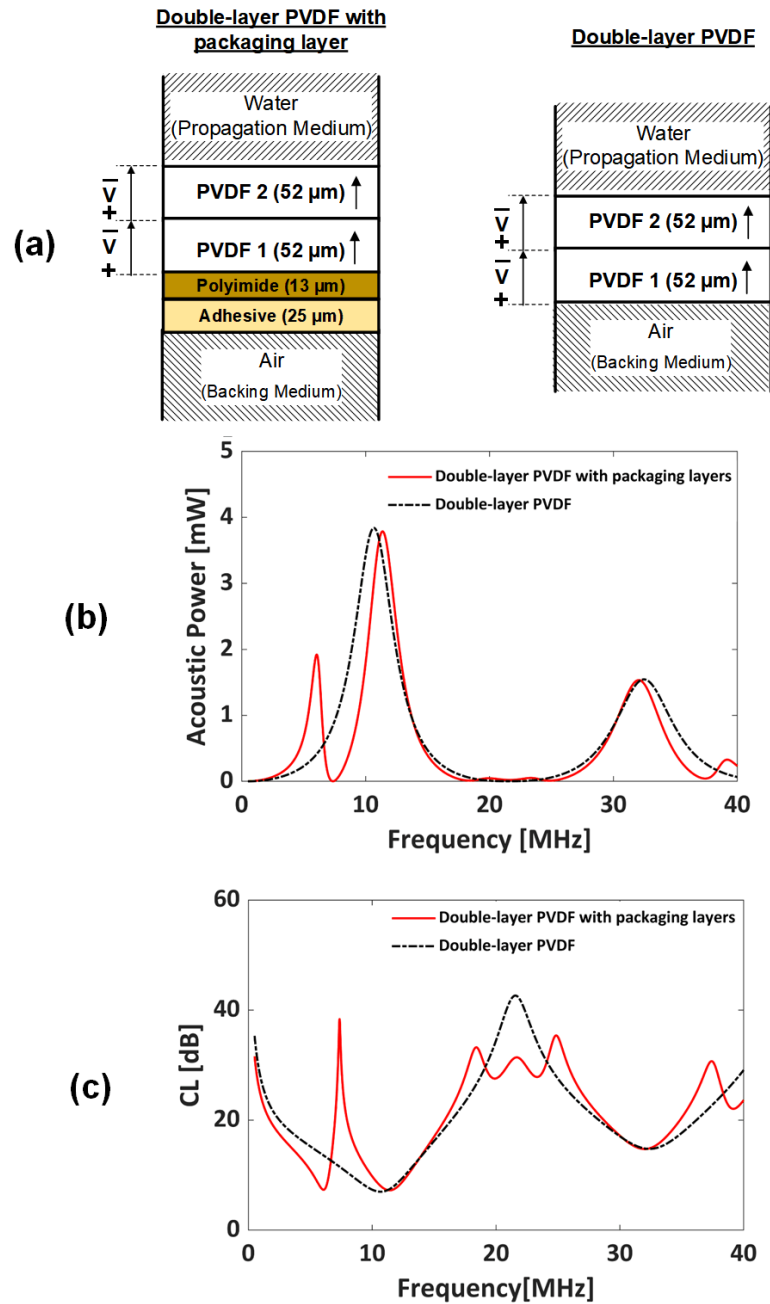


**Figure 4.11:** The effect of the packaging on the ultrasonic performance of the double-layer PVDF. The acoustic output power and CL are calculated for the double-layer 52- $\mu\text{m}$ -thick PVDF with and without the packaging layers of a 13- $\mu\text{m}$ -thick polyimide layer and a 25- $\mu\text{m}$ -thick silicone adhesive layer on the back side. The structural configuration of the simulation (a), the acoustic power (b), and CL (c) are shown. Active ultrasound area = 4  $\text{cm}^2$  and input voltage = 1 V are assumed.

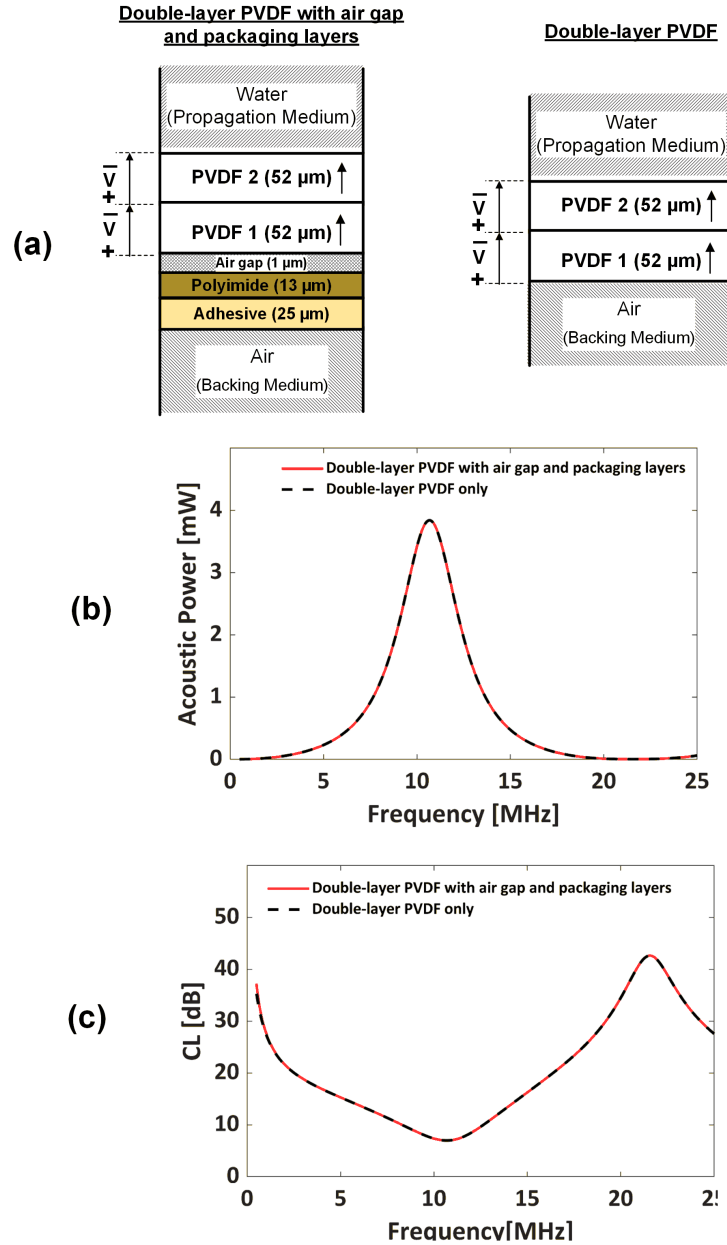


**Figure 4.12:** The isolation of the packaging effect on the ultrasonic performance of the double-layer PVDF by creating an air gap. The acoustic power and CL are calculated for double-layer 52- $\mu\text{m}$ -thick PVDF with 1  $\mu\text{m}$  air gap on the back side between the PVDF layers and the packaging layers of polyimide and silicone adhesive (13- $\mu\text{m}$ -thick polyimide layer and 25- $\mu\text{m}$ -thick silicon adhesive layer), and, for comparison, the double-layer 52- $\mu\text{m}$ -thick PVDF only. The structural configuration of the simulation (a), the acoustic power (b), and the CL (c) are shown. Active ultrasound area = 4  $\text{cm}^2$  and input voltage = 1 V are assumed.

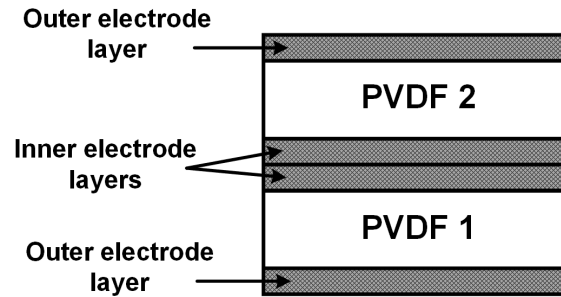


**Figure 4.13:** Illustration of the inner and outer electrode layers of the double-layer PVDF.

The double-layer PVDF WUS would have four electrode layers: two inner electrode layers and two outer electrode layers, as shown in **Figure 4.13**. In order to investigate the effect of the electrode layers, the inner and outer electrode layers are first investigated separately and then combined.

In the following, the effect of only the inner electrode layers is investigated here excluding the outer electrode layer. The effect of inner electrode layers on the ultrasonic performers is illustrated in **Figure 4.14**. The figure shows the calculated acoustic power and CL of a double-layer 52- $\mu\text{m}$ -thick PVDF sensor with two 10  $\mu\text{m}$ -thick inner electrode layers (total of 20  $\mu\text{m}$ ). Three types of the electrode materials are simulated to represent the typical acoustic impedance range of the silver electroding materials: 5.15 MRayls (silver epoxy), 12.24 MRayls (silver ink), 38.16 MRayls (silver).

The acoustic impedance of the electrode would have a different degree of impact. The electrode of a higher acoustic impedance (38.16 MRayls) shows a minimal effect as it causes nearly no shift in the operating frequency and a slight decrease in the acoustic power (by 0.2 mW), as shown in **Figure 4.14** (b) and (c). In contrast, the electrode of relatively low acoustic impedance (5.15 MRayls) shows a larger effect on lowering the operating frequency from 10.7 MHz to 9.1 MHz and increasing CL from 6.98 dB to 7.5 dB. The shift in the operating frequency and the increase of the CL causes a reduction of the acoustic power from

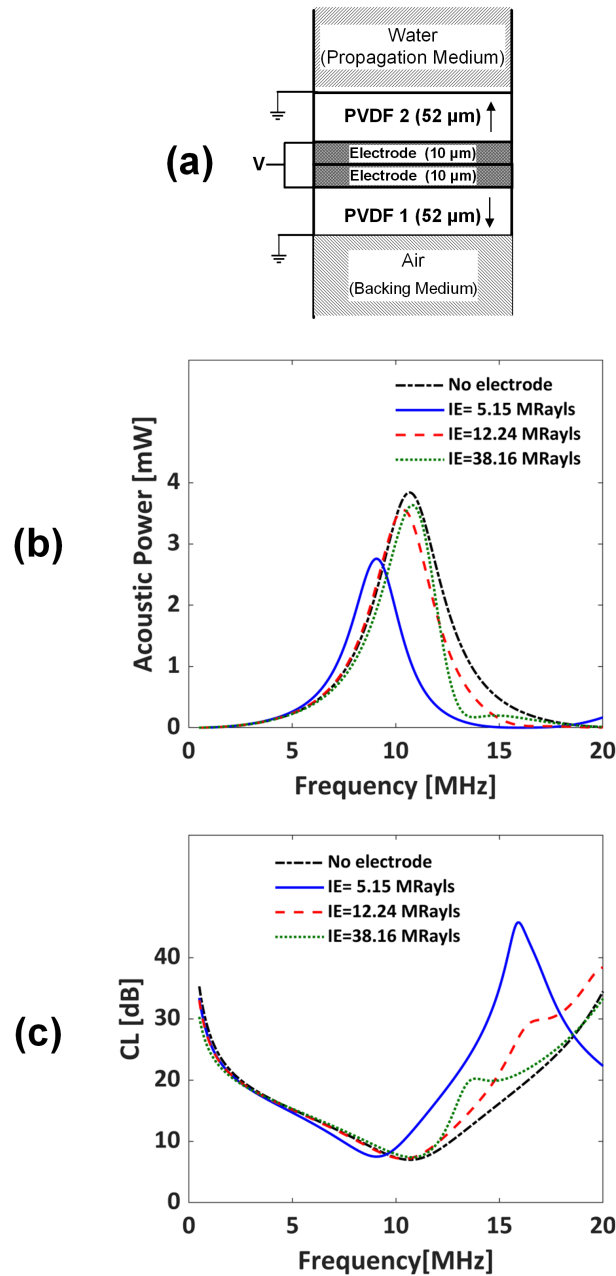


**Figure 4.14:** The effect of the inner electrode layer acoustic impedance on the ultrasonic performance of the double-layer PVDF sensor. The acoustic power and CL are calculated for the double-layer 52- $\mu\text{m}$ -thick PVDF with a 10- $\mu\text{m}$ -thick inner electrode layer each for three silver electrode materials: 5.15 MRayls (silver epoxy), 12.24 MRayls (silver ink), 38.16 MRayls (pure silver). The structural configuration of the simulation (a), the acoustic power (b), and the CL (c) are shown. Active ultrasound area = 4  $\text{cm}^2$  and input voltage = 1 V are assumed.

3.84 mW to 2.76 mW. In general, inner electrode layers of 12.24 MRayls acoustic impedance and higher would have a small impact as the calculated acoustic power in **Figure 4.14** (b) shows a small shift in the operating frequency to a lower range by less than 0.4 MHz and a reduction of the acoustic power by less than  $0.3 \text{ mW/V}^2$ . Also, the calculated CL in **Figure 4.14** (c) shows a small increase of less than 0.2 dB.

In addition, it is important to investigate the influence of the electrode thickness. As the electrode material of interest for a PVDF ultrasonic sensor is silver ink, the operating frequency, frequency bandwidth percentage, maximum acoustic power and minimum CL at the operating frequency of the double-layer 52  $\mu\text{m}$ -thick PVDF are computed as a function of the thickness of inner silver ink electrode layers (12.24 MRayls). The results are presented in **Figure 4.15**. The nearly linear relation between the inner electrode thickness and the corresponding parameters can be observed from the curves in **Figure 4.15** (b), (d), and (e). For a 1  $\mu\text{m}$  increase of each inner electrode layer thickness, the operating frequency, acoustic power, and CL are changed by approximately -0.033 MHz, -0.028 mW, and 0.017 dB, respectively. Regarding the frequency bandwidth, the inner electrode layer of silver ink slightly narrows the bandwidth from 35% to 33.7% at the 10- $\mu\text{m}$ -thick electrode layer and to 31.8 % at the 20- $\mu\text{m}$ -thick electrode layer. The impact of the inner electrode layers (of a thickness of up to 10  $\mu\text{m}$  per layer) could be considered negligible on the double-layer 52- $\mu\text{m}$  PVDF WUS when their acoustic impedance is relatively much higher than the acoustic impedance of a PVDF such as silver ink (12.24 MRayls).

In the following, the effect of only the outer electrode layers is investigated excluding the inner electrode layers. Similarly to the inner electrode effect simulation, the three types of silver electrode materials are considered. **Figure 4.16** shows the calculated acoustic power and CL for double-layer 52- $\mu\text{m}$ -thick PVDF with a 10- $\mu\text{m}$ -thick layer on each of the outer electrodes. Contrary to the effect of the inner electrode layers, an electrode of higher acoustic

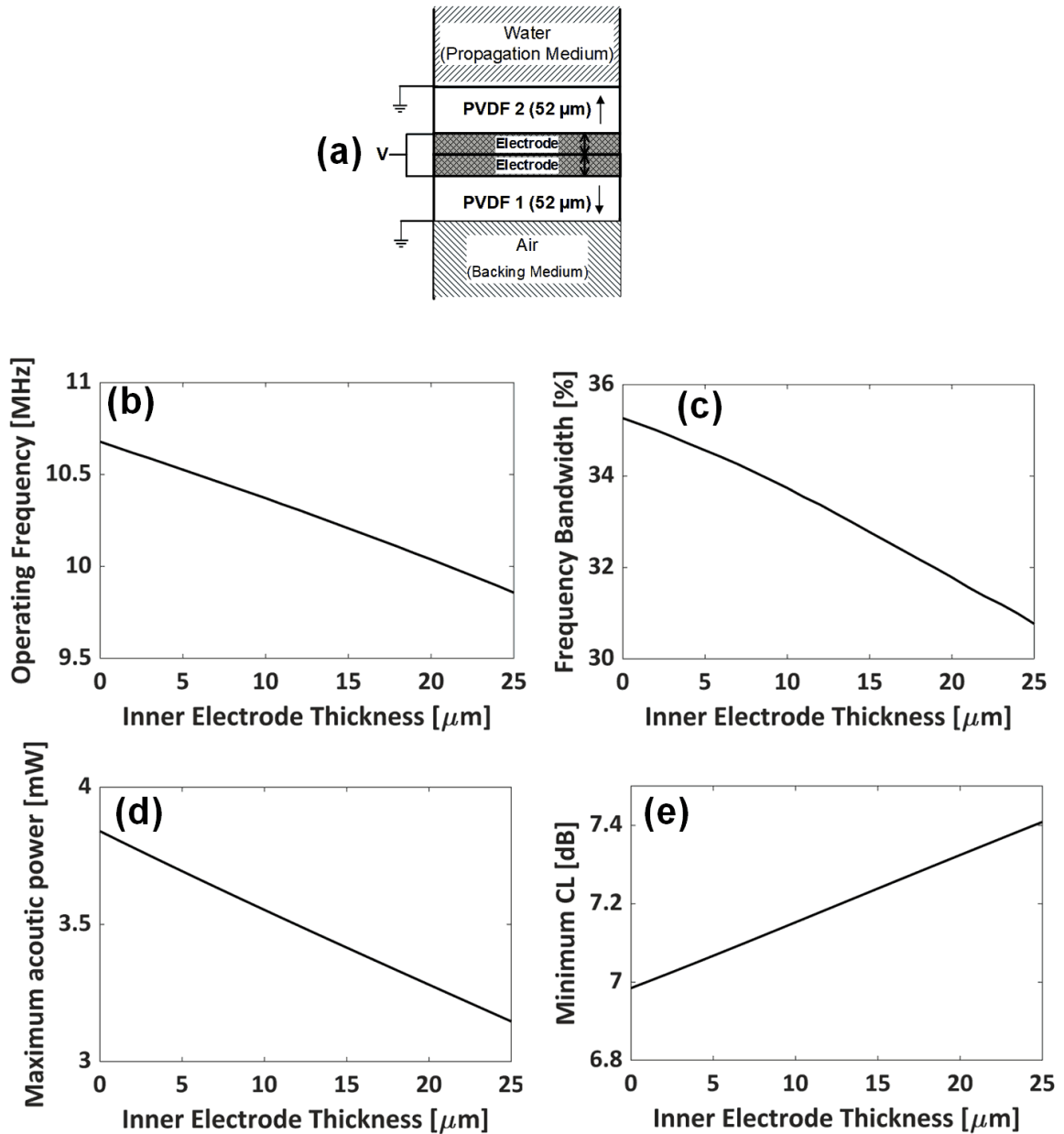


**Figure 4.15:** The effect of the inner electrode layers thickness on the ultrasonic performance of the double-layer PVDF. The operating frequency, bandwidth, acoustic power, and CL are computed for the double-layer 52- $\mu\text{m}$ -thick PVDF as a function of the individual layer thickness (0 – 25  $\mu\text{m}$ ) of silver ink (12.24 MRayls) inner electrode. The structural configuration of the simulation (a), operating frequency (b), frequency bandwidth (c), maximum acoustic power (d), and minimum CL (e) are shown. Active ultrasound area = 4  $\text{cm}^2$  and input voltage = 1 V are assumed.

impedance would have a higher impact than an electrode of lower acoustic impedance. The 10- $\mu\text{m}$ -thick layer of silver (38.16 MRayls) causes a higher operating frequency shift from 10.7 MHz (without electrode case) to 5.5 MHz and narrows the bandwidth from 35% (no electrode case) to 27 %. While the silver ink (12.24 MRayls) and silver epoxy (5.15 MRayls) cause the double 52- $\mu\text{m}$ -thick PVDF to operate at 7.9 MHz and 8.3 MHz with bandwidths of 34.8% and 32.9%, respectively, as shown in **Figure 4.16** (b). The outer electrode layers show the interesting effect of decreasing the CL (increasing the conversion efficiency). The CL values at the operating frequency decreased from 6.84 dB (no electrode case) to 6.23 dB, 6.41 dB, and 6.52 dB for the silver, silver ink, and silver epoxy, respectively, as shown in **Figure 4.16** (c). The acoustic power of the double-layer 52- $\mu\text{m}$ -thick PVDF decreases as the operating frequency shifts to the lower range. This is due to the higher electric impedance of double-layer PVDF at a lower frequency. The silver ink (12.24 MRayls) and silver epoxy (5.15 MRayls) reduces the acoustic power at the operating frequency of the double-layer 52- $\mu\text{m}$ -thick PVDF by approximately 0.4 mW. In comparison, the silver electrode layers (38.16 MRayls) have a greater acoustic power reduction of 1.15 mW due to the larger operating frequency shift.

To study the influence of the thickness of outer electrode layers, the operating frequency, bandwidth, acoustic power, and CL of the double-layer 52- $\mu\text{m}$ -thick PVDF are computed as a function of the thickness of the outer layer of the silver ink electrode (12.24 MRayls), as shown in **Figure 4.17**. **Figure 4.17** (b) shows that the increase of the outer electrode layer thickness causes a greater shift in the operating frequency to the lower range. For instance, the 25- $\mu\text{m}$ -thick outer electrode layers of silver ink shift the operating frequency of the double-layer 52- $\mu\text{m}$ -thick PVDF by nearly half (6 MHz). At the same time, the frequency bandwidth narrows as the outer electrode layer becomes more than 4- $\mu\text{m}$ -thick, as shown in **Figure 4.17** (c). Although, the impact on the frequency bandwidth might be considered

small as the bandwidth narrowed from 35% (no electrode case) to 29% (at the 25- $\mu\text{m}$ -thick electrode layer). The acoustic power shows a nearly linear decrease by approximately 0.043 mW per a 1- $\mu\text{m}$  increase of each outer electrode layer thickness, as shown in **Figure 4.17** (d). Also, the CL shows a continuous decrease of 0.57 dB and 0.74 at the outer electrode layer thickness of 10  $\mu\text{m}$  and 25  $\mu\text{m}$ , respectively, as shown in **Figure 4.17** (e). The CL curve shows that the decreasing rate of the CL becomes smaller as the thickness increases.

As the effects of the inner and outer electrode layers were discussed separately, now the combined effect of the inner and outer electrode layers is investigated. In **Figure 4.18**, the operating frequency, frequency bandwidth, acoustic power, and CL of the double-layer 52- $\mu\text{m}$ -thick PVDF are computed as a function of the thickness of inner and outer electrode layers. It can be observed that the impact of the outer electrode layers is more dominant as the electrode of a higher acoustic impedance has a more substantial effect, as shown in **Figure 4.18** (b), (c), and (e). The electrode layers would have a substantial effect on lowering the operating frequency where silver ink electrode layers of 10- $\mu\text{m}$ -thick shift the operating frequency from 10.7 MHz to 7.8 MHz, as shown in **Figure 4.18** (b). Also, the frequency bandwidth narrows as the operating frequency shifts further to a lower range due to the electrode layer thickness increase, as shown in **Figure 4.18** (c). For **Figure 4.18** (d), the decrease of the acoustic power can be understood since the electric impedance is higher at a lower frequency (as shown in **Figure 4.5**). The CL at the operating frequency shows a decrease before it begins to increase, as shown in **Figure 4.18** (e). In addition, the silver ink shows a minimal impact in comparison to the electroding of silver and silver epoxy.

It may be concluded that the four electrode layers of the double-layer PVDF impact the WUS performance by shifting the operating frequency to a lower range, narrowing the frequency bandwidth, and decreasing the CL. The acoustic power of the double-layer PVDF WUS would be decreased due to the operating frequency shift. Also, electrodes of very high

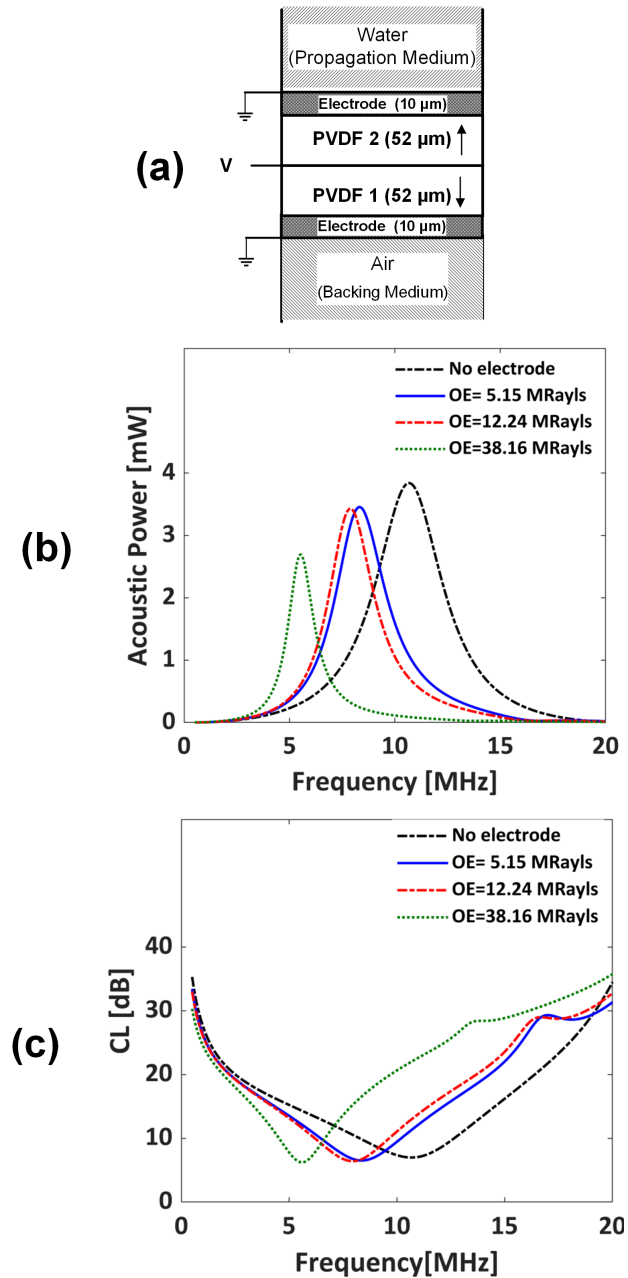


**Figure 4.16:** The effect of the outer electrode layers on the ultrasonic performance of the double-layer PVDF sensor. The acoustic power and CL are calculated for the double-layer 52- $\mu\text{m}$ -thick PVDF with a 10- $\mu\text{m}$ -thick outer electrode layer each for three silver electrode materials: 5.15 MRayls (silver epoxy), 12.24 MRayls (silver ink), 38.16 MRayls (silver). The structural configuration of the simulation (a), the acoustic power (b), and the CL (c) are shown. Active ultrasound area = 4  $\text{cm}^2$  and input voltage = 1 V are assumed.

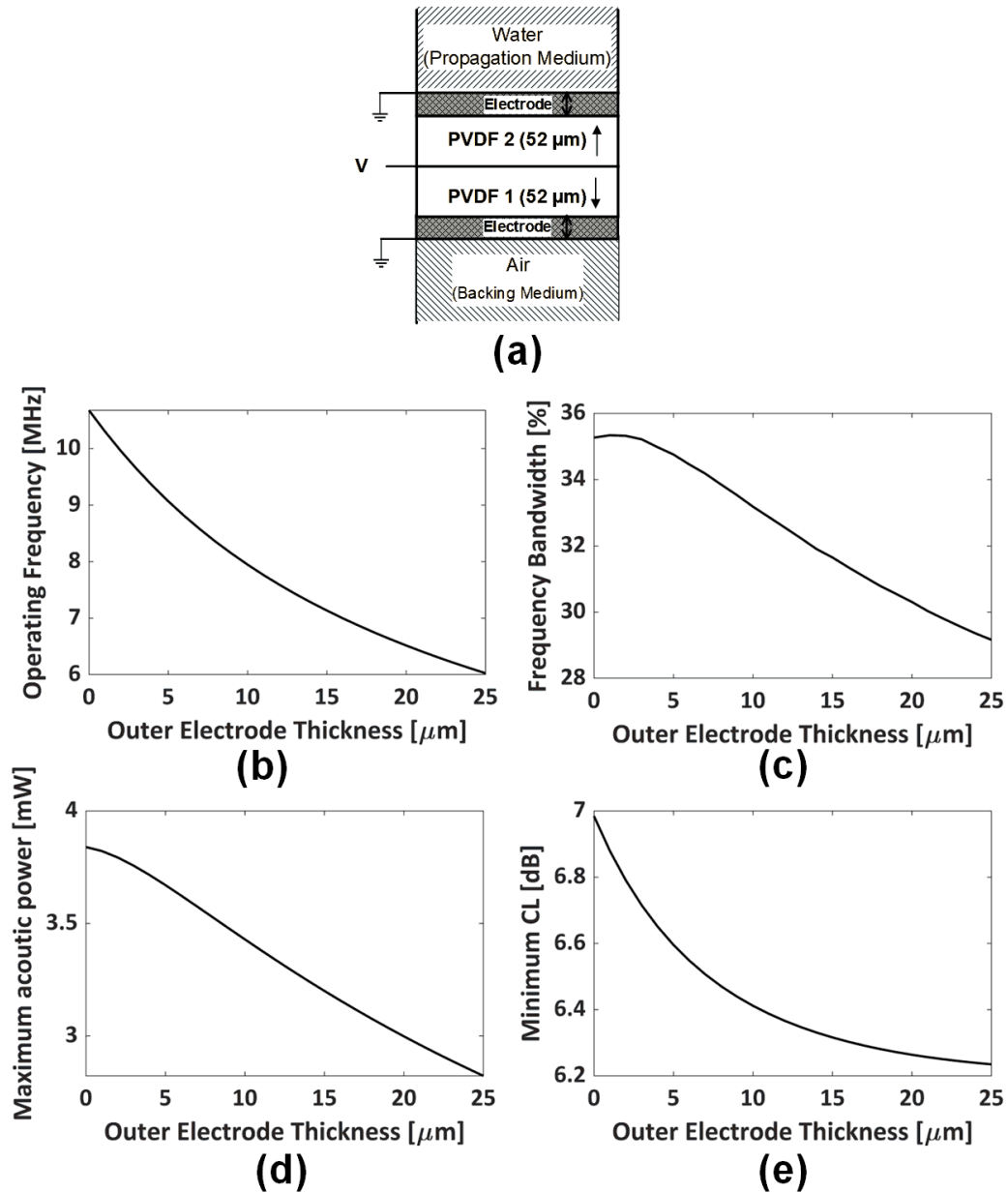


**Figure 4.17:** The effect of the outer electrode layers thickness on the ultrasonic performance of the double-layer PVDF sensor. The parameters are computed for the double-layer 52- $\mu\text{m}$ -thick PVDF as a function of the individual layer thickness (0 – 25  $\mu\text{m}$ ) of silver ink (12.24 MRayls) outer electrode. The structural configuration of the simulation (a), operating frequency (b), frequency bandwidth (c), maximum acoustic power (d), and minimum CL (e) are shown. Active ultrasound area = 4  $\text{cm}^2$  and input voltage = 1 V are assumed.

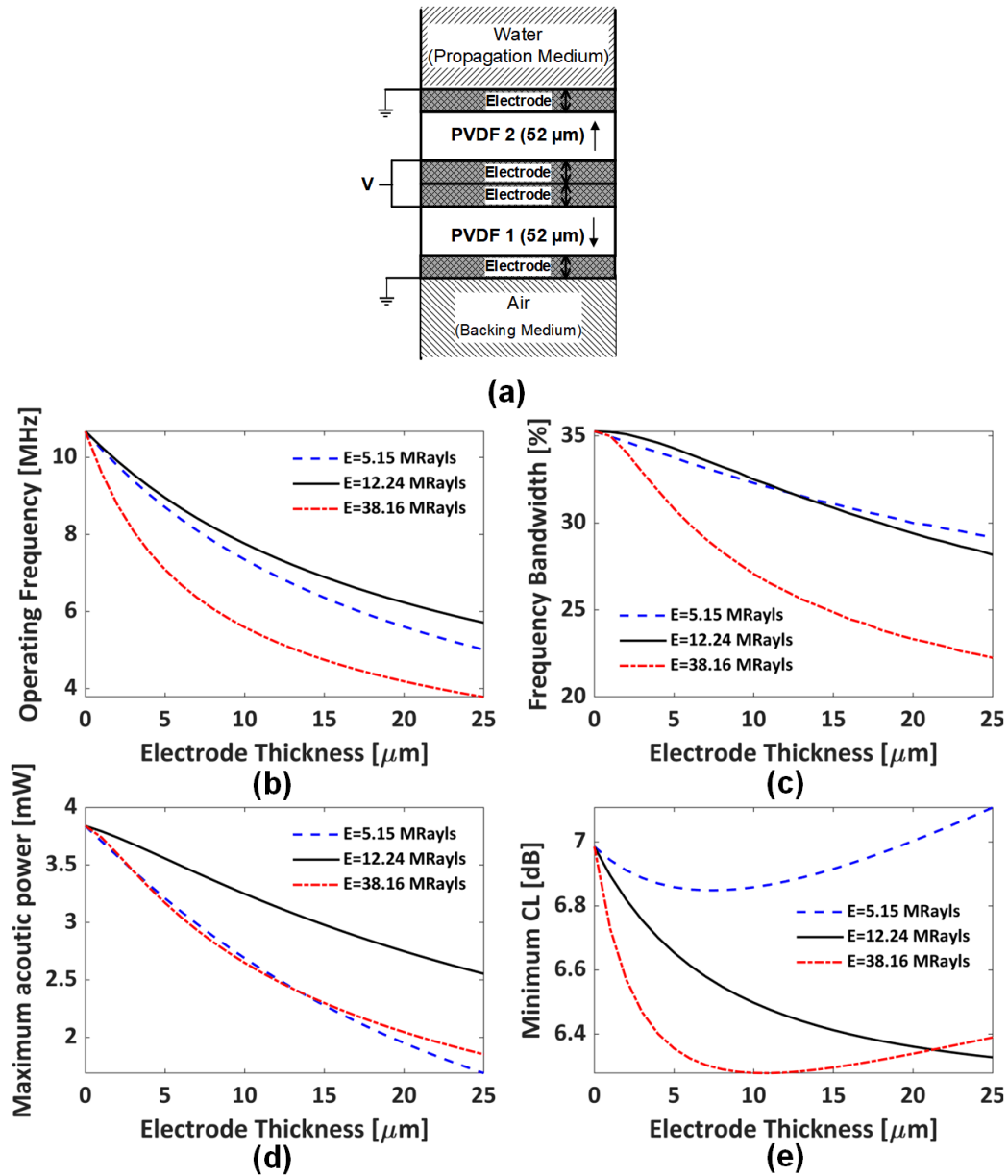


**Figure 4.18:** The effect of the inner and outer electrode layers thickness on the ultrasonic performance of the double-layer PVDF sensor. The parameters are computed for the double-layer 52- $\mu\text{m}$ -thick PVDF as a function of the thickness of each electrode layer (0 – 25  $\mu\text{m}$ ). It is calculated for electrode materials of 5.15 MRayls (silver epoxy), 12.24 MRayls (silver ink), 38.16 MRayls (silver). The structural configuration of the simulation (a), operating frequency (b), frequency bandwidth (c), maximum acoustic power (d), and minimum CL (e) are shown. Active ultrasound area = 4  $\text{cm}^2$  and input voltage = 1 V are assumed.

acoustic impedance, such as silver, substantially affect the double-layer PVDF WUS. The silver ink electrode of 12.24 MRayls acoustic impedance range would have a less impact overall. An air-backed double-layer 52- $\mu\text{m}$ -thick PVDF with silver ink electrode layers with a thickness of 1-10  $\mu\text{m}$  would have an acoustic power range of 3.8 – 3.25 mW and an operating frequency in the range of 10.28 – 7.8 MHz with bandwidth range of 35—32.5%. Thus, the silver ink is considered an excellent electrode choice. It offers more flexibility and has a small overall negative impact on the ultrasonic performance of the double-layer PVDF WUS.

#### 4.2.5 Effect of Bonding Layer

The double-layer PVDF configuration is constructed by bonding two PVDF layers using an adhesive material such as epoxy resin. For the double-layer PVDF WUS, the bonding layer would be sandwiched between the two adjacent inner electrode layers of the PVDF as each PVDF layer has top and bottom electrode layers. Thus, the double-layer PVDF WUS would have an intervening layer between the inner electrode layers known as the bonding layer. In the previous sections, the double-layer PVDF and the electrode layers were characterized excluding the effect of the bonding layer. In addition, it is advantageous to connect both inner electrode layers, those on the top and the bottom of the bonding layer, to the common electrical terminal in order to avoid unnecessary voltage drop within the bonding layer, as shown in **Figure 3.6 (Chapter 3)**. Therefore, the bonding layer is a pure mechanical loading between the two PVDF layers with no voltage drop between its top and bottom surface or current flow through its thickness. It is important to characterize the bonding layer effect on the performance of the double-layer PVDF sensor to help determine the preferable properties of the bonding layer. Since the bonding layer is a pure mechanical

layer, the acoustic impedance and the thickness of the bonding layer would be the contributing factors affecting the ultrasonic performance of the double-layer PVDF sensor. The effect of the bonding layer would be characterized for an air-backed double-layer PVDF sensor since it is the preferred backing approach, as discussed in the previous section (**Section 4.2.3**). In order to understand the effect of the bonding layer, the simulations of the bonding layer effect on the double-layer PVDF sensor in this section are assumed without any electrode layers as the effect of the electrode layers were discussed separately in **Section 4.2.4**.

The bonding layer is expected to impact the double-layer PVDF sensor performance similarly to the inner electrode layers since they are placed between the two PVDF layers. To investigate the effect of the bonding layer in detail, the acoustic impedance, the operating frequency, bandwidth, acoustic power, and CL of the double-layer PVDF are calculated for a different adhesive material at a constant thickness first. The bonding layer thickness of 7.5  $\mu\text{m}$  is used as an example to investigate the effect of acoustic impedance effect on the bonding layer since it is the thickness of interest in the double-layer PVDF WUS construction (a detailed explanation is given in the following chapter). In **Figure 4.19**, an air-backed double-layer 52- $\mu\text{m}$ -thick PVDF with a 7.5  $\mu\text{m}$ -thick bonding layer is simulated for five types of adhesive materials: 1.07 MRayls (Sylgard), 2.4 MRayls (Spurr's epoxy), 3.04 MRayls (Araldite 10phe), 6.18 MRayls (Araldite 50phe), and 11.7 MRayls (Ecosorb). The five adhesive materials are chosen to represent the broad acoustic impedance range of common adhesive materials. **Figure 4.19** (b) and (c) show that the bonding layer shifts the operating frequency to the lower range and increases the CL, causing the reduction of the acoustic power. The impact of the bonding layer has shown to be related to the acoustic impedance of the adhesive material. The lower the acoustic impedance of the bonding material, the larger the impact on the operating frequency, acoustic output power, and CL. For the 7.5- $\mu\text{m}$ -thick bonding layer, a bonding material of very low acoustic impedance (1.07 MRayls) shifts the

operating frequency from 10.7 MHz to 6.8 MHz and increases the CL value at the operating frequency from 6.98 dB to 8.71 dB, where a bonding material of high acoustic impedance (11.7 MRayls) shifts the operating frequency to 10.5 MHz and increases the CL value at the operating frequency to 7.07 dB. For the acoustic output power, the 1.07-MRayls bonding material causes a substantial reduction from 3.84 mW to 1.5 mW in comparison to the 11.7-MRayls bonding material that reduces the acoustic power to 3.7 mW. The bonding materials of acoustic impedance values between 2.4 – 6.18 MRayls have a relatively small impact in shifting the operating frequency, reducing acoustic power, and increasing CL by -1.2 – -0.5 MHz, -0.74 – -0.34 mW, and 0.3 – 0.13 dB, respectively.

In order to study the effect of the bonding layer thickness, the five types of bonding materials are calculated for the double-layer PVDF as a function of the bonding layer thickness of 0 – 25  $\mu\text{m}$ . **Figure 4.20** shows the calculated operating frequency, bandwidth, maximal acoustic power, and minimal CL of the double-layer 52- $\mu\text{m}$ -thick PVDF as a function of the bonding layer thickness. As the bonding layer thickness increases, the operating frequency of the double-layer PVDF shifts to the lower range with narrower bandwidth, and the CL increases. The lowering of operating frequency and increasing of CL cause the reduction of the acoustic power. The thicker bonding layer would have a larger impact, and a bonding material of a higher acoustic impedance would have a smaller effect as the thickness of the bonding layer increases. For instance, the 25- $\mu\text{m}$ -thick bonding layer of 1.07 MRayls, 2.4 MRayls, and 6.18 MRayls reduced the acoustic power from 3.84 mW to 0.38 mW, 1.9 mW, and 2.8 mW, respectively, as shown in **Figure 4.20** (d). In addition, the 1.07-MRayls bonding material shows a larger effect than the 2.4-MRayls and 6.18-MRayls materials. Therefore, the adhesive materials of acoustic impedance in the range of 1 MRayls should be avoided due to their substantial impact on the ultrasonic performance of the double-layer PVDF. The frequency bandwidth of the double-layer PVDF

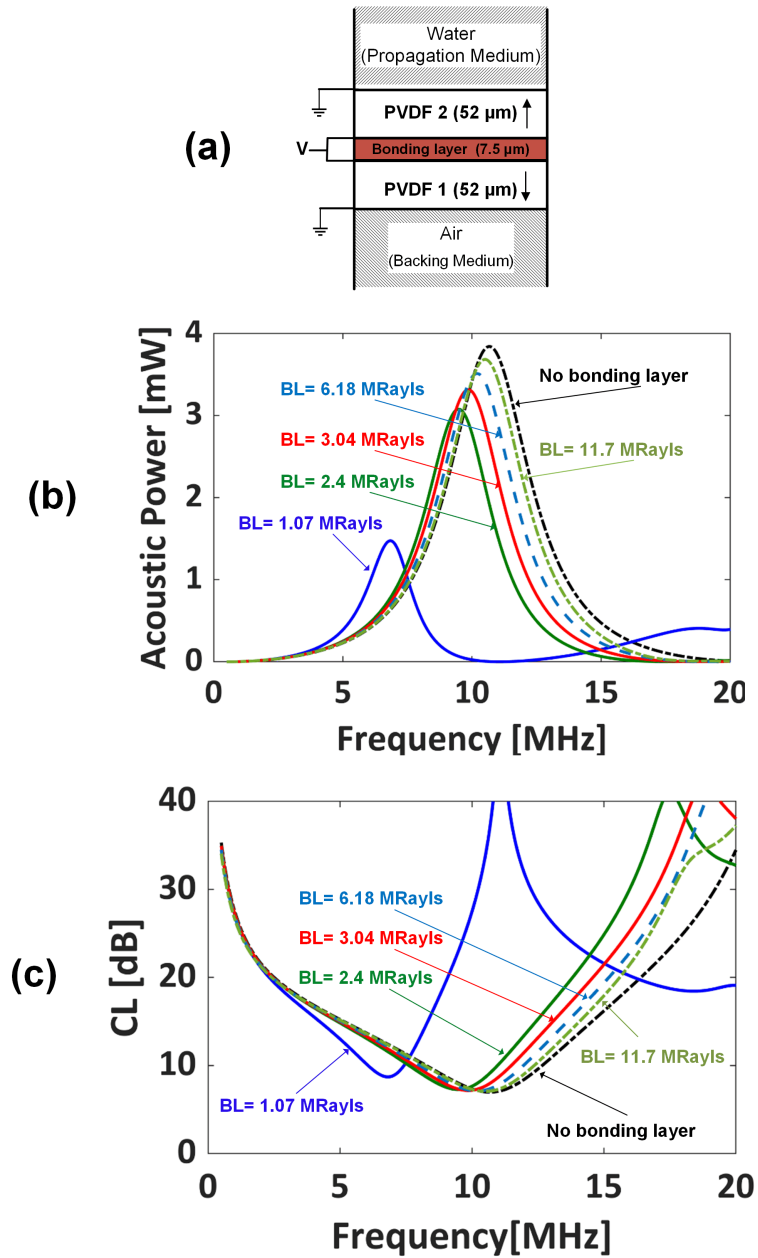


**Figure 4.19:** The effect of the acoustic impedance of the bonding layer on the ultrasonic performance of the double-layer PVDF sensor. The acoustic power and CL are calculated for the double-layer 52- $\mu\text{m}$ -thick PVDF with a 7.5- $\mu\text{m}$ -thick bonding layer of five types of adhesive materials: 1.07-MRayls Sylgard, 2.4-MRayls Spurr's epoxy, 3.04-MRayls Araldite 10phe, 6.18-MRayls Araldite 50phe, and 11.7-MRayls Ecosorb. The structural configuration of the simulation (a), the acoustic power (b), and the CL (c) are shown. Active ultrasound area = 4  $\text{cm}^2$  and input voltage = 1 V are assumed.

with the 1.07-MRayls bonding material is observed to increase as the bonding layer thickness becomes thicker than 6  $\mu\text{m}$ , as shown in **Figure 4.20** (c). This might be due to the tendency of the double-layer PVDF to operate in  $\lambda/4$  mode.

To summarize, the bonding layer negatively affects the conversion efficiency and consequently reduces the acoustic output power of the double-layer PVDF sensor. In addition, the selection of an adhesive material of higher acoustic impedance and a reduction in thickness of the bonding layer would be preferred in order to minimize the impact of the bonding layer. A bonding layer of low acoustic impedance (range of 1 MRayls) substantially reduces the ultrasonic signal strength of the double-layer PVDF WUS; therefore, it should be avoided.

Furthermore, for the conducted numerical simulation study it can be concluded that a double-layer 52- $\mu\text{m}$ -thick PVDF sensor with a bonding layer of 10- $\mu\text{m}$  and thinner and an adhesive material of Spurr's epoxy (2.4 MRayls) would have approximately three times or higher acoustic output power (2.86 mW) in comparison to a single-layer 104  $\mu\text{m}$ -thick PVDF of the equivalent total PVDF thickness (0.97 mW).

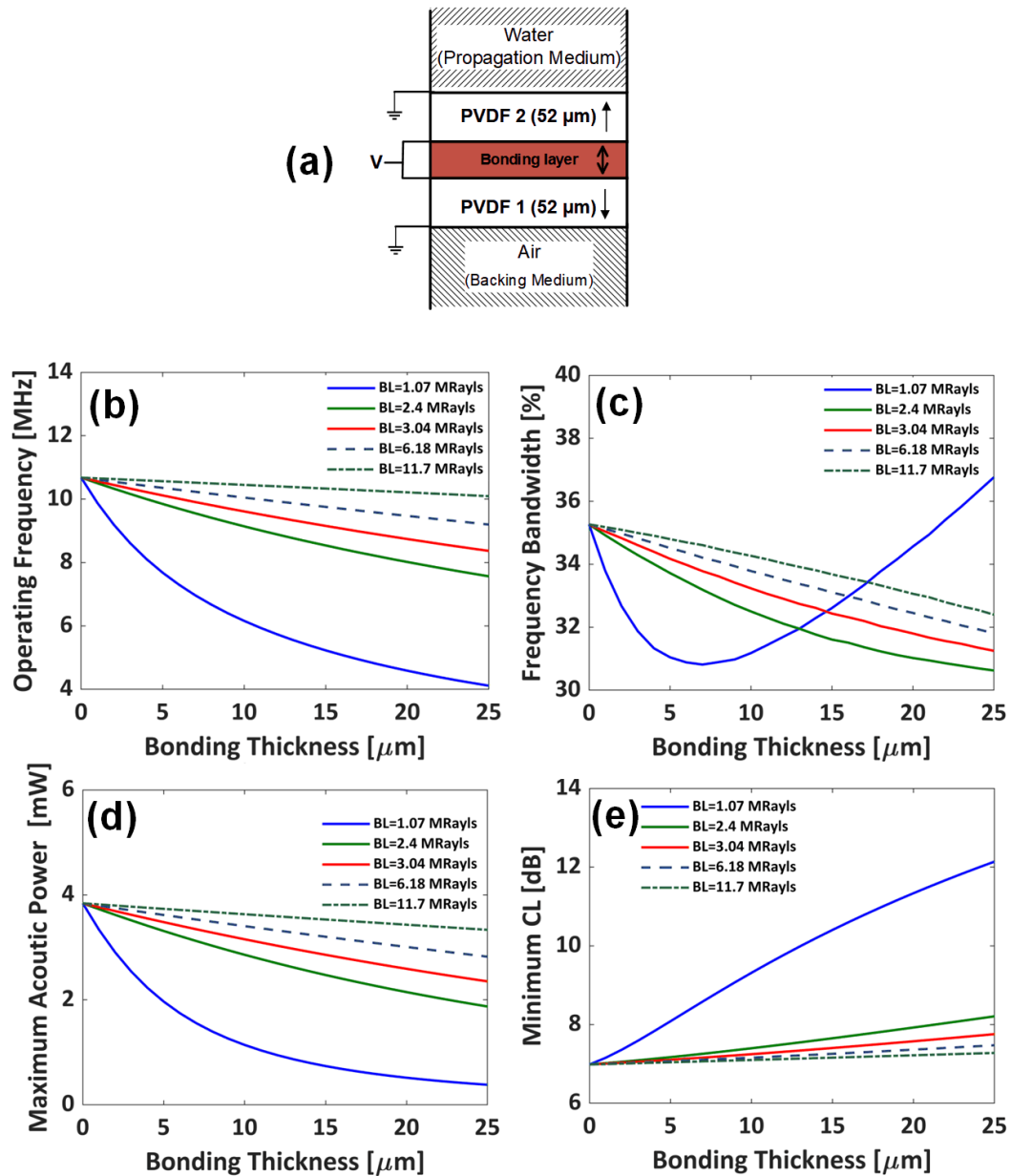


**Figure 4.20:** The effect of the bonding layer thickness on the double-layer PVDF. The operating frequency, bandwidth, acoustic power, and CL are calculated for the double-layer 52- $\mu\text{m}$  PVDF as a function of the thickness of the bonding layer. Five types of adhesive materials are assumed: 1.07-MRayls Sylgard, 2.4-MRayls Spurr's epoxy, 3.04-MRayls Araldite 10phe, 6.18-MRayls Araldite 50phe, and 11.7-MRayls Ecosorb. The structural configuration of the simulation (a), operating frequency (b), frequency bandwidth (c), maximum acoustic power (d), and minimum CL (e) are shown. Active ultrasound area = 4  $\text{cm}^2$  and input voltage = 1 V are assumed.

### 4.3 Design Considerations of Double-Layer PVDF WUS

The WUS design should meet the desired characteristics for the application of muscle contraction monitoring, such as the operating frequency, ultrasound signal strength, sensor flexibility, and small size. In general, the ultrasound performance of the double-layer PVDF WUS, such as operating frequency, bandwidth, acoustic output power, and conversion loss, mainly depends on its physical structures. These physical structures include the PVDF layer thickness, active ultrasound area, double-layer PVDF configuration, backing, bonding layer, and electrode layers. In the previous section, the effects of these physical structures on the ultrasound performance of the double-layer PVDF WUS were studied. This section discusses the considerations, approaches, and material selection for the double-layer PVDF WUS design based on the numerical simulation study presented in **Section 4.2**.

#### 4.3.1 Double-Layer PVDF Arrangement Considerations

As discussed in **Section 4.2.2**, the weak piezoelectricity of the PVDF requires special consideration to improve the transmitting acoustic power. The numerical simulation in **Figure 4.5** shows that the configuration of two PVDF layers that are electrically in parallel and acoustically in series improves the ratio of acoustic output power to the input electric voltage of the PVDF ultrasonic sensor by a factor of nearly four. Therefore, the use of the double-layer configuration PVDF instead of a single-layer PVDF in the construction of the PVDF WUS would increase the transmitted ultrasound signal strength and consequently increases the SNR of the received ultrasound signal.

In addition, the operating frequency of the double-layer PVDF configuration is shown to be dependent on the arrangement of the polarization directions of the two PVDF layers.

The parallel polarization directions would resonate equivalently to a single-layer PVDF of the total thickness (lower operating frequency). In contrast, the antiparallel polarization directions would resonate equivalently to a single-layer PVDF of individual PVDF layer thickness (higher operating frequency).

For the double-layer PVDF WUS design, achieving the required operating frequency range with minimum thickness for mechanical flexibility is desirable. Also, thinner PVDF films have the additional advantage of higher polarity due to the difficulty of poling thicker PVDF films. The poling process is one of the main procedures in the making of piezoelectric PVDF film. A high electric field is applied during the poling process in order to obtain aligned PVDF crystallites [212]. The difficulty in poling thick PVDF films is due to the high electric field requirement in the range of 500 – 700 kV/cm [213, 214]. Thus, the thinner PVDF film in the double-layer configuration would have better ultrasound signal strength than the single-layer of a thicker PVDF film due to the higher polarity. Therefore, a double-layer PVDF sensor that is electrically parallel with their polarization directions in parallel would be the preferred design for the WUS due to the higher acoustic power and minimal PVDF thickness. Using more PVDF layers (multiple-layer PVDF configuration) could further increase the acoustic power ratio to the input electric voltage but impose more practical challenges of electrically interconnecting and adhering the individual PVDF layers with thin and uniform bonding layers.

### **4.3.2 PVDF Film Thickness and Active Ultrasound Area Selection**

As discussed in **Section 4.2.1**, the operating frequency is inversely proportional to the thickness of the PVDF film. Thus, the thinner the PVDF layer, the higher the operating frequency of the PVDF. The selection of the PVDF layer thickness is determined by the

required frequency range of the ultrasound. Ultrasound frequencies in diagnostic medical imaging range from approximately 2.5 MHz to 15 MHz [148, 193]. In general, the choice of ultrasound frequency is dictated by the trade-off between the spatial resolution along the depth and the penetration depth. A higher frequency provides a higher spatial resolution, but the attenuation is greater since it increases with ultrasound frequency. For musculoskeletal ultrasound imaging, the ultrasound frequencies of 5-8 MHz are commonly used [215–219]. Therefore, such an ultrasound frequency range would be adequate for the WUS to measure muscle thickness changes. In addition, the minimum thickness of the PVDF layer should be considered in order to minimize the overall thickness of the WUS for the mechanical flexibility.

From **Figure 4.2** and **Eq. 4.1**, the individual PVDF layer thickness of 50 – 125  $\mu\text{m}$  for the double-layer PVDF with parallel polarization directions would resonate at 11.1 – 4.4 MHz. Taking into consideration the bonding and the electrode layers effect in shifting the operating frequency to the lower range as discussed in **Section 4.2.5** and **Section 4.2.4**, the double-layer PVDF WUS of 50 – 60  $\mu\text{m}$ -thick PVDF layer would be expected to operate at 7.2 – 6.4 MHz. In this thesis, the selection of the PVDF film thickness would be subject to its commercial availability from the vendors. TE Connectivity Ltd. (formally Measurement Specialties Inc., Berwyn, PA, USA) offers PVDF piezoelectric film sheet with printed silver ink electrode layers on each side of the film. The PVDF film sheet from TE Connectivity is available in a thickness of 28  $\mu\text{m}$ , 52  $\mu\text{m}$ , and 110  $\mu\text{m}$ . Therefore, the 52- $\mu\text{m}$ -thick PVDF with silver ink electrode is selected for constructing the double-layer PVDF WUS due to the operating frequency range, minimum thickness, and availability from local vendors.

The overlap electrode area between the top and bottom electrode layers of the PVDF layers determines the ultrasonic sensing area of the WUS. The selection of the ultrasonic sensing area is subject to the ultrasonic signal strength of the double-layer PVDF WUS and

the measurement of the area of interest. The larger the active surface area of the PVDF layers, the higher the ultrasonic signal strength (acoustic output power) of the WUS. However, the ultrasonic sensing area should not be larger than the measured area of interest. As one of the advantages of the PVDF piezoelectric polymer film is the ease of fabrication in the desired size, the ultrasonic sensing area of the WUS can be selected based on the size of the muscle of interest. For the conducted measurements of muscle contraction in this thesis research, the ultrasonic sensing area of 20 mm × 20 mm has been chosen.

### 4.3.3 Electrode and Electrical Connection Considerations

The first consideration of the electrical connections to electrodes is the separation of the active ultrasonic area from the lead attachment area in order to avoid the mass-loading of the lead attachment area on the ultrasonic performance. Therefore, the surface area of the PVDF layer is extended to take into account the lead attachment area, as shown in **Figure 4.21**. The PVDF layer surfaces on both sides are separated into an active ultrasonic area and an interconnection area. The electrode layers on the top and bottom of the active ultrasonic area are overlapped where there is no overlapping between the top and bottom electrode layers at the interconnection area.

Another consideration is the complexity of the lead attachment to the four electrode layers of the double-layer PVDF WUS. In order to simplify the lead attachments, the inner electrode layers are connected to the common electrical lead. The common lead attachment provides the advantage of one lead attachment for both inner electrode layers at the interconnection area. In addition, the outer electrode layers should be connected to the ground terminal to serve as the grounded shielding protection.

The lead attachment technique also requires special consideration as direct soldering

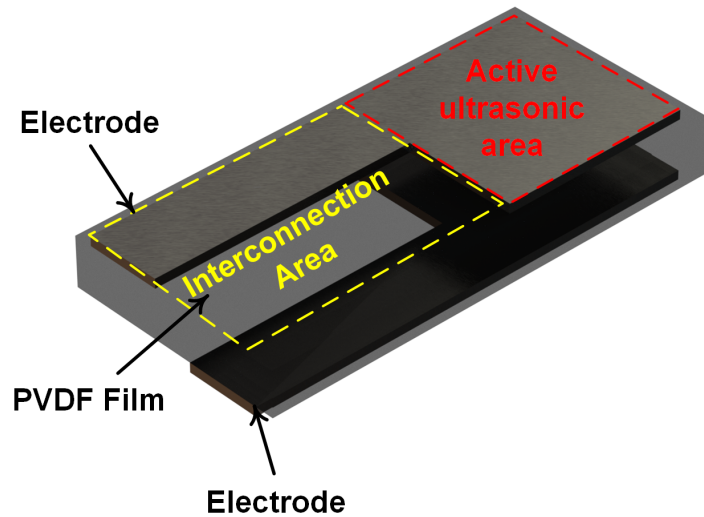


**Figure 4.21:** A schematic of the active ultrasonic area and interconnection area of a single PVDF layer.

cannot be used due to the low melting and Curie temperature of the PVDF. This imposes the need for an alternative attachment method, such as the use of conductive epoxy. The lead attachment for the double-layer PVDF WUS will be further discussed in the next chapter. Furthermore, silver ink would be preferred as an electrode material for the PVDF due to its flexibility, high conductivity, and high operating voltage, as discussed in **Section 4.2.4**. Therefore, the PVDF film with silver ink electrodes is employed for constructing the WUS.

#### 4.3.4 Bonding of the Two PVDF Layers Considerations

Adhering two PVDF layers demands careful consideration. The mass-loading due to the large thickness of the bonding layer would negatively affect the WUS performance. Thus, the bonding layer thickness should be minimized, as discussed in **Section 4.2.5**. Also, an adhesive material of relatively low acoustic impedance (range of 1 MRayls) has shown to have a substantial impact on the double-layer PVDF performance; therefore, adhesives of

low acoustic impedance should be avoided. In addition, the flexible profile of the WUS should be taken into account during the selection of adhesive material for the bonding.

Another important consideration is the uniformity of the bonding layer thickness between the two PVDF layers since the double-layer PVDF should ideally be parallelly aligned. This imposes a practical difficulty [72] and the need for an addressed technique of bonding the two PVDF layers, which will be discussed in the following chapter regarding the construction of the double-layer PVDF WUS. Epoxy adhesives, among other types of adhesive materials, could be an excellent choice. There are a wide range of epoxy adhesives that offer desirable features such as good adhesion, low viscosity before curing, and flexibility after curing. Brown [220] reported the construction of a double-layer 110  $\mu\text{m}$ -thick PVDF ultrasonic sensor using an epoxy resin as a bonding layer. The constructed double-layer PVDF sensor by [220] showed a superior ultrasonic signal strength with a bonding layer thickness of 4  $\mu\text{m}$ . In practice, it can be difficult to achieve a very thin ( $\sim 1 \mu\text{m}$ ) and an ideally uniform bonding layer. Alternatively, the quality of the bonding layer (thickness and uniformity) could be evaluated by comparing the ultrasonic signal strength to the single-layer PVDF of equivalent total PVDF layer thickness.

#### **4.3.5 Acoustic Insulation and Packaging Considerations**

The construction of the double-layer PVDF WUS requires the need for an additional layer to pack the WUS structure and to provide protection and electrical insulation. The thin and flexible profile of the WUS, good isolation and the simplicity of construction should all be taken into consideration when selecting the packaging method/material. Several packaging methods and materials for the PVDF ultrasonic sensor were discussed in [70]. A polyimide film as an adhesive tape was found to be the most suitable choice. The polyimide film with

silicone adhesive as a packaging of the double-layer PVDF WUS provides desirable features such as flexibility, good adhesion, and ease of application. In addition to the adhesive polyimide layer, housing the double-layer PVDF WUS in a thin, flexible metal layer such as aluminum/brass foil would provide electromagnetic (EM) noise shielding to the WUS. Thus, the packaging of the double-layer PVDF WUS would consist of an adhesive polyimide film and flexible metal foil layers for protection and EM shielding.

One of the important considerations in constructing the packaging layers is the acoustic loading on the back side of the double-layer PVDF WUS, which could negatively affect the ultrasonic performance. In this thesis work, the isolation of the acoustic loading of the packaging layers is proposed by creating an air gap between the outer electrode layer and packaging layers on the back side of the WUS, as discussed in **Section 4.2.3**. Therefore, the design of the double-layer PVDF WUS includes an acoustic insulator layer that maintains an air gap. The air gap could be created by placing a thin layer over the active ultrasonic area of the outer electrode layer on the back side without adhering. The details of the construction of the insulator layer will be discussed in the following chapter detailing the construction of the double-layer PVDF WUS.

Another consideration is the attenuation of the transmitted/received ultrasound due to the packaging layers on the front (sensing) side of the WUS. In order to avoid ultrasonic attenuation, the packaging layers are removed at the ultrasonic sensing area. The ultrasonic sensing area is the active ultrasonic area of the PVDF layers that transmits/receives ultrasound. By removing the packaging layers at the ultrasonic sensing area, the grounded electrode layer on the front side of the WUS is in direct contact with the skin surface. This approach takes advantage of the close matching of the PVDF to the human soft tissue.

## 4.4 Double-Layer PVDF WUS Design

The double-layer PVDF WUS design is described in this section under the guidance of the numerical simulation results in **Section 4.2.3** and the design considerations in **Section 4.3**.

The double-layer PVDF WUS design proposed in this thesis consists of twelve layers, as shown in the schematic of **Figure 4.22**. The WUS has two layers of 52- $\mu\text{m}$ -thick PVDF as a piezoelectric element. Each PVDF layer has printed silver ink electrodes on each side. The two layers of the PVDF are arranged in antiparallel polarization directions and adhered to the inner electrode layers by using an adhesive material as a bonding layer. The inner electrode layers are both connected to the same active electrical terminal. Therefore, an inversed voltage orientation is applied to the double-layer PVDF causing it to operate as if the polarization directions were in parallel. Both the top and bottom outer electrode layers next to the acoustic insulator layer and the ultrasonic sensing area, respectively, are connected to the ground electrical terminal.

The entire structure of WUS is wrapped by the packaging layers except for the ultrasonic sensing area where the ultrasound is transmitted and/or received. The packaging layers consist of flexible metal foil and polyimide film with adhesive. The flexible metal foil is connected to the grounded lead for EM shielding to reduce the electrical noise. The polyimide film with the adhesive binds the WUS structure layers and provides protection and electrical insulation. The EM shielding and protection layers are not applied to the ultrasonic sensing area in order to avoid ultrasonic attenuation and reflection within these layers. At the back side of the double-layer PVDF, an acoustic insulator layer is placed without adhering between the EM shielding and the outer electrode layer. Thus, the WUS is practically air-backed to isolate the acoustic loading of the packaging layers and eliminate the backward ultrasonic reflection. The overall dimensions that have been selected for the

developed double-layer PVDF WUS in this thesis research are 50 mm × 24 mm, and the ultrasonic sensing area is 20 mm × 20 mm.

The design of the double-layer PVDF WUS in this thesis work improve the initial design proposed in the previous work [70] in a number of aspects. The initial design of the WUS was consisting of a 110- $\mu$ m thick PVDF having a bottom and top silver ink electrode, and a polyimide adhesive covered the entire structure of the sensor as packaging layers. The first improvement of this thesis work design is increasing the transmitted ultrasound power by using a double-layer PVDF configuration and removing the packaging layer from the ultrasonic sensing area. The second addresses the undesired dual operating frequency of the initial design by isolating the acoustic loading of the packaging layers. Lastly, the packaging layers in this proposed design include an electromagnetic shielding of the sensor to reduce the surrounding environmental noise.

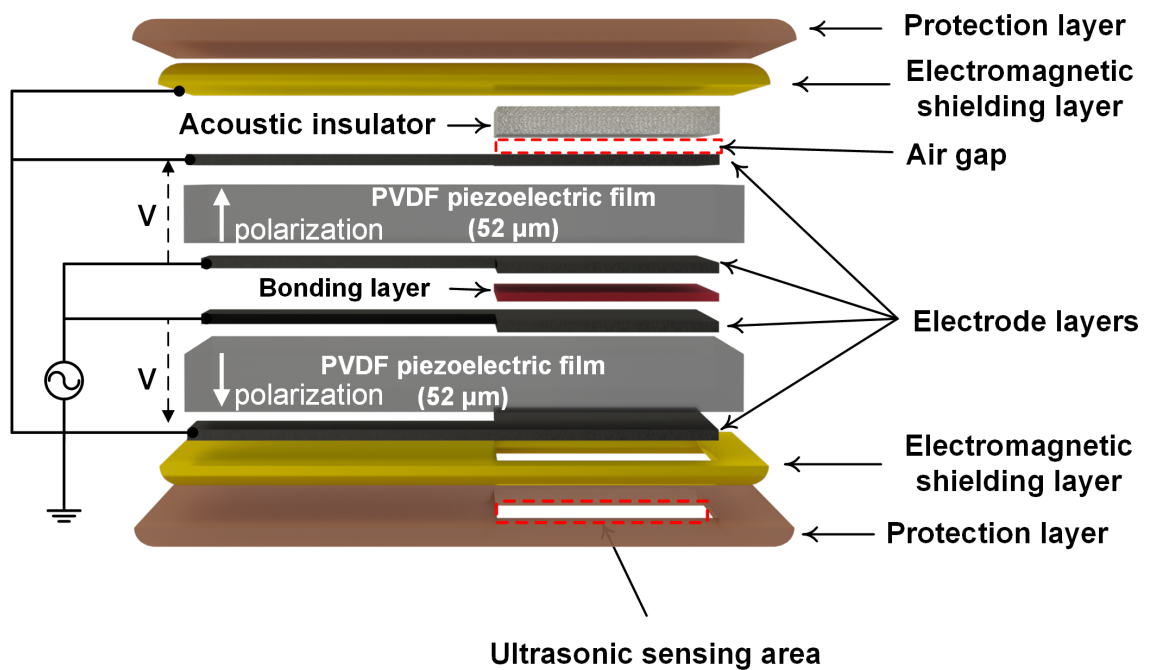


**Figure 4.22:** A schematic design of the double-layer PVDF WUS

## **Chapter 5**

# **Construction and Experimental Performance Evaluation of the Double-Layer PVDF WUS**

One of the objectives of this thesis work is to design and construct the double-layer PVDF WUS for the monitoring of muscle contraction. This chapter presents the construction procedure and techniques of the double-layer PVDF WUS based on the ultrasonic PVDF sensor design presented in the previous chapter (**Chapter 4**). The construction procedure of the double-layer PVDF WUS is followed by the performance evaluation. The operating ultrasound frequency, ultrasonic signal strength, and noise interference reduction are evaluated experimentally.

This chapter is divided into two sections; the construction procedure and the performance evaluation of the double-layer PVDF WUS. The first section explains the construction steps of the double-layer PVDF WUS and the approaches to overcome the practical difficulties of bonding the two PVDF layers, attachment of the electrical wires, and the acoustic insulation of the packaging layers. The second section deals with the evaluation of the operating

ultrasound frequency, ultrasonic signal strength, and the electromagnetic (EM) shielding of the constructed double-layer PVDF WUS.

## 5.1 Construction Procedure of Double-Layer PVDF WUS

This section explains the construction procedure of the double-layer PVDF WUS. The construction procedure consists of the preparation of the PVDF layers, the bonding of the two PVDF layers, the attachment of electrical wires, the creation of the acoustic insulation at the back side, and the packaging of the double-layer PVDF WUS.

### 5.1.1 PVDF Layers Preparation

As discussed in **Section 4.3.2**, the PVDF film sheet (203.2 mm wide  $\times$  279.4 mm long  $\times$  52  $\mu\text{m}$  thick) in the form of a metalized sheet was selected for the construction of the double-layer PVDF WUS (Model: 2-1004346-0, TE Connectivity Ltd., Berwyn, PA, USA). The metalized PVDF film sheet has printed silver ink electrode layers on both surfaces (top and bottom sides of the film). The PVDF layers are first prepared by marking the desired dimensions and highlighting the polarization direction on the PVDF film sheet in order to facilitate the bonding of the two layers in the antiparallel orientation of the polarization.

According to the marked lines, a piece of 100 mm  $\times$  24 mm was cut from the PVDF film sheet. The film piece was then cut into halves to obtain the two PVDF layers with the same dimensions of 50 mm  $\times$  24 mm, as shown in **Figure 5.1**. Each PVDF layer was divided into two parts: an active ultrasound area of 20 mm  $\times$  20 mm and an interconnection area of 20 mm  $\times$  26 mm, as shown in **Figure 5.1** (a).

The active ultrasonic area is the functional part of the double-layer PVDF WUS which transmits and/or receives ultrasound where the electrode layers on both sides of the PVDF

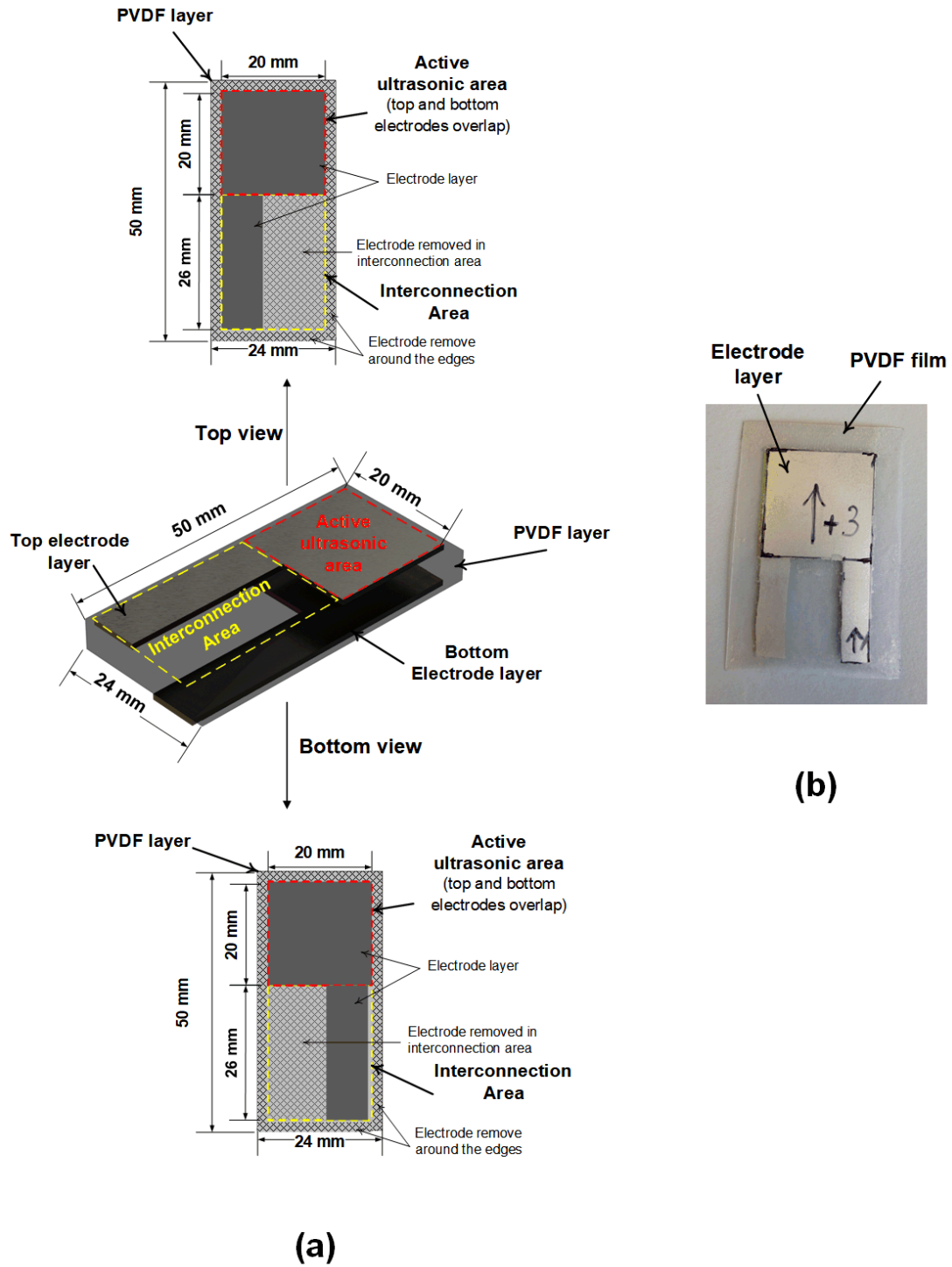


**Figure 5.1:** PVDF layers preparation. A schematic of the single PVDF layer with electrodes (a) and a photo of the PVDF layer at the bottom view (b).

layer surface are overlapped. The interconnection area is the part where the electrical wires are attached to the electrode layers. There is no overlap between the top and bottom electrode layers at the interconnection area of the PVDF layer. The large interconnection area provides a larger electrical attachment surface in order to avoid the concentration of the electrical current, which may damage the electrode layers. 2-mm of the electrode layer around the edges was removed to ensure the prevention of electrical shorting between the top and bottom electrode layers. **Figure 5.1** (b) shows the photo of a single PVDF layer after removing the overlapping electrode at the interconnection area and around the edges.

The silver ink electrode layers were removed by gently scratching the electrode surface using a sharp blade. The scratching method was found to be more practical than using a liquid solvent such as acetone to dissolve the undesired silver ink electrode. Removing a small and specific area of the silver ink electrode using a solvent requires more time and effort compared to the scratching method. Using acetone to remove the electrode layer causes the difficulty in controlling the acetone within the desired area.

### 5.1.2 Bonding the Two PVDF Layers

Adhering the two PVDF layers imposes practical difficulty and demands careful consideration. First is the selection of an adhesive material. Some adhesives may react with the electrode material or cause rigidity of the double-layer PVDF WUS. In an attempt to use a cyanoacrylate adhesive (also commonly known as instant glue or super glue) as a bonding layer it was found to cause rigidity of the double-layer PVDF after curing. The second is the thickness of the adhesive layer. The acoustic loading and attenuation due to a thick adhesive layer would negatively affect the WUS ultrasonic performance, as discussed in **Section 4.2.5** and **Section 4.3.4**. Besides, a thicker adhesive layer could reduce the flexibility

of WUS. Thus, the construction of the double-layer PVDF WUS should aim to minimize the bonding layer thickness. The third is the uniformity of the adhesive layer thickness between the two PVDF layers since the double-layer PVDF should ideally be parallel. Lastly, is the existence of air microbubbles within the adhesive layer. The trapped air microbubbles in the adhesive layer cause an undesired reflection of ultrasound, which impacts the WUS performance negatively.

In this work, several approaches were attempted before achieving a good quality bonding of the two PVDF layers. As discussed in the design considerations in **Section 4.3.4**, the quality of the bonding layer can be assessed by observing the ultrasonic signal strength of the double-layer PVDF. In order to establish a reference value of the signal strength, an ultrasonic gel couplant was used first as a temporary bonding layer. The gel couplant was applied between the two PVDF layers to serve as a temporary bonding layer while observing the received ultrasonic signal amplitude from a test sample. The gel couplant, as a temporary bonding layer, can be spread between the two PVDF layers by hand rubbing the bonding area of the double-layer PVDF using a soft material (rubber) to obtain a thin and evenly distributed layer of the gel couplant. However, the gel couplant is not suitable as an actual bonding material of two PVDF layers since it is not an adhesive material. A polymethyl methacrylate (PMMA), also known as plexiglass, was used as a test sample for the ultrasonic signal strength evaluation. The solid PMMA sample provides the ability to rub the sensor on the flat PMMA sample surface. The reflected ultrasonic signal amplitude from the sample was used to assess the ultrasonic signal strength of the bonded PVDF layers, as shown in **Figure 5.2**. While observing the received ultrasonic signal amplitude from the sample, a hand rubbing was applied using a flat rubber object to control the temporary bonding layer thickness and uniformity. This procedure was repeated several times, and the observed maximum amplitude was used as a reference value to evaluate the bonding quality with the

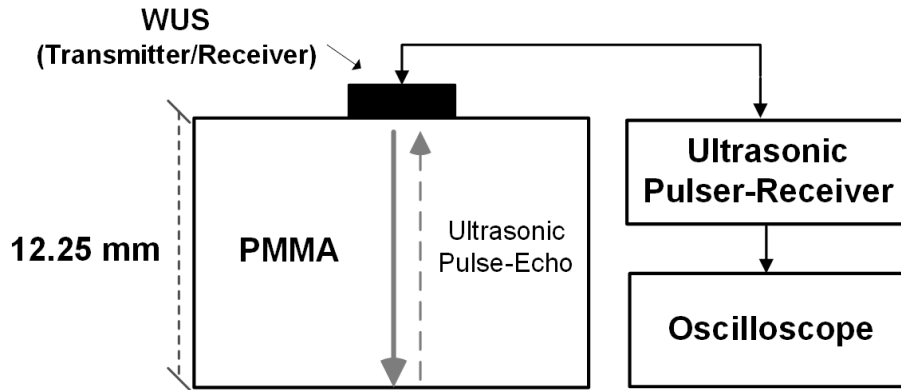


**Figure 5.2:** Experimental configuration of the ultrasonic signal strength evaluation of the bonded double-layer PVDF.

actual adhesive.

Epoxy adhesives are commonly used with piezoelectric materials and are a suitable choice for the bonding layer [72, 151, 188, 221, 222]. A fast-curing epoxy adhesive (model: Gorilla epoxy, Gorilla Glue Company, Cincinnati, Ohio, USA), also known as 5-min epoxy, was first attempted in order to adhere the two PVDF layers at the inner electrode layers. Before applying the epoxy mixture, the two 52- $\mu\text{m}$  PVDF layers were covered using an adhesive tape, except for the bonding area (the active ultrasound area of the two PVDF layers) in order to prevent the transfer of epoxy to the other surfaces. Then, the two PVDF layers were lined up next to each other so that the second PVDF layer could be easily flipped after applying the epoxy to the first PVDF layer. The two parts of the epoxy were mixed by stirring slowly to avoid the occurrence of air microbubbles in the epoxy mixture. A thin layer of the epoxy mixture was spread using a small thin stick such as a toothpick over the bonding area of the first PVDF layer; the active ultrasound area of the inner electrode. Then, the second PVDF layer was flipped over the first PVDF layer. Next, a hand rubbing was applied over the second PVDF layer using a soft material to spread the epoxy mixture evenly between the two PVDF layers. Any excess epoxy was removed after the rubbing. Afterward,

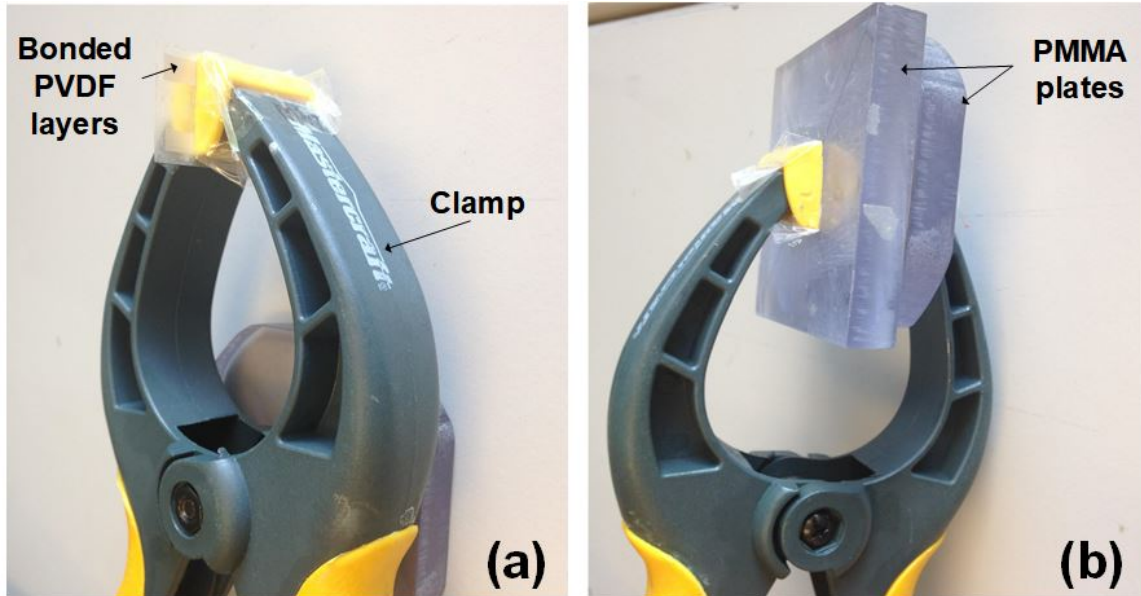


**Figure 5.3:** Photos of the bonded double-layer PVDF attachment to clamp jaws: directly (a) and sandwiched between two PMMA plates (b).

the bonded PVDF layers were held by a clamp, as shown in **Figure 5.3** (a), until the epoxy was fully cured (24 h, according to the manufacturer's instructions).

After curing, the epoxy layer thickness was measured at five points over the bonding area. The average thickness was  $20\ \mu\text{m}$  with a large variation of  $\pm 10\ \mu\text{m}$ . It was found that the variation of the epoxy thickness between the two PVDF layers was caused by the unequal pressure distribution along the jaws of the clamp during the curing process of the epoxy. Therefore, in the second attempt at bonding the two PVDF layers, this was addressed by reducing the amount of the epoxy mixture applied and placing the bonded PVDF layers between two flat PMMA plates in the clamp, as shown in **Figure 5.3** (b). The average thickness of the epoxy obtained after the second attempt was  $13.6\ \mu\text{m}$  with an average variation of  $5\ \mu\text{m}$ , which was thinner and had less variation than the first attempt. However, the observed ultrasonic signal amplitude was 51% lower than the reference value obtained with the gel couplant as a temporary bonding layer.

To further reduce the bonding layer thickness and its distribution, an improved approach to control the epoxy thickness would be required. In the previous attempts, achieving a thin and uniform epoxy layer was attempted by applying pressure over the bonding area, which was unsuccessful. Since the purpose of a thin and uniform bonding layer is to achieve the maximum ultrasonic signal of the double-layer PVDF, the epoxy application should be under the guidance of the ultrasonic signal amplitude. Therefore, the proposed alternative approach in this thesis work is to apply the epoxy while observing the ultrasonic signal amplitude by the experimental configuration described in **Figure 5.2**. The spread of epoxy between the two PVDF layers is controlled by rubbing over the bonding area using a soft material until the reference signal amplitude is obtained. However, this procedure led to the difficulty in using the fast-curing epoxies. Spreading the epoxy between the two PVDF layers proved challenging due to the high viscosity of the epoxy mixture. **Table 5.1** lists the typical viscosity of some epoxies and common fluids. In addition, achieving the reference ultrasonic signal amplitude involves a repeated rubbing over the bonding area to spread the fast-curing epoxy evenly. The epoxy mixture quickly became more viscous and harder to spread within less than a minute. Therefore, the procedure of applying epoxy while the double-layer PVDF under testing reacquired an epoxy of lower viscosity and a longer curing process time so that it could be spread easily between the PVDF layers.

Common epoxy adhesives of very low viscosity such as the Spurr's epoxy ( $\eta \approx 65 \text{ mPa}\cdot\text{s}$ ) require an elevated temperature to cure ( $60 - 70^\circ\text{C}$  or higher [223]). Therefore, the curing process must involve placing the bonded PVDF layers in heated boxes or ovens in order to maintain the high temperature required for curing. In an attempt to use low-viscous Spurr's epoxy (model: Embed-It Low Viscosity Epoxy, Polysciences, Inc., Warrington, PA, USA) as a bonding layer, placing the bonded PVDF layers in a heated box of  $65^\circ\text{C}$  after applying the Spurr's epoxy imposed the difficulty of maintaining the achieved epoxy layer thickness.

The step of placing the bonded double-layer PVDF in a heated box for epoxy curing was found to be challenging and time-consuming.

Instead, an epoxy (model: Clearcast 7000, The Epoxy Resin Store, Lake Elsinore, CA, USA) of moderate viscosity (1800 – 2500 mPa·s) that cures at room temperature was used. In the application of the moderate-viscosity epoxy, the epoxy mixture was slowly stirred for 3-5 min to avoid creating air bubbles within the mixture. Then, the mixture was left to stand for another 3-5 min to bring any air bubbles to the surface, where they could be released. Afterward, a small amount ( $\approx 0.1$  ml) of the epoxy mixture was applied in the middle of the bonding area of the first PVDF layer using a syringe. After applying the epoxy mixture to the first layer, the second PVDF layer was flipped over. Controlling the amount of the applied epoxy mixture raised practical difficulties as an excessive amount would leak to the other sides of the PVDF layers and the remaining amount would be insufficient to bond the two PVDF layers. Thus, the process was first repeated several times with test samples of the transparent plastic film until the adequate amount of epoxy was achieved. The applied epoxy mixture was spread by repeated hand rubbing over the second PVDF layer using a soft material until around 98% of the reference ultrasonic signal amplitude was obtained. Then, the bonded PVDF layers were left on the PMMA sample until the epoxy mixture was fully cured ( $\approx 48$  h). The bonding layer that was obtained after fully curing was  $7.5 \pm 2.7$   $\mu\text{m}$ .

### 5.1.3 Attachment of Electrical Wire

As described in **Section 4.3.3**, the interconnection area of the electrical wire attachment was separated from the active ultrasound area, as shown in **Figure 5.1**. Therefore, there was no overlap between the electrode layers of the two sides of the PVDF layer surfaces in the interconnection area. PVDF has a Curie temperature of approximately 135°C and a melting

**Table 5.1:** Typical viscosity of epoxy resins and common Fluids

<b>Material</b>	<b>Viscosity, <math>\eta</math> (mPa·s)</b>
Water at 20 °C [224]	1
Whole milk at 20 °C [224]	2.12
Spurr's epoxy (low viscosity) [223]	65
Olive oil at 20 °C [224]	84
Cycloaliphatic epoxy (moderate viscosity) [225, 226]	1800-2500
Honey [227]	2000 – 10000
Fast curing epoxy (high viscosity) [228]	18000 – 30000

temperature of approximately 150°C [72]. For this reason, direct wire soldering to the electrode surface cannot be used due to the high temperature of soldering ( $\approx 180 - 250^\circ\text{C}$ ).

Several approaches were attempted to achieve a reliable electrical wire connection to the electrode layers of the PVDF in the previous work [70]. One approach was using a rivet where the ring tongue terminal and the wire were mechanically pressed against the PVDF and electrode layers by a rivet through a hole. The major drawback of this technique was the pressure exerted by the rivet, which limits the WUS flexibility at the interconnection area. Instead, the wire was first soldered to a small piece of thin, flexible foil made of a conductive material (12- $\mu\text{m}$ -thick brass shim). The brass layer was then affixed directly to the electrode surface with an adhesive polyimide tape (packaging layers). This approach provides the simplicity of construction and preserves the flexibility of the WUS. However, wire disconnection and electrical noise were experienced during the prolonged usage of the WUS.

In order to improve the electrical wire attachment and address the wire connection reliability, an electrically conductive adhesive tape (Conductive Tin-Plated Copper Foil Tape,

3M, St. Paul, MN, USA) was used instead of the brass shim. The electrical wires were soldered to the top side of the conductive adhesive tape first, and then the adhesive side was applied to the electrode surface. In addition, a larger surface area of attachment (8 mm × 20 mm) was considered to ensure the reliability of the electrical connection to the electrode layers.

For the inner electrode layers, a piece of the conductive adhesive tape was folded between the inner electrode layers, where its electrical wire was connected to the active terminal of the power source (ultrasonic pulser-receiver), as shown in **Figure 5.4**. Keeping a space of approximately 6 mm between the folded conductive adhesive tape and the active ultrasound area (bonding area) was taken into consideration to avoid the effect of the folded tape thickness in the bonding layer thickness and uniformity near the interconnection area. For the outer electrode layers, a piece of the conductive adhesive tape was wrapped over the interconnection area of the outer electrode layers, where its wire would be connected to the grounded terminal.

#### **5.1.4 Creation of Acoustic Insulator Layer**

As discussed in **Section 4.3.5**, an air gap is proposed in the design of the double-layer PVDF WUS to isolate the effect of the packaging layer applied at the back of the WUS. Thus, air-backing of the WUS was achieved by using an acoustic insulation layer at the back side electrode of the bonded PVDF layers. The acoustic insulation layer was a small air gap created at the back side (the outer electrode layer at the back side of the bonded PVDF layers) by inserting a piece of paper (100 μm thick) without adhering. This air gap isolate the acoustic loading of the packaging layers (EM shielding and protection layers) to the outer electrode layer surface at the back side. Thus, the non-adhered paper layer creates an air gap

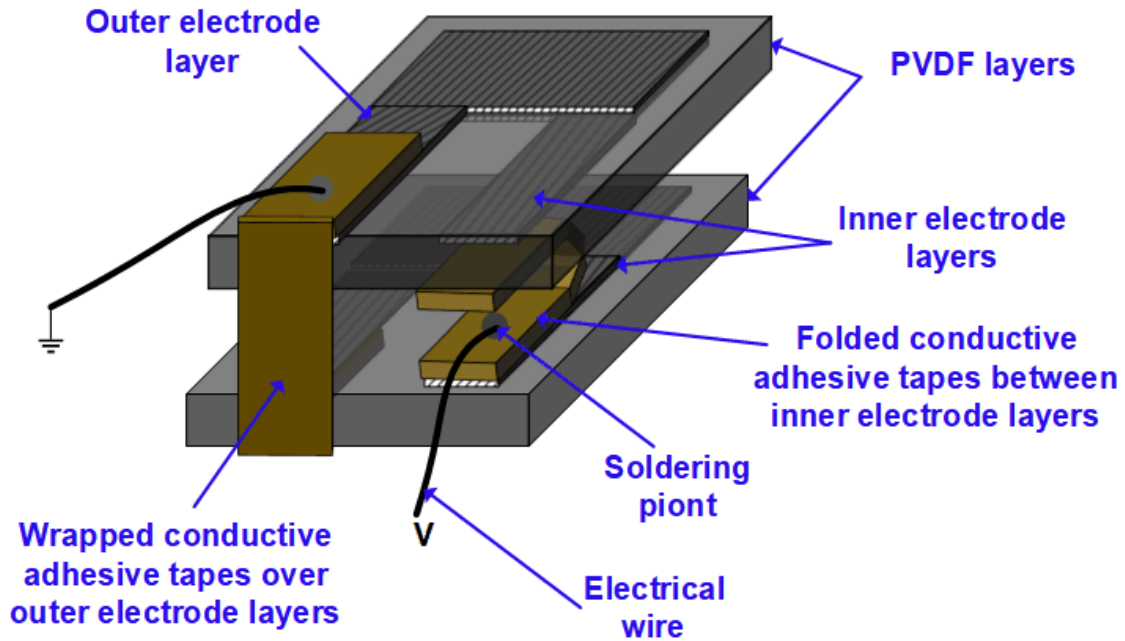


**Figure 5.4:** A schematic of the electrical wire attachment to the inner and outer electrode layers using conductive adhesive tapes.

above the outer electrode layer at the back side to serve as a backing medium, making the double-layer PVDF WUS air-backed.

### 5.1.5 Complete Construction With Packaging

The packaging of the double-layer PVDF WUS consists of a flexible metal foil and a polyimide film with adhesive layers. The flexible metal foil serves as an EM shielding layer to reduce environmental noises. The polyimide film with adhesive serves as a sealant and protective layer for the entire structure of the double-layer PVDF WUS as well as electrical insulation. The packaging layers were applied to wrap the entire WUS structure except for the ultrasonic sensing area where the ultrasound is transmitted and/or received.

First, the EM shielding layer consisting of a flexible and thin conductive metal was constructed. As the outermost electrode layers were connected to the ground terminal, the

metal foil covering the front and back sides of the double-layer PVDF WUS (including the active ultrasound and the interconnection areas) was also connected to the ground. A thin, flexible metal foil such as brass or aluminum could be used as an EM shielding layer. In this construction, a thin brass foil (12  $\mu\text{m}$  thick) was used.

After covering the WUS with the EM shielding layer, the entire structure of the double-layer PVDF WUS was wrapped with an adhesive polyimide film to bind and protect the structural layers of the WUS. Afterward, the EM shielding and the protection layers were removed from the ultrasonic sensing area of 20 mm  $\times$  20 mm, as shown in **Figure 5.5**. The packaging layers were also extended to cover electrical wires.

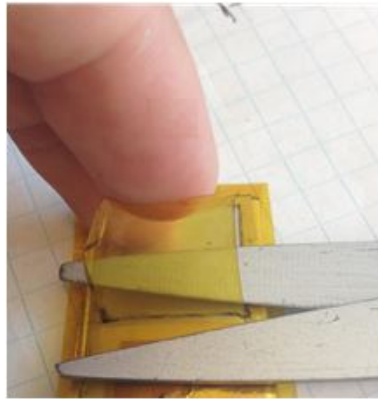


**Figure 5.5:** A photo of the removal of the protection layer from the ultrasonic sensing area.

**Figure 5.6** shows the photos of the constructed double-layer PVDF WUS. The overall dimensions of the constructed WUS were 56 mm  $\times$  30 mm with a total thickness of 350  $\mu\text{m}$ . The the ultrasonic sensing area was 20 mm  $\times$  20 mm. The developed double-layer PVDF WUS is flexible, lightweight (less than 1 g), thin, and small in size, which could be attached to a skin surface and measure the muscle contraction without affecting the motion dynamics.

The flexible double-layer PVDF WUS was constructed using basic equipment and ordinary hand tools, such as scalpels and a soldering device, and did not require advanced technology such as microfabrication processing or equipment used in MEMS-based UT

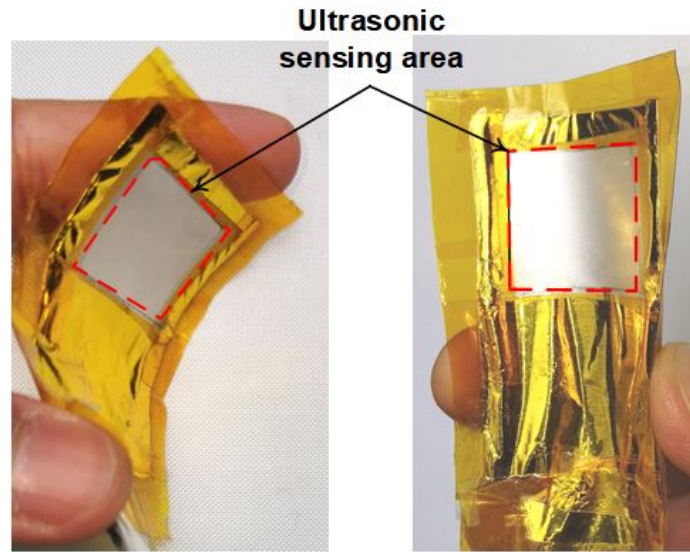


**Figure 5.6:** Photos of the constructed double-layer PVDF WUS.

fabrication [7–9, 11, 15]. The overall cost of the materials used in constructing the double-layer PVDF WUS was inexpensive (less than 20 CAN \$). Thus, the developed double-layer PVDF WUS could be used as a disposable sensor to monitor muscle contractions.

The constructed double-layer PVDF WUS consists of two layers of 52- $\mu\text{m}$ -thick PVDF piezoelectric as an active element. Each PVDF layer has an electrode layer on both sides of 10- $\mu\text{m}$ -thick silver ink. It is worth noting that the thickness of the silver ink electrode layer of the 52 $\mu\text{m}$  PVDF film by the manufacturer's specification was 6  $\mu\text{m}$ . However, the measured thickness of the silver ink electrode layer at several points along the film sheet was  $10 \pm 1 \mu\text{m}$ . The two PVDF layers were arranged in antiparallel polarization directions and bonded at the inner electrode layers by an epoxy layer of 7.5  $\mu\text{m}$ . The outer electrode layers, next to the acoustic insulator layer and the ultrasonic sensing area, are connected to the ground terminal, and the inner electrode layers, between the bonded PVDF layers, are connected to the active terminal. Thus, a reversal voltage orientation is applied to the two PVDF layers. The antiparallel direction of the polarization with the reversal voltage

orientation results in the parallel polarization direction arrangement. In order to isolate the effect of the packaging layers and air backed the double-layer PVDF WUS, an acoustic insulator layer is placed at the back side of the double-layer PVDF film without adhering. The non-adhered insulator layer maintains an air gap over the back side of the electrode to allow the air-backing of the PVDF layers. In order to isolate the WUS from the interference of the electrical noise and improve the SNR of the received signal, the WUS structure was covered by a thin, flexible metal foil as an EM shielding layer. Then, the polyimide film with adhesive as a protection layer was applied over the WUS to hold the layer structure and protect the WUS. The EM shielding and protection layers were not constructed on the ultrasonic sensing area, where the ultrasound is transmitted and received, to improve the SNR by avoiding undesired ultrasonic attenuation and internal reflections within the EM shielding and protection layers. Since the PVDF has an acoustic impedance close to that of soft tissues, a matching layer at the front side is not required to facilitate the ultrasound transmission between the double-layer PVDF WUS and the tissue. An ultrasonic couplant is required between the double-layer PVDF WUS and skin surface in order to displace the air and facilitate the ultrasound transmission between them.

## 5.2 Performance Evaluation of Double-Layer PVDF

### WUS

In this section, the ultrasonic performance of the double-layer PVDF WUS is evaluated experimentally and discussed with the numerical simulation results. The operating frequency and ultrasonic signal strength of the constructed double-layer PVDF WUS are evaluated by an impedance measurement using a network analyzer and an ultrasonic pulse-echo measurement with a PMMA sample. The performance of the double-layer PVDF WUS is also compared to that of the single-layer PVDF WUS. The single-layer WUS has the almost equivalent total PVDF thickness (110  $\mu\text{m}$ ) of the double-layer PVDF WUS (104  $\mu\text{m} = 2 \times 52 \mu\text{m}$ ). Also, both the double-layer and single-layer PVDF WUSs were constructed as described in **Section 5.1** and have the same sensing area of 20 mm  $\times$  20 mm.

#### 5.2.1 Operating Ultrasound Frequency

The operating frequency of the constructed double-layer 52- $\mu\text{m}$  PVDF WUS was experimentally evaluated using the electrical impedance measurement. An impedance analyzer device (model: E5061B, Keysight Technologies, Santa Rosa, CA, USA) was used to measure the electrical impedance as a function of frequency. At the operating frequency, the impedance phase takes a peak value between the local maxima and minima in the impedance magnitude [72, 229, 230]. For the purpose of comparison, an operating frequency evaluation was conducted for a single-layer 52- $\mu\text{m}$ -thick PVDF WUS, a single-layer 110- $\mu\text{m}$ -thick PVDF WUS, and a double-layer 110- $\mu\text{m}$ -thick PVDF WUS.

In the previous chapter, the acoustic impedance of the silver ink electrode used in the numerical study was estimated. The acoustic impedance of the silver ink electrode employed

on the obtained PVDF films was not provided by the manufacturer. Also, a thorough search of the relevant literature yielded no report of the silver ink acoustic properties, to the best of the author's knowledge. Therefore, the acoustic impedance of the silver ink electrode was estimated by matching the calculated impedance using the simulation model to the experimentally measured impedance using the impedance analyzer. The estimation of the silver ink acoustic impedance was conducted using the single-layer 52  $\mu\text{m}$ -thick and 110- $\mu\text{m}$ -thick PVDF sensors to avoid the effect of the bonding layer of double-layer PVDF on the impedance measurement. The measured layer thickness of the silver electrode from the obtained 52  $\mu\text{m}$ -thick and 110  $\mu\text{m}$ -thick PVDF film sheets were 10  $\mu\text{m}$  and 9  $\mu\text{m}$ , respectively. **Figure 5.7** shows the measured (dotted line) and calculated (solid lines) electrical impedance for the single-layer 52  $\mu\text{m}$ -thick and 110  $\mu\text{m}$ -thick PVDF sensors. The electrical impedance of the single-layer PVDF sensors were also calculated for the cases of silver and silver epoxy electrodes. The operating frequency that was obtained from the measured electrical impedance of the air-loaded (air/air) single-layer 52- $\mu\text{m}$ -thick PVDF with the silver ink electrode was around 12.8 MHz, whereas the calculated operating frequencies, assuming the electrode as silver epoxy (5.15 MRayls) and silver (38.16 MRayls), were 13.7 MHz and 8.3 MHz, respectively, as shown in **Figure 5.7** (b). For the single-layer 110  $\mu\text{m}$ -thick PVDF, the operating frequency from the measured impedance was at 7.8 MHz, whereas the calculated operating frequency with silver epoxy and silver electrode layers were at 8.1 MHz and 5.6 MHz, respectively, as shown in **Figure 5.7** (d). Thus, the acoustic impedance of the silver ink can be estimated somewhere between the acoustic impedance values of the silver and silver epoxy. Based on the attempts of matching local maxima and minima at the operating frequency of the simulated impedance to the measured ones, an approximate acoustic impedance value of 12.24 MRayls for the silver ink would give be a close match to the operating frequency obtained for the single-layer 52  $\mu\text{m}$  and 110  $\mu\text{m}$  PVDF sensors from

the measured impedance. In addition, the properties of the materials used in the simulation, such as PVDF and epoxy, may slightly differ from the actual values since they were obtained from several sources, as indicated in **Table 4.1** and **Table 4.2**. It is challenging to obtain the actual values of the properties of the materials due to the variations within the same material, such as the composition ratio, synthesis method, and processing conditions. Therefore, an error between the measured and simulated results was anticipated.

**Figure 5.8** shows the operating frequency obtained from the measured impedance for the single-layer and the double-layer cases of 52  $\mu\text{m}$ -thick and 110  $\mu\text{m}$ -thick PVDF. The resonance frequency from the calculated input impedance using the simulation model for the same conditions conducted in the experimental measurement is also shown in the figure, assuming that the acoustic impedance of the silver ink was 12.24 MRayls. The calculated operating frequencies of the four PVDF WUS configurations showed a close agreement with the measured values. The constructed double-layer 52  $\mu\text{m}$ -thick PVDF WUS has an operating frequency of 6.8 MHz obtained from the measured impedance. The operating frequency of the constructed double-layer PVDF WUS is a result of the combined effect of the PVDF thickness and the acoustic loading of the electrode and bonding layers. **Figure 5.9** illustrates the effect of the electrode and bonding layers in decreasing the operating frequency of double-layer PVDF WUS. **Figure 5.9** (a) shows the four structural configurations in the simulation: double-layer PVDF only, double-layer PVDF with bonding layer only, double-layer PVDF with electrode layers only, and the full structure of the constructed double-layer PVDF WUS. From the calculated impedance in **Figure 5.9** (b), the acoustic loading of the bonding layer (7.5- $\mu\text{m}$ -thick epoxy layer) shifts the double-layer 52- $\mu\text{m}$ -thick PVDF operating frequency from 10.7 MHz to 9.5 MHz where the electrode layers (10- $\mu\text{m}$ -thick silver ink each) cause a larger shift to 7.7 MHz. Thus, the combined effect of the electrode and bonding layers further decreases the operating frequency to 7 MHz.

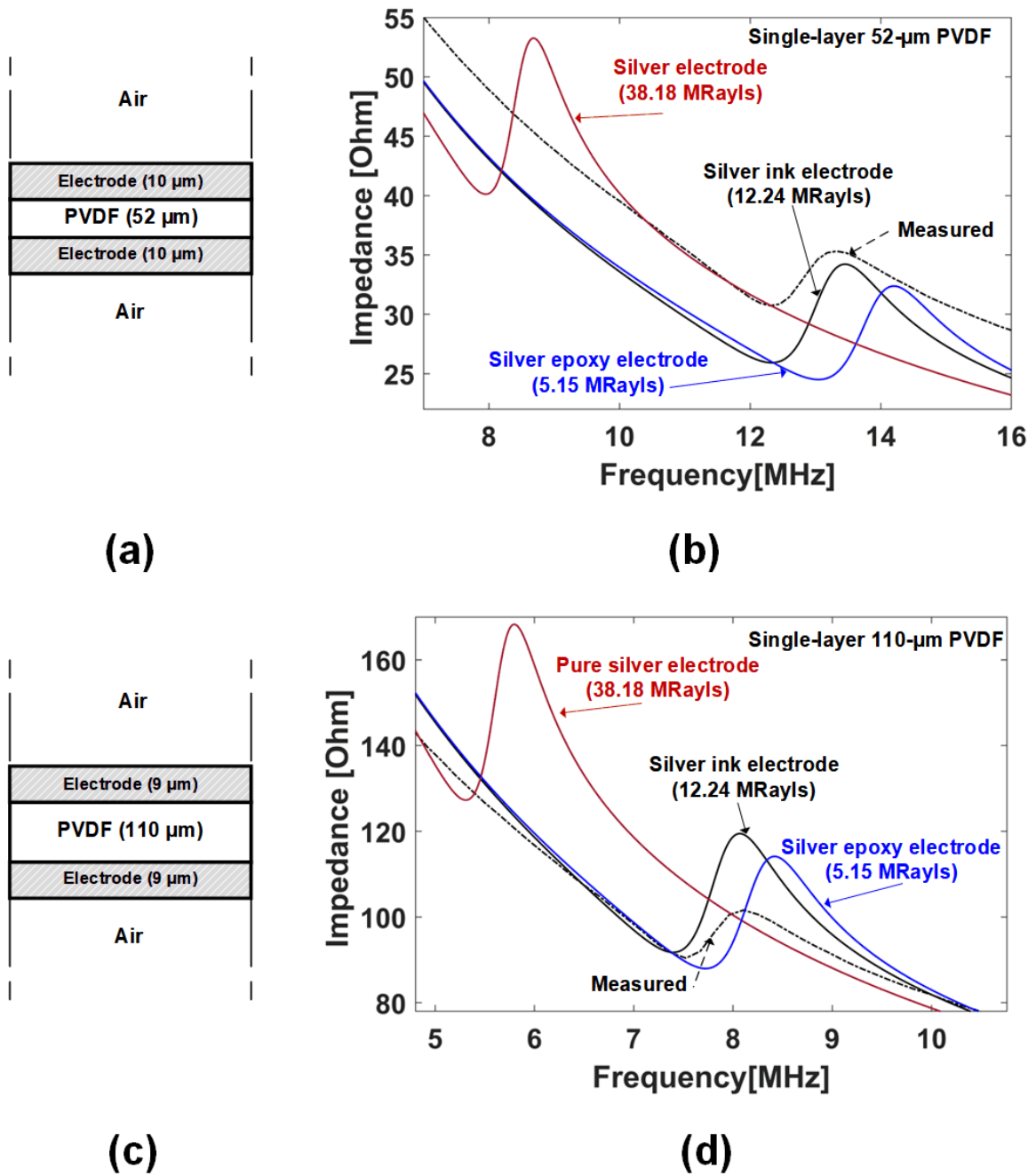
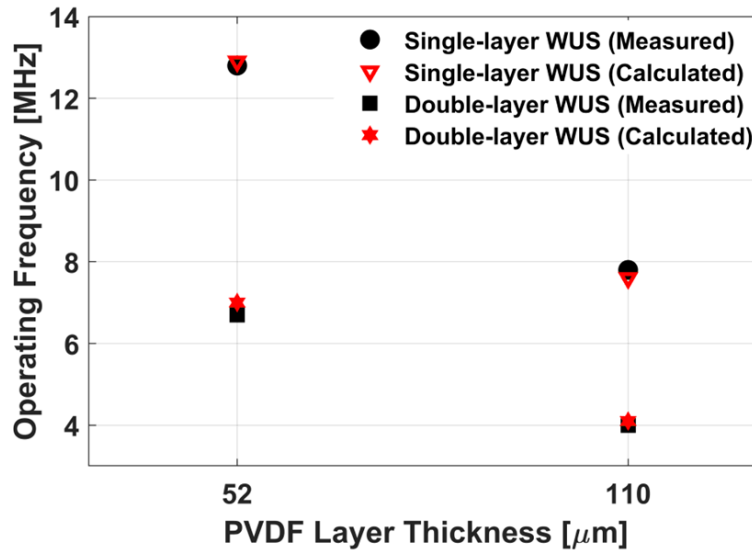
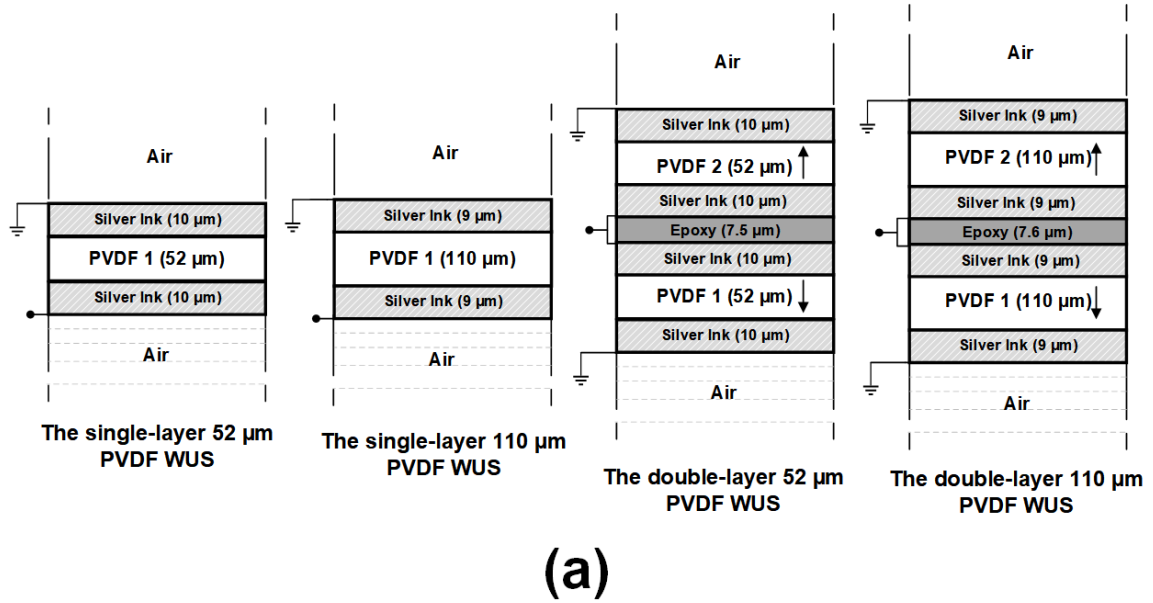
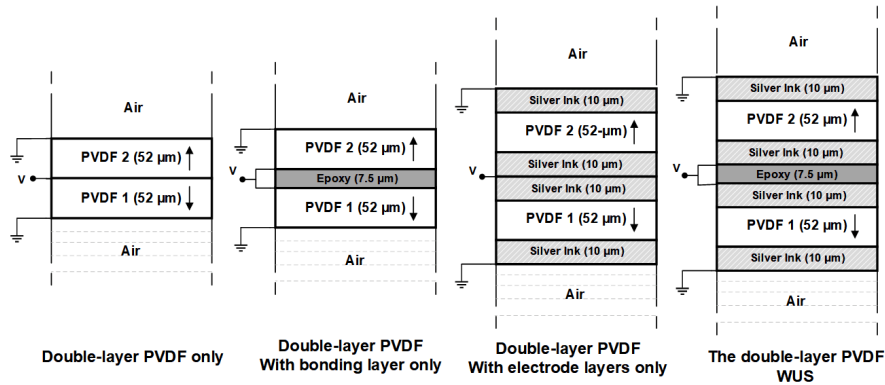


**Figure 5.7:** Measured (dotted line) and calculated (solid lines) electrical input impedance of an air-loaded single-layer PVDF with an electrode layer on the top and bottom surfaces. The structural configuration (a) and electrical impedance (b) of the single-layer 52- $\mu\text{m}$ -thick PVDF, and the structural configuration (c) and impedance (d) of the single-layer 110- $\mu\text{m}$ -thick PVDF. The active ultrasound area is  $4 \text{ cm}^2$ .

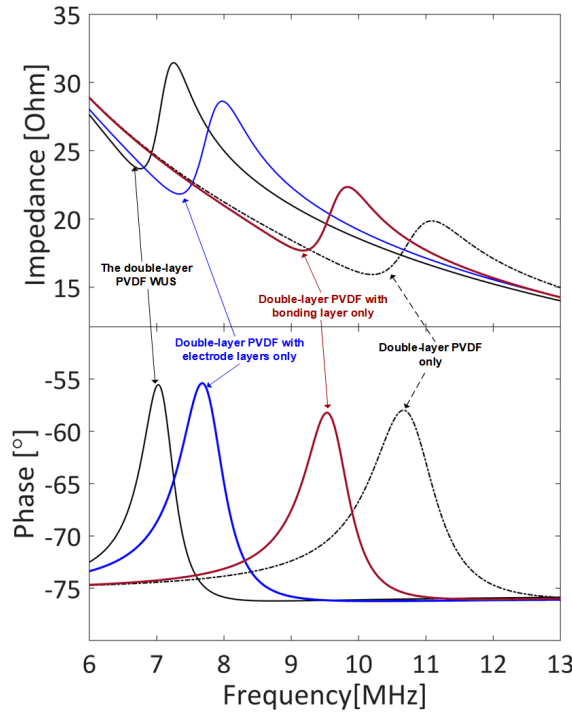


(b)

**Figure 5.8:** The operating frequencies obtained from the measured and calculated impedance for the air-loaded (air/air): single-layer 52  $\mu\text{m}$ -thick PVDF WUS, single-layer 110  $\mu\text{m}$ -thick PVDF WUS, double-layer 52  $\mu\text{m}$ -thick PVDF WUS, and double-layer 110  $\mu\text{m}$ -thick PVDF WUS.



(a)



(b)

**Figure 5.9:** Calculated electrical input impedance for the air-loaded double-layer PVDF only, double-layer PVDF with bonding layer only, double-layer PVDF with electrode layers only, and the full structure of constructed double-layer PVDF WUS to illustrates the loading effect of the electrode and bonding layers that led to the operating frequency of double-layer 52  $\mu\text{m}$ -thick PVDF WUS. The structural configurations of the simulations (a) and the input impedance magnitude and phase (b) are shown. Active ultrasound area is 4  $\text{cm}^2$ .

### 5.2.2 Ultrasonic Signal Strength

The ultrasonic signal strength of the constructed double-layer PVDF WUS was evaluated experimentally using an ultrasonic pulse-echo technique, and compared to that of the single-layer WUS. The single-layer 110- $\mu\text{m}$  PVDF WUS has the almost equivalent total PVDF thickness of the double-layer 52- $\mu\text{m}$  WUS. Also, both of the WUSs have the same sensing area of 20 mm  $\times$  20 mm. The WUSs were attached to a 12.25-mm thick PMMA plate sample (60 mm  $\times$  60 mm  $\times$  12.25 mm) with an ultrasonic gel couplant, and the ultrasonic signal which was reflected from the bottom surface of the sample was acquired with the measurement configuration shown in **Figure 5.2**. Then, the reflected signal amplitude was evaluated.

The WUSs were driven by an ultrasonic pulser-receiver (Model: DPR300, JSR Ultrasonics, Pittsford, NY, USA) in the ultrasonic pulse-echo mode. The received ultrasonic RF signals from each WUS were acquired by an oscilloscope (Model: TDS2024B, Tektronix, Beaverton, OR, USA). The same settings of the pulser-receiver were used for both the WUSs. In order to ensure the steady contact of the ultrasonic sensor area of WUSs to the surface of the PMMA sample, hand rubbing using a soft material was applied over the back side of WUSs. The measurements were repeated several times to ensure the consistency of the obtained amplitude of the reflected ultrasonic signal.

**Figure 5.10** (a) shows the reflected ultrasonic signal obtained by the double-layer 52- $\mu\text{m}$  PVDF WUS (solid line) and the single-layer 110- $\mu\text{m}$  PVDF WUS (dotted line), respectively. The constructed double-layer 52- $\mu\text{m}$  PVDF WUS exhibited 1.7 times greater reflected signal peak-to-peak amplitude compared to the single-layer 110- $\mu\text{m}$  PVDF WUS of almost the equivalent total PVDF thickness. Thus, the result of the pulse-echo experiment showed that the voltage amplitude of received signal increases with the double-layer PVDF configuration.

This experimental result agrees with the numerical study using the simulation model in the previous chapter. The numerical study predicted that the double-layer PVDF configuration leads to increased transmitted ultrasound signals and consequently increases the received ultrasonic signal. Thus, the developed double-layer PVDF WUS in this thesis work improved the ultrasonic signal strength of the PVDF piezoelectric allowing for higher SNR of the received ultrasonic signal. Others have employed the multiple-layer configuration to improve the ultrasonic performance of piezoelectric polymer sensors [199, 231, 232]. Nakazawa et al. [199] investigated the multiple-layer ultrasonic transducer using polyurea piezoelectric polymer material for high-frequency ultrasound applications (30 – 100 MHz). Their pulse-echo experiment showed that the voltage amplitudes of the received signal increased with the multiple-layer configuration of polyurea. Also, Xi et al. [232] reported the improvement in sensitivity using multiple-layer PVDF compared to the single-layer configuration for the photoacoustic imaging application.

### 5.2.3 Noise Interference Reduction

The EM shielding of the double-layer PVDF WUS was evaluated experimentally. The received ultrasonic signal acquired from the *in vivo* measurement in the pulse-echo mode was compared to a double-layer PVDF WUS before and after applying the EM shielding layer. The double-layer PVDF WUS that had no EMS shielding layer was employed in transmitting and receiving the reflected ultrasound (pulse-echo mode) from the tissue-bone interface at the biceps muscle in the upper arm. Then, the same procedure was repeated after applying the EM shielding layer to the double-layer PVDF WUS. The WUSs were operated by an ultrasonic pulser-receiver system (Model: DPR300, JSR Ultrasonics, Pittsford, NY, USA). The ultrasonic RF signals received by WUS were filtered by the pulser-receiver's built-in

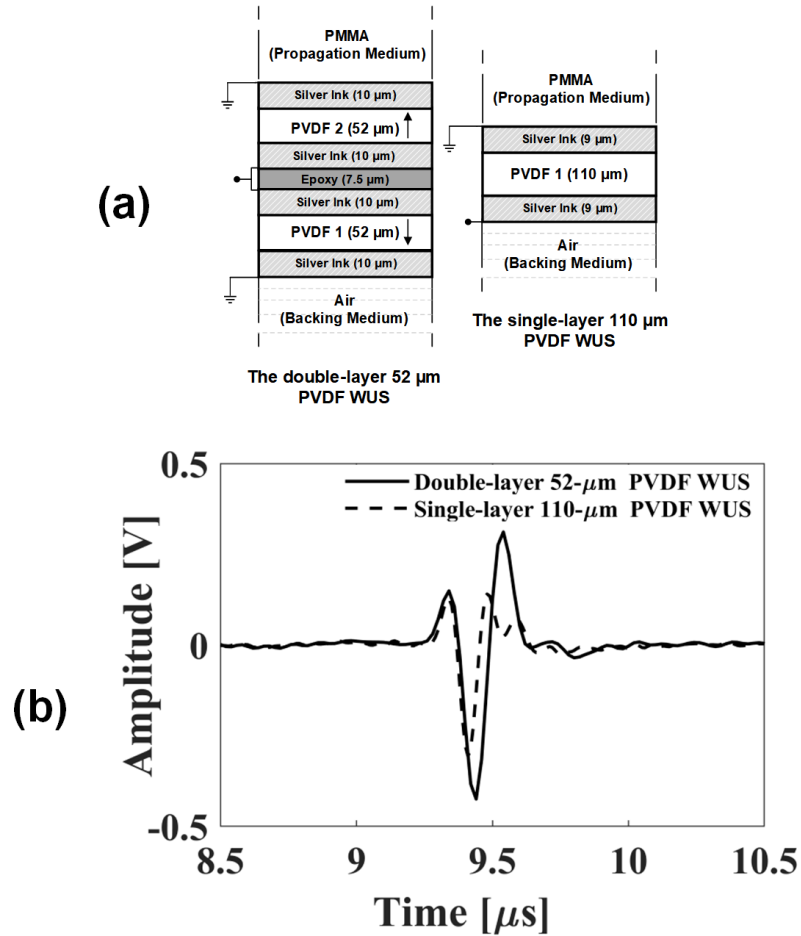


**Figure 5.10:** Experimental evaluation of signal strength. The structural configuration of double-layer 52- $\mu\text{m}$  PVDF WUS and single-layer 110- $\mu\text{m}$  PVDF WUS (a) and the Ultrasonic RF signals obtained in pulse-echo mode (b).

analog band-pass filter of 1–22.5 MHz bandwidth. Then, the received ultrasonic RF signals were digitized at a sampling frequency of 125 MHz and stored by the data acquisition (DAQ) system (Model: ATS 9440, Alazartech, Montreal, QC, Canada) connected to a personal computer (PC).

**Figure 5.11** shows the two acquired ultrasonic RF signals. It can be observed in **Figure 5.11** (a) that the noise RMS (root mean square) of 14.1  $\text{mV}_{\text{rms}}$  was reduced after applying the EM shielding layer to 5  $\text{mV}_{\text{rms}}$ , as shown in **Figure 5.11** (b). Without the EM

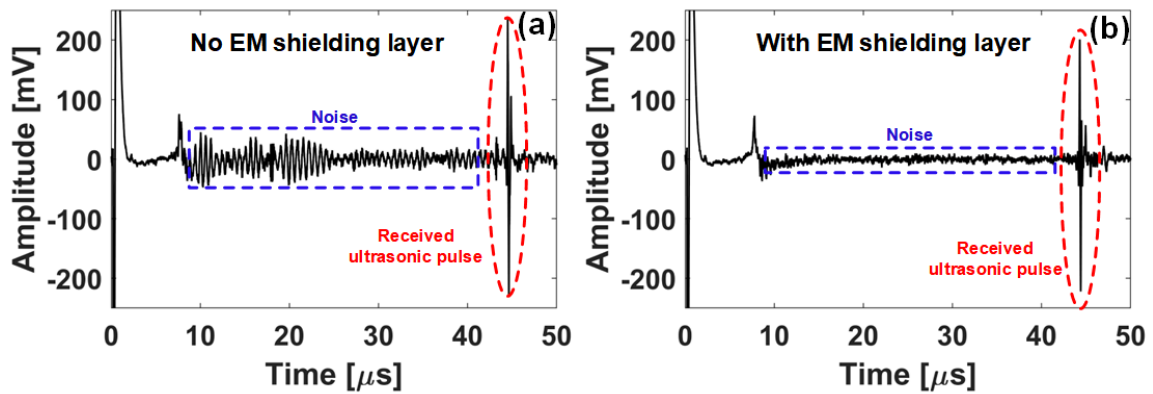


**Figure 5.11:** Noise reduction with the electromagnetic shielding layer. The received ultrasonic signals were acquired from *in vivo* measurements to compare between a double-layer PVDF WUS before and after applying the EM shielding layer. The received ultrasonic RF signals using the double-layer PVDF WUS before applying the EM shield layer (a) and after applying the EM shielding layer (b).

shielding, the ultrasonic signals of the WUS would be contaminated by the various sources of environmental and instrumental noise such as noise. The soft tissue estimation accuracy from the received ultrasonic RF signals can be affected by unwanted signals interference. Thus, the EM shielding of the double-layer PVDF WUS has improved the SNR from 18.3 dB to 26.6 dB (+ 40%) under the experimental conditions.

## **Chapter 6**

# ***In Vivo* Experimental Evaluation of the Double-Layer PVDF WUS for the measurement of Skeletal Muscle Contractile Parameters**

In this chapter, the evaluation, demonstration, and discussion of the *in vivo* monitoring of muscle contraction using the developed double-layer PVDF WUS is presented. It investigates the double-layer PVDF WUS and the ultrasonic measurement method performance in monitoring the skeletal muscle contractions and the quantitative assessment of the contractile properties. In this chapter, the ultrasonic measurements by the double-layer PVDF WUS are demonstrated to estimate the tissue thickness changes during the electrically-evoked contraction, electrically-evoked tetanic contraction, and dynamic voluntary contraction of the skeletal muscle. Several parameters are extracted from the obtained thickness changes/time curve to assess the muscle contractile properties quantitatively. The obtained contractile parameters are evaluated for their measurement variability. The *in vivo* evaluation includes the

comparison between the double-layer PVDF WUS and the LDS methods in the measurement results of relative tissue thickness changes and extraction of the contractile parameters. The comparative evaluation of the motion artifact influence on the measurement of muscle contractile parameters between the double-layer PVDF WUS and LDS methods is also presented. Additionally, the capability of the double-layer PVDF WUS in the quantitative assessment of the muscle tetanic contraction progression and dynamic voluntary contractile properties are demonstrated as non-invasive and inexpensive tool for the measurement of the skeletal muscle contractile properties.

This chapter is organized into five sections as follows. **Section 6.1** describes the *in vivo* ultrasonic measurement methodology. **Section 6.2** presents the comparative *in vivo* evaluation between the double-layer PVDF WUS and LDS measurements. **Section 6.3** presents the *in vivo* demonstration of the quantitative assessment of skeletal muscle tetanic contractions and dynamic voluntary contractions. **Section 6.4** discusses the results of the presented *in vivo* experiments. **Section 6.5** discusses the limitations of the ultrasonic measurement using the double-layer PVDF WUS.

## 6.1 Double-Layer PVDF WUS Measurement

### Methodology

The developed double-layer PVDF WUS performs the tissue thickness measurement due to muscle contraction in two ultrasonic modes: pulse-echo (PE) or through-transmission (TT) mode. This section describes the measurement principle of the two ultrasonic modes, the *in vivo* experimental configuration of the double-layer PVDF WUS measurement conducted in this chapter, and the extraction method of the skeletal muscle contractile parameters.

### 6.1.1 Ultrasonic Soft Tissue Thickness Measurement Methods

**Figure 6.1** (a) shows the measurement configuration of the ultrasonic PE mode. In the PE mode, one double-layer PVDF WUS is employed as a transmitter of ultrasound and a receiver of the reflected ultrasound. The WUS transmits ultrasonic pulses through the tissue and receives the reflected ultrasonic pulses from the tissue-bone boundary. The transmitted ultrasound wave reflects back to the double-layer PVDF WUS at the tissue/bone interface due to the high acoustic impedance of bone (7.75 MRayls) compared to soft tissue (1.63 MRayls). During contractions, thickness changes between the double-layer PVDF WUS and bone due to the muscle contraction are measured. The tissue thickness,  $Thickness_{PE}$ , between the double-layer PVDF WUS and bone is obtained by measuring the time-of-flight (TOF) of the round trip ultrasound reflected at the tissue-bone boundary,  $TOF_{PE}$ , as:

$$Thickness_{PE} = v_{st} \times \frac{TOF_{PE}}{2}, \quad (6.1)$$

where  $v_{st}$  is the average sound velocity assumed in soft tissue (1540 m/s).

**Figure 6.1** (b) shows the measurement configuration of the ultrasonic TT mode. In the TT mode, two double-layer PVDF WUSs are employed to measure the tissue thickness. One double-layer PVDF WUS serves as an ultrasonic transmitter, and the second double-layer PVDF WUS serves as an ultrasonic receiver. The transmitter WUS generates ultrasonic pulses that propagate through the soft tissue toward the receiver WUS. During muscle contraction, the tissue thickness between the two double-layer PVDF WUS is measured. The tissue thickness,  $Thickness_{TT}$ , between the transmitter and receiver WUSs is obtained

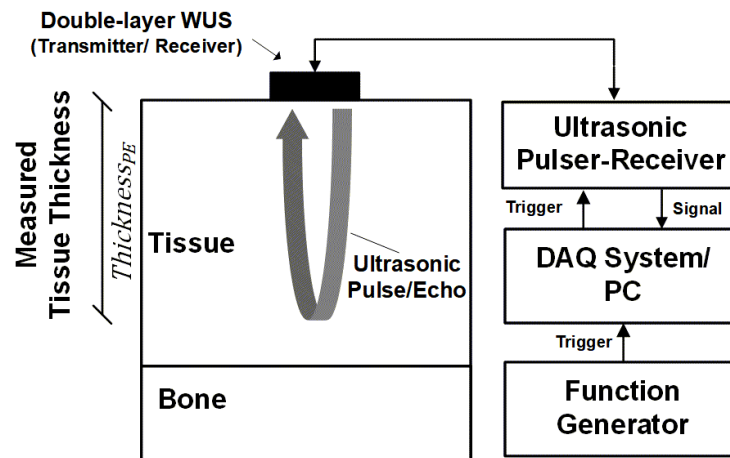
by measuring the TOF of the received ultrasound,  $TOF_{TT}$ , as:

$$Thickness_{TT} = v_{st} \times TOF_{TT} . \quad (6.2)$$

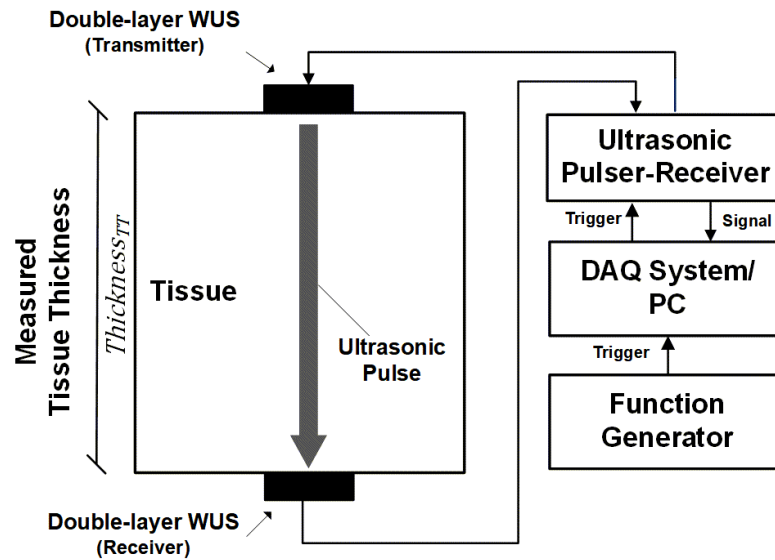
### 6.1.2 *In Vivo* Measurement Configuration

The double-layer PVDF WUS was attached to the skin at a location of interest by applying an ultrasonic gel couplant between the skin surface and the ultrasonic sensing area. In order to maintain the firmness of attachment to the skin surface during the measurement, the double-layer PVDF WUS and the electric wires were fixed with non-elastic adhesive tapes. Considerations were taken to prevent the applied adhesive tape from exerting pressure so that it would not impede the movements of the underlying tissues, including muscle contraction.

For both PE and TT modes, the double-layer PVDF WUS was operated by an ultrasonic pulser/receiver system (Model: DPR300, JSR Ultrasonics, Pittsford, NY, USA). The pulser/receiver system excites the double-layer PVDF WUS with an electric pulse of 300-400 V and 50-70 ns duration to generate an ultrasonic pulse [233]. The short excitation pulse is not perceptible on the skin due to the very low power (maximum of 304  $\mu$ J [233]) and the electrical grounding at the WUS-skin attachment side. The pulse repetition rate (PRR) of the ultrasonic pulser/receiver system was controlled by a function generator. The PPR was at 1.0 kHz for the measurements conducted in **Section 6.2.1**, **Section 6.2.2**, and **Section 6.3.1**, where it was at 0.2 kHz for the conducted measurement in **Section 6.3.2**. The received ultrasonic RF signals were filtered by the pulser/receiver's built-in analog band-pass filter of 1–22.5 MHz bandwidth. Then, the received ultrasonic RF signals were digitized at a sampling frequency of 125 MHz and stored by the data acquisition (DAQ) system (Model: ATS 9440, Alazartech, Montreal, QC, Canada) connected to a personal computer (PC). It is



(a)



(b)

**Figure 6.1:** Schematic diagram of *in vivo* measurement configuration using double-layer PVDF WUS in ultrasonic pulse-echo (PE) mode (a) and through-transmission (TT) mode (b).

noted that the sampling frequency of 125 MHz was the highest of the DAQ system employed, which was much higher than the Nyquist frequency of the received pulsed ultrasound since the real-time measurement was not the focus of this study.

For the preprocessing of the acquired ultrasonic RF signals, a moving average of 9 and 15 frames for PPR of 0.2 kHz and 1.0 kHz, respectively, were applied to the digitized RF signals to remove random noise and improve the SNR of the desired signals. The moving average of 15 frames at the PPR of 1 kHz and 9 frames at the PPR of 0.2 kHz were equivalent to the frame rate of 22.2 Hz and 66.7 Hz, respectively, which were multiple times greater than the maximum motion frequency of the conducted *in vivo* measurements. The frames with poor received ultrasound SNR ( $< 11$  dB) were considered an outliers and excluded from the thickness estimation of the conducted experiments. The outlier frames have a negligible effect on the monitored thickness changes due to the high PPR as the excluded frames accounted for less than 1% of the acquired frames. Thus, the motion smoothing effect on the measured tissue motion may be negligible.

**Figure 6.2** shows an example of the received ultrasonic RF pulses in the PE and TT modes in the relaxed ( $TOF_{PE} = 62.28 \mu\text{s}$  and  $TOF_{TT} = 74.95 \mu\text{s}$ ) and contracted ( $TOF_{PE} = 65.34 \mu\text{s}$  and  $TOF_{TT} = 77.98 \mu\text{s}$ ) states of the muscle indicated by the dashed lines and the solid lines, respectively. The received ultrasonic pulses were clearly observed in the acquired ultrasound RF signals. The TOFs of the ultrasonic pulses were obtained using the peak detection technique of the received ultrasonic pulse peak. The tissue thickness was then estimated by the equation given in **Eq. 6.1** for the PE mode and **Eq. 6.2** for the TT mode.

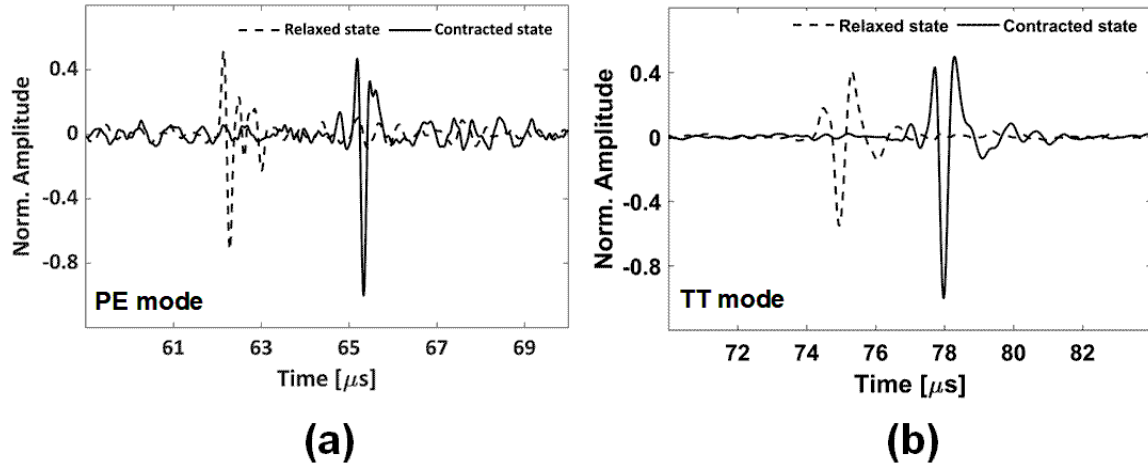


**Figure 6.2:** Examples of the received ultrasonic RF signals using the developed double-layer PVDF WUS in the PE mode (a) and TT mode (b). The dashed lines indicate a relaxed state of the measured skeletal muscle contraction, where the solid lines indicate a contracted state.

### 6.1.3 Muscle Contractile Parameters Extraction

The skeletal muscle is considered a near-constant volume system; therefore, muscle length changes due to contractions are paralleled by the changes in muscle thickness [46, 51]. The monitoring of muscle thickness changes during contractions would reflect the mechanical function of the muscle. The works of Burger et al. [234] and Valenčič and Knez [52] were earlier studies used to measure muscle thickness changes and assess the contractile properties using a high-precision displacement sensor, which later became known as tensiomyography (TMG) [113]. More recently, TMG (**Figure 6.3** (a)) and laser displacement sensor (LDS) (**Figure 6.3** (b)) have been commonly used methods to obtain the muscle mechanical response known as the contraction twitch displacement/time curve [31, 108, 113, 235]. Likewise, the ultrasonic measurement by the double-layer PVDF WUS can be employed in measuring the thickness changes due to muscle contraction and obtaining the thickness changes/time curve, as shown in **Figure 6.4**.

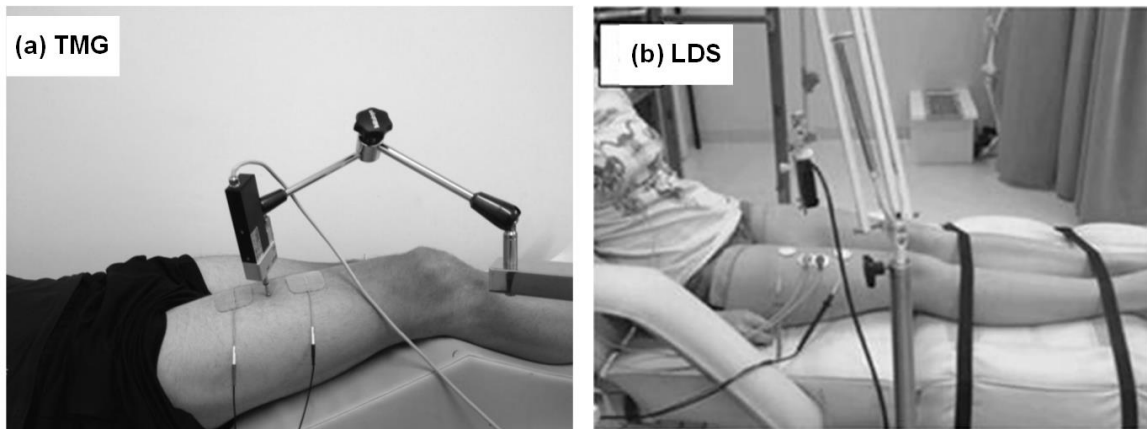


**Figure 6.3:** Photos of the tensiomyography (TMG) [30] (a) and laser displacement sensor (LDS) [31] (b) measurement methods.

The contractile properties of muscle can be assessed by analyzing the thickness changes/time curve and extracting the following parameters [46]: maximum thickness change ( $Th$ ), contraction time ( $Tc$ ), sustain time ( $Ts$ ), half-relaxation time ( $Tr$ ), and contraction velocity ( $Vc$ ).  $Th$  represents the relative maximum thickness changes during the contraction twitch of the muscle expressed in millimeters.  $Tc$  indicates the time elapsed from 10% of  $Th$  until 90% of  $Th$ . The parameter of  $Ts$  represents the time which the contraction is sustained and is calculated by measuring the time between the moment when  $Th$  50% during the ascending (contracting) phase, and the moment when  $Th$  returns to 50% during the descending (relaxing) phase.  $Tr$  indicates the time elapsed from 90% of  $Th$  until 10% of  $Th$  during the relaxing phase.  $Vc$  represents the rate of contraction given by:  $Vc = (90\% Th - 10\% Th) / Tc$ . **Table 6.1** lists the definition of the contractile parameters used in this thesis work. The time parameters ( $Tc$ ,  $Ts$ , and  $Tr$ ) are expressed in milliseconds where the  $Vc$  is expressed in millimeter per second.

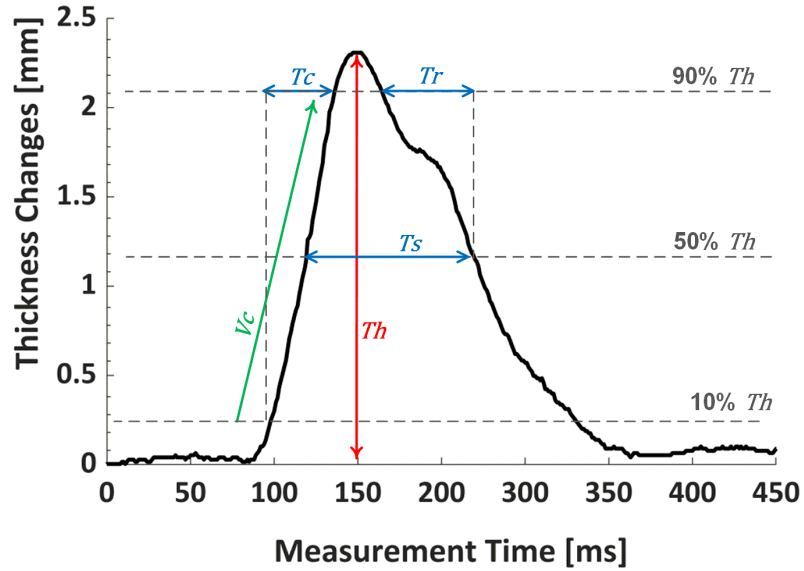


**Figure 6.4:** Example of the thickness changes/time curve of a single contraction twitch obtained by double-layer PVDF WUS and the contractile parameters.

**Table 6.1:** Definition of contractile parameters.

Parameter	Definition	Unit
Maximum thickness changes ( $Th$ )	Maximum thickness change of a contraction twitch curve	mm
Contraction time ( $Tc$ )	Time between 10% and 90% of $Th$ in ascending phase	ms
Sustain time ( $Ts$ )	Time between 50% of $Th$ on ascending and descending phases	ms
Half-relaxation time ( $Tr$ )	Time between 90% and 50% of $Th$ in descending phase	ms
Contraction velocity ( $Vc$ )	Rate of $Th$ between 10% and 90% relative to $Tc$	mm/s

## 6.2 Performance Evaluation

This section presents the *in vivo* performance evaluation of skeletal muscle contraction. It evaluates and validates the double-layer PVDF WUS in measuring the contractile parameters of skeletal muscle in comparison with the LDS method. **Section 6.2.1** compares the difference between the double-layer PVDF WUS and LDS measurements. **Section 6.2.2** evaluates the motion artifact effect on the double-layer PVDF WUS and LDS measurements.

### 6.2.1 Comparative Study of Double-Layer PVDF WUS and LDS

The objective of the *in vivo* experimental evaluation conducted in this section is to compare the double-layer PVDF WUS ability with the LDS in measuring the skeletal muscle evoked contractions. The electrically-evoked muscle contractions were monitored using LDS, as one of the current mechanomyography (MMG) measurement sensors, and the developed double-layer PVDF WUS to compare the extracted muscle contractile parameters obtained by the two methods employed.

The LDS and TMG have been favored for the assessment of the contractile parameters of muscle contraction among the current measurement methods [31, 46, 106–112]. LDS, as described in the literature review in **Chapter 2**, is a non-contact method that measures the displacement at the skin surface due to muscle thickness changes during contraction. On the contrary, the TMG method employs a contact displacement sensor where the sensor tip is pressed on the skin surface with a controlled pre-tension to measure the displacement during muscle contraction. Therefore, the non-contact LDS can be used to measure muscle contraction simultaneously with the ultrasonic measurement of the double-layer PVDF WUS. The LDS and double-layer PVDF WUS can be compared in obtaining relative thickness

changes due to muscle contraction. LDS provides high accuracy up to  $\pm 2.2 \mu\text{m}$  within the measurement range [236], and has been employed as a reference measurement method to compare with other methods of interest [100, 237–239].

In this experimental evaluation, the tissue thickness changes due to the electrically-evoked biceps muscle contractions in the left upper arm of a healthy male subject were measured using the LDS and double-layer PVDF WUS in the PE mode simultaneously. The biceps muscle was chosen due to its accessibility to obtain the relative thickness changes by both the double-layer PVDFWUS and LDS simultaneously. The biceps muscle contraction was electrically-evoked by an electrical muscle stimulator (EMS) (Model: EMS 7500, Compass Health, Middleburg Heights, OH, USA) at an EMS pulse repetition frequency of 2 Hz. The double-layer PVDF WUS was attached to the front (anterior) side of the upper arm at the biceps muscle, as shown in **Figure 6.5** of the experimental setup. The LDS (Model: CL-P070, Keyence, Osaka, Japan) was placed on a support fixture so that the laser beam pointed perpendicular to the backside of the double-layer PVDF WUS in the middle of the active ultrasonic area. The subject was sitting on a chair with his left arm extended over the experiment table. To minimize the motion artifact, the measurement was conducted under the static contraction (isometric contraction) of the biceps. Additionally, the subject was asked to relax his arm and remain still during the measurement.

**Figure 6.6** (a) shows the measured tissue thickness by the LDS and double-layer PVDF WUS during the electrically-evoked contraction of the biceps muscle. The biceps contractions were electrically-evoked four times, and each stimulation lasted for  $5.86 \pm 1.87$  seconds separated by  $6.78 \pm 3.3$  seconds intervals. The EMS power level was adjusted to evoke the isometric contraction and to the comfort level of the human subject. The measurement time was segmented into four groups (S1, S2, S3, and S4) corresponding to the stimulation periods of the EMS, where the resting intervals were segmented into five groups (R1, R2,

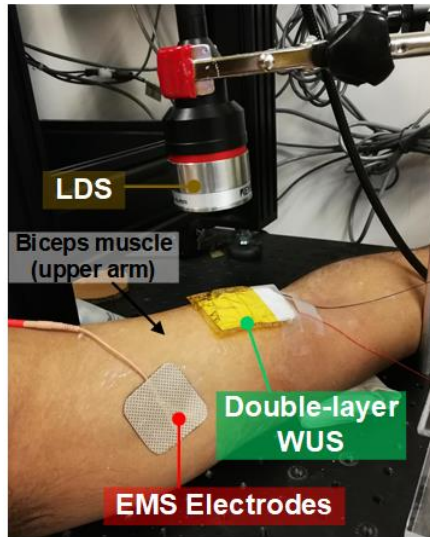
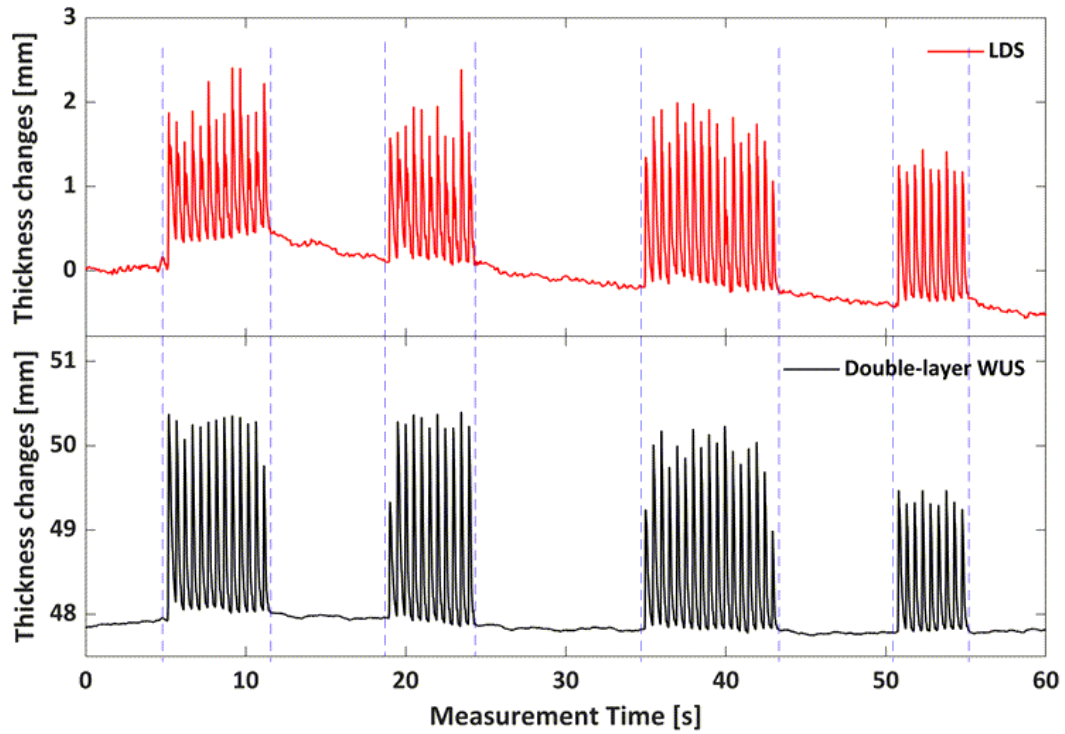
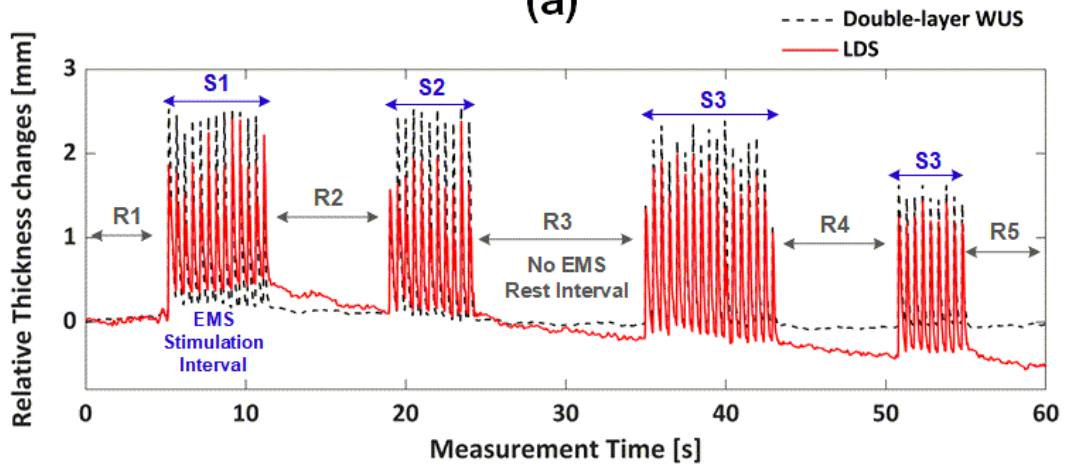


**Figure 6.5:** Photo of the experimental setup for monitoring the electrically-evoked contractions of the biceps muscle using the LDS and the double-layer PVDF WUS in ultrasonic PE mode. The double-layer PVDF WUS and electrical muscle stimulator (EMS) electrodes were attached to the skin surface of the upper arm while the LDS was placed on a support fixture.

R3, R4, and R5) corresponding to the periods where no EMS was applied, as shown in **Figure 6.6**. The contractile parameters ( $Th$ ,  $Tc$ ,  $Ts$ ,  $Tr$ , and  $Vc$ ) in each single contraction twitch were extracted from the thickness changes obtained by the LDS and double-layer PVDF WUS. **Figure 6.7** shows the multiple twitches in each stimulation interval with indication of 0%, 10%, 50%, 90%, and 100% of the maximal thickness changes,  $Th$ , from which the contractile parameters ( $Tc$ ,  $Ts$ ,  $Tr$ , and  $Vc$ ) were extracted. The first two twitches and last two twitches in each stimulation interval were excluded from the extraction of contractile parameters due to the instability of the EMS power level during the manual on/off switching. The same EMS power level was applied in the simulation intervals S1, S2, and S3 in **Figure 6.7** (a), (b), and (c), while the EMS level was intentionally reduced for the S4 stimulation interval in **Figure 6.7** (d). However, a slight EMS power difference between S1, S2, and S3 was expected due to the manual adjustment of EMS.



(a)



(b)

**Figure 6.6:** Tissue thickness changes, measured by the LDS and double-layer PVDF WUS (in PE mode), due to the electrically-evoked contraction of the biceps muscle at EMS frequencies of 2 Hz (a). The comparison of the thickness changes between the LDS and double-layer PVDF WUS measurements with indications of the stimulation and rest intervals (b).

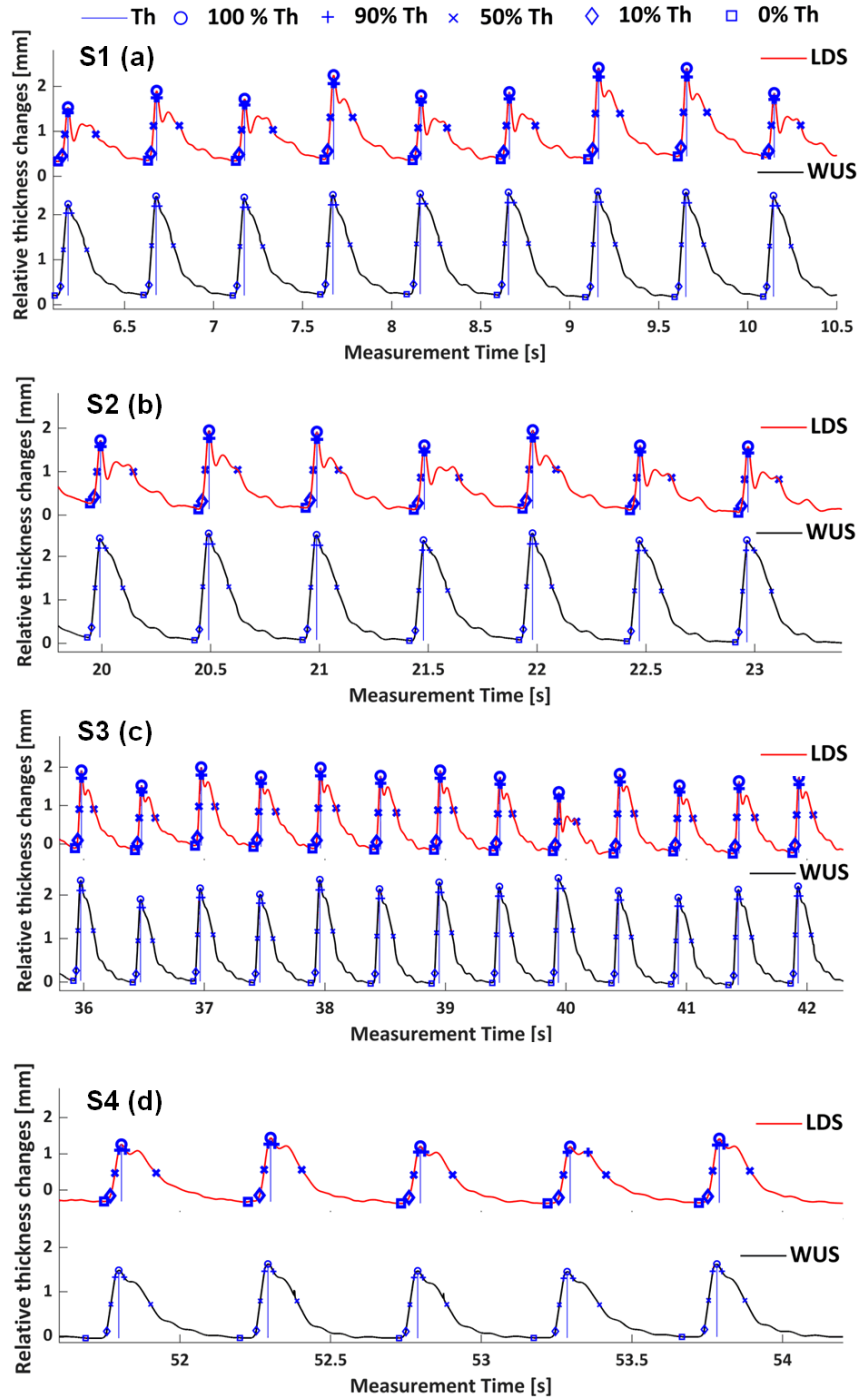


**Figure 6.7:** Contractile parameter of  $Th$  extracted from the individual twitch using the thickness changes measured by the LDS and double-layer PVDF WUS in S1 (a), S2 (b), S3 (c), and S4 (d). The 0%, 10%, 50%, 90%, and 100% of  $Th$  were indicated.

**Table 6.2:** Mean values  $\pm$  standard deviation (SD) and coefficient of variation (CV) of the contractile parameters from the monitored electrically-evoked contractions of the biceps muscle using the LDS and double-layer PVDF WUS showed in **Figure 6.7**.

	Extracted Parameters Mean $\pm$ SD (CV)							
	Laser Displacement Sensor				Double-layer PVDF WUS			
	S1	S2	S3	S4	S1	S2	S3	S4
<b><i>Th</i> (mm)</b>	1.60 $\pm$ 0.29 (18.1%)	1.61 $\pm$ 0.17 (10.6%)	1.91 $\pm$ 0.17 (8.9%)	1.65 $\pm$ 0.11 (6.7%)	2.23 $\pm$ 0.09 (4.0%)	2.37 $\pm$ 0.07 (3.0%)	2.18 $\pm$ 0.15 (6.9%)	1.57 $\pm$ 0.08 (5.1%)
<b><i>Tc</i> (ms)</b>	25.31 $\pm$ 0.59 (2.3%)	24.05 $\pm$ 0.53 (2.2%)	25.10 $\pm$ 0.73 (2.9%)	28.45 $\pm$ 0.45 (1.6%)	31.84 $\pm$ 0.97 (3.0%)	31.88 $\pm$ 0.49 (1.5%)	29.01 $\pm$ 1.06 (3.7%)	27.36 $\pm$ 0.46 (1.7%)
<b><i>Ts</i> (ms)</b>	153.27 $\pm$ 18.32 (12.0%)	149.79 $\pm$ 21.88 (14.6%)	138.01 $\pm$ 11.52 (8.3%)	131.05 $\pm$ 7.02 (5.4%)	126.80 $\pm$ 4.78 (3.8%)	124.69 $\pm$ 7.07 (5.7%)	131.37 $\pm$ 5.00 (3.8%)	126.02 $\pm$ 5.95 (4.7%)
<b><i>Tr</i> (ms)</b>	128.41 $\pm$ 20.22 (15.7%)	126.53 $\pm$ 22.83 (18.0%)	110.08 $\pm$ 12.83 (11.7%)	85.97 $\pm$ 15.99 (18.6%)	81.20 $\pm$ 2.95 (3.6%)	77.50 $\pm$ 3.36 (4.3%)	87.61 $\pm$ 3.83 (4.4%)	82.03 $\pm$ 5.45 (6.6%)
<b><i>Vc</i> (mm/s)</b>	50.39 $\pm$ 8.72 (17.3%)	53.57 $\pm$ 4.63 (8.6%)	60.83 $\pm$ 5.88 (9.7%)	46.32 $\pm$ 3.27 (7.1%)	56.01 $\pm$ 3.48 (6.2%)	59.47 $\pm$ 2.67 (4.5%)	60.29 $\pm$ 4.24 (7.0%)	46.00 $\pm$ 2.33 (5.1%)

The periodical contraction twitches measured by the LDS and double-layer PVDF WUS were observed at the frequency of  $2.02 \pm 0.02$  Hz, which corresponded to the applied EMS frequency of 2 Hz. The average contractile parameters obtained from the multiple contraction twitches of each stimulation interval (S1, S2, S3, and S4) are listed in **Table 6.2**. The coefficient of variation, CV, in percentage ( $CV = \text{Mean} / \text{SD} \times 100$ ) is also presented for each contractile parameter in **Table 6.2**.

The ***Th*** obtained by the double-layer PVDF WUS showed lower CV values in the range of 3.0 – 6.9% for the multiple contraction twitches than the ***Th*** obtained by the LDS whose CV values are in the range of 6.7 – 18.1%. **Figure 6.8** (a), (b), (c), and (d) show the ***Th*** values for the comparison between the double-layer PVDF WUS and LDS. It can be noted that the difference in the average ***Th*** parameter between the LDS and double-layer PVDF WUS was inconsistent between the stimulation groups given by percentage difference ( $\% \Delta = \text{difference} / \text{mean} \times 100$ ) of 32.9%, 38.2%, 13.2%, and 5% for S1, S2, S3, and S4, respectively. This may be due to the high variability of the ***Th*** values obtained by the LDS as

the larger difference of 32.9% and 38.2% for S1 and S2 corresponds to the LDS CV values 18.1% and 10.6%, respectively. In addition, the LDS showed a variation of thickness changes among the rest intervals R1 – R5 by an average of  $\pm 0.26$  mm, while the double-layer PVDF WUS had less thickness changes during the rest intervals ( $\pm 0.08$  mm). The higher variation of measured thickness changes by LDS during the rest intervals may indicate the presence of motion artifact, which might affect the estimation of the maximum thickness changes. Furthermore, a reduction in  $Th$  was observed with the double-layer PVDF WUS for the S4 group by approximately 0.69 mm (36%) compared to the average  $Th$  of S1 – S3 since S4 was subjected to a lower EMS power level. The reduction of  $Th$  was not observed with LDS, as shown in **Figure 6.8** (e).

**Figure 6.9** shows the  $Tc$  variation comparison plots between the double-layer PVDF WUS and LDS obtained from the multiple contraction twitches and the line graphs of mean  $\pm$  SD  $Tc$  values of the stimulation intervals. The double-layer PVDF WUS measurement demonstrated longer  $Tc$  than the LDS except for the S4 interval, where LDS was slightly longer. LDS and double-layer PVDF WUS both demonstrated a low variability of 3.7% or less for  $Tc$  parameter. The difference in the mean  $Tc$  values between LDS and double-layer PVDF WUS was higher for the S1 (22.9%) and S2 (28%) intervals than the S3 (14.5%) and S4 (3.9%) intervals. The double-layer PVDF WUS mean  $Tc$  of S3 and S4 showed a shorter time by 9.4% and 15.2%, respectively, compared to the average  $Tc$  for S1 and S2. In contrast, the LDS mean  $Tc$  for S4 was longer by 13.6% than the  $Tc$  average of S1, S2, and S3, as shown in **Figure 6.9** (e).

**Figure 6.10** shows the  $Ts$  variation comparison plots between the double-layer PVDF WUS and LDS obtained from the multiple contraction twitches and the line graphs of mean  $\pm$  SD  $Ts$  values of the stimulation intervals. The double-layer PVDF WUS demonstrated lower variability of the obtained  $Ts$  from the stimulation intervals S1 – S4 given by the

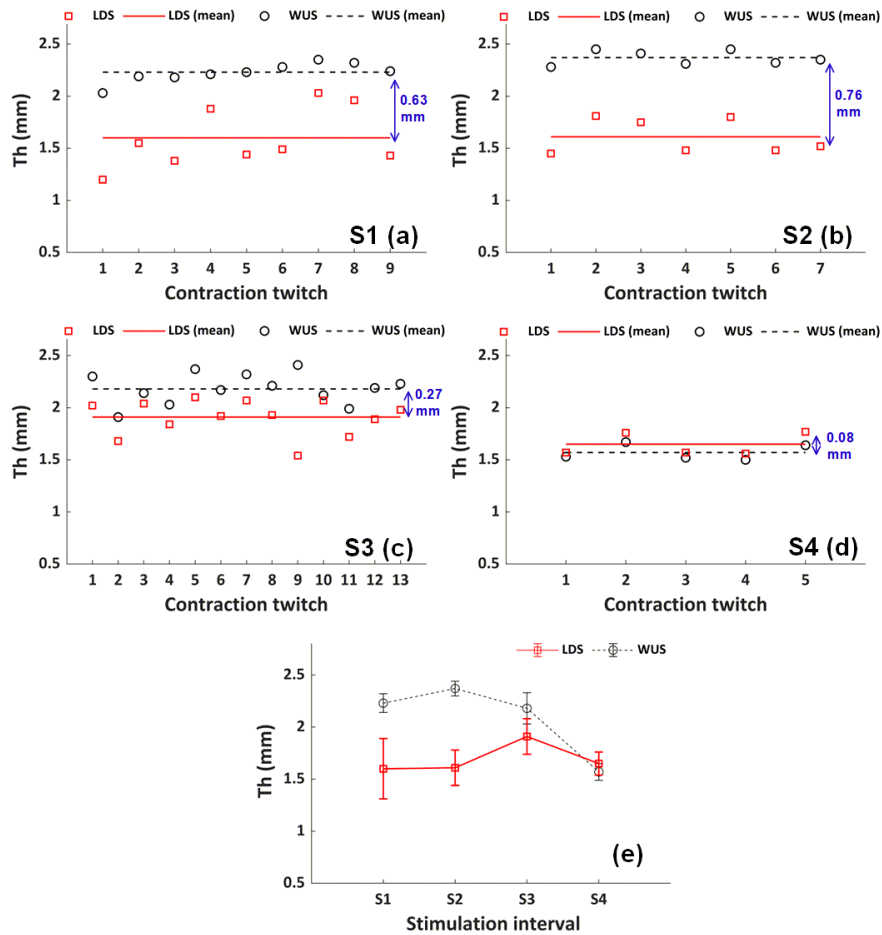


**Figure 6.8:**  $Th$  variation plots for comparison between the double-layer PVDF WUS and LDS obtained from the multiple contraction twitches of the S1 (a), S2 (b), S3 (c), and S4 (d) intervals. Line graphs of mean  $\pm$  SD  $Th$  values for each interval (e).

CV values range of 3.8 – 5.7%, while LDS demonstrated CV ranging from 2.9 – 12% for  $Ts$ . The LDS measurement showed longer  $Ts$  than double-layer PVDF WUS by (18.9%), (18.3%), (4.9%), and (3.9%) for the S1, S2, S3, and S4 stimulation groups, respectively. The difference between the S1, S2, S3, and S4 for the  $Tc$  mean values of the double-layer PVDF WUS was 5.2% or less. In contrast, LDS demonstrated shorter  $Ts$  for S3 and S4 by 9% and 14.5%, respectively, to the average  $Ts$  obtained for S1 and S2, as shown in **Figure 6.10** (e).

**Figure 6.11** shows the  $Tr$  variation comparison plots between the double-layer PVDF

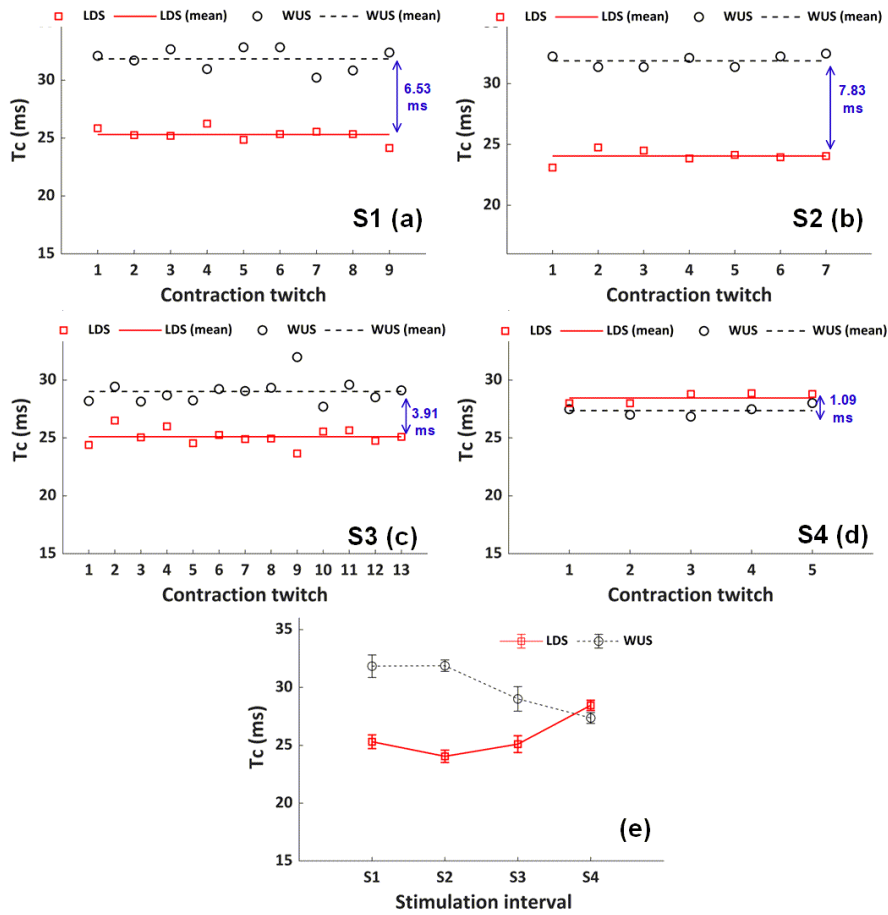


**Figure 6.9:**  $T_c$  variation plots of comparison between the double-layer PVDF WUS and LDS obtained from the multiple contraction twitches of the S1 (a), S2 (b), S3 (c), and S4 (d) intervals. Line graphs of mean  $\pm$  SD  $T_c$  values for each interval (e).

WUS and LDS obtained from the multiple contraction twitches and the line graphs of mean  $\pm$  SD  $T_r$  values of the stimulation intervals. The double-layer PVDF WUS demonstrated lower variability of the obtained  $T_r$  from the stimulation intervals S1 – S4 given by the CV values range of 3.6 – 6.6%, while LDS demonstrated higher variability with CV values ranging from 11.7 – 18.6% for  $T_s$ . The LDS measurement obtained longer  $T_r$  than double-layer PVDF WUS by 45%, 48.1%, 22.7%, and 4.7% for the S1, S2, S3, and S4 stimulation intervals, respectively. For the double-layer PVDF WUS, S2 showed the shortest  $T_r$  by 5.2%

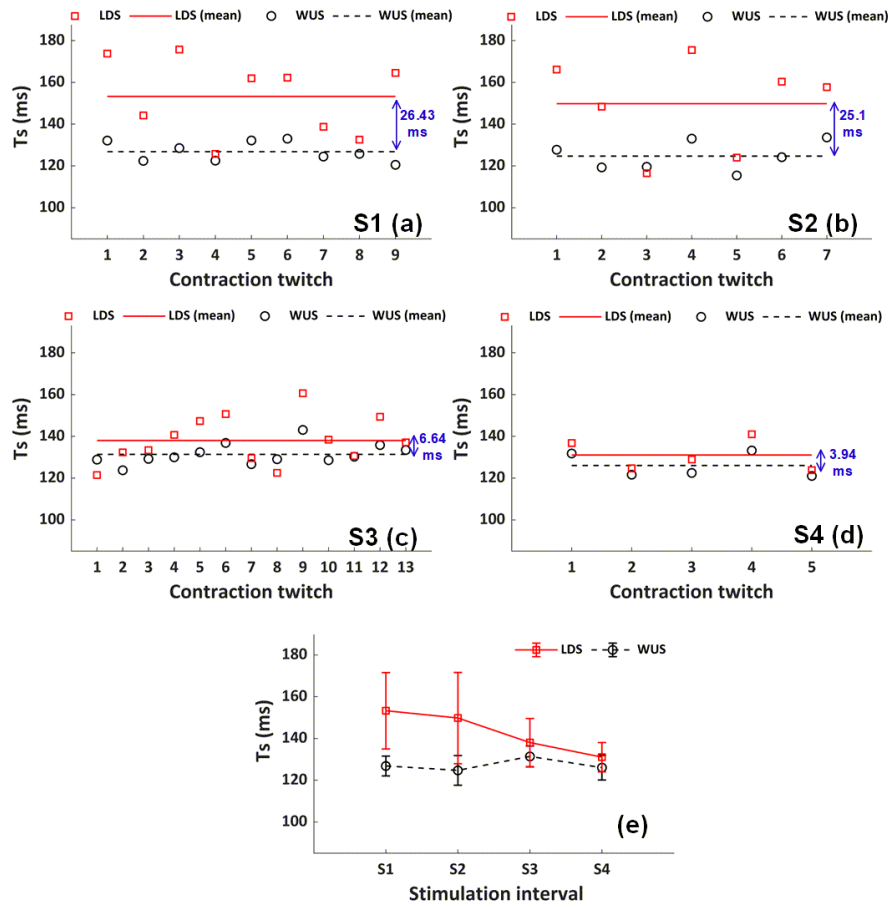


**Figure 6.10:**  $T_s$  variation plots for comparison between the double-layer PVDF WUS and LDS obtained from the multiple contraction twitches of the S1 (a), S2 (b), S3 (c), and S4 (d) intervals. Line graphs of mean  $\pm$  SD  $T_s$  values for each interval (e).

and S3 showed the longest  $Tr$  by 7.1% compared to the average  $Tr$  of S1 and S3 in which they have a very close  $Tr$  given by a difference of 1%. For LDS, S1 and S2 demonstrated the longest  $Tr$  where S3 and S4 have shorter  $Tr$  by 14.6% and 38.9%, respectively, as shown in **Figure 6.10** (e).

**Figure 6.12** shows the  $Vc$  variation comparison plots between the double-layer PVDF WUS and LDS obtained from the multiple contraction twitches and the line graphs of mean  $\pm$  SD  $Vc$  values of the stimulation intervals. The double-layer PVDF WUS demonstrated

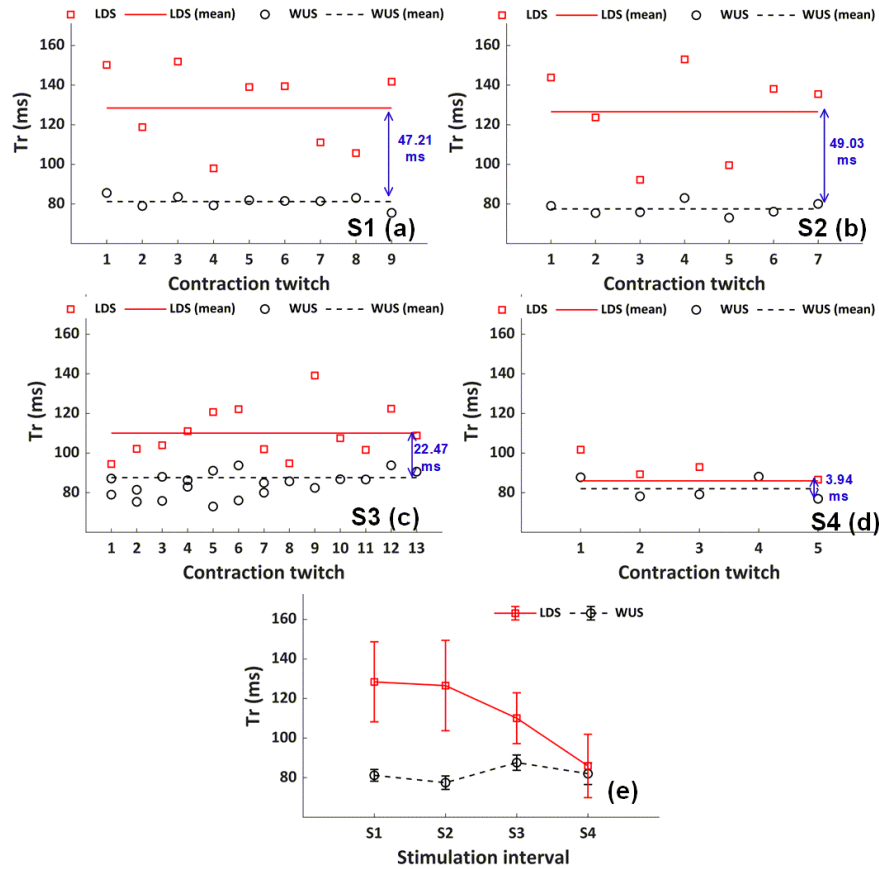


**Figure 6.11:**  $Tr$  variation plots for comparison between the double-layer PVDF WUS and LDS obtained from the multiple contraction twitches of the S1 (a), S2 (b), S3 (c), and S4 (d) intervals. Line graphs of mean  $\pm$  SD  $Tr$  values for each interval (e).

lower variability with  $Vc$  given by the CV values range of 3.6 – 6.6% for the stimulation intervals S1 – S4, while LDS demonstrated higher variability with CV values ranging from 7.1 – 17.3%. The double-layer PVDF WUS obtained faster mean  $Vc$  than LDS for S1 and S2 by approximately 10.5%, whilst both methods obtained similar mean values for S3 and S4 by a difference less than 1%. It can be observed from the  $Vc$  mean values obtained by the double-layer PVDF WUS that S4 has the slowest contraction velocity by 19% compared to S1, which has lowest value among S2 (6%) and S3 (7.4%), as shown in **Figure 6.12** (e).

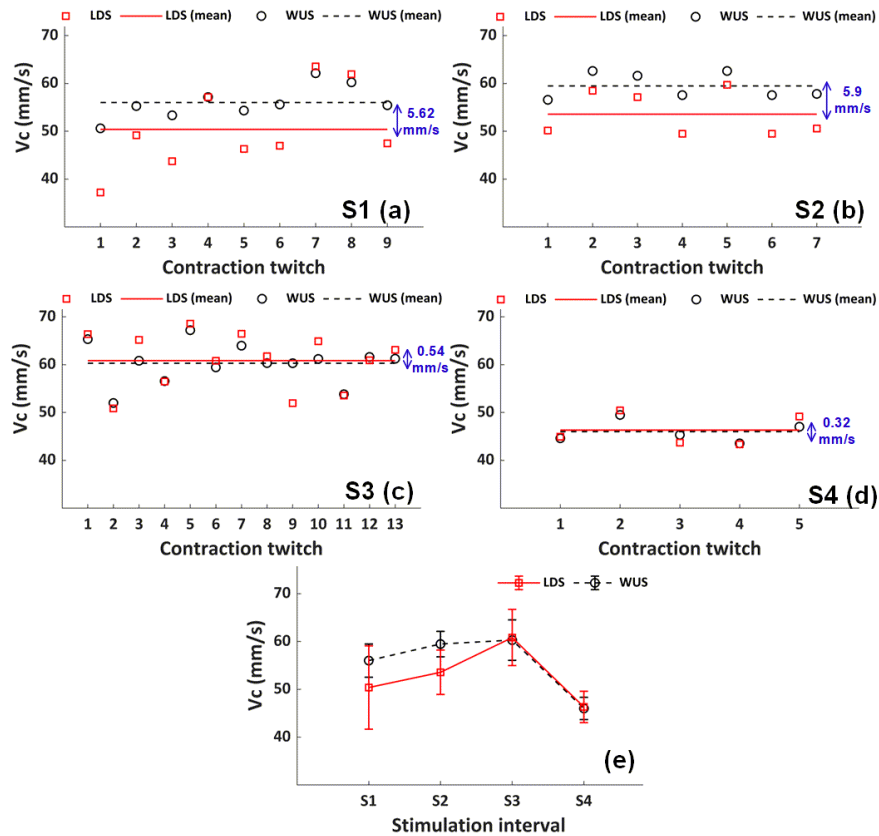


**Figure 6.12:**  $V_c$  variation plots for comparison between the double-layer PVDF WUS and LDS obtained from the multiple contraction twitches of the S1 (a), S2 (b), S3 (c), and S4 (d) intervals. Line graphs of mean  $\pm$  SD  $V_c$  values for each interval (e).

## 6.2.2 Influence of Motion Artifact on Measurement Variability

The objective of the *in vivo* experiment conducted in this section is to investigate the effect of motion artifact on the double-layer PVDF WUS measurement in comparison to the LDS measurement for the extraction of the skeletal muscle contractile parameters. The experiment was conducted with the same experimental configuration shown in **Figure 6.5** and the subject in **Section 6.2.1**. The biceps muscle contraction in the right forearm was electrically-evoked by the EMS at a frequency of 2 Hz. Additionally, a body limb motion was intentionally

induced during the measurement in order to investigate the motion artifact influence on the measurement by assessing the variability of the muscle contractile parameters extracted from the WUS and LDS methods employed. To induce the motion artifact, the subject was asked to perform repetitive elbow flexion-extension (bending the elbow from 0° to about 140°) of the right forearm (non-measured forearm) approximately every one second during the measurement, which introduced a global motion of the right forearm measured.

**Figure 6.13** shows the changes in tissue thickness obtained during the electrically-evoked biceps muscle contraction with the induced motion artifact. The substantial deformation due to the motion artifact can be clearly observed in the monitored muscle contraction using LDS, causing the difficulty in identifying the distorted multiple contraction twitches. In contrast, the multiple contraction twitches can be clearly identified in the monitored muscle contraction using the double-layer PVDF WUS. The high contamination of the LDS measurement by the induced motion artifact imposed difficulty in extracting the contractile parameters. Nevertheless, the same method of extracting the contractile parameters was applied to both tissue thickness changes obtained by the LDS and double-layer PVDF WUS in order to assess the effect of the induced motion artifact quantitatively. The contractile parameters were extracted based on finding the maximal thickness observed for each twitch, denoted by the circle mark in **Figure 6.14**.

**Table 6.3** lists the mean values  $\pm$  SD and CV of the contractile parameters extracted from the monitored electrically-evoked contractions of the biceps muscle with the induced motion artifact using the double-layer PVDF WUS and LDS shown in **Figure 6.14**. The LDS measurement demonstrated greater CV values of the extracted contractile parameters among the multiple contraction twitches than the double-layer PVDF WUS, especially for the  $Tc$ ,  $Ts$ , and  $Tr$  parameters, where the CV values ranged from 22.8% to 82%. In contrast, the double-layer PVDF WUS measurement maintained a smaller variability with CV values

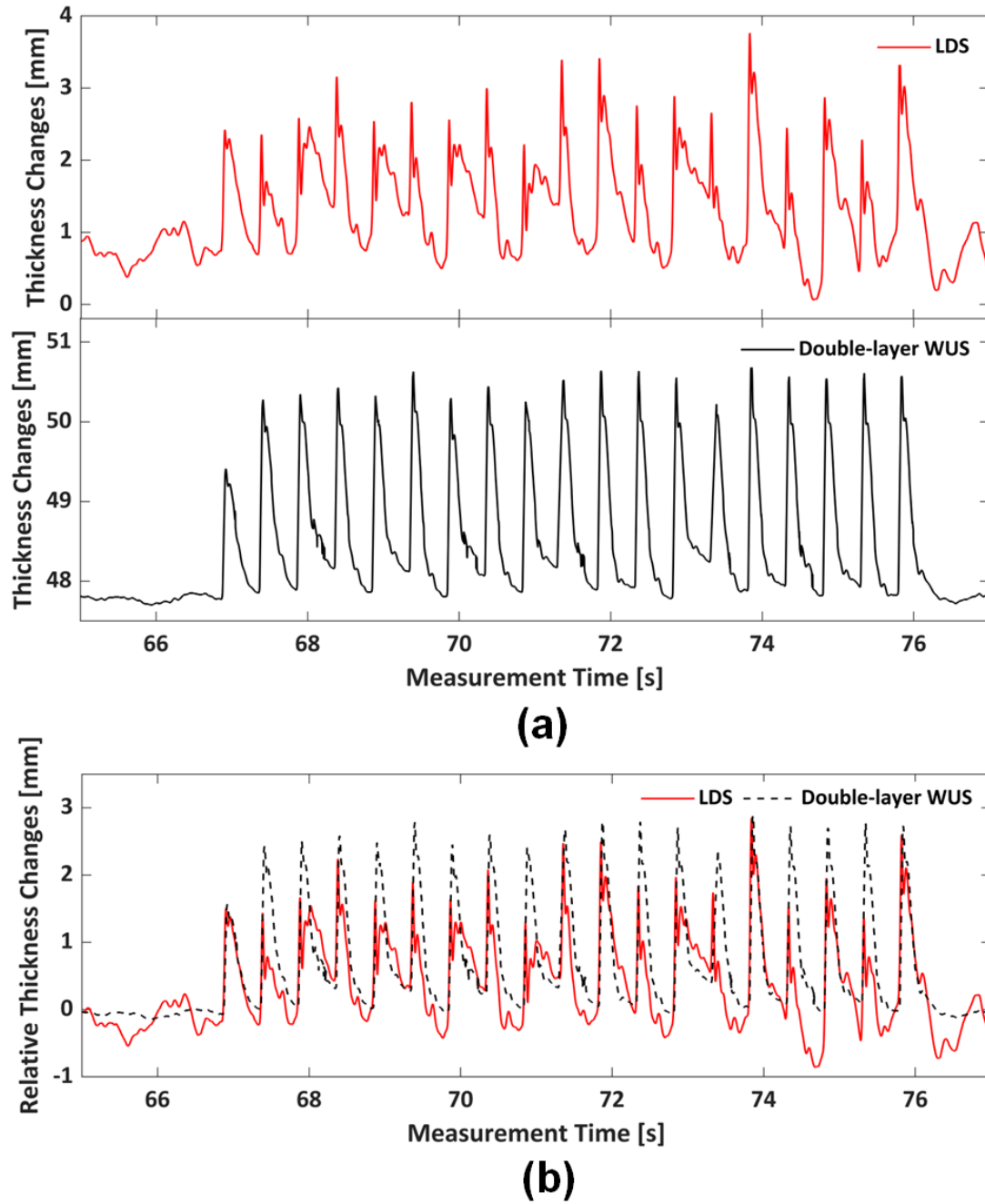


**Figure 6.13:** Tissue thickness changes, measured by the LDS and double-layer PVDF WUS (PE mode), due to the electrically-evoked contraction of the biceps muscle at EMS frequency of 2 Hz during an induced motion artifact (a). The comparison of the thickness changes between LDS and double-layer PVDF WUS measurements (b).

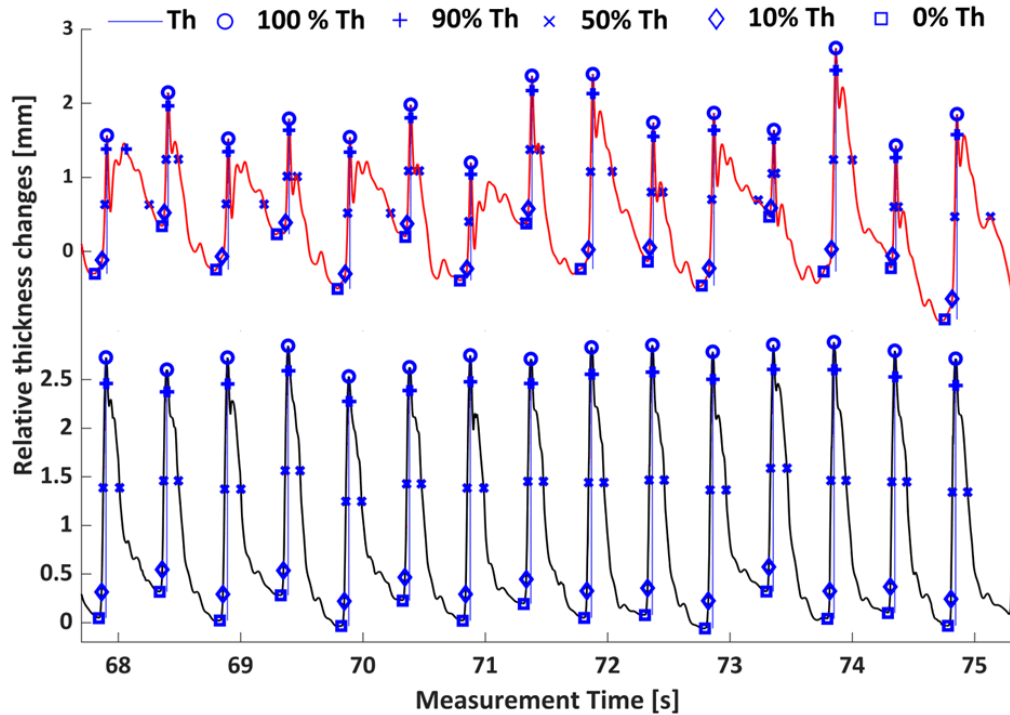


**Figure 6.14:** Contractile parameter of  $Th$  extracted from the individual twitch using the thickness changes measured by the LDS and double-layer PVDF WUS with the induced motion artifact in **Figure 6.13** measured. The 0%, 10%, 50%, 90%, and 100% of  $Th$  were indicated.

of 8.5% or less. **Figure 6.15** shows the comparison of the contractile parameters variation between the double-layer PVDF WUS and LDS.

**Table 6.4** compares between the CV values of the contractile parameters with (**Table 6.3**) and without (**Table 6.2**) the induced motion artifact. The LDS measurement showed an increase in the CV values with the induced motion artifact in comparison to those obtained in the experiment without the induced motion in **Section 6.2.1**. The greater CV of the contractile parameters using the LDS measurement indicates that the LDS is highly susceptible to the motion artifact induced by body/limb movement. On the contrary, the double-layer PVDF WUS maintained low variability ( $CV < 8.5\%$ ) even with the induced motion artifact, comparable to the CV values without the induced body/limb movement.

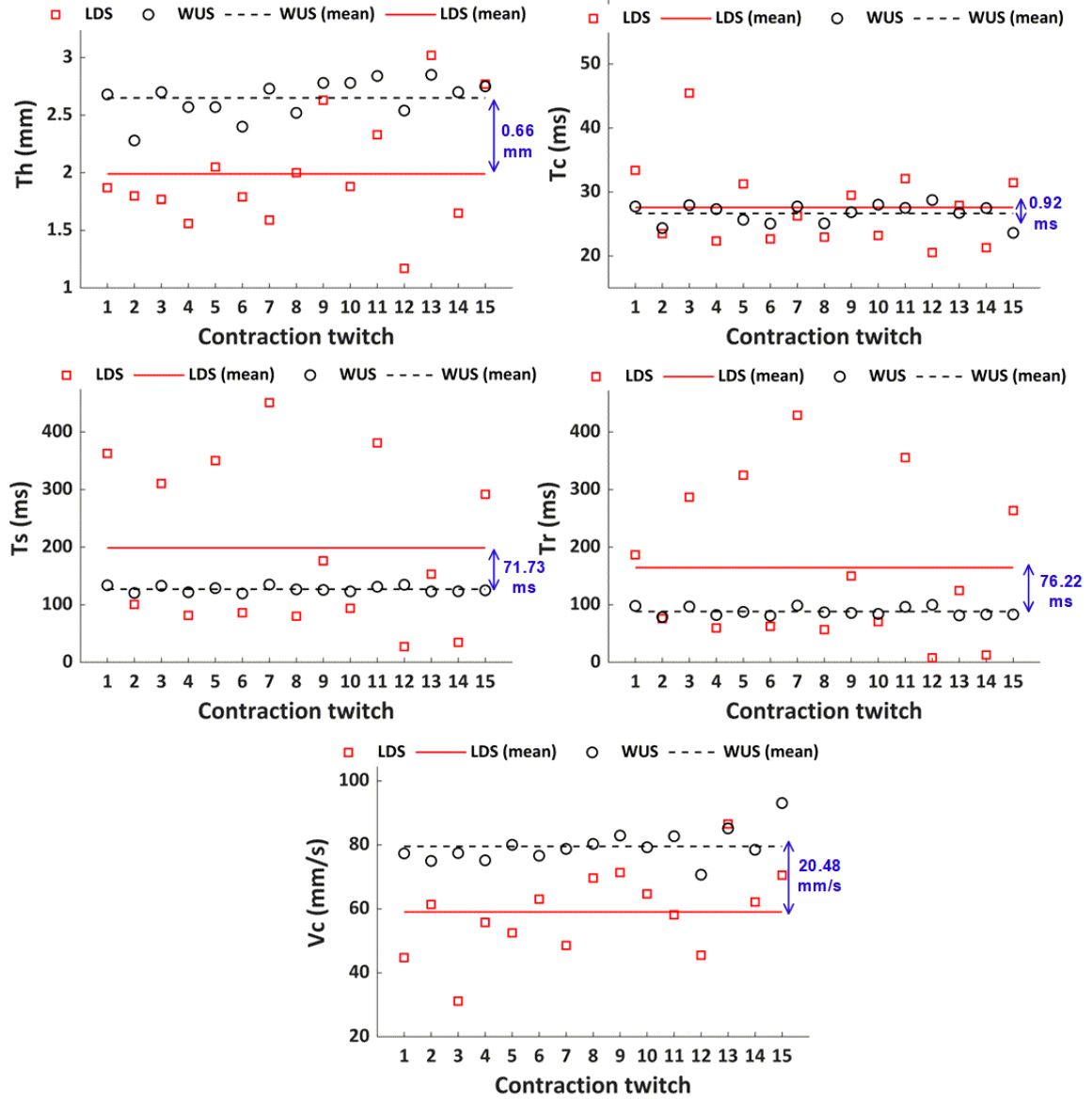


**Figure 6.15:** Contractile parameters variation plots for comparison between the double-layer PVDF WUS and LDS obtained from the multiple contraction twitches of the electrically-evoked biceps muscle contraction with induced motion artifact

**Table 6.3:** Mean values  $\pm$  SD (CV) of the contractile parameters obtained from the monitored electrically-evoked contractions of biceps muscle with induced motion artifact using the double-layer PVDF WUS and LDS showed in **Figure 6.14**.

Extracted Parameters Mean $\pm$ SD (CV)		
	LDS	Double-layer PVDF WUS
<i>Th</i> (mm)	1.99 $\pm$ 0.50 (25.1%)	2.65 $\pm$ 0.16 (6.0%)
<i>Tc</i> (ms)	27.58 $\pm$ 6.58 (23.9%)	26.66 $\pm$ 1.53 (5.7%)
<i>Ts</i> (ms)	198.78 $\pm$ 143.39 (72.1%)	127.05 $\pm$ 5.31 (4.2%)
<i>Tr</i> (ms)	164.50 $\pm$ 135.30 (82.2%)	88.28 $\pm$ 7.50 (8.5%)
<i>Vc</i> (mm/s)	59.04 $\pm$ 13.49 (22.8)%	79.52 $\pm$ 5.17 (6.5%)

## 6.3 *In Vivo* Demonstration

This section presents the *in vivo* monitoring of the skeletal muscle tetanic and dynamic contractions. It demonstrates the double-layer PVDF WUS capability in the quantitative assessment of the skeletal muscle tetanic contraction progression and voluntary contractions during dynamic muscle action. **Section 6.3.1** demonstrates the monitoring of an electrically-evoked tetanic contraction of the gastrocnemius (GC) muscle. **Section 6.3.2** demonstrates the assessment of the voluntary activation of the biceps muscle during dynamic contractions.

### 6.3.1 Skeletal Muscle Tetanic Contraction Progression

The muscle contraction is controlled by the number of recruited motor units (MU) and their firing frequency. The summation of the muscle contraction twitches caused by the increase in the firing frequency is known as a tetanic contraction (tetanus) [34, 240]. The muscular activities of the human body often exhibit some level of tetanic contractions to

**Table 6.4:** CV values of the contractile parameters from the monitored electrically-evoked contractions of biceps muscle with and without induced motion artifact using the double-layer PVDF WUS and LDS.

		No motion artifact				Induced motion artifact
		S1	S2	S3	S4	
LDS	<b><i>Th</i> (mm)</b>	18.1%	10.6%	8.9%	6.7%	25.1%
	<b><i>Tc</i> (ms)</b>	2.3%	2.2%	2.9%	1.6%	23.9%
	<b><i>Ts</i> (ms)</b>	12.0%	14.6%	8.3%	5.4%	72.1%
	<b><i>Tr</i> (ms)</b>	15.7%	18.0%	11.7%	18.6%	82.2%
	<b><i>Vc</i> (mm/s)</b>	17.3%	8.6%	9.7%	7.1%	22.8%
Double-layer PVDF WUS	<b><i>Th</i> (mm)</b>	4.0%	3.0%	6.9%	5.1%	6.0%
	<b><i>Tc</i> (ms)</b>	3.0%	1.5%	3.7%	1.7%	5.7%
	<b><i>Ts</i> (ms)</b>	3.8%	5.7%	3.8%	4.7%	4.2%
	<b><i>Tr</i> (ms)</b>	3.6%	4.3%	4.4%	6.6%	8.5%
	<b><i>Vc</i> (mm/s)</b>	6.2%	4.5%	7.0%	5.1%	6.5%

maintain posture or to produce movement. The tetanic contractions of a muscle can also be induced by electrical stimulation. The quantitative assessment of a tetanic progression could be useful for various medical applications. Therefore, the double-layer PVDF WUS was applied for the tetanic contraction monitoring. The tetanic progression was quantified using the fusion index (IF) parameter. Additionally, the contractile parameters at several electrical stimulation frequencies were measured. In this conducted *in vivo* demonstration, the tissue thickness changes due to GC muscle contractions evoked by the EMS in the lower leg of a healthy male subject were measured using the double-layer PVDF WUSs in the ultrasonic TT mode. As shown in **Figure 6.16** of the experimental setup, the transmitter double-layer PVDF WUS was attached to the medial side of the GC muscle at the back of the tibia and

fibula bones, whereas the receiver double-layer PVDF WUS was placed on the opposite side.

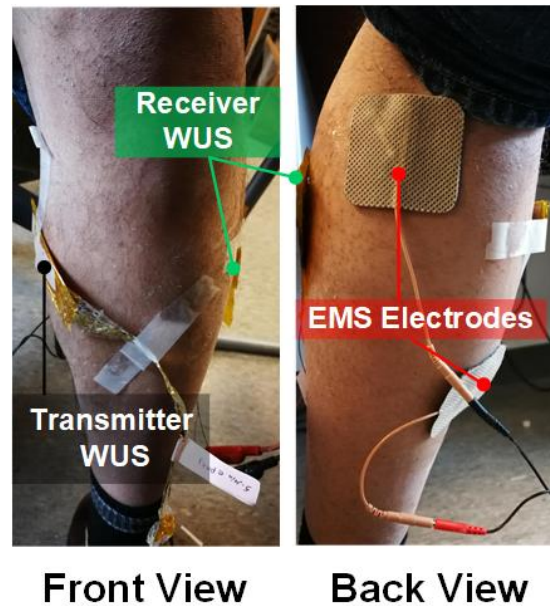


**Figure 6.16:** Photos of the experimental setup for monitoring the tetanic contractions of the gastrocnemius (GC) muscle in the TT mode. The two double-layer PVDF WUSs (transmitter and receiver) and EMS electrodes were attached to the skin surface of a lower leg.

**Figure 6.17** shows the schematic diagram of the ultrasonic measurement configuration to monitor the electrically-evoked GC muscle contraction. The contractions of the GC muscle were evoked by the EMS device at EMS frequencies of 2 Hz, 6 Hz, 8 Hz, 10 Hz, 12 Hz, and 30 Hz with an electric pulse width of 300  $\mu$ s. The amplitude of the stimulation pulse was adjusted to the comfort level of the human subject depending on the EMS frequency employed.

**Figure 6.18** shows the changes in tissue thickness obtained during the evoked GC muscle contraction by the EMS at different EMS frequencies. The periodical change of the tissue thickness corresponding to EMS frequency was clearly observed from the GC muscle contraction at the EMS frequency from 2 Hz to 12 Hz. At the EMS frequencies

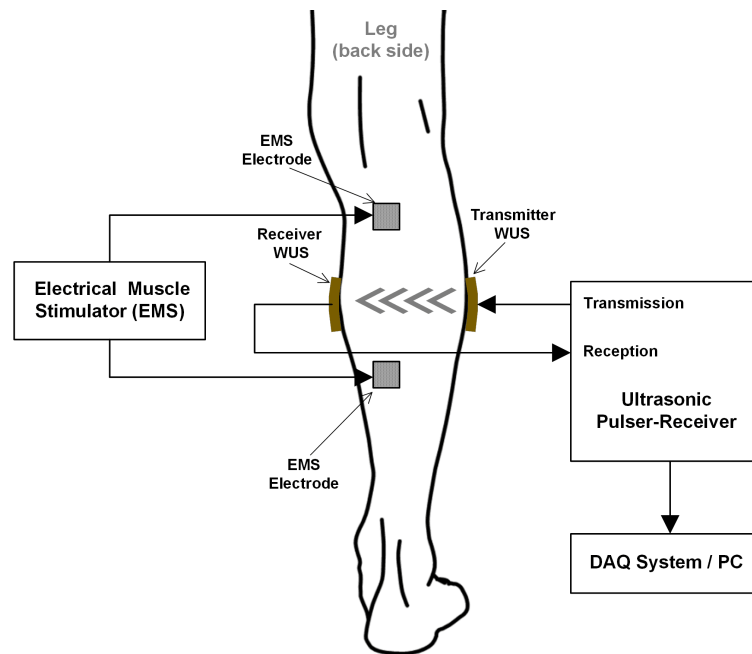


**Figure 6.17:** A schematic of the measurement configuration of GC muscle contractions in the lower leg. The muscle contraction was evoked by EMS, and the tissue thickness were measured using two developed WUSs in the TT mode.

of 2 Hz and 4 Hz, the GC muscle was able to relax completely between the intervals of two consecutive twitches. However, partial relaxations between the consecutive twitches were seen at the EMS frequencies of 6 Hz to 12 Hz, indicating the progression of tetanic contraction of the GC muscle. No relaxation was observed at the EMS frequency of 30 Hz under our experimental conditions. From the monitored thickness changes at each EMS frequency, the tetanic contraction progression level can be quantified using FI [32–34]. The FI is defined (in %) by:

$$FI = (a/b) \times 100 \quad (6.3)$$

where  $a$  is the difference between the initial thickness (before the EMS applied) and the minimal thickness during the contraction, whereas  $b$  is the difference between the initial thickness and the maximal thickness during contraction, as illustrated in **Figure 6.19**. Thus,

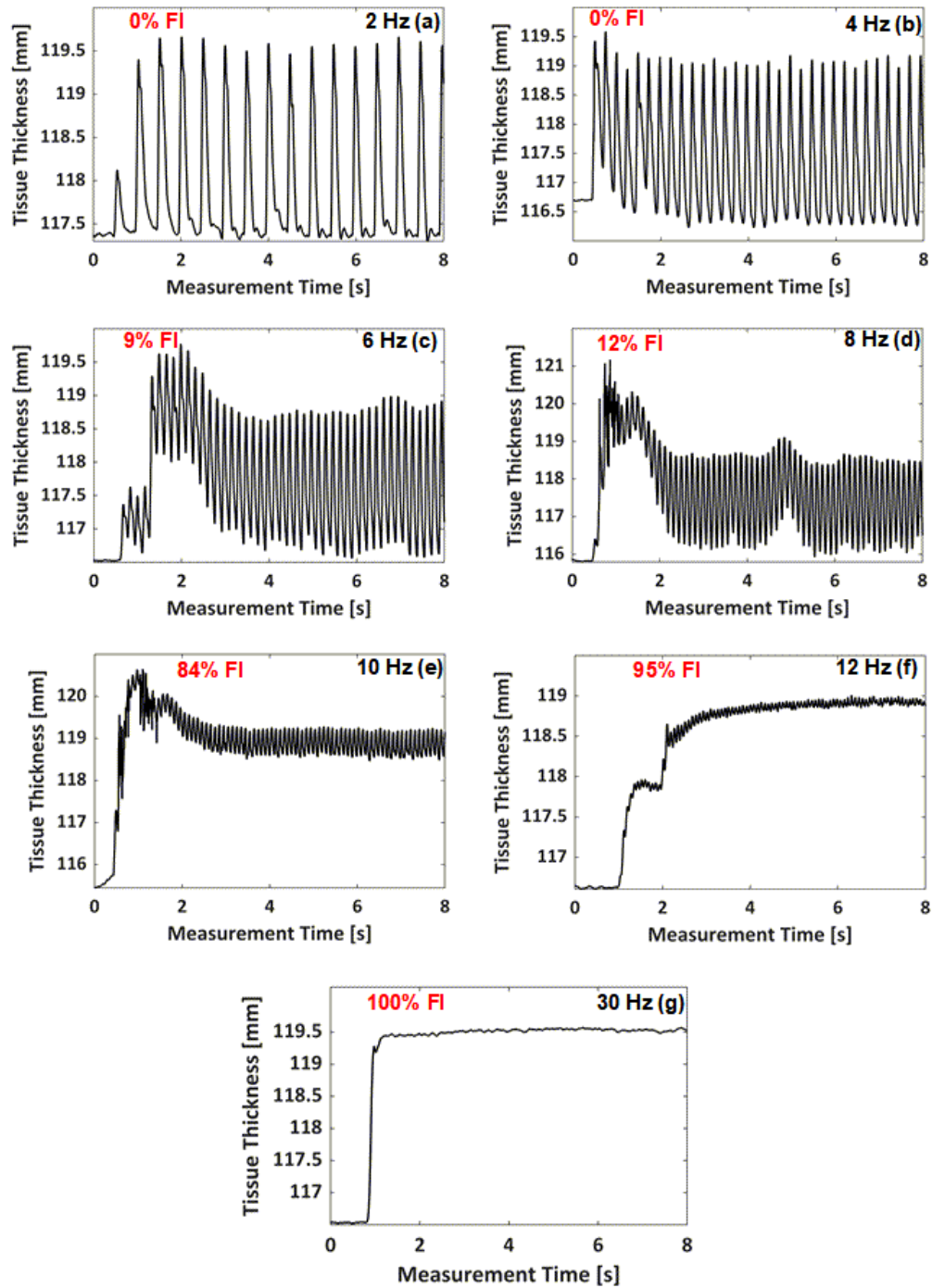


**Figure 6.18:** Tissue thickness changes, measured by the WUSs, due to the electrically evoked contraction of GC muscle at EMS frequencies of: 2 Hz (a), 4 Hz (b), 6 Hz (c), 8 Hz (d), 10 Hz (e), 12 Hz (f), and 30 Hz (g).

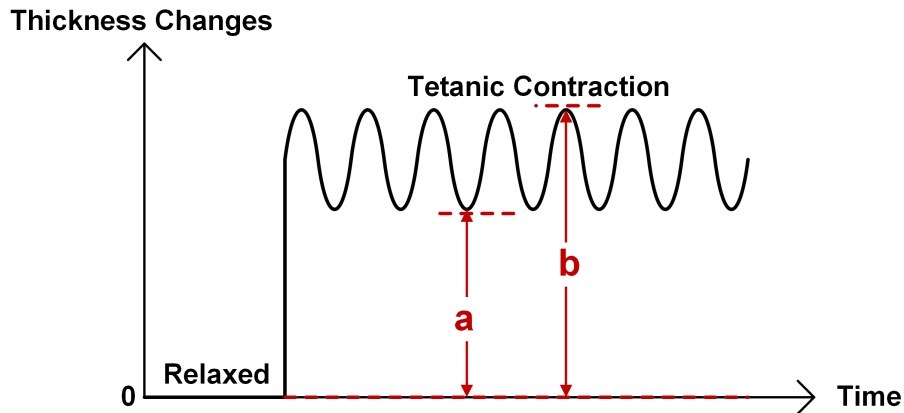


**Figure 6.19:** Definition of fusion index (FI) quantifying the tetanic contraction progression level [32–34].

the FI of 0% means the twitch contraction with complete relaxation of the muscle, and that of 100% means the completely fused tetanic contraction.

The FI value at each EMS frequency was obtained by taking the average of the calculated FI values between each electrical stimulation interval, after two seconds of initiating the EMS. **Figure 6.20** presents the FI value, denoted by the cross mark, with the standard deviation (SD), denoted by the error bar, obtained at each EMS frequency. As seen in **Figure 6.18** (a) and (b) at the EMS frequencies of 2 Hz and 4 Hz, respectively, the GC muscle had a complete relaxation between the consecutive stimuli, which indicates the FI of 0%. As the EMS frequency increased to 6 Hz and 8 Hz, the muscle would progress to a partial relaxation represented by the FI values of  $8.6 \pm 4.4\%$  and  $15.7 \pm 9.1\%$  (mean  $\pm$  SD), respectively. At 10 Hz and 12 Hz, the tetanic contraction progressed further, and the FI values became  $83.8 \pm 1.2\%$  and  $95.3 \pm 0.5\%$ , respectively. The FI value of 100% was assigned at 30 Hz since no muscular relaxation between the consecutive stimuli was observed at 30 Hz, as shown in **Figure 6.20** (g). In general, the unfused and fused tetanus is considered at FI value greater than 10% and 90%, respectively [241]. Therefore, based on the S-shaped (sigmoid function) curve fitting (solid line) of the obtained FI-EMS frequency relationships shown

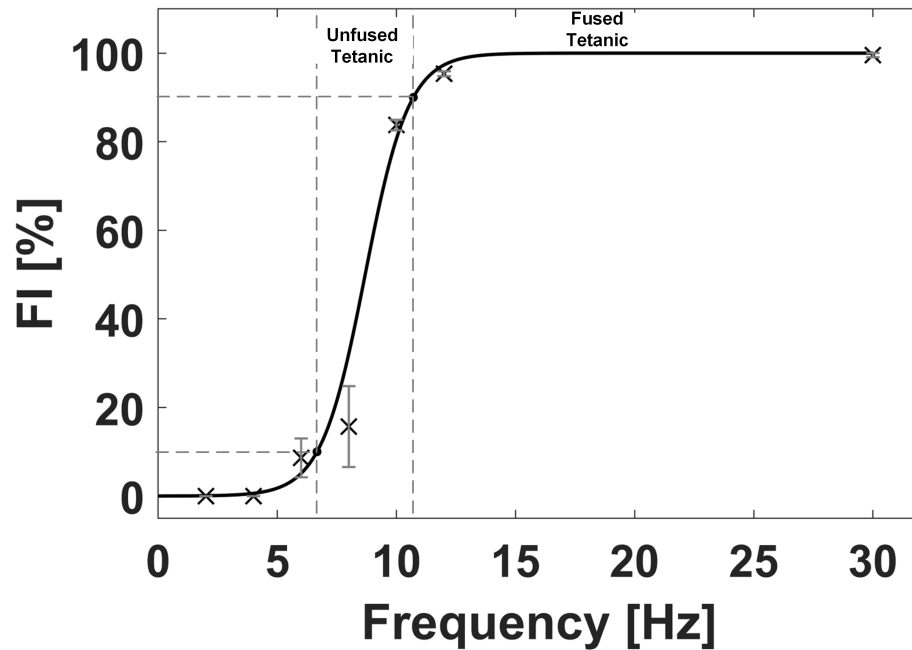


**Figure 6.20:** FI value (cross mark) with the standard deviation (error bar) at each EMS frequency, obtained from the results shown in **Figure 6.18**. The FI-EMS frequency curve denoted by the solid line was obtained by curve fitting of a sigmoid function.

in **Figure 6.20**, the minimum stimulation frequencies necessary to evoke the unfused and fused tetanus were given at FI values of 10% and 90%, respectively. Thus, the GC muscle would be evoked to the unfused and fused tetanic contraction at EMS frequencies of 6.7 Hz and 10.7 Hz, respectively, under the experimental conditions employed.

The monitored muscle contractions of the GC muscle were further analyzed by extracting the contractile parameters ( $Th$ ,  $Tc$ ,  $Ts$ ,  $Tr$ , and  $Vc$ ) from the multiple contraction twitches. **Figure 6.21** shows the extraction of the contractile parameters from a chosen single contraction twitch of the monitored GC muscle at each EMS frequency in the range of 2–10 Hz, which were not in a fused tetanus state in the experiments. At the EMS frequency of 2 Hz, the  $Th$  was 2.24 mm from the relaxed state to the maximum contracted state. The  $Tc$  during which the thickness increased from 10% to 90% of the  $Th$  was 38 ms. During the  $Tc$ ,

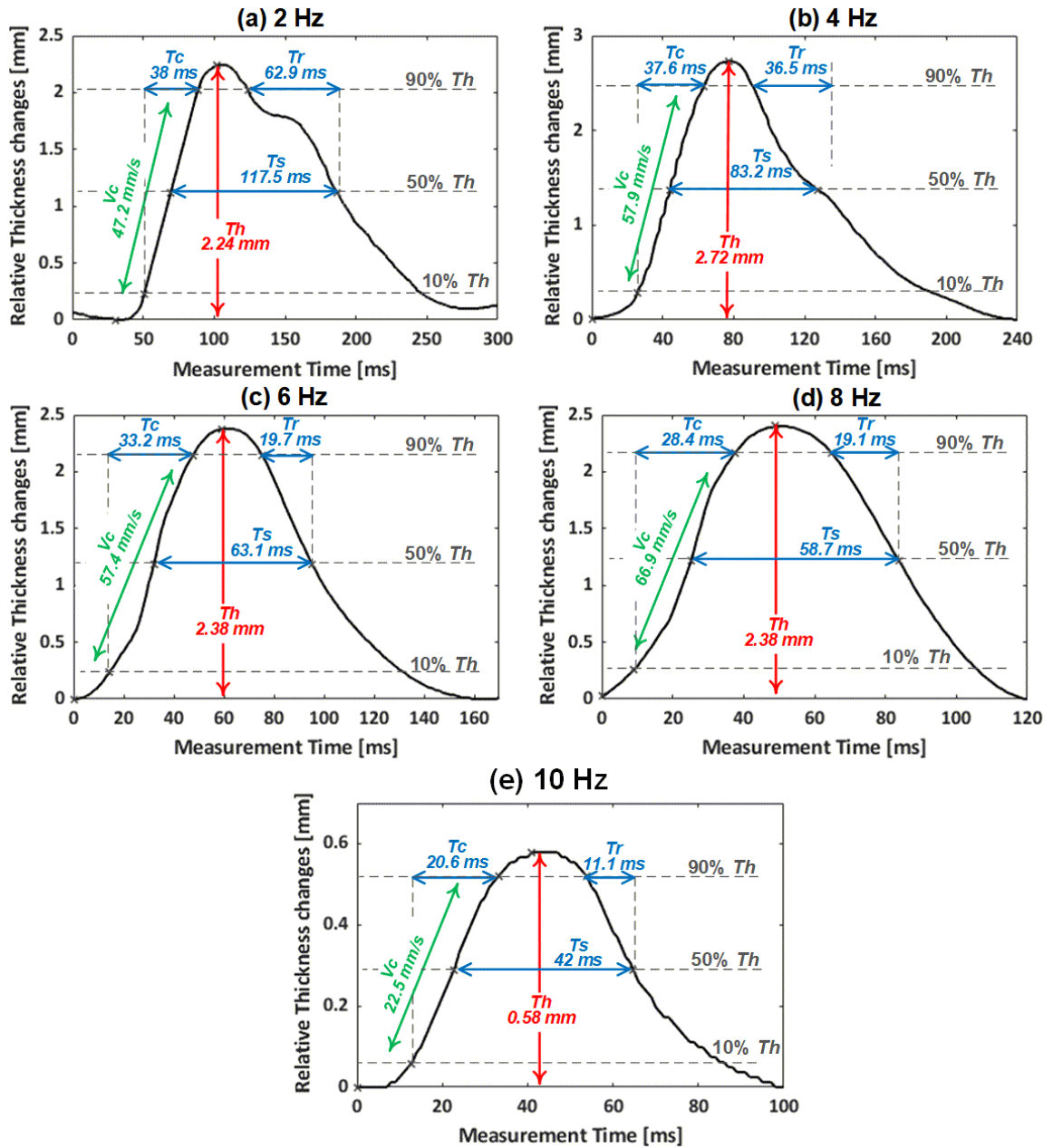


**Figure 6.21:** Extracted contractile parameters from a chosen single contraction twitch of the GC muscle evoked at EMS frequencies of: 2 Hz (a), 4 Hz (b), 6 Hz (c), 8 Hz (d), and 10 Hz (e).

**Table 6.5:** Average values  $\pm$  SD and CV of the contractile parameters from the monitored tetanic contraction of GC muscle at the EMS frequencies in **Figure 6.18**.

EMS	Extracted Parameters Mean $\pm$ SD (CV)				
	<i>Th</i> (mm)	<i>Tc</i> (ms)	<i>Ts</i> (ms)	<i>Tr</i> (ms)	<i>Vc</i> (mm/s)
2 Hz	2.20 $\pm$ 0.08 (3.6%)	38.25 $\pm$ 1.50 (3.9%)	116.28 $\pm$ 12.75 (11%)	63.49 $\pm$ 12.12 (19.1%)	46.13 $\pm$ 2.76 (6%)
4 Hz	2.77 $\pm$ 0.09 (3.2%)	37.12 $\pm$ 1.05 (2.8%)	77.57 $\pm$ 7.29 (9.4%)	31.46 $\pm$ 6.76 (21.5%)	59.68 $\pm$ 2.05 (3.4%)
6 Hz	2.04 $\pm$ 0.15 (7.4%)	32.54 $\pm$ 0.88 (2.7%)	61.77 $\pm$ 2.23 (3.6%)	19.54 $\pm$ 1.81 (9.3%)	50.22 $\pm$ 3.68 (7.3%)
8 Hz	2.36 $\pm$ 0.19 (8.1%)	27.51 $\pm$ 1.41 (5.1%)	58.10 $\pm$ 2.00 (3.4%)	19.72 $\pm$ 1.64 (8.3%)	68.56 $\pm$ 5.47 (8.0%)
10 Hz	0.59 $\pm$ 0.03 (5.1%)	21.62 $\pm$ 1.58 (7.3%)	40.07 $\pm$ 3.07 (7.7%)	10.80 $\pm$ 2.08 (19.3%)	22.03 $\pm$ 1.58 (7.2%)

*Vc* was 47.21 mm/s. The *Ts* during which the GC muscle sustained the 50% of the *Th* was 117.5 ms. After reaching the maximum thickness, the thickness began to decrease, which indicates the relaxation period. The *Tr* during which the thickness decreased from 90% to 50% of the *Th* was 62.9 ms. **Table 6.5** lists the average contractile parameters obtained from the multiple twitches of the electrically evoked GC muscle contractions at each applied EMS frequency, shown in **Figure 6.18**. An average was taken from the twitches observed after the first two seconds of initiating the EMS, where the twitches became stable. The CV values for *Th*, *Vc*, and *Tc* were 8.1% or less, and those for *Ts* were 11% or less. The CV values for *Tr* showed greater values (8.3%–21.5%) comparing with the other parameters

The values of *Tc*, *Ts*, and *Tr* with respect to EMS frequencies from 2 Hz to 10 Hz

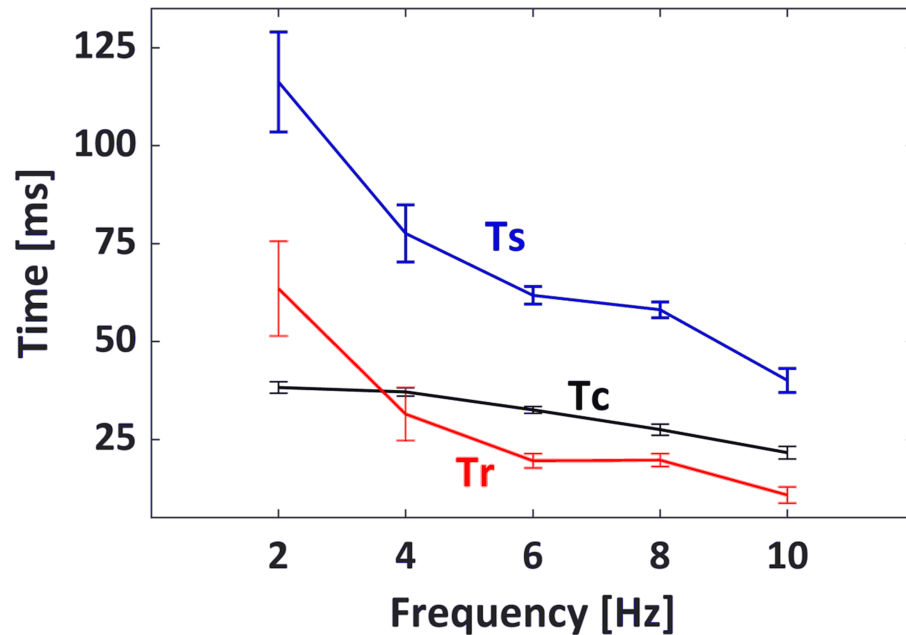


**Figure 6.22:** The average contractile parameters of  $T_c$ ,  $T_s$ , and  $T_r$  of the monitored muscle contractions with respect to the EMS frequencies. The error bar indicates the standard deviation.

are presented in **Figure 6.22**. It was observed from these extracted contractile parameters that the contraction and relaxation periods of the GC muscle became shorter as the EMS frequency increased. As the EMS frequency increased from 2 Hz to 10 Hz, the average  $T_c$  values decreased from 38.25 ms to 21.62 ms, and the average  $T_r$  values decreased from 63.49 ms to 10.80 ms. In addition, the GC muscle sustained a shorter contraction as the frequency progressed further, which was indicated by the average  $T_s$  of 116.28 ms at 2 Hz compared to  $T_s$  of 40.07 ms at 10 Hz.

### 6.3.2 Dynamic Voluntary Contraction

The current assessment methods of the contractile parameters, LDS and TMG, focus on the static (isometric) contractions of the muscle [46, 96]. In addition, the reported

measurements using the above-mentioned methods were focused solely on the electrically-evoked contractions [46, 242]. The measurement of the skin surface displacement during the dynamic contractions is challenging due to the contamination by motion artifact. The experimental investigation in **Section 6.2.2** has shown that the double-layer PVDF WUS is less susceptible to motion artifact. Therefore, this *in vivo* experiment was attempted to demonstrate the advantage of the proposed double-layer PVDF WUS and ultrasonic method in the quantitative assessment of the muscle contractile properties during the dynamic (isotonic) voluntary contractions.

The double-layer PVDF WUS was attached to the skin above the biceps muscle of a healthy male subject's left upper arm, as shown in **Figure 6.23**. The ultrasonic experimental configuration was similar to the experiment conducted in **Section 6.2.1**, where the biceps muscle contractions were monitored using the double-layer PVDF WUS in the ultrasonic PE mode. The subject was sitting on a chair with his left arm extended over the experiment table. The dynamic contraction of the biceps muscle was performed by the voluntary flexion and extension of the forearm (bending the elbow from 0° to about 90°).

**Figure 6.24** shows the measured tissue thicknesses during the dynamic contraction of the biceps muscle. The periodical tissue thickness change between the double-layer PVDF WUS and the bone (the humerus) corresponding to the performed contraction of the muscles was monitored for four cycles of the forearm flexion-extension. It can be seen from the monitored dynamic contraction that the thickness of tissue in the relaxed state (where the forearm was extended) was about 31.1 mm, while the thickness increased to about 34.1 mm in the contracted state (where the forearm was flexed). The double-layer PVDF WUS demonstrated the ability to track the thickness changes during the muscle dynamic contraction, similar to the case of static contractions demonstrated in the previous sections. This allows for further analysis of the monitored thickness changes by extracting the contractile parameters. As

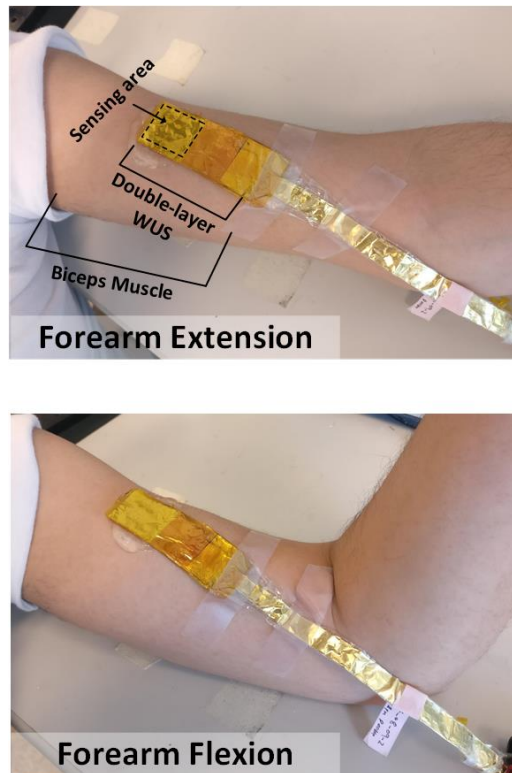


**Figure 6.23:** Photos of double-layer PVDF WUS attachment to skin surface for monitoring the voluntary dynamic contraction of biceps muscle in PE mode.

the contractile parameters are extracted from the twitch contraction evoked by an EMS, the contractile parameters of the voluntary contraction could be extracted from the repetitive contracting-relaxing cycle, as shown in **Figure 6.25**.

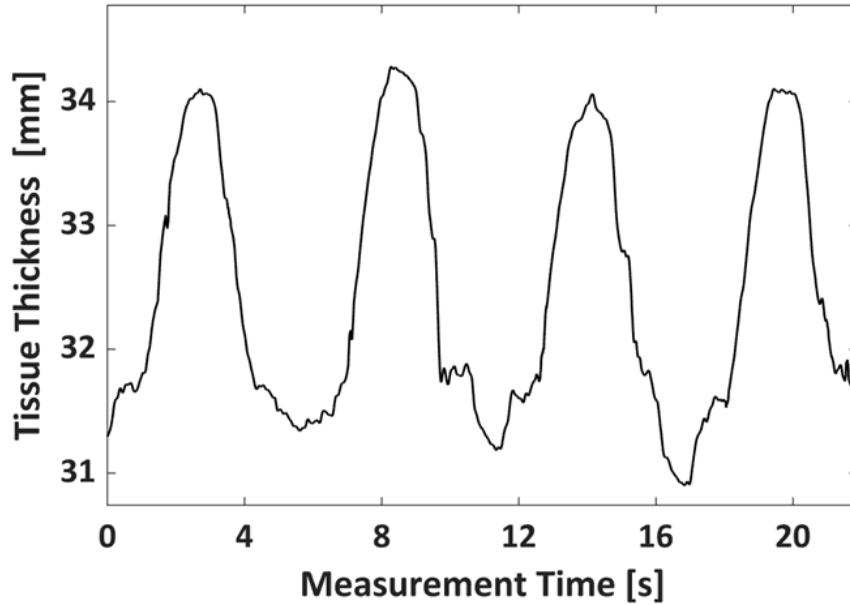


**Figure 6.24:** Monitored tissue thickness changes during the dynamic contraction of the biceps muscle performed by the voluntary flexion and extension of the forearm and measured by the double-layer PVDF WUS in the PE mode.

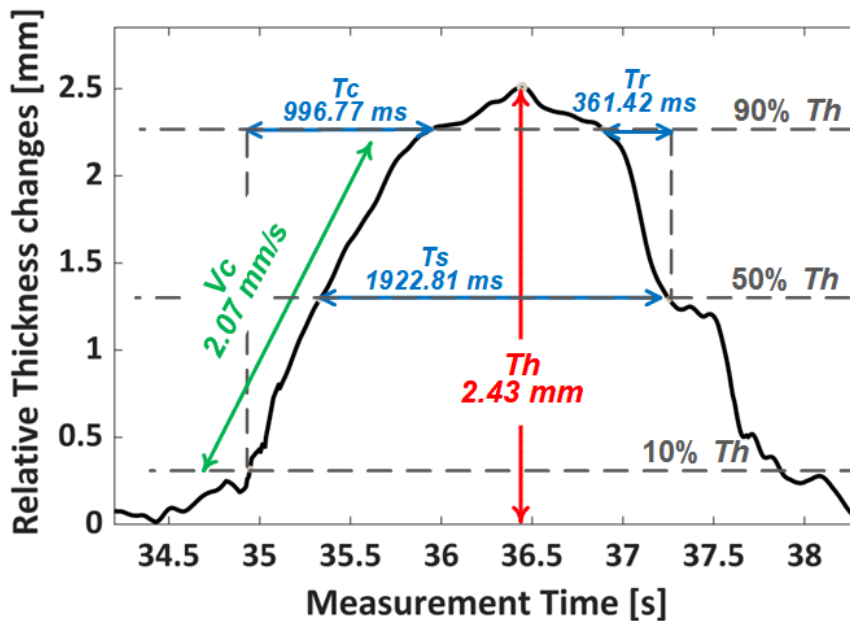


**Figure 6.25:** Extracted contractile parameters from a chosen single contracting-relaxing cycle of the voluntary biceps muscle.

**Table 6.6:** Extracted contractile parameters from the monitored dynamic contraction of the biceps muscle in **Figure 6.24**.

Parameters	Voluntary flexion-extension cycles				Mean $\pm$ SD	CV
	1	2	3	4		
<b><i>Th</i> (mm)</b>	2.45	2.82	2.43	2.67	2.59 $\pm$ 0.19	7.20%
<b><i>Tc</i> (ms)</b>	1064.51	1031.76	996.77	1034.01	1031.76 $\pm$ 27.70	2.70%
<b><i>Ts</i> (ms)</b>	2086.52	2160.51	1922.81	1909.06	2019.73 $\pm$ 123.72	6.10%
<b><i>Tr</i> (ms)</b>	490.64	513.13	361.42	302.68	416.97 $\pm$ 101.36	24.30%
<b><i>Vc</i> (mm/s)</b>	1.84	2.19	1.95	2.07	2.01 $\pm$ 0.15	7.50%

In these four cycles of muscle contractions, the average changes in the thickness of the biceps muscle from the relaxed state to the contracted state, ***Th***, was  $2.59 \pm 0.19$  mm. The average time of the biceps muscle to reach the contraction state, ***Tc***, was  $1031.76 \pm 27.70$  ms with an average rate, ***Vc***, of  $2.01 \pm 0.15$  mm/s. The average sustaining time of the contraction, ***Ts*** was  $2019.73 \pm 123.72$  ms. The average half-relaxation time, ***Tr***, which indicates the beginning of the forearm extension was  $416.97 \pm 101.36$  ms (***Tr***). The extracted parameters were listed in **Table 6.6**.

## 6.4 Discussion

### 6.4.1 Comparison Between the Double-Layer PVDF WUS and LDS

The measurement of the double-layer PVDF WUS was compared and validated with the LDS measurement of the electrically-evoked biceps muscle contractions. The double-layer PVDF WUS in the comparative measurement (**Section 6.2.1**) demonstrated an overall lower variability with CV values of 7% or less for all of the extracted contractile parameters than

the LDS, which demonstrated CV values up to 18.6%. Among the stimulation intervals in the conducted comparative measurement, the S1 and S2 intervals have greater differences between the obtained mean values of the extracted contractile parameters from the LDS and double-layer PVDF WUS measurement, whilst S3 and S4 have the smallest difference between the two methods. The relaxation phase of the contraction twitches of the S1 and S2 intervals obtained using LDS showed a different response compared to the S3 and S4 intervals. This might be due to the larger effect of motion artifact that caused some deformation to the contraction twitches in S1 and S2. In contrast, the double-layer PVDF WUS maintained a consistent shape of the contraction twitches among the stimulation intervals (S1-S4).

Additionally, the difference of the measurement principle between the double-layer PVDF and LDS may also contribute to the difference between the obtained contractile parameters using the two methods. The LDS measures the displacement at the skin surface caused by the muscle thickness change during the contraction, whereas the ultrasonic method measures the internal tissue thickness between the double-layer PVDF WUS and the tissue-bone boundary. However, Seidl et al. [31] indicated the differences between TMG and LDS measurements while both methods obtained good to excellent test-retest reliability. The differences could be clinically irrelevant as different methods should not be used interchangeably within a single study [31, 113]. For clinical applications, the parameters would be used to find the changes in the muscle contractile properties that are related to the progression of disease, recovery, or training [46, 113].

### 6.4.2 Double-Layer PVDF WUS and Motion Artifact

Motion artifact is a known problem in the application of MMG measurements [63]. Therefore, the presence of concurrent limb or body motion led to the preclusion of the dynamic contraction apart from most muscle contractile properties assessment studies [63, 243, 244]. The poor performance of the LDS in the presence of concurrent limb or body motion is indicated by the substantial high variability (22.8% to 82%) of the extracted contractile parameters obtained from the induced motion artifact experiment (**Section 6.2.2**). On the contrary, the double-layer PVDF WUS demonstrated superior performance in the presence of concurrent limb or body motion as it maintained the low variability of the extracted parameters ( $\leq 8.5\%$ ). The induce motion artifact experiment confirms that double-layer PVDF WUS is less susceptible to contamination by motion artifact. The flexibility, light weight, thinness, and smallness in size of the double-layer PVDF WUS offer the ability to follow the global limb or body motion while maintaining stable attachment on the skin surface. As discussed in **Section 6.2.2**, the double-layer PVDF WUS is less affected by undesired limb or body motion allowing the measurement with less strict posture positions and during dynamic contractions in contrast to LDS.

### 6.4.3 Assessment of Muscle Contractile Properties

The conducted *in vivo* measurements investigate the capability of the developed double-layer PVDF WUS and the ultrasonic method to perform the continuous and quantitative assessment of the skeletal muscle contractile properties. It was demonstrated in obtaining the tissue thickness changes corresponding to the partial relaxation of the muscle during the progression of the tetanic contraction. The monitored thickness changes were directly analyzed to quantify the tetanic progression using the FI parameter as well as to extract

the contractile parameters for each stimulation frequency of unfused tetanic without the requirement of special post-processing or filtering. In the experiment of monitoring tetanic contraction (**Section 6.3.1**), the CV values for  $Tr$  showed greater values (8.3%–21.5%) comparing with the other parameters (**Table 6.5**). It was reported in the TMG measurements with multiple subjects that the  $Tr$  parameter exhibited high variability and was indicated as an unreliable parameter [108]. Though our CV values were estimated from the multiple twitches with only a single subject, a similar tendency of the measurement variability was shown in the results of the tetanic contraction progression experiment.

Several studies have presented the measurement of the biceps and GC muscles contractile parameters [30, 44, 245–251]. However, the lack of a standardized measurement protocol led to a variety of measurement conditions which limit the comparison between the muscle contractile parameters, as discussed in [108, 251–253]. The sensor position, EMS conditions (amplitude, pulse width, and inter-electrode distance), and individual differences (gender, age, body mass, and physical activity level) impose difficulties for the direct comparison between the values of the contractile parameters. Therefore, the comparison of the parameter values obtained in this thesis study with those of other studies would not be applicable due to the different measurement conditions employed and is beyond the scope of the objectives of this thesis.

In addition, the extraction of the contractile parameters from the dynamic voluntary contraction (**Section 6.3.2**) demonstrated the feasibility of the double-layer PVDF WUS to extend the current scope of muscle contractile parameters measurement. It would facilitate future exploration of the skeletal muscle contractile parameters of voluntary contractions during various physical activities that involve dynamic contractions. Thus, the novel ultrasonic technique presented in this thesis work allows the measurement of the skeletal muscle contractile parameters beyond the limitations of TMG and LDS methods, such as

fixed posture and/or limited measurement location, which are currently the popular tools for assessment of muscle contractile properties [46, 104]. The double-layer PVDF WUS offers the advantage of the ultrasonic A-mode method by measuring the internal thickness changes of the tissue where the TMG and LDS methods may not be feasible, such as during dynamic contractions and/or body motion. The ultrasonic measurement method using the developed double-layer PVDF WUS could provide a practical tool for the inexpensive, non-invasive, and continuous measurement of the skeletal muscle contractile properties with less strict posture conditions in comparison with the TMG and LDS.

The proposed double-layer PVDF WUS and ultrasound method of the measurement of the skeletal muscle contractile parameters could be applied to various medical applications, for instance: monitoring the treatment progression before and after ligament reconstruction surgery [43, 44, 249], investigating the ratio of slow-twitch and fast-twitch fibers in muscles [52, 105, 245], assessing muscle fatigue [57, 109] and physical training effectiveness [46, 90]. In addition, the FI-EMS frequency curve would be used to investigate the degree of muscle fatigue [32] and to evaluate the muscle fiber type and fiber composition ratio [33]. Additionally, the double-layer PVDF WUS offers the measurement of both the static and dynamic contractions, contrary to the TMG and LDS, which are only applicable for the examination of static contraction [46, 104].

SEMG has been used for decades to evaluate neuromuscular response, especially the muscle fatigue [62]. It provides wearability on the skin surface. However, The SEMG signals are susceptible to various types of noises requiring extensive signal processing techniques to reduce the adverse effects on the measurement [254]. The noise contamination is caused by various sources that originate from the sensitivity to the skin-electrode displacement, undesired signals from musculature other than the muscle of interest (crosstalk), skin impedance, and surrounding electrical interference. These noises affect the quality of the

SEMG signal and impose the difficulty of analyzing the muscle function, especially during dynamic contraction [255, 256].

Nevertheless, SEMG provides a distinctive feature of measuring the electrical activity of the muscle, while the ultrasonic measurement by the double-layer PVDF WUS provides the mechanical counterpart of the muscle function. Thus, the combination of the SEMG and double-layer PVDF WUS measurements may provide information on various aspects of the electromechanical function of the muscle. For example, the simultaneous measurement by SEMG and double-layer PVDF WUS could estimate the time delay parameter between the motor unit activation and the start of the mechanical contraction. In addition, the SEMG would provide the alteration of electric potential generated during muscle contraction due to the fatigue [256], while the double-layer PVDF WUS would provide the quantification of the contractile mechanism alteration [256]. In this thesis work, the SEMG was not conducted because the *in vivo* measurements in this stage of research were conducted to test the ability of double-layer PVDF WUS in the measurement of the muscle contractile parameters with a method of a comparable principle of measurement such as LDS. The next stage of future work would investigate the clinical benefit of the simultaneous measurement of the muscle contractions using the SEMG and the double-layer PVDF WUS.

## 6.5 Limitations

### 6.5.1 Assumed Sound Velocity

The estimation accuracy of the tissue thickness using the ultrasonic measurement method is influenced by the assumed velocity of the sound in tissues. The ultrasound wave path includes tissue segments with different sound velocity such as skin, fat, and muscle. **Table 6.7**

**Table 6.7:** Typical sound velocity values in body tissues [35–37].

Tissue	$v$ (m/s)
Blood	1570–1575
Bone	4080
Brain	1530–1550
Eye	1525–1650
Fat	1450
Heart	1570
Kidney	1561–1570
Liver	1549–1590
Muscle	1568–1590
Skin	1730

shows the sound velocity of several body tissue types. In ultrasound imaging, the sound velocity is typically assumed to be constant, which results in a direct relationship between the TOF and the thickness [257]. In practice, the sound velocity of 1540 m/s is the accepted or standard average sound propagation velocity used to compute the soft tissue thickness [258, 259]. For the contractile parameters, the assumed sound velocity would be reflected in the change of the  $Th$  and  $Vc$  parameters value. The temporal parameters ( $Tc$ ,  $Ts$ , and  $Tr$ ) are dependent on the PRR of the ultrasonic measurement and therefore are not affected by the assumed sound velocity. Also, the FI parameter is independent of the actual velocity of sound since it is given by the thickness ratio between the contracted and relaxed states of a muscle. Thus, the  $Th$  and  $Vc$  parameters are subject to an estimation error due to the difference between the assumed and actual velocity of sound in tissues.

### 6.5.2 Alignment of an Ultrasonic Beam

The ultrasonic measurement of tissue thickness during the skeletal muscle contractions may encounter a misalignment between the double-layer PVDF WUS and the tissue-bone boundary in the PE mode or between the two employed double-layer PVDF WUSs in the TT mode. The changing of muscle thickness during the contraction affects the degree of alignment, which would lead to a reflected/received signal with poor SNR or no ultrasound pulse. In the conducted experiments of this thesis work, the *in vivo* measurements in the ultrasonic TT mode were found to maintain a better alignment, between the transmitter and receiver double-layer PVDF WUSs, during the muscle contraction compared to the ultrasonic PE mode, between the double-layer PVDF WUS and tissue-bone boundary. The average SNR of the received ultrasound RF signals for the measurement conducted in TT mode (**Figure 6.18**), after the preprocessing, was 25 dB with a minimum of 14 dB. In comparison, the average SNR of received ultrasound RF signals for the measurement conducted in PE mode (**Figure 6.6**) was 21 dB with few frames of 0 dB (no ultrasonic pulse). The double-layer PVDF WUS was ensured to have good alignment during the resting and contracting states of the muscle of interest before starting the muscle measurement. Furthermore, the effect of misalignment could be further reduced by adopting a more robust signal processing method that improves the accuracy of the thickness changes estimation with ultrasound RF signals of low SNR. The amplitude peak detection method used in the conducted measurement has a poor estimation with low SNR signals due to the signal amplitude variation and the deformation of the ultrasound pulse shape. Some other works have discussed and investigated different signal processing techniques, such as quadrature demodulation, for the tissue thickness estimation from the ultrasonic RF signal [260–263].

### 6.5.3 Ultrasonic PE and TT Modes

The choice between the ultrasonic PE or TT would depend on the thickness and accessibility to a muscle of interest with regard to its anatomical location and direction of the muscle fibers. The ultrasonic TT mode measurement would have, in general, a higher SNR of the received ultrasound RF signals. As the TT mode uses two double-layer PVDF WUSs, the ultrasound travels from the transmitter WUS to the receiver WUS making a single trip. Since ultrasound attenuates during the propagation within the tissues due to absorption, scattering, and/or diffraction, the TT mode has the advantage of measuring thicker tissue layer as it exhibits a superior SNR in comparison with the PE mode. Indeed, the target ultrasound signals to measure the total thickness of the lower leg in the PE mode were not observed under our experimental configuration described in **Section 6.3.1**. Also, the TT mode could provide better measurement accuracy of the total thickness of tissue between the transmitter and receiver WUSs due to the better SNR than PE mode.

The reflected ultrasound signals in the PE mode contain small reflections from different soft tissue boundaries, which are considered noise signals to the target ultrasound signal. However, these small reflections could be useful to identify the local motion of a soft tissue layer such as fat and skin during muscle contractions. For example, **Figure 6.26** shows the M-mode image of the biceps muscle voluntary contraction that was measured in the PE mode described in **Section 6.3.2**. The soft tissue boundary at the depth of 5-7 mm can be observed, which might indicate the fat-muscle interface. The motion of the soft tissue boundary corresponded to the motion observed at the bone interface at 31-35 mm. Additionally, some reflections at the depth of 20 mm could be seen. These reflections are contained in very low SNR signals; however, with an adequate signal processing technique, they could be quantitatively analyzed.

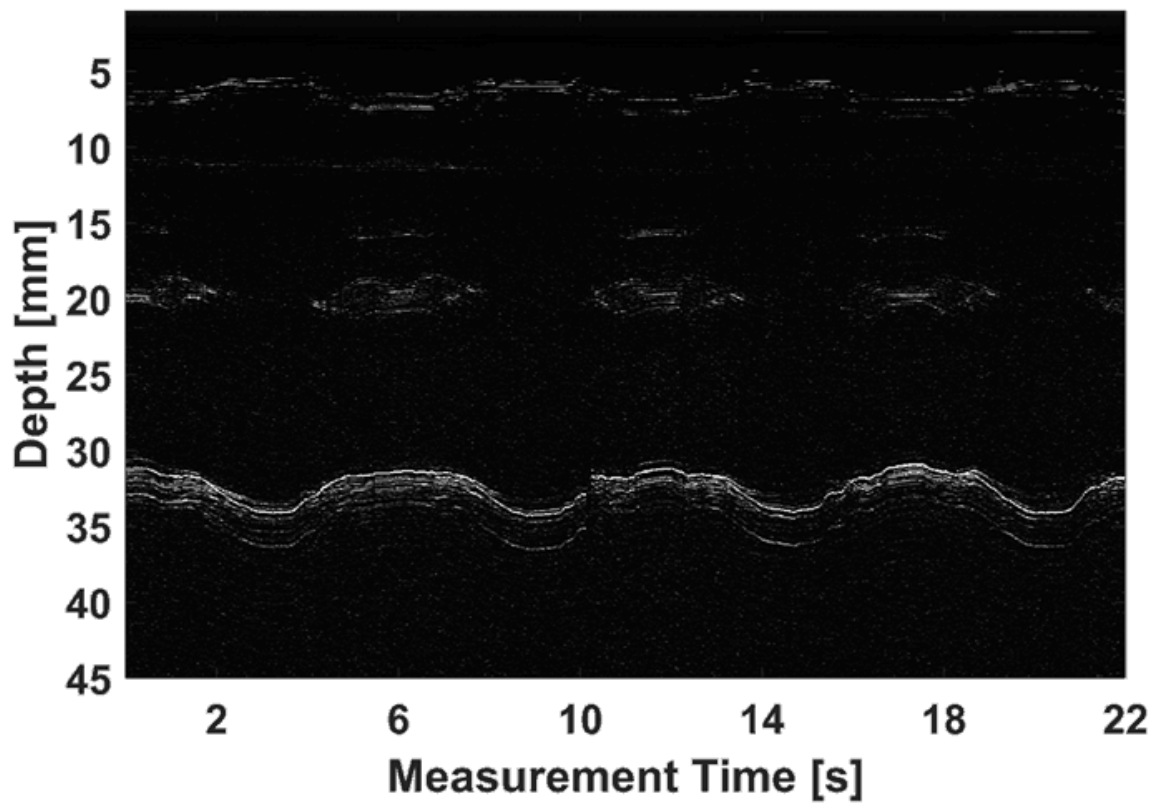


**Figure 6.26:** M-mode ultrasonic measurement of the biceps voluntary contraction in pulse-echo mode to illustrate local motion of soft tissue boundaries at the depth of 5 – 7 mm, 18 – 20 mm, and 31 – 35 mm.

# Chapter 7

## Conclusions and Future Research

The following chapter summarizes and concludes the main findings of the thesis, and provides suggestions for future research.

### 7.1 Summary of Thesis Research

In this thesis, the development of a wearable ultrasonic sensor has been conducted to provide a tool for the quantitative assessment of the skeletal muscle contractile properties. The feature of the developed double-layer PVDF WUS include flexibility, lightweight, thinness, and smallness in size which allow the steady attachment to the skin surface without restricting the underlying tissue motion or causing undesirable displacement of the sensor over the skin surface. Thus, the developed double-layer PVDF WUS is applicable to the measurement of the muscle contractile parameters during static and dynamic contractions. The following subsections summarize each chapter of this thesis work.

#### 7.1.1 Numerical Simulation Model

A complete derivation and formulation of the PVDF  $3 \times 3$ -matrix expression by [158] was expanded into  $4 \times 4$ -matrix expressions that are suitable for simulating and characterizing

the double-layer PVDF WUS in **Chapter 3**. The voltage orientation reversal of the parallel electrically connected double-layer PVDF and the internal losses of the PVDF piezoelectric polymer were accounted for in the formulation of the transfer  $4 \times 4$ -matrix expression. The introduced numerical model was used to simulate the double-layer PVDF WUS performance, such as the operating frequency, frequency bandwidth, acoustic power, and conversion efficiency, in order to design the double-layer PVDF WUS.

### 7.1.2 Numerical Study and Design Considerations

A detailed study of the double-layer PVDF characteristics and the effect of non-piezoelectric layers, such as backing, bonding, and electrode layers for several materials and layer thicknesses, on the ultrasonic performance was presented in **Chapter 4** using the simulation model developed in **Chapter 3**. The numerical simulation study has shown that the double-layer PVDF ultrasonic sensor, that is electrically connected in parallel with the polarization directions in parallel, resonates at the same ultrasonic frequency and bandwidth but with four times higher acoustic output power to input voltage ratio in comparison with a single-layer PVDF of the equivalent total PVDF layer thickness. Also, electrodes of very high acoustic impedance, such as silver (38.16 MRayls), have shown to substantially affect the operating frequency and bandwidth of the double-layer PVDF sensor. Where electrodes of moderate acoustic impedance, such as silver ink (12.24 MRayls), have a less impact overall. In addition, the bonding layer has been shown to affect the conversion efficiency negatively and consequently reduces the acoustic output power of the double-layer PVDF sensor, especially for a bonding material of low acoustic impedance (range of 1 MRayls). Therefore, the selection of an adhesive material of higher acoustic impedance and the reduction in thickness of the bonding layer would be preferred in order to minimize the

impact of the bonding layer.

The double-layer PVDF WUS design considered the desired ultrasonic sensor performances for muscle contraction monitoring, such as the operating frequency, ultrasound signal strength, and sensor flexibility and thinness. The considerations, approaches, and material selections for the double-layer PVDF WUS have been discussed based on the numerical simulation study. The double-layer PVDF WUS packaging requirement provided the impetus for finding an approach to isolate the mass-loading of the packaging layers without impeding the WUS flexibility or increasing its thickness. The numerical study of the backing layer effect on the double-layer PVDF sensor has shown that the backing of an acoustic impedance close to that of the PVDF (4.02 MRayls) leads to a substantially lower efficiency in ultrasonic performance (largest CL) compared to the backing of a very low acoustic impedance such as air (413 Rayls). This problem was addressed in the double-layer PVDF WUS design by creating an air gap between the back side of the double-layer PVDF and the packaging layers to isolate their mass-loading effect. The numerical simulation has shown that creating an air gap at the backside would make the double-layer PVDF practically air-backed.

### **7.1.3 Construction and Experimental Evaluation**

The double-layer PVDF WUS was constructed using two 52- $\mu\text{m}$ -thick PVDF layers with electrode layers of silver ink on the top and bottom surfaces, based on the design considerations discussed in **Chapter 4**. The two 52- $\mu\text{m}$ -thick PVDF layers were bonded using a moderate-viscosity epoxy and were connected electrically in parallel and acoustically in series with their piezoelectric polarization directions antiparallel. Adhering the two PVDF layers imposed practical difficulty and demanded careful consideration. Several approaches

and techniques have been attempted to achieve a thin bonding layer with good uniformity. The structure of the double-layer PVDF WUS was electrically isolated by an electromagnetic shielding layer and sealed using a polyimide film with an adhesive except for the ultrasonic sensing area where the ultrasound is transmitted or received. The constructed double-layer PVDF WUS was lightweight (less than 1 g), thin (350  $\mu\text{m}$ ), and small in size (50 mm  $\times$  24 mm). The ultrasonic sensing area was 20 mm  $\times$  20 mm. It was constructed using basic equipment and ordinary hand tools, such as scalpels and a soldering device, and did not require expensive equipment.

The ultrasonic performances of the double-layer PVDF WUS were evaluated experimentally using an ultrasonic pulse-echo technique with a comparison of the single-layer PVDF WUS which has the equivalent total PVDF layer thickness. The double-layer PVDF WUS shows an operating frequency of 6.7 MHz, which is in the preferable frequency range of medical ultrasound (1-10 MHz). The ultrasonic signal strength of the double-layer PVDF WUS exhibited 1.7 times greater ultrasonic signal amplitude compared to the single-layer PVDF WUS.

#### **7.1.4 *In Vivo* Performance Evaluation and Experimental**

##### **Demonstration**

The double-layer PVDF WUS was evaluated in the *in vivo* measurement of the muscle contractile parameters ( $Th$ ,  $Tc$ ,  $Ts$ ,  $Tr$ , and  $Vc$ ) in comparison to LDS measurement. In the comparative evaluation, the double-layer PVDF WUS and LDS were employed in measuring the muscle contractile parameters during the electrically-evoked static contraction of the bicep muscle by the EMS. The measured periodical tissue thickness obtained by both methods corresponded to the applied EMS frequency of 2 Hz. The double-layer

PVDF WUS demonstrated an overall lower variability ( $CV < 7\%$ ) compared to LDS ( $CV$  up to 18.6%) for all the measured contractile parameters. In addition, the influence of motion artifact on the double-layer PVDF WUS and LDS measurements were investigated. The LDS measurement was highly susceptible to contamination by the induced body/limb motion. On the contrary, the double-layer PVDF WUS was substantially less affected by the motion artifact and maintained the low variability ( $CV \leq 8.5\%$ ) of the measured contractile parameters, comparable to the  $CV$  values without the induced body/limb motion ( $CV < 7\%$ ). On the other hand, the LDS measurement demonstrated greater  $CV$  values of the measured contractile parameters (ranging from 22.8% to 82%).

The developed double-layer PVDF WUS was demonstrated in the *in vivo* quantitative assessment of the tetanic contraction progression and the dynamic voluntary contractions. The contractile parameters were successfully extracted from the monitored tissue thickness changes due to the GC muscle tetanic contractions at the EMS frequencies of 2 – 10 Hz. Also, the tetanic contraction progression was quantified by the FI parameter obtained from the tissue thickness changes at each EMS frequency. The fused and unfused tetanus frequencies were estimated from the obtained FI-EMS frequency curve. To the best of the author's knowledge, no such study has yet been reported using the proposed wearable ultrasonic method. In addition, the successful extraction of the contractile parameters from the dynamic voluntary contraction demonstrated the potential advantage of the double-layer PVDF WUS and ultrasound measurement over the current methods (TMG and LDS).

## 7.2 Scope and Limitation

This thesis research focused on the development of a wearable ultrasonic sensor for the measurement of skeletal muscle contractile parameters. The scope of this thesis includes:

(1) the examination of literature for the applications of muscle contraction monitoring and the current measurement methods limitations, (2) formulation of the numerical simulation model of multiple-layer PVDF ultrasonic sensors, (3) the numerical study and the design considerations of the double-layer PVDF WUS, (4) the construction and experimental evaluation of the developed double-layer WUS, and (5) *in vivo* the evaluation of the double-layer WUS in the measurement of muscle contractile parameters. It is expected that the proposed ultrasound method and the wearability of the developed double-layer PVDF ultrasonic sensor could provide reliable measurements of the muscle contractile parameters by reducing motion artifact and could be applicable to the measurements for both static and dynamic muscle contractions. However, the *in vivo* measurements in this thesis were conducted on a single subject for this stage of research as a preliminary evaluation of the double-layer PVDF WUS. The preliminary evaluation is the first step to assess the double-layer PVDF WUS capability and sensitivity to motion artifact and discuss the measurement limitations. Nevertheless, with the results obtained in this thesis research, future research is encouraged to investigate the reliability of the double-layer PVDF WUS measurement with multiple subjects, as discussed in the following section of future research.

### **7.3 Future Research**

This thesis worked toward developing a flexible and wearable ultrasonic sensor for the monitoring of muscle contraction and the measurements of the contractile parameters. The developed double-layer PVDF WUS and ultrasonic method could be a practical tool for the quantitative assessment of skeletal muscles during both the static and dynamic contractions. There is still further research required for the clinical employment of the developed double-layer PVDF WUS. The suggested future research is listed as follows:

### **1) Improvement of Signal Processing Technique**

The development of a reliable tissue thickness estimation technique of the A-mode ultrasound measurement is a highly recommended next step for this research topic. This thesis research focused on the ultrasonic performance improvement of the wearable PVDF ultrasonic sensor and its measurement capability. The amplitude peak detection technique has been used to determine the TOF of the ultrasound pulse in the experiments conducted in this thesis. It is a simple technique and can achieve a good estimation of TOF. However, this method is limited to high SNR ultrasonic signals and it has proved challenging to determine the amplitude peak with low SNR signals and distorted ultrasonic pulses. A carefully considered signal processing technique is required for the improvement of the tissue thickness estimation in the low SNR signal. It would be beneficial to analyze the motion of individual soft tissue layer quantitatively during the muscle contraction in the ultrasonic PE mode measurement, in which the desired ultrasonic signals often have a very low SNR. Several studies have proposed signal processing techniques for the estimation of the ultrasonic TOF such as quadrature demodulation [264, 265], phase-correlation [266], and threshold and peak analysis [267]. Preprocessing techniques such as time gain compensation, Gaussian filtering, and log compression can also be employed to improve the SNR of the raw A-mode ultrasonic signal [5]. Therefore, a study to evaluate the above-mentioned techniques for the TOF estimation and develop an automated signal processing procedure for the double-layer PVDF WUS measurement is recommended for future research. In addition, it would be advantageous for the automated processing procedure to provide real-time measurement.

### **2) In-vivo Experiments and Clinical Trials**

This thesis work provided the *in vivo* evaluation for the double-layer PVDF WUS measurement performance with a single subject. Further evaluations with multiple subjects and with more iteration per subject are required in the next steps. Also, studies to explore the clinical significance of the measurement of the muscle contractile parameters during voluntary contractions and physical activities are highly suggested. Therefore, the studies for reliability and repeatability of the double-layer PVDF WUS measurement would be performed in accordance with Munro's statistical methods [268]. The studies should include the examination of inter-individual variability, test-retest reliability, long-term stability, reliability of the muscle parameters during exercises, and correlation of the contractile parameters with the performed muscle function [30, 103, 104, 247, 250, 269–271]. In addition, investigating the clinical benefit of the simultaneous measurement of the muscle contractions using the SEMG and the double-layer PVDF WUS is suggested for the future clinical research. In this study, clinical grade ultrasound gel couplant was used. Suitable couplant materials that can last longer needs to be investigated for long-term monitoring. Furthermore, the feasibility of the double-layer PVDF WUS in the measurement of the cardiac tissue motion has been conducted and demonstrated in **Appendix A**. The ability of the double-layer PVDF WUS to observe the reflected ultrasonic signal from the cardiac tissue proposes its potential in the prolonged continuous monitoring of the cardiac wall motion. Thus, a future study is recommended to further explore the application in cardiac monitoring.

### **3) Development of Wearable Ultrasonic Measurement System**

The long-term objective of this thesis research is the development of a wearable ultrasonic measurement system for the continuous monitoring of muscle contraction.

For a wearable system, the sensor is the fundamental element of the system and essential to the implementation of a body-worn measurement system. The sensing part of the wearable muscle contraction measurement system may be the most challenging. Thus, this thesis work focused on overcoming the challenges and limitations imposed by the measurement of the sensor. There are a number of reported wearable ultrasound systems for piezoceramic ultrasonic sensors [4, 272]. These systems will be tested to drive the developed PVDF WUS. However, the PVDF WUS usually requires a higher voltage excitation pulse than piezoceramic sensors. Also, an ultrasound system with adjustable impedance matching for different double-layer PVDF WUS sizes would be desired. Therefore, the development of a wearable pulser/receiver system dedicated to the double-layer PVDF WUS is required. The recent advancement in electronics and battery technologies demonstrated in [143, 272–277] support the feasibility of developing a lightweight and small ultrasonic measurement system.

# Appendix A

## In Vivo Measurement of Cardiac Muscle Motion

The demonstrated ability of the developed double-layer PVDF WUS in monitoring the tissue motion due to the skeletal muscle contraction suggests the potential application in cardiac monitoring. The measurement of cardiac muscle motion is demonstrated in this section to assess the feasibility of the double-layer PVDF WUS in monitoring cardiac mechanical activity. The cardiac tissue motion associated with the cardiac cycle was monitored by the double-layer PVDF WUS in the ultrasonic pulse-echo mode. In addition to the ultrasonic monitoring, electrocardiography (ECG) signal was obtained in synchronization with the ultrasonic measurement as the ultrasonic and ECG signals were acquired simultaneously by the DAQ system. The double-layer PVDF WUS was attached to the left third intercostal space, and the ECG electrodes were positioned in the lead II configuration, as shown in **Figure A.1**. **Figure A.2** shows the M-mode image of the cardiac tissue measured using the double-layer PVDF WUS (bottom) along with the ECG signal (top). The cardiac tissue motion was observed at a depth of around 30 mm, in which the periodic change of the cardiac tissue corresponded with the cardiac cycles obtained from the ECG signal.

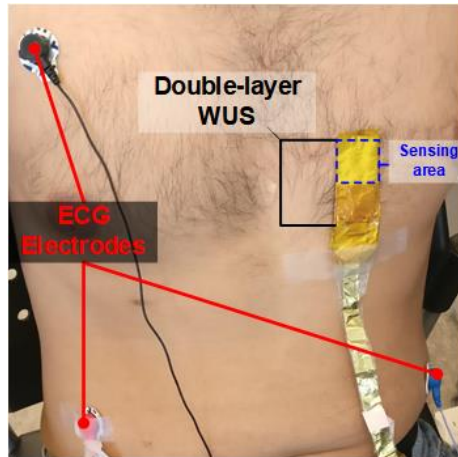


**Figure A.1:** Photo of double-layer PVDF WUS and ECG electrodes attachment to skin surface for the ultrasonic monitoring of cardiac tissue motion in pulse-echo mode.

This measurement demonstrated the ability of double-layer PVDF WUS to observe the reflected ultrasonic signal from the cardiac tissue. Also, it proposes the potential of the double-layer PVDF WUS for prolonged continuous monitoring of the cardiac wall motion. Moreover, monitoring of a particular cardiac region could be achieved with the assistance of an echocardiography imaging system in locating the optimal position of the double-layer PVDF WUS on the subject's skin surface.

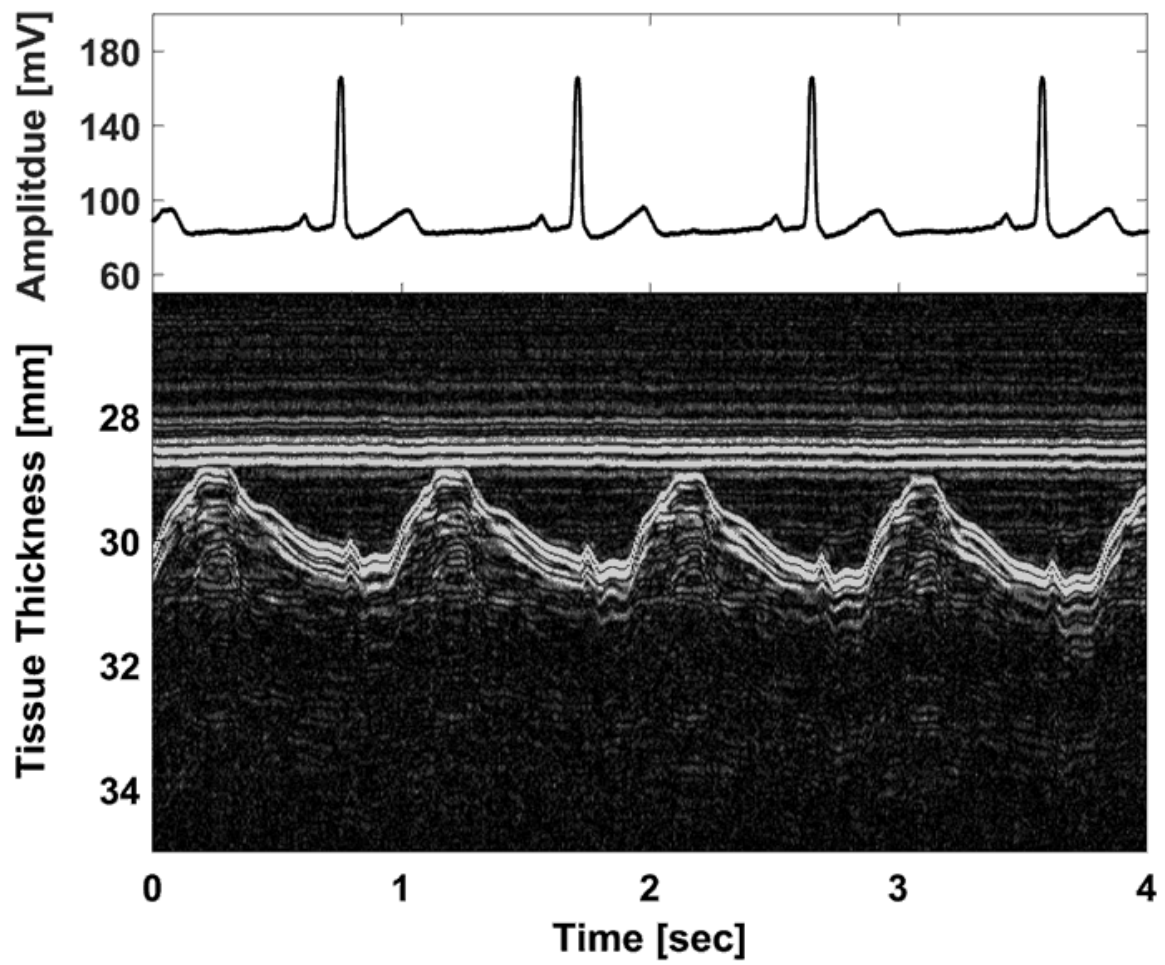


**Figure A.2:** Monitored cardiac tissue motion. ECG signal (top) and M-mode ultrasonic measurement of cardiac muscle motion (bottom).

## References

- [1] Jing-Yi Guo, Yong-Ping Zheng, Qing-Hua Huang, and Xin Chen. Dynamic monitoring of forearm muscles using one-dimensional sonomyography system. *The Journal of Rehabilitation Research and Development*, 45(1):187–196, 2008. doi: 10.1682/JRRD.2007.02.0026.
- [2] Xueli Sun, Yuefeng Li, and Honghai Liu. Muscle fatigue assessment using one-channel single-element ultrasound transducer. In *proceeding of International IEEE/EMBS Conference on Neural Engineering (NER)*, pages 122–125. IEEE, 2017. doi: 10.1109/NER.2017.8008307.
- [3] Xingchen Yang, Yuefeng Li, Yinfeng Fang, and Honghai Liu. A preliminary study on the relationship between grip force and muscle thickness. In *Proceeding of International IEEE/EMBS Conference on Neural Engineering (NER)*, pages 118–121. IEEE, 2017.
- [4] Xingchen Yang, Xueli Sun, Dalin Zhou, Yuefeng Li, and Honghai Liu. Towards Wearable A-Mode Ultrasound Sensing for Real-Time Finger Motion Recognition. *IEEE Transactions on Neural Systems and Rehabilitation Engineering*, 26(6):1199–1208, 2018. doi: 10.1109/TNSRE.2018.2829913.
- [5] Yu Zhou, Jia Zeng, Kairu Li, Yinfeng Fang, and Honghai Liu. Voluntary and FES-Induced Finger Movement Estimation Using Muscle Deformation Features. *IEEE*

- Transactions on Industrial Electronics*, 67(5):4002–4012, 2020. doi: 10.1109/TIE.2019.2920595.
- [6] Amirhossein Shahshahani, Carl Laverdiere, Sharmistha Bhadra, and Zeljko Zilic. Ultrasound Sensors for Diaphragm Motion Tracking: An Application in Non-Invasive Respiratory Monitoring. *Sensors*, 18(8):2617, 2018. doi: 10.3390/s18082617.
- [7] Yi Yang, He Tian, Bing Yan, Hui Sun, Can Wu, Yi Shu, Li-Gang Wang, and Tian-Ling Ren. A flexible piezoelectric micromachined ultrasound transducer. *RSC Advances*, 3(47):24900, 2013. doi: 10.1039/c3ra44619k.
- [8] Zhe Wang, Qing-Tang Xue, Yuan-Quan Chen, Yi Shu, He Tian, Yi Yang, Dan Xie, Jian-Wen Luo, and Tian-Ling Ren. A flexible ultrasound transducer array with micro-machined bulk PZT. *Sensors*, 15(2):2538–2547, 2015. doi: 10.3390/s150202538.
- [9] Vincenzo Mariano Mastronardi, Francesco Guido, Massimiliano Amato, Massimo De Vittorio, and Simona Petroni. Piezoelectric ultrasonic transducer based on flexible AlN. *Microelectronic Engineering*, 121:59–63, 2014. doi: 10.1016/j.mee.2014.03.034.
- [10] Sheng Sun, Menglun Zhang, Chuanhai Gao, Bohua Liu, and Wei Pang. Flexible Piezoelectric Micromachined Ultrasonic Transducers Towards New Applications. In *proceeding of IEEE International Ultrasonics Symposium (IUS)*, pages 1–4. IEEE, 2018. doi: 10.1109/ULTSYM.2018.8580227.
- [11] R. S. Singh, M.O. Culjat, M. Lee, D.B. Bennett, S. Natarjan, B.P. Cox, E.R. Brown, W.S. Grundfest, and H. Lee. Conformal ultrasound imaging system. In *Acoustical Imaging*, volume 30, pages 211–222. Springer Netherlands, 2011. doi: 10.1007/978-90-481-3255-3\25.

- [12] Sina Sadeghpour, Bram Lips, Michael Kraft, and Robert Puers. Flexible SoI-Based Piezoelectric Micromachined Ultrasound Transducer (PMUT) Arrays. In *proceeding of Solid-State Sensors, Actuators Microsystems Eurosensors XXXIII (TRANSDUCERS EUROSENSORS XXXIII)*, pages 250–253. IEEE, 2019. doi: 10.1109/TRANSDUCERS.2019.8808793.
- [13] Hongjie Hu, Xuan Zhu, Chonghe Wang, Lin Zhang, Xiaoshi Li, Seunghyun Lee, Zhenlong Huang, Ruimin Chen, Zeyu Chen, Chunfeng Wang, Yue Gu, Yimu Chen, Yusheng Lei, Tianjiao Zhang, NamHeon Kim, Yuxuan Guo, Yue Teng, Wenbo Zhou, Yang Li, Akihiro Nomoto, Simone Sternini, Qifa Zhou, Matt Pharr, Francesco Lanza di Scalea, and Sheng Xu. Stretchable ultrasonic transducer arrays for three-dimensional imaging on complex surfaces. *Science Advances*, 4(3):eaar3979, 2018. doi: 10.1126/sciadv.aar3979.
- [14] Ching-Hsiang Cheng, Chen Chao, Xiaomei Shi, and Wallace W. F. Leung. A flexible capacitive micromachined ultrasonic transducer (CMUT) array with increased effective capacitance from concave bottom electrodes for ultrasonic imaging applications. In *proceeding of IEEE Ultrason. Symp.*, pages 996–999. IEEE, 2009. doi: 10.1109/ULTSYM.2009.5441724.
- [15] Po-Fat Chong, Xiaomei Shi, and Ching-Hsiang Cheng. A novel flexible capacitive micromachined ultrasonic transducer (CMUT) array with isolated metallic islands riveted to a polymer film. In *proceeding of IEEE International Conference on Nano/Micro Engineered and Molecular Systems*, volume 1, pages 923–926. IEEE, 2013. doi: 10.1109/NEMS.2013.6559874.
- [16] Antonio Lanata, Enzo Pasquale Scilingo, and Danilo De Rossi. A multimodal

transducer for cardiopulmonary activity monitoring in emergency. *IEEE Transactions on Information Technology in Biomedicine*, 14(3):817–825, 2010. doi: 10.1109/titb.2009.2024414.

- [17] Chonghe Wang, Xiaoshi Li, Hongjie Hu, Lin Zhang, Zhenlong Huang, Muyang Lin, Zhuorui Zhang, Zhenan Yin, Brady Huang, Hua Gong, Shubha Bhaskaran, Yue Gu, Mitsutoshi Makihata, Yuxuan Guo, Yusheng Lei, Yimu Chen, Chunfeng Wang, Yang Li, Tianjiao Zhang, Zeyu Chen, Albert P. Pisano, Liangfang Zhang, Qifa Zhou, and Sheng Xu. Monitoring of the central blood pressure waveform via a conformal ultrasonic device. *Nature Biomedical Engineering*, 2(9):687–695, 2018. doi: 10.1038/s41551-018-0287-x.
- [18] A. Ferrone, F. Maita, L. Maiolo, M. Arquilla, A. Castiello, A. Pecora, X. Jiang, C. Menon, A. Ferrone, and L. Colace. Wearable band for hand gesture recognition based on strain sensors. In *Proceeding of IEEE International Conference on Biomedical Robotics and Biomechatronics (BioRob)*, pages 1319–1322. IEEE, 2016. doi: 10.1109/biorob.2016.7523814.
- [19] Le Cai, Li Song, Pingshan Luan, Qiang Zhang, Nan Zhang, Qingqing Gao, Duan Zhao, Xiao Zhang, Min Tu, Feng Yang, Wenbin Zhou, Qingxia Fan, Jun Luo, Weiya Zhou, Pulickel M. Ajayan, and Sishen Xie. Super-stretchable, Transparent Carbon Nanotube-Based Capacitive Strain Sensors for Human Motion Detection. *Scientific Reports*, 3(1):3048, 2013. doi: 10.1038/srep03048.
- [20] Sang Shengbo, Liu Lihua, Jian Aoqun, Duan Qianqian, Ji Jianlong, Zhang Qiang, and Zhang Wendong. Highly sensitive wearable strain sensor based on silver nanowires

and nanoparticles. *Nanotechnology*, 29(25):255202, 2018. doi: 10.1088/1361-6528/aabbba.

- [21] Yusuke Takei, Manabu Yoshida, Toshihiro Takeshita, and Takeshi Kobayashi. Wearable muscle training and monitoring device. In *Proceeding of IEEE Micro Electro Mechanical Systems (MEMS)*, pages 55–58. IEEE, 2018.
- [22] Xi Wang, Xiaoming Tao, Raymond C H So, Lin Shu, Bao Yang, and Ying Li. Monitoring elbow isometric contraction by novel wearable fabric sensing device. *Smart Materials and Structures*, 25(12):125022, 2016.
- [23] Aaron Belbasis and Franz Konstantin Fuss. Development of Next-generation Compression Apparel. *Procedia Technology*, 20:85–90, 2015. doi: 10.1016/j.protcy.2015.07.015.
- [24] Katherine Plewa, Matthew Silverman, Silvia Orlandi, Tom Chau, and Michael Thaut. Designing a wearable MMG-based mobile app for gait rehab. In *Proceeding of IEEE Life Sciences Conference (LSC)*, pages 238–241. IEEE, 2017. doi: 10.1109/lsc.2017.8268187.
- [25] Praveen Bhat and Ajay Gupta. A novel approach to detect localized muscle fatigue during isometric exercises. In *Proceeding of IEEE International Conference on Wearable and Implantable Body Sensor Networks (BSN)*, pages 224–229. IEEE, 2016. doi: 10.1109/bsn.2016.7516264.
- [26] Samuel Wilson and Ravi Vaidyanathan. Upper-limb prosthetic control using wearable multichannel mechanomyography. In *Proceeding of International Conference on Rehabilitation Robotics (ICORR)*, pages 1293–1298. IEEE, 2017.

- [27] Frank Mokaya, Roland Lucas, Hae Young Noh, and Pei Zhang. MyoVibe: vibration based wearable muscle activation detection in high mobility exercises. In *Proceeding of ACM International Joint Conference on Pervasive and Ubiquitous Computing*, pages 27–38. ACM Press, 2015. doi: 10.1145/2750858.2804258.
- [28] Weichao Guo, Xinjun Sheng, Honghai Liu, and Xiangyang Zhu. Mechanomyography assisted myoelectric sensing for upper-extremity prostheses: A hybrid approach. *IEEE Sensors Journal*, 17(10):3100–3108, 2017. doi: 10.1109/jsen.2017.2679806.
- [29] Christina Zong-Hao Ma, Yan To Ling, Queenie Tsung Kwan Shea, Li-Ke Wang, Xiao-Yun Wang, and Yong-Ping Zheng. Towards Wearable Comprehensive Capture and Analysis of Skeletal Muscle Activity during Human Locomotion. *Sensors*, 19(1): 195, 2019. doi: 10.3390/s19010195.
- [30] Rauno Álvaro de Paula Simola, Nico Harms, Christian Raeder, Michael Kellmann, Tim Meyer, Mark Pfeiffer, and Alexander Ferrauti. Tensiomyography reliability and prediction of changes in muscle force following heavy eccentric strength exercise using muscle mechanical properties. *Sports Technology*, 8(1-2):58–66, 2015. doi: 10.1080/19346182.2015.1117475.
- [31] Laura Seidl, Danijel Tosovic, and J. Mark Brown. Test-retest reliability and reproducibility of laser- versus contact-displacement sensors in mechanomyography: Implications for musculoskeletal research. *Journal of Applied Biomechanics*, 33(2): 130–136, 2017. doi: 10.1123/jab.2016-0085.
- [32] Claudio Orizio, Massimiliano Gobbo, and Bertrand Diemont. Changes of the force–frequency relationship in human tibialis anterior at fatigue. *Journal of Elec-*

- tromyography and Kinesiology*, 14(5):523–530, 2004. doi: 10.1016/j.jelekin.2004.03.009.
- [33] J. Celichowski and K. Grottel. The relationship between fusion index and stimulation frequency in tetani of motor units in rat medial gastrocnemius. *Archives italiennes de biologie*, 133(2):81–7, 1995.
- [34] S. Watanabe, T. Kitawaki, and H. Oka. Mathematical equation of fusion index of tetanic contraction of skeletal muscles. *Journal of Electromyography and Kinesiology*, 20(2):284–289, 2010. doi: 10.1016/j.jelekin.2009.02.007.
- [35] Robert C. Murry Thomas S. Curry, James E. Dowdey. Ultrasound. In *Christensen's physics of diagnostic radiology*, chapter 20, pages 323–371. Williams & Wilkins, Media, PA, USA, 1990.
- [36] David Dowsett, Patrick A Kenny, and R Eugene Johnston. Principles of ultrasound. In *The Physics of Diagnostic Imaging*, chapter 17, pages 511–529. Hodder Arnold, London, UK, 2 edition, 2006. doi: 10.1201/b13462.
- [37] Haim Azhari. Appendix a: Typical acoustic properties of tissues. In *Basics of Biomedical Ultrasound for Engineers*, pages 313–314. John Wiley & Sons, Inc., 2010. doi: 10.1002/9780470561478.app1.
- [38] Y. Yoshitake, H. Ue, M. Miyazaki, and T. Moritani. Assessment of lower-back muscle fatigue using electromyography, mechanomyography, and near-infrared spectroscopy. *European Journal of Applied Physiology*, 84(3):174–179, 2001. doi: 10.1007/s004210170001.
- [39] Mei Yee Ng, Maryam Pourmajidian, and Nur Azah Hamzaid. Mechanomyography

sensors for detection of muscle activities and fatigue during Fes-evoked contraction. In *Proceeding of IEEE International Functional Electrical Stimulation Society Annual Conference (IFESS)*, pages 1–3. IEEE, 2014. doi: 10.1109/ifess.2014.7036759.

- [40] K. Akataki, K. Mita, K. Itoh, N. Suzuki, and M. Watakabe. Acoustic and electrical activities during voluntary isometric contraction of biceps brachii muscles in patients with spastic cerebral palsy. *Muscle & Nerve*, 19(10):1252–1257, 1996. doi: 10.1002/(sici)1097-4598(199610)19:10<1252::aid-mus2>3.0.co;2-d.
- [41] S. W. Pedersen, E. Bäckman, and B. Öberg. Characteristics of tetanic muscle contraction in Parkinson patients. *Acta Neurologica Scandinavica*, 84(3):250–255, 1991. doi: 10.1111/j.1600-0404.1991.tb04946.x.
- [42] Esther Barreiro and Joaquim Gea. Respiratory and Limb Muscle Dysfunction in COPD. *Journal of Chronic Obstructive Pulmonary Disease (COPD)*, 12(4):413–426, 2015. doi: 10.3109/15412555.2014.974737.
- [43] Pedro S. Dias, Joan S. Fort, Daniel A. Marinho, Albano Santos, and Mario C. Marques. Tensiomyography in Physical Rehabilitation of High Level Athletes. *The Open Sports Sciences Journal*, 3(1):47–48, 2010. doi: 10.2174/1875399x010030100047.
- [44] Pedro Alvarez-Diaz, Eduard Alentorn-Geli, Silvia Ramon, Miguel Marin, Gilbert Steinbacher, Marta Rius, Roberto Seijas, Jordi Ballester, and Ramon Cugat. Effects of anterior cruciate ligament reconstruction on neuromuscular tensiomyographic characteristics of the lower extremity in competitive male soccer players. *Knee Surgery, Sports Traumatology, Arthroscopy*, 23(11):3407–3413, 2015. doi: 10.1007/s00167-014-3165-4.

- [45] Eduard Alentorn-Geli, Pedro Alvarez-Diaz, Silvia Ramon, Miguel Marin, Gilbert Steinbacher, Juan José Boffa, Xavier Cuscó, Jordi Ballester, and Ramon Cugat. Assessment of neuromuscular risk factors for anterior cruciate ligament injury through tensiomyography in male soccer players. *Knee Surgery, Sports Traumatology, Arthroscopy*, 23(9):2508–2513, 2015. doi: 10.1007/s00167-014-3018-1.
- [46] Lewis J Macgregor, Angus M Hunter, Claudio Orizio, Malcolm M Fairweather, and Massimiliano Ditroilo. Assessment of Skeletal Muscle Contractile Properties by Radial Displacement: The Case for Tensiomyography. *Sports medicine*, 48(7): 1607–1620, 2018. doi: 10.1007/s40279-018-0912-6.
- [47] Huijun Ding, Qing He, Lei Zeng, Yongjin Zhou, Minmin Shen, and Guo Dan. Motion intent recognition of individual fingers based on mechanomyogram. *Pattern Recognition Letters*, 88:41–48, 2017. doi: 10.1016/j.patrec.2017.01.012.
- [48] Kenneth R. Lyons, Sanjay S. Joshi, Sanjay S. Joshi, and Kenneth R. Lyons. Upper Limb Prosthesis Control for High-Level Amputees via Myoelectric Recognition of Leg Gestures. *IEEE transactions on neural systems and rehabilitation engineering : a publication of the IEEE Engineering in Medicine and Biology Society*, 26(5): 1056–1066, 2018. doi: 10.1109/tnsre.2018.2807360.
- [49] Joan Lobo-Prat, Peter N. Kooren, Arno HA Stienen, Just L. Herder, Bart FJM Koopman, and Peter H. Veltink. Non-invasive control interfaces for intention detection in active movement-assistive devices. *Journal of NeuroEngineering and Rehabilitation*, 11(1): 168, 2014. doi: 10.1186/1743-0003-11-168.
- [50] Domen Novak and Robert Riener. A survey of sensor fusion methods in wearable

- robotics. *Robotics and Autonomous Systems*, 73:155–170, 2015. doi: 10.1016/j.robot.2014.08.012.
- [51] RJ Baskin and PJ Paolini. Volume change and pressure development in muscle during contraction. *American Journal of Physiology-Legacy Content*, 213(4):1025–1030, 1967. doi: 10.1152/ajplegacy.1967.213.4.1025.
- [52] Vojko Valenčič and Nataša Knez. Measuring of Skeletal Muscles' Dynamic Properties. *Artificial Organs*, 21(3):240–242, 1997. doi: 10.1111/j.1525-1594.1997.tb04658.x.
- [53] Takanori Uchiyama, Kaito Saito, and Katsuya Shinjo. Muscle stiffness estimation using a system identification technique applied to evoked mechanomyogram during cycling exercise. *Journal of Electromyography and Kinesiology*, 25(6):847–852, 2015.
- [54] C. K. Thomas, B. Bigland-Richie, and R. S. Johansson. Force-frequency relationships of human thenar motor units. *Journal of Neurophysiology*, 65(6):1509–1516, 1991. doi: 10.1152/jn.1991.65.6.1509.
- [55] Nor Mohamad, Nur Hamzaid, Glen Davis, Ahmad Abdul Wahab, and Nazirah Hasnan. Mechanomyography and Torque during FES-Evoked Muscle Contractions to Fatigue in Individuals with Spinal Cord Injury. *Sensors*, 17(7):1627, 2017. doi: 10.3390/s17071627.
- [56] Brandon N. VanderVeen, Justin P. Hardee, Dennis K. Fix, and James A. Carson. Skeletal muscle function during the progression of cancer cachexia in the male Apc Min/+ mouse. *Journal of Applied Physiology*, 124(3):684–695, 2018.
- [57] Thimo Wiewelhove, Christian Raeder, Tim Meyer, Michael Kellmann, Mark Pfeiffer,

and Alexander Ferrauti. Markers for Routine Assessment of Fatigue and Recovery in Male and Female Team Sport Athletes during High-Intensity Interval Training. *PLOS ONE*, 10(10):e0139801, 2015. doi: 10.1371/journal.pone.0139801.

- [58] Sangit Sasidhar, Sanjib Kumar Panda, and Jianxin Xu. A wavelet feature based mechanomyography classification system for a wearable rehabilitation system for the elderly. In Jit Biswas, Hisato Kobayashi, Lawrence Wong, Bessam Abdulrazak, and Mounir Mokhtari, editors, *Inclusive Society: Health and Wellbeing in the Community, and Care at Home*, pages 45–52. Springer Berlin Heidelberg, 2013. doi: 10.1007/978-3-642-39470-6\_6.
- [59] Kazumi Masuda, Tadashi Masuda, Tsugutake Sadoyama, Mitsuharu Inaki, and Shigeru Katsuta. Changes in surface EMG parameters during static and dynamic fatiguing contractions. *Journal of Electromyography and Kinesiology*, 9(1):39–46, 1999. doi: 10.1016/s1050-6411(98)00021-2.
- [60] M.A. Cavalcanti Garcia and T.M. M. Vieira. Surface electromyography: Why, when and how to use it. *Revista Portuguesa De Pneumologia*, 4(1):17–28, 2011.
- [61] Morufu Olusola Ibitoye, Nur Azah Hamzaid, Jorge M. Zuniga, and Ahmad Khairi Abdul Wahab. Mechanomyography and muscle function assessment: A review of current state and prospects. *Clinical Biomechanics*, 29(6):691–704, 2014. doi: 10.1016/j.clinbiomech.2014.04.003.
- [62] Georgios I. Papagiannis, Athanasios I. Triantafyllou, Ilias M. Roumpelakis, Frantzeska Zampeli, Pinioti Garyfallia Eleni, Panayiotis Koulouvaris, Elias C. Papadopoulos, Panayiotis J. Papagelopoulos, and George C. Babis. Methodology of surface elec-

- tromyography in gait analysis: review of the literature. *Journal of Medical Engineering & Technology*, 43(1):59–65, 2019. doi: 10.1080/03091902.2019.1609610.
- [63] A.O. Posatskiy and T. Chau. The effects of motion artifact on mechanomyography: A comparative study of microphones and accelerometers. *Journal of Electromyography and Kinesiology*, 22(2):320–324, 2012. doi: 10.1016/j.jelekin.2011.09.004.
- [64] Wonkeun Youn and Jung Kim. Feasibility of using an artificial neural network model to estimate the elbow flexion force from mechanomyography. *Journal of Neuroscience Methods*, 194(2):386–393, 2011. doi: 10.1016/j.jneumeth.2010.11.003.
- [65] Levon N. Nazarian. The Top 10 Reasons Musculoskeletal Sonography Is an Important Complementary or Alternative Technique to MRI. *American Journal of Roentgenology*, 190(6):1621–1626, 2008. doi: 10.2214/ajr.07.3385.
- [66] P.W. Hodges, L.H.M. Pengel, R.D. Herbert, and S.C. Gandevia. Measurement of muscle contraction with ultrasound imaging. *Muscle & Nerve*, 27(6):682–692, 2003. doi: 10.1002/mus.10375.
- [67] Li Khim Kwah, Rafael Z. Pinto, Joanna Diong, and Robert D. Herbert. Reliability and validity of ultrasound measurements of muscle fascicle length and pennation in humans: A systematic review. *Journal of Applied Physiology*, 114(6):761–769, 2013. doi: 10.1152/jappphysiol.01430.2011.
- [68] Tayla E. Kuehne, Noam Yitzchaki, Matthew B. Jessee, B. Sue Graves, and Samuel L. Buckner. A comparison of acute changes in muscle thickness between A-mode and B-mode ultrasound. *Physiological Measurement*, 40(11):0–6, 2019. doi: 10.1088/1361-6579/ab4f14.

- [69] Dale R. Wagner, Brennan J. Thompson, D. Andy Anderson, and Sarah Schwartz. A-mode and B-mode ultrasound measurement of fat thickness: a cadaver validation study. *European Journal of Clinical Nutrition*, 73(4):518–523, 2019. doi: 10.1038/s41430-018-0085-2.
- [70] Ibrahim AlMohimeed. Development of Wearable Ultrasonic Sensors for Monitoring Muscle Contraction. Master’s thesis, Carleton University, 2013.
- [71] R.G. G Swartz and J.D. D Plummer. On the Generation of High-Frequency Acoustic Energy with Polyvinylidene Fluoride. *IEEE Transactions on Sonics and Ultrasonics*, 27(6):295–302, 1980. doi: 10.1109/T-SU.1980.31193.
- [72] L.F. Brown. Design considerations for piezoelectric polymer ultrasound transducers. *IEEE Transactions on Ultrasonics, Ferroelectrics and Frequency Control*, 47(6):1377–96, 2000. doi: 10.1109/58.883527.
- [73] Warren P Mason. *Properties and Equivalent Circuit of Transducer Materials*, chapter 3. D. Van Nostrand Company, 1958.
- [74] Ibrahim AlMohimeed and Yuu Ono. Ultrasound measurement of skeletal muscle contractile parameters using flexible and wearable single-element ultrasonic sensor. *Sensors*, 20(13):3616, 2020. doi: 10.3390/s20133616.
- [75] Ibrahim AlMohimeed and Yuu Ono. Flexible and wearable ultrasonic sensor for assessment of skeletal muscle contractile properties. In *proceeding of IEEE International Conference on Flexible and Printable Sensors and Systems (FLEPS)*. IEEE, 2019. doi: 10.1109/fleps.2019.8792301.
- [76] Ibrahim AlMohimeed, Manas Agarwal, and Yuu Ono. Wearable Ultrasonic Sensor

- Using Double-Layer PVDF Films for Monitoring Tissue Motion. In *proceeding of IEEE Canadian Conference on Electrical & Computer Engineering (CCECE)*, pages 1–4, 2018. doi: 10.1109/ccece.2018.8447859.
- [77] Elliot Yeung, Ibrahim AlMohimeed, and Yuu Ono. Ultrasonic sensor and method for monitoring of skeletal muscle contraction evoked by electromyostimulation. In *proceeding of international symposium on advanced biomedical ultrasound*, pages 1–2, 2020.
- [78] Elliot Yeung, Ibrahim AlMohimeed, and Yuu Ono. Estimation of tissue thickness changes due to electrical muscle stimulation using wearable ultrasonic sensor in pulse echo mode. In *proceeding of IEEE Sensors*, pages 1–4. IEEE, 2019. doi: 10.1109/sensors43011.2019.8956742.
- [79] Kenneth S. Saladin, Stephen J. Sullivan, and Christina A. Gan. *Human Anatomy*, chapter 10, pages 235–262. McGraw-Hill, New York, NY, USA, 5th edition, 2017.
- [80] Bryan Derrickson Gerard J. Tortora. *Introduction to the Human Body: The Essentials of Anatomy and Physiology*, volume 1. John Wiley & Sons, 9th edition, 2012.
- [81] Julie McDowell. *Encyclopedia of human body systems*. Greenwood, 2010.
- [82] Lauralee Sherwood. *Human physiology: from cells to systems*. Brooks/Cole, 7th edition, 2010.
- [83] Elaine Nicpon Marieb and Katja Hoehn. *Human anatomy and physiology*. Pearson, 7th edition, 2007.
- [84] Ingo Morano. Muscles and motility. In *Neurosciences - From Molecule to Behavior:*

*a university textbook*, chapter 22, pages 461–478. Springer Berlin Heidelberg, 2013. doi: 10.1007/978-3-642-10769-6\_22.

- [85] Amy Adams. The Muscular System. In Julie McDowell, editor, *Encyclopedia of human body systems*, chapter 7, pages 323–378. Greenwood, 2010.
- [86] Yasuhide Yoshitake, Yasuo Kawakami, Hiroaki Kanehisa, and Tetsuo Fukunaga. Surface Mechanomyogram Reflects Length Changes in Fascicles of Human Skeletal muscles. *International Journal of Sport and Health Science*, 3(Special\_Issue): 280–285, 2005.
- [87] V. Linnamo, T. Moritani, C. Nicol, and P.V Komi. Motor unit activation patterns during isometric, concentric and eccentric actions at different force levels. *Journal of Electromyography and Kinesiology*, 13(1):93–101, 2003. doi: 10.1016/s1050-6411(02)00063-9.
- [88] Charles F. Bolton, Anthony Parkes, Terry R. Thompson, Michael R. Clark, and Chris J. Sterne. Recording sound from human skeletal muscle: Technical and physiological aspects. *Muscle & Nerve*, 12(2):126–134, 1989. doi: 10.1002/mus.880120207.
- [89] Jeffery R. Stout, Terry J. Housh, Glen O. Johnson, Tammy K. Evetovich, and Douglas B. Smith. Mechanomyography and oxygen consumption during incremental cycle ergometry. *European Journal of Applied Physiology*, 76(4):363–367, 1997.
- [90] Ligia D Rusu, Germina GH Cosma, Sorina M Cernaianu, Mihnea N Marin, Petre Florinel A Rusu, Daniel P Ciocănescu, and Florin N Neferu. Tensiomyography method used for neuromuscular assessment of muscle training. *Journal of NeuroEngineering and Rehabilitation*, 10(1):67, 2013. doi: 10.1186/1743-0003-10-67.

- [91] Heloyse Uliam Kuriki, Fabio Micolis de Azevedo, Luciana Sanae Ota Takahashi, Emanuelle Moraes Mello, Ruben de Faria Negrao Filho, and Neri Alves. The Relationship Between Electromyography and Muscle Force. In Mark Schwartz, editor, *EMG Methods for Evaluating Muscle and Nerve Function*, chapter 3, pages 31–54. InTech, 2012. doi: 10.5772/25381.
- [92] Rubana Chowdhury, Mamun Reaz, Mohd Ali, Ashrif Bakar, Kalaivani Chellappan, and Tae Chang. Surface electromyography signal processing and classification techniques. *Sensors*, 13(9):12431–12466, 2013. doi: 10.3390/s130912431.
- [93] D. Farina, R Merletti, and D. F. Stegeman. Biophysics of the Generation of EMG Signals. In Roberto Merletti and Philip Parker, editors, *Electromyography*, volume c, pages 81–105. John Wiley & Sons, Inc., 2005. doi: 10.1002/0471678384.ch4.
- [94] Claudio Orizio, Diego Liberati, Cecilia Locatelli, Domenico De Grandis, and Arsenio Veicsteinas. Surface mechanomyogram reflects muscle fibres twitches summation. *Journal of Biomechanics*, 29(4):475–481, 1996. doi: 10.1016/0021-9290(95)00063-1.
- [95] Md Anamul Islam, Kenneth Sundaraj, R. Badlishah Ahmad, Nizam Uddin Ahamed, and Md Asraf Ali. Mechanomyography sensor development, related signal processing, and applications: A systematic review. *IEEE Sensors Journal*, 13(7):2499–2516, 2013. doi: 10.1109/jsen.2013.2255982.
- [96] Irsa Talib, Kenneth Sundaraj, Chee Kiang Lam, and Sebastian Sundaraj. A systematic review of muscle activity assessment of the biceps brachii muscle using mechanomyography. *Journal of musculoskeletal & neuronal interactions*, 18(4): 446–462, 2018.

- [97] Travis W. Beck, Terry J. Housh, Glen O. Johnson, Joseph P. Weir, Joel T. Cramer, Jared W. Coburn, and Moh H. Malek. Comparison of a piezoelectric contact sensor and an accelerometer for examining mechanomyographic amplitude and mean power frequency versus torque relationships during isokinetic and isometric muscle actions of the biceps brachii. *Journal of Electromyography and Kinesiology*, 16(4):324–335, 2006. doi: 10.1016/j.jelekin.2005.07.013.
- [98] M. Watakabe, K. Mita, K. Akataki, and Y. Itoh. Mechanical behaviour of condenser microphone in mechanomyography. *Medical & Biological Engineering & Computing*, 39(2):195–201, 2001. doi: 10.1007/BF02344804.
- [99] Simon Krašna, Srđan Đorđević, Marija Hribernik, and Ana Trajkovski. A Novel Approach to Measuring Muscle Mechanics in Vehicle Collision Conditions. *Sensors*, 17(6):1389, 2017. doi: 10.3390/s17061389.
- [100] M. Watakabe, Katsumi Mita, K. Akataki, and K. Ito. Reliability of the mechanomyogram detected with an accelerometer during voluntary contractions. *Medical & Biological Engineering & Computing*, 41(2):198–202, 2003. doi: 10.1007/BF02344888.
- [101] Matthew S. Stock, Travis W. Beck, Jason M. DeFreitas, and Michael A. Dillon. Linearity and reliability of the mechanomyographic amplitude versus dynamic torque relationships for the superficial quadriceps femoris muscles. *Muscle & Nerve*, 41(3): 342–349, 2010. doi: 10.1002/mus.21491.
- [102] T. Uchiyama and K. Shinohara. System identification of mechanomyograms detected with an acceleration sensor and a laser displacement meter. In *Proceeding of IEEE Engineering in Medicine and Biology Society*, pages 7131–7134. IEEE, 2011. doi: 10.1109/iembs.2011.6091802.

- [103] D. Tosovic, C. Than, and J. M. M. Brown. The effects of accumulated muscle fatigue on the mechanomyographic waveform: implications for injury prediction. *European Journal of Applied Physiology*, 116(8):1485–1494, 2016. doi: 10.1007/s00421-016-3398-7.
- [104] Christian Than, Laura Seidl, Danijel Tosovic, and J. Mark Brown. Test-retest reliability of laser displacement mechanomyography in paraspinal muscles while in lumbar extension or flexion. *Journal of Electromyography and Kinesiology*, 41:60–65, 2018. doi: 10.1016/j.jelekin.2018.05.001.
- [105] R. Dahmane, V. Valenčič, N. Knez, and I. Eržen. Evaluation of the ability to make non-invasive estimation of muscle contractile properties on the basis of the muscle belly response. *Medical & Biological Engineering & Computing*, 39(1):51–55, 2001. doi: 10.1007/bf02345266.
- [106] D. McAndrew, M. Gorelick, and J. M. M. Brown. MUSCLES WITHIN MUSCLES: A MECHANOMYOGRAPHIC ANALYSIS OF MUSCLE SEGMENT CONTRACTILE PROPERTIES WITHIN HUMAN GLUTEUS MAXIMUS. *Journal of Musculoskeletal Research*, 10(01):23–35, 2006. doi: 10.1142/s0218957706001704.
- [107] Dejan Križaj, Boštjan Šimunič, and Tomaž Žagar. Short-term repeatability of parameters extracted from radial displacement of muscle belly. *Journal of Electromyography and Kinesiology*, 18(4):645–651, 2008. doi: 10.1016/j.jelekin.2007.01.008.
- [108] Saúl Martín-Rodríguez, Irineu Loturco, Angus M. Hunter, David Rodríguez-Ruiz, and Diego Munguia-Izquierdo. Reliability and measurement error of tensiomyography to assess mechanical muscle function. *Journal of Strength and Conditioning Research*, 31(12):3524–3536, 2017. doi: 10.1519/JSC.0000000000002250.

- [109] Juan Manuel García-manso, David Rodríguez-Ruiz, Dario Rodríguez-Matoso, Yves de Saa, Samuel Sarmiento, and Miriam Quiroga. Assessment of muscle fatigue after an ultra-endurance triathlon using tensiomyography (TMG). *Journal of Sports Sciences*, 29(6):619–625, 2011. doi: 10.1080/02640414.2010.548822.
- [110] Ezequiel Rey, Carlos Lago-Peñas, and Joaquín Lago-Ballesteros. Tensiomyography of selected lower-limb muscles in professional soccer players. *Journal of Electromyography and Kinesiology*, 22(6):866–872, 2012. doi: 10.1016/j.jelekin.2012.06.003.
- [111] M. L. Gorelick and J. M. M. Brown. Mechanomyographic assessment of contractile properties within seven segments of the human deltoid muscle. *European Journal of Applied Physiology*, 100(1):35–44, 2007. doi: 10.1007/s00421-007-0397-8.
- [112] Danijel Tosovic, Laura Seidl, Estifanos Ghebremedhin, and Mark J. Brown. Determining minimal stimulus intensity for mechanomyographic analysis. *Journal of Electromyography and Kinesiology*, 25(5):749–753, 2015. doi: 10.1016/j.jelekin.2015.06.003.
- [113] Oscar García-García, Alba Cuba-Dorado, Tania Álvarez-Yates, Javier Carballo-López, and Mario Iglesias-Caamaño. Clinical utility of tensiomyography for muscle function analysis in athletes. *Open Access Journal of Sports Medicine*, Volume 10:49–69, 2019. doi: 10.2147/OAJSM.S161485.
- [114] Thimo Wiewelhove, Christian Raeder, Rauno Alvaro de Paula Simola, Christoph Schneider, Alexander Döweling, and Alexander Ferrauti. Tensiomyographic Markers Are Not Sensitive for Monitoring Muscle Fatigue in Elite Youth Athletes: A Pilot Study. *Frontiers in Physiology*, 8(JUN):1–9, 2017. doi: 10.3389/fphys.2017.00406.

- [115] Tetsuya Kimura, Mami Fujibayashi, Seitaro Tanaka, and Toshio Moritani. Mechanomyographic responses in quadriceps muscles during fatigue by continuous cycle exercise. *European Journal of Applied Physiology*, 104(4):651–656, 2008. doi: 10.1007/s00421-008-0816-5.
- [116] Morufu Ibitoye, Nur Hamzaid, Jorge Zuniga, Nazirah Hasnan, and Ahmad Wahab. Mechanomyographic Parameter Extraction Methods: An Appraisal for Clinical Applications. *Sensors*, 14(12):22940–22970, 2014. doi: 10.3390/s141222940.
- [117] Eddy Krueger, Eduardo M. Scheeren, Guilherme N. Nogueira-Neto, Eduardo Borba Neves, Vera Lúcia S. N. Button, and Percy Nohama. Influence of Skinfold Thickness in Mechanomyography Features. In *Proceeding of World Congress on Medical Physics and Biomedical Engineering*, pages 2030–2033. Springer Berlin Heidelberg, 2013. doi: 10.1007/978-3-642-29305-4\\_533.
- [118] Jun Shi, Yongping Zheng, Xin Chen, and Hongbo Xie. Modeling the relationship between wrist angle and muscle thickness during wrist flexion-extension based on the bone-muscle lever system: A comparison study. *Medical Engineering and Physics*, 31(10):1255–1260, 2009. doi: 10.1016/j.medengphy.2009.08.003.
- [119] Xin Chen, Yong Ping Zheng, Jing Yi Guo, and Jun Shi. Sonomyography (smg) control for powered prosthetic hand: A Study with normal subjects. *Ultrasound in Medicine and Biology*, 36(7):1076–1088, 2010. doi: 10.1016/j.ultrasmedbio.2010.04.015.
- [120] Terry K.K. Koo, Chunwah Wong, and Yongping Zheng. Reliability of Sonomyography for Pectoralis Major Thickness Measurement. *Journal of Manipulative and Physiological Therapeutics*, 33(5):386–394, 2010. doi: 10.1016/j.jmpt.2010.05.009.

- [121] Jackie L. Whittaker and Maria Stokes. Ultrasound Imaging and Muscle Function. *Journal of Orthopaedic & Sports Physical Therapy*, 41(8):572–580, 2011. doi: 10.2519/jospt.2011.3682.
- [122] Xin Chen, Yong Ping Zheng, Jing Yi Guo, Zhenyu Zhu, Shing Chow Chan, and Zhiguo Zhang. Sonomyographic responses during voluntary isometric ramp contraction of the human rectus femoris muscle. *European Journal of Applied Physiology*, 112(7): 2603–2614, 2012. doi: 10.1007/s00421-011-2227-2.
- [123] Guangquan Zhou and Yong ping Zheng. Human motion analysis with ultrasound and sonomyography. In *proceeding of IEEE Engineering in Medicine and Biology Society*, pages 6479–6482. IEEE, 2012. doi: 10.1109/embc.2012.6347478.
- [124] Angela V. Dieterich, Christine M. Pickard, Geoffrey R. Strauss, Louise E. Deshon, William Gibson, and Janice McKay. Muscle thickness measurements to estimate gluteus medius and minimus activity levels. *Manual Therapy*, 19(5):453–460, 2014. doi: 10.1016/j.math.2014.04.014.
- [125] Jizhou Li, Yongjin Zhou, Yi Lu, Guangquan Zhou, Lei Wang, and Yong Ping Zheng. The sensitive and efficient detection of quadriceps muscle thickness changes in cross-sectional plane using ultrasonography: A feasibility investigation. *IEEE Journal of Biomedical and Health Informatics*, 18(2):628–635, 2014. doi: 10.1109/JBHI.2013.2275002.
- [126] Shuang Qiu, Jing Feng, Jiapeng Xu, Rui Xu, Xin Zhao, Peng Zhou, Hongzhi Qi, Lixin Zhang, and Dong Ming. Sonomyography Analysis on Thickness of Skeletal Muscle during Dynamic Contraction Induced by Neuromuscular Electrical Stimulation: A

- Pilot Study. *IEEE Transactions on Neural Systems and Rehabilitation Engineering*, 25(1):59–67, 2017. doi: 10.1109/TNSRE.2016.2556687.
- [127] Xin Chen, Xudong Zhang, Wenxiu Shi, Jun Wang, Yun Xiang, Yongjin Zhou, and Wan-Zhang Yang. Ultrasonic Measurement of Dynamic Muscle Behavior for Poststroke Hemiparetic Gait. *BioMed Research International*, 2017:1–8, 2017. doi: 10.1155/2017/8208764.
- [128] Guang Quan Zhou, Yong Ping Zheng, and Ping Zhou. Measurement of Gender Differences of Gastrocnemius Muscle and Tendon Using Sonomyography during Calf Raises: A Pilot Study. *BioMed Research International*, 2017, 2017. doi: 10.1155/2017/6783824.
- [129] Mohammad Hassan Jahanandish, Nicholas P. Fey, and Kenneth Hoyt. Lower Limb Motion Estimation Using Ultrasound Imaging: A Framework for Assistive Device Control. *IEEE Journal of Biomedical and Health Informatics*, 23(6):2505–2514, 2019. doi: 10.1109/JBHI.2019.2891997.
- [130] Xingchen Yang, Jipeng Yan, and Honghai Liu. Comparative Analysis of Wearable A-mode Ultrasound and sEMG for Muscle-Computer Interface. *IEEE Transactions on Biomedical Engineering*, PP(c):1–1, 2019. doi: 10.1109/tbme.2019.2962499.
- [131] Gabriela Macedo Fraiz, Luiza Herminia Gallo, Estela Iraci Rabito, Anna Raquel Silveira Gomes, and Maria Eliana Madalozzo Schieferdecker. Relationship between muscle thickness and calf circumference in healthy older women. *Archives of Gerontology and Geriatrics*, 86(September 2019):103942, 2020. doi: 10.1016/j.archger.2019.103942.

- [132] Alon Abraham, Vivian E. Drory, Yaara Fainmesser, Leif E. Lovblom, and Vera Bril. Quantitative sonographic evaluation of muscle thickness and fasciculation prevalence in healthy subjects. *Muscle and Nerve*, 61(2):234–238, 2020. doi: 10.1002/mus.26758.
- [133] Alon Abraham, Vivian E. Drory, Yaara Fainmesser, Avi A. Algom, Leif E. Lovblom, and Vera Bril. Muscle thickness measured by ultrasound is reduced in neuromuscular disorders and correlates with clinical and electrophysiological findings. *Muscle and Nerve*, 60(6):687–692, 2019. doi: 10.1002/mus.26693.
- [134] J Sallinen, T Ojanen, L Karavirta, J P Ahtiainen, and K Häkkinen. Muscle mass and strength, body composition and dietary intake in master strength athletes vs untrained men of different ages. *The Journal of sports medicine and physical fitness*, 48(2): 190–6, 2008.
- [135] Juha P. Ahtiainen, Simon Walker, Heikki Peltonen, Jarkko Holviala, Elina Sillanpää, Laura Karavirta, Janne Sallinen, Jussi Mikkola, Heli Valkeinen, Antti Mero, Juha J. Hulmi, and Keijo Häkkinen. Heterogeneity in resistance training-induced muscle strength and mass responses in men and women of different ages. *AGE*, 38(1):10, 2016. doi: 10.1007/s11357-015-9870-1.
- [136] Konrad Mahlfeld, Jörg Franke, and Friedemann Awiszus. Postcontraction changes of muscle architecture in human quadriceps muscle. *Muscle & Nerve*, 29(4):597–600, 2004. doi: 10.1002/mus.20021.
- [137] M V Narici, T Binzoni, E Hiltbrand, J Fasel, F Terrier, and P Cerretelli. In vivo human gastrocnemius architecture with changing joint angle at rest and during graded isometric contraction. *The Journal of Physiology*, 496(1):287–297, 1996. doi: 10.1113/jphysiol.1996.sp021685.

- [138] Neil D. Reeves, Constantinos N. Maganaris, and Marco V. Narici. Ultrasonographic assessment of human skeletal muscle size. *European Journal of Applied Physiology*, 91(1):116–118, 2004. doi: 10.1007/s00421-003-0961-9.
- [139] Tetsuo Fukunaga, Keitaro Kubo, Yasuo Kawakami, Senshi Fukashiro, Hiroaki Kanehisa, and Constantinos N. Maganaris. In vivo behaviour of human muscle tendon during walking. *Proceedings of the Royal Society of London. Series B: Biological Sciences*, 268(1464):229–233, 2001. doi: 10.1098/rspb.2000.1361.
- [140] Jerry L Prince and Jonathan M Links. The Physics of Ultrasound. In *Medical imaging signals and systems*, chapter 10, pages 335– 362. Pearson, 2 edition, 2006.
- [141] Jason Silver, Yuu Ono, and Andy Adler. An ultrasonic technique for imaging of tissue motion due to muscle contraction. In *proceeding of IEEE International Ultrasonics Symposium*, pages 2441–2444. IEEE, 2009. doi: 10.1109/ULTSYM.2009.5441477.
- [142] Jing Yi Guo, Yong Ping Zheng, Qing Hua Huang, Xin Chen, Jun Feng He, and Helen Lai-Wa Chan. Performances of One-Dimensional Sonomyography and Surface Electromyography in Tracking Guided Patterns of Wrist Extension. *Ultrasound in Medicine and Biology*, 35(6):894–902, 2009. doi: 10.1016/j.ultrasmedbio.2008.11.017.
- [143] Nalinda Hettiarachchi, Zhaojie Ju, and Honghai Liu. A New Wearable Ultrasound Muscle Activity Sensing System for Dexterous Prosthetic Control. In *Proceeding of IEEE International Conference on Systems, Man, and Cybernetics*, pages 1415–1420, 2015. doi: 10.1109/smc.2015.251.
- [144] Amirhossein Shahshahani, Zeljko Zilic, and Sharmistha Bhadra. A 4-channel piezo transducer based flexible hybrid sensor for respiratory monitoring. In *proceeding*

- of *IEEE International Conference on Flexible and Printable Sensors and Systems (FLEPS)*, pages 4–6. IEEE, 2019. doi: 10.1109/fleps.2019.8792242.
- [145] Carlos D. Gerardo, Edmond Cretu, and Robert Rohling. Fabrication and testing of polymer-based capacitive micromachined ultrasound transducers for medical imaging. *Microsystems Nanoeng.*, 4(1), 2018. doi: 10.1038/s41378-018-0022-5.
- [146] Ibrahim AlMohimeed, Hisham Turkistani, and Yuu Ono. Development of wearable and flexible ultrasonic sensor for skeletal muscle monitoring. In *proceeding of IEEE International Ultrasonics Symposium (IUS)*, pages 1137–1140. IEEE, 2013. doi: 10.1109/ultsym.2013.0291.
- [147] Hisham Turkistani, Ibrahim AlMohimeed, and Yuu Ono. Continuous monitoring of muscle thickness changes during isometric contraction using a wearable ultrasonic sensor. In *proceeding of Canadian Medical and Biological Engineering Society (CMBES)*, volume 36, 2013.
- [148] F.S. Foster, K.A. Harasiewicz, and M.D. Sherar. A history of medical and biological imaging with polyvinylidene fluoride (PVDF) transducers. *IEEE Transactions on Ultrasonics, Ferroelectrics and Frequency Control*, 47(6):1363–1371, 2000. doi: 10.1109/58.883525.
- [149] Rayyan Manwar, Karl Kratkiewicz, and Kamran Avanaki. Overview of ultrasound detection technologies for photoacoustic imaging. *Micromachines*, 11(7):692, 2020. doi: 10.3390/mi11070692.
- [150] Meaghan A O'Reilly and Kullervo Hynynen. A PVDF receiver for ultrasound monitoring of transcranial focused ultrasound therapy. *IEEE Transactions on Biomedical Engineering*, 57(9):2286–2294, 2010. doi: 10.1109/tbme.2010.2050483.

- [151] M.D. Sherar and F.S. Foster. The design and fabrication of high frequency poly(vinylidene fluoride) transducers. *Ultrasonic Imaging*, 11(2):75–94, 1989. doi: 10.1177/016173468901100201.
- [152] Dan-Dan Zheng, Yang Mao, and Sheng-Hong Lv. Research and validation of design principles for PVDF wideband ultrasonic transducers based on an equivalent circuit model. *Measurement*, 141:324–331, 2019. doi: 10.1016/j.measurement.2019.04.050.
- [153] Saleem Khan and Leandro Lorenzelli. Recent advances of conductive nanocomposites in printed and flexible electronics. *Smart Materials and Structures*, 26(8):083001, 2017. doi: 10.1088/1361-665x/aa7373.
- [154] Byeong Wan An, Jung Hwal Shin, So-Yun Kim, Joohee Kim, Sangyoon Ji, Jihun Park, Youngjin Lee, Jiuk Jang, Young-Geun Park, Eunjin Cho, Subin Jo, and Jang-Ung Park. Smart Sensor Systems for Wearable Electronic Devices. *Polymers*, 9(12):303, 2017. doi: 10.3390/polym9080303.
- [155] Shayan Seyedin, Peng Zhang, Maryam Naebe, Si Qin, Jun Chen, Xungai Wang, and Joselito M. Razal. Textile strain sensors: a review of the fabrication technologies, performance evaluation and applications. *Materials Horizons*, 6(2):219–249, 2019.
- [156] J. McLaren, R. J.N. Helmer, S. L. Horne, and I. Blanchonette. Preliminary development of a wearable device for dynamic pressure measurement in garments. *Procedia Engineering*, 2(2):3041–3046, 2010. doi: 10.1016/j.proeng.2010.04.108.
- [157] Frank O. Mokaya, Brian Nguyen, Cynthia Kuo, Quinn Jacobson, Anthony Rowe, and Pei Zhang. MARS: A Muscle Activity Recognition System enabling self-configuring musculoskeletal sensor networks. In *Proceeding of ACM/IEEE International Confer-*

- ence on Information Processing in Sensor Networks (IPSN)*, volume 2, pages 191–202, 2013. doi: 10.1145/2461381.2461406.
- [158] Hiroji Ohigashi. Ultrasonic transducers in the megahertz range. In T T Wang, J M Herbert, and A M Glass, editors, *The Application of Ferroelectric Polymers*, chapter 11, pages 237–273. Blackie, 1987.
- [159] Henno Allik and Thomas J. R. Hughes. Finite element method for piezoelectric vibration. *International Journal for Numerical Methods in Engineering*, 2(2):151–157, 1970. doi: 10.1002/nme.1620020202.
- [160] R. Lerch. Finite element analysis of piezoelectric transducers. In *IEEE Ultrasonics Symposium Proceedings.*, volume 2, pages 643–654. IEEE, 1988. doi: 10.1109/ultsym.1988.49457.
- [161] Vinh-Tan Nguyen, Pankaj Kumar, and Jason Leong. Finite element modelling and simulations of piezoelectric actuators responses with uncertainty quantification. *Computation*, 6(4):60, 2018. doi: 10.3390/computation6040060.
- [162] Gerges Dib, Michael Larche, Aaron A. Diaz, Susan L. Crawford, Matthew S. Prowant, and Michael T. Anderson. Experimental validation of ultrasonic NDE simulation software. In *proceeding of American Institute of Physics*. AIP Publishing LLC, 2016. doi: 10.1063/1.4940627.
- [163] Sushanta Kundu and Harshal B. Nemade. Modeling and simulation of a piezoelectric vibration energy harvester. *Procedia Engineering*, 144:568–575, 2016. doi: 10.1016/j.proeng.2016.05.043.
- [164] Tarjei Rommetveit, Tonni F. Johansen, and Roy Johnsen. Using a multi-layered

- transducer model to estimate the properties of paraffin wax deposited on steel. *Ultrasonics*, 51(1):85–93, 2011. doi: 10.1016/j.ultras.2010.06.002.
- [165] Ming zhu CHEN, Qiao zhen ZHANG, Xiang yong ZHAO, and Fei fei WANG. Modeling and simulation of aluminium nitride-based piezoelectric micromachined ultrasonic transducer for ultrasound imaging. In *proceeding of Piezoelectricity, Acoustic Waves and Device Applications (SPAWDA)*. IEEE, 2019. doi: 10.1109/SPAWDA48812.2019.9019254.
- [166] Yongrae Roh and Kookjin Kang. Analysis and design of a flextensional transducer by means of the finite element method. *Japanese Journal of Applied Physics*, 47(5): 3997–4002, 2008. doi: 10.1143/JJAP.47.3997.
- [167] Reshmi Maity, Kalpana Gogoi, and N. P. Maity. Micro-electro-mechanical-system based capacitive ultrasonic transducer as an efficient immersion sensor. *Microsystem Technologies*, 25(12):4663–4670, 2019. doi: 10.1007/s00542-019-04384-5.
- [168] Dongdong Chen, Chenxue Hou, Chunlong Fei, Di Li, Pengfei Lin, Jun Chen, and Yintang Yang. An optimization design strategy of 1–3 piezocomposite ultrasonic transducer for imaging applications. *Materials Today Communications*, 24:100991, 2020. doi: 10.1016/j.mtcomm.2020.100991.
- [169] B. Patzák and Z. Bittnar. OOFEM: An object oriented framework for finite element analysis. *Journal of Advanced Engineering*, 44(5-6):54–60, 2004. doi: 10.4203/ccp.80.54.
- [170] Bořek Patzák. Oofem - an object-oriented simulation tool for advanced modeling of materials and structures. *Journal of Advanced Engineering*, 52(6):59–66, 2012. cited By 72.

- [171] Kin Wing Kwok, H.L.W. Chan, and C.L. Choy. Evaluation of the material parameters of piezoelectric materials by various methods. *IEEE Transactions on Ultrasonics, Ferroelectrics and Frequency Control*, 44(4):733–742, 1997. doi: 10.1109/58.655188.
- [172] Warren P Mason. *Electromechanical Transducer and Wave Filters*. Van Nostrand Reinhold, 2nd edition, 1948.
- [173] M. Redwood. Transient performance of a piezoelectric transducer. *The Journal of the Acoustical Society of America*, 33(4):527–536, 1961. doi: 10.1121/1.1908709.
- [174] R. Krimholtz, D.A. Leedom, and G.L. Matthaei. New equivalent circuits for elementary piezoelectric transducers. *Electronics Letters*, 6(13):398, 1970. doi: 10.1049/el:19700280.
- [175] D.A. Leedom, R. Krimholtz, and G.L. Matthaei. Equivalent circuits for transducers having arbitrary even- or odd-symmetry piezoelectric excitation. *IEEE Transactions on Sonics and Ultrasonics*, 18(3):128–141, 1971. doi: 10.1109/t-su.1971.29608.
- [176] T.L. Rhyne. An improved interpretation of mason's model for piezoelectric plate transducers. *IEEE Transactions on Sonics and Ultrasonics*, 25(2):98–103, 1978. doi: 10.1109/t-su.1978.30994.
- [177] W.M. Leach. Controlled-source analogous circuits and SPICE models for piezoelectric transducers. *IEEE Transactions on Ultrasonics, Ferroelectrics and Frequency Control*, 41(1):60–66, 1994. doi: 10.1109/58.265821.
- [178] Stewart Sherrit, Sean P. Leary, Benjamin P. Dolgin, and Yoseph Bar-Cohen. Comparison of the mason and KLM equivalent circuits for piezoelectric resonators in the

- thickness mode. In *proceeding of IEEE Ultrasonics Symposium*, volume 2, pages 921–926. IEEE, 1999. doi: 10.1109/ultsym.1999.849139.
- [179] Heiji Kawai. The piezoelectricity of poly (vinylidene fluoride). *Japanese Journal of Applied Physics*, 8(7):975–976, 1969. doi: <https://doi.org/10.1143/JJAP.8.975>.
- [180] R. Holland. Representation of dielectric, elastic, and piezoelectric losses by complex coefficients. *IEEE Transactions on Sonics and Ultrasonics*, 14(1):18–20, 1967. doi: 10.1109/t-su.1967.29405.
- [181] H. Ohigashi, K. Koga, M. Suzuki, T. Nakanishi, K. Kimura, and N. Hashimoto. Piezoelectric and ferroelectric properties of p (VDF-TrFE) copolymers and their application to ultrasonic transducers. *Ferroelectrics*, 60(1):263–276, 1984. doi: 10.1080/00150198408017527.
- [182] E.K. Sittig. Transmission parameters of thickness-driven piezoelectric transducers arranged in multilayer configurations. *IEEE Transactions on Sonics and Ultrasonics*, 14(4):167–174, 1967. doi: 10.1109/t-su.1967.29434.
- [183] Qian Zhang, P.A. Lewin, and P.E. Bloomfield. PVDF transducers-a performance comparison of single-layer and multilayer structures. *IEEE Transactions on Ultrasonics, Ferroelectrics and Frequency Control*, 44(5):1148–1156, 1997. doi: 10.1109/58.655640.
- [184] Qian Zhang, Peter A. Lewin, and Philip E. Bloomfield. Variable-frequency multilayer PVDF transducers for ultrasound imaging. In K. Kirk Shung, editor, *proceeding of SPIE Medical Imaging Ultrasonic Transducer Engineering*. SPIE, 1997. doi: 10.1117/12.271314.

- [185] B. Rashidian and M. Rahnavard. A translation matrix formulation for an arbitrarily interconnected stack of piezoelectric transducers. *IEEE Transactions on Ultrasonics, Ferroelectrics and Frequency Control*, 47(3):756–758, 2000. doi: 10.1109/58.842065.
- [186] B. Rashidian and M. Rahnavard. Applying phase accumulation to design of transducers and measurement of acoustic loss, experiments and extended models. In *proceeding of IEEE Ultrasonics Symposium*, volume 2, pages 1057–1060. IEEE, 1997. doi: 10.1109/ultsym.1997.661762.
- [187] P.E. Bloomfield. Multilayer transducer transfer matrix formalism. *IEEE Transactions on Ultrasonics, Ferroelectrics and Frequency Control*, 49(9):1300–1311, 2002. doi: 10.1109/tuffc.2002.1041547.
- [188] E.K. Sittig. Effects of bonding and electrode layers on the transmission parameters of piezoelectric transducers used in ultrasonic digital delay lines. *IEEE Transactions on Sonics and Ultrasonics*, 16(1):2–9, 1969. doi: 10.1109/t-su.1969.29486.
- [189] Hiroji Ohigashi, Toru Itoh, Kuniko Kimura, Toshiharu Nakanishi, and Miyo Suzuki. Analysis of frequency response characteristics of polymer ultrasonic transducers. *Japanese Journal of Applied Physics*, 27(Part 1, No. 3):354–360, 1988. doi: 10.1143/jjap.27.354.
- [190] E.K. Sittig. Definitions relating to conversion losses in piezoelectric transducers. *IEEE Transactions on Sonics and Ultrasonics*, 18(4):231–234, 1971. doi: 10.1109/t-su.1971.29624.
- [191] Clive Poole and Izzat Darwazeh. *Gain and stability of active networks*, chapter 7, pages 205–244. Elsevier, 2016. doi: 10.1016/b978-0-12-407823-9.00007-x.

- [192] Petia Dineva, Dietmar Gross, Ralf Müller, and Tsviatko Rangelov. Piezoelectric materials. In *Encyclopedia of Thermal Stresses*, pages 7–32. Springer Netherlands, Switzerland, 2014. doi: 10.1007/978-3-319-03961-9\_2.
- [193] M. S. Vijaya. Medical Applications of Piezoelectric Materials. In *Piezoelectric Materials and Devices*, pages 109–124. CRC Press, 2012. doi: 10.1201/b12709.
- [194] Anjana Jain, Prashanth K. J., Asheesh Kr. Sharma, Arpit Jain, and Rashmi P.N. Dielectric and piezoelectric properties of PVDF/PZT composites: A review. *Polymer Engineering & Science*, 55(7):1589–1616, 2015. doi: 10.1002/pen.24088.
- [195] Stephen W. Freiman and Grady S. White. Intelligent Ceramic Materials: Issues of Brittle Fracture. *Journal of Intelligent Material Systems and Structures*, 6(1):49–54, 1995. doi: 10.1177/1045389x9500600107.
- [196] O. Guillon, F. Thiebaud, D. Perreux, C. Courtois, P. Champagne, A. Leriche, and J. Crampon. New considerations about the fracture mode of PZT ceramics. *Journal of the European Ceramic Society*, 25(12):2421–2424, 2005. doi: 10.1016/j.jeurceramsoc.2005.03.074.
- [197] Lewis F. Brown, Joel L. Mason, Monte L. Klinkenborg, Jerry I. Scheinbeim, and Brian A. Newman. Ferroelectric nylon materials and their feasibility for ultrasound transducers. *IEEE Transactions on Ultrasonics, Ferroelectrics and Frequency Control*, 44(5):1049–1059, 1997. doi: 10.1109/58.655630.
- [198] Yoshikazu Takahashi, Masayuki Iijima, and Eiichi Fukada. Pyroelectricity in poled thin films of aromatic polyurea prepared by vapor deposition polymerization. *Japanese Journal of Applied Physics*, 28(Part 2, No. 12):L2245–L2247, 1989. doi: 10.1143/jjap.28.L2245.

- [199] Marie Nakazawa, Masaya Tabaru, Kentaro Nakamura, Sadayuki Ueha, and Akihiro Maezawa. Multilayered transducers using polyurea film. *Japanese Journal of Applied Physics*, 46(7B):4466–4473, 2007. doi: 10.1143/jjap.46.4466.
- [200] Yuetao Zhao, Xin He, Wenyao Yang, Xiling Mao, Yajie Yang, Jianhua Xu, and Yujiu Zhou. Influence of isocyanate index on the mechanical and dielectric properties of polyurea. In Mingbo Pu, Xue Feng, Yadong Jiang, Xiong Li, Xiaoliang Ma, and Bernard Kippelen, editors, *International Symposium on Advanced Optical Manufacturing and Testing Technologies: Optoelectronic Materials and Devices for Sensing and Imaging*. SPIE, 2019. doi: 10.1117/12.2506334.
- [201] Gordon Kino. *Sound Wave Propagation*, chapter 1, pages 1–84. Prentice-Hall, 1987. doi: 10.1117/12.351043.
- [202] Antonio Arnau Vives, editor. *Piezoelectric Transducers and Applications*. Springer Berlin Heidelberg, Berlin, Germany, 2008. doi: 10.1007/978-3-540-77508-9.
- [203] Takeshi Hattori, Yoshikazu Takahashi, Masayuki Iijima, and Eiichi Fukada. Piezoelectric properties of nylon 79 thin films prepared by vapor deposition polymerization. *Japanese Journal of Applied Physics*, 35(Part 1, No. 11):5763–5764, 1996. doi: 10.1143/jjap.35.5763.
- [204] J. David N. Cheeke. Acoustic properties of materials. In *Fundamentals and Applications of Ultrasonic Waves*, chapter Appendix B, pages 447–468. CRC Press, Boca Raton, USA, 2012. doi: 10.1201/b12260.
- [205] A.R. Selfridge. Approximate material properties in isotropic materials. *IEEE Transactions on Sonics and Ultrasonics*, 32(3):381–394, 1985. doi: 10.1109/t-su.1985.31608.

- [206] C.-K. Jen, D.R. França, Z. Sun, and I. Ihara. Clad polymer buffer rods for polymer process monitoring. *Ultrasonics*, 39(2):81–89, 2001. doi: 10.1016/s0041-624x(00)00056-1.
- [207] Y. Yamashita, Y. Hosono, and K. Itsumi. Low sound velocity and acoustic attenuation silicone rubber lens based on nano-powder-composite for medical echo ultrasound array probes. In *IEEE International Symposium on the Applications of Ferroelectrics*. IEEE, 2007. doi: 10.1109/ISAF.2007.4393391.
- [208] Tung Manh, Anh-Tuan Thai Nguyen, Tonni F. Johansen, and Lars Hoff. Microfabrication of stacks of acoustic matching layers for 15 MHz ultrasonic transducers. *Ultrasonics*, 54(2):614–620, 2014. doi: 10.1016/j.ultras.2013.08.015.
- [209] Marc Lethiecq, Franck Levassort, Dominique Certon, and Louis Pascal Tran-Huu-Hue. Piezoelectric transducer design for medical diagnosis and NDE. In *Piezoelectric and Acoustic Materials for Transducer Applications*, chapter 10, pages 191–215. Springer US, 2008. doi: 10.1007/978-0-387-76540-2\_10.
- [210] L F Brown. The effects of material selection for backing and wear protection/quarter-wave matching of piezoelectric polymer ultrasound transducers. In *proceeding of IEEE International Ultrasonics Symposium*, volume 2, pages 1029–1032, 2002.
- [211] Adit Decharat, Sanat Wagle, Svein Jacobsen, and Frank Melandsø. Using silver nano-particle ink in electrode fabrication of high frequency copolymer ultrasonic transducers: Modeling and experimental investigation. *Sensors*, 15(4):9210–9227, 2015. doi: 10.3390/s150409210.
- [212] Liuxia Ruan, Xiannian Yao, Yufang Chang, Lianqun Zhou, Gaowu Qin, and Xianmin

- Zhang. Properties and applications of the  $\beta$  phase poly(vinylidene fluoride). *Polymers*, 10(3):228, 2018. doi: 10.3390/polym10030228.
- [213] H. L. W. Chan, Z. Zhao, K. W. Kwok, C. L. Choy, C. Alquié, C. Boué, and J. Lewiner. Polarization of thick polyvinylidene fluoride/trifluoroethylene copolymer films. *Journal of Applied Physics*, 80(7):3982–3991, 1996. doi: 10.1063/1.363356.
- [214] Yung Ting, Hariyanto Gunawan, Amelia Sugondo, and Chun-Wei Chiu. A new approach of polyvinylidene fluoride (PVDF) poling method for higher electric response. *Ferroelectrics*, 446(1):28–38, 2013. doi: 10.1080/00150193.2013.820983.
- [215] Maria Stokes, Julie Hides, and Dariush K. Nassiri. Musculoskeletal ultrasound imaging: diagnostic and treatment aid in rehabilitation. *Physical Therapy Reviews*, 2(2):73–92, 1997. doi: 10.1179/ptr.1997.2.2.73.
- [216] R. J. Wakefield. Musculoskeletal ultrasonography: what is it and should training be compulsory for rheumatologists? *Rheumatology*, 43(7):821–822, 2004. doi: 10.1093/rheumatology/keh227.
- [217] Michael G. Bemben. Use of diagnostic ultrasound for assessing muscle size. *Journal of Strength and Conditioning Research*, 16(1):103–108, 2002.
- [218] Rogan E.A. Henderson, Bruce F. Walker, and Kenneth J. Young. The accuracy of diagnostic ultrasound imaging for musculoskeletal soft tissue pathology of the extremities: A comprehensive review of the literature. *Chiropractic and Manual Therapies*, 23(1):1–29, 2015. doi: 10.1186/s12998-015-0076-5.
- [219] Małgorzata Serafin-Król, , and Artur Maliborski and. Diagnostic errors in muscu-

- loskeletal ultrasound imaging and how to avoid them. *Journal of Ultrasonography*, 17(70):188–196, 2017. doi: 10.15557/JoU.2017.0028.
- [220] Richard H Brown. Ultrasonic pvdf transducer for 3-4 mhz operation. Technical report, measurement specialties, 2001.
- [221] Goldberg, Richard L. and Smith, Stephen W. Multilayer Piezoelectric Ceramics for Two-Dimensional Array Transducers. *IEEE Transactions on Ultrasonics, Ferroelectrics, and Frequency Control*, 41(5):761–771, 1994. doi: 10.1109/58.308512.
- [222] B. Jadidian, N. Hagh, A. Winder, and A. Safari. 25 MHz ultrasonic transducers with lead- free piezoceramic, 1-3 PZT fiber-epoxy composite, and PVDF polymer active elements. *IEEE Transactions on Ultrasonics, Ferroelectrics and Frequency Control*, 56(2):368–378, 2009. doi: 10.1109/tuffc.2009.1046.
- [223] *Technical Data Sheet 622 : Embeded-It Low Viscosity Epoxy Kit*. Polysciences, Inc., Warrington, USA, 2010. 622.
- [224] P Fellows. Properties of food and principles of processing. In *Food processing technology : principles and practice*, Woodhead Publishing Series in Food Science, Technology and Nutrition, chapter 1, pages 3–200. Woodhead Publishing/Elsevier Science, Cambridge, USA, fourth edition, 2016.
- [225] *Product Data Sheet DENACOL EX-252*. Nagase ChemteX Corporation, Tokyo, Japan, 2014. 140606R01E.
- [226] *Technical Data Sheet EPONEX Resin 1510*. Hexion Inc., Columbus, USA, 2005. 7/15/2015.

- [227] S. Yanniotis, S. Skaltsi, and S. Karaburnioti. Effect of moisture content on the viscosity of honey at different temperatures. *Journal of Food Engineering*, 72(4): 372–377, 2006. doi: 10.1016/j.jfoodeng.2004.12.017.
- [228] *Speed Set Professional Epoxy Technical Data Sheet*. Henkel Canada Corporation, Mississauga, Canada, 2014. 193468/331.
- [229] L. Ngalamou, N. Noury, E. Chamberod, and Ph. Benech. Analysis of the sensitivity and the temperature influence of a static force sensor based on a PVDF resonator. *Sensors and Actuators A: Physical*, 57(3):173–177, 1996. doi: 10.1016/s0924-4247(97)80110-0.
- [230] L. Mateu, J. Knauer, P. Spies, and H. Zessin. Autonomous tuning methods for piezoelectric energy harvesting generators. In *AMA Sensor*, pages 540–545. AMA Service GmbH, Von-Münchhausen-Str. 49, 31515 Wunstorf, Germany, 2017. doi: 10.5162/sensor2017/D7.3.
- [231] Takahiro Aoyagi, Daisuke Koyama, Kentaro Nakamura, and Marie Tabaru. Equivalent circuit analysis and design of multilayered polyurea ultrasonic transducers. *Japanese Journal of Applied Physics*, 49(7):07HD05, 2010. doi: 10.1143/jjap.49.07hd05.
- [232] Lei Xi, Xiaoqi Li, and Huabei Jiang. Variable-thickness multilayered polyvinylidene fluoride transducer with improved sensitivity and bandwidth for photoacoustic imaging. *Applied Physics Letters*, 101(17):173702, 2012. doi: 10.1063/1.4764051.
- [233] JSR Ultrasonics. *DPR300 Pulser/Receiver Operator Manual*. Pittsford, NY, USA, 2011.
- [234] H Burger, V Valenčič, Č Marinček, and N Kogovšek. Properties of musculus gluteus

- maximus in above-knee amputees. *Clinical Biomechanics*, 11(1):35–38, 1996. doi: 10.1016/0268-0033(95)00032-1.
- [235] Katja Koren, Boštjan Šimunič, Enrico Rejc, Stefano Lazzar, and Rado Pišot. Differences between skeletal muscle contractile parameters estimated from transversal tensiomyographic and longitudinal torque twitch response. *Kinesiology*, 47(1):19–26, 2015.
- [236] *Confocal Displacement Sensor CL-3000 Series*. KEYENCE CANADA INC., Mississauga, ON, Canada, 2019.
- [237] J. Dong, Z. W. Liu, and J. X. Gao. 3d deformation measurement of soft material under indentation using improved diffraction-assisted image correlation. *Experimental Mechanics*, 58(1):87–98, 2018. doi: 10.1007/s11340-017-0326-7.
- [238] Sasan Moghimi, Saman Kiumehr, Javad Amoozadeh, and Ghasem Fakhraie. Axial length measurement in asteroid hyalosis: Comparing laser interferometry and ultrasound a-scan. *Iranian Journal of Ophthalmology*, 21(1):29–34, 2009.
- [239] N. Nitta, T. Aoki, K. Hyodo, M. Misawa, and K. Homma. Direct measurement of speed of sound in cartilage in situ using ultrasound and magnetic resonance images. In *International Conference of the IEEE Engineering in Medicine and Biology Society (EMBC)*, pages 6063–6066. IEEE, 2013. doi: 10.1109/embc.2013.6610935.
- [240] Kumi Akataki, Katsumi Mita, Makoto Watakabe, and Kunihiro Itoh. Mechanomyogram and force relationship during voluntary isometric ramp contractions of the biceps brachii muscle. *European Journal of Applied Physiology*, 84(1-2):19–25, 2001. doi: 10.1007/s004210000321.

- [241] Shogo Watanabe, Shinichi Fukuhara, Takeshi Fujinaga, and Hisao Oka. Estimating the minimum stimulation frequency necessary to evoke tetanic progression based on muscle twitch parameters. *Physiological Measurement*, 38(3):466–476, 2017. doi: 10.1088/1361-6579/aa5bd1.
- [242] C. Lohr, T. Schmidt, I. Medina-Porqueres, K.-M. Braumann, R. Reer, and J. Porthun. Diagnostic accuracy, validity, and reliability of tensiomyography to assess muscle function and exercise-induced fatigue in healthy participants. a systematic review with meta-analysis. *Journal of Electromyography and Kinesiology*, 47:65–87, 2019. doi: 10.1016/j.jelekin.2019.05.005.
- [243] Travis W Beck, Terry J Housh, Joel T Cramer, Joseph P Weir, Glen O Johnson, Jared W Coburn, Moh H Malek, and Michelle Mielke. Mechanomyographic amplitude and frequency responses during dynamic muscle actions: a comprehensive review. *BioMedical Engineering OnLine*, 4(1):1–27, 2005. doi: 10.1186/1475-925X-4-67.
- [244] Emiliano Cè, Susanna Rampichini, and Fabio Esposito. Novel insights into skeletal muscle function by mechanomyography: from the laboratory to the field. *Sport Sciences for Health*, 11(1):1–28, 2015. doi: 10.1007/s11332-015-0219-z.
- [245] Rado Pišot, Marco V. Narici, Boštjan Šimunič, Maarten De Boer, Olivier Seynnes, Mihaela Jurdana, Gianni Biolo, and Igor B. Mekjavić. Whole muscle contractile parameters and thickness loss during 35-day bed rest. *European Journal of Applied Physiology*, 104(2):409–414, 2008. doi: 10.1007/s00421-008-0698-6.
- [246] Boštjan Šimunič, Dejan Križaj, Marco Narici, and Rado Pišot. Twitch parameters in transversal and longitudinal biceps brachii response. *Annales Kinesiologiae*, 1(1): 61–80, 2010.

- [247] Massimiliano Ditroilo, Iain J. Smith, Malcolm M. Fairweather, and Angus M. Hunter. Long-term stability of tensiomyography measured under different muscle conditions. *Journal of Electromyography and Kinesiology*, 23(3):558–563, 2013. doi: 10.1016/j.jelekin.2013.01.014.
- [248] Pedro Alvarez-Diaz, Eduard Alentorn-Geli, Silvia Ramon, Miguel Marin, Gilbert Steinbacher, Juan José Boffa, Xavier Cuscó, Oscar Ares, Jordi Ballester, and Ramon Cugat. Effects of anterior cruciate ligament injury on neuromuscular tensiomyographic characteristics of the lower extremity in competitive male soccer players. *Knee Surgery, Sports Traumatology, Arthroscopy*, 24(7):2264–2270, 2016. doi: 10.1007/s00167-014-3319-4.
- [249] Eduard Alentorn-Geli, Pedro Alvarez-Diaz, Silvia Ramon, Miguel Marin, Gilbert Steinbacher, Marta Rius, Roberto Seijas, Oscar Ares, and Ramon Cugat. Assessment of gastrocnemius tensiomyographic neuromuscular characteristics as risk factors for anterior cruciate ligament injury in male soccer players. *Knee Surgery, Sports Traumatology, Arthroscopy*, 23:2502–2507, 2015. doi: 10.1007/s00167-014-3007-4.
- [250] Damir Zubac, Armin Paravlić, Katja Koren, Urzi Felicita, and Boštjan Šimunič. Plyometric exercise improves jumping performance and skeletal muscle contractile properties in seniors. *Journal of musculoskeletal & neuronal interactions*, 19(1): 38–49, 2019.
- [251] Hannah V Wilson, Ashley Jones, Mark I Johnson, and Peter Francis. The effect of inter-electrode distance on radial muscle displacement and contraction time of the biceps femoris, gastrocnemius medialis and biceps brachii, using tensiomyography

- in healthy participants. *Physiological Measurement*, 40(7):075007, 2019. doi: 10.1088/1361-6579/ab1cef.
- [252] AD Jones, K Hind, H Wilson, MI Johnson, and P Francis. A standardised protocol for the assessment of lower limb muscle contractile properties in football players using tensiomyography. *Advances in Skeletal Muscle Function Assessment*, 2017.
- [253] Francisco Piqueras-Sanchiz, Saúl Martín-Rodríguez, Fernando Pareja-Blanco, Luis Baraja-Vegas, Jorge Blázquez-Fernández, Iker J. Bautista, and Óscar García-García. Mechanomyographic measures of muscle contractile properties are influenced by electrode size and stimulation pulse duration. *Scientific Reports*, 10(1), 2020. doi: 10.1038/s41598-020-65111-z.
- [254] N Amrutha and V H Arul. A review on noises in emg signal and its removal. *Int J Sci Res Publ*, 7(5):23–27, 2017.
- [255] Dario Farina. Interpretation of the surface electromyogram in dynamic contractions. *Exercise and Sport Sciences Reviews*, 34(3):121–127, 2006. doi: 10.1249/00003677-200607000-00006.
- [256] Susanna Rampichini, Taian Martins Vieira, Paolo Castiglioni, and Giampiero Merati. Complexity analysis of surface electromyography for assessing the myoelectric manifestation of muscle fatigue: A review. *Entropy*, 22(5):529, 2020. doi: 10.3390/e22050529.
- [257] Marko Jakovljevic, Scott Hsieh, Rehman Ali, Gustavo Chau Loo Kung, Dongwoon Hyun, and Jeremy J. Dahl. Local speed of sound estimation in tissue using pulse-echo ultrasound: Model-based approach. *The Journal of the Acoustical Society of America*, 144(1):254–266, 2018. doi: 10.1121/1.5043402.

- [258] Matthew Hussey. *A-Mode Scanning Instruments*, pages 51–73. Macmillan Education UK, London, UK, 1985. doi: 10.1007/978-1-349-17737-0\_4.
- [259] Jeffrey A. Strakowski. Physics of ultrasound. In *Introduction to Musculoskeletal Ultrasound*, chapter 2, pages 3–16. Springer Publishing LLC, 2015.
- [260] Jason Silver. *Development of ultrasound based techniques for measuring skeletal muscle motion*. Masc thesis, Carleton University, Ottawa, Canada, 2009.
- [261] Andy Huang. *Effect of ultrasonic probe movement on tissue displacement measurements for muscle monitoring*. Masc thesis, Carleton University, Ottawa, Canada, 2013.
- [262] Hisham Turkistani. *Ultrasonic Signal Processing for Continuous Measurements of Tissue Displacement and Thickness During Muscle Contraction*. Masc thesis, Carleton University, Ottawa, Canada, 2014.
- [263] Elliot Ming Hing Yeung. A method to characterize skeletal muscle contractile properties using a wearable ultrasonic sensor. Master’s thesis, Carleton University, Ottawa, Canada, 2020.
- [264] L. Angrisani and R. Schiano Lo Moriello. Estimating ultrasonic time-of-flight through quadrature demodulation. *IEEE Transactions on Instrumentation and Measurement*, 55(1):54–62, 2006. doi: 10.1109/tim.2005.861251.
- [265] P. Levesque and M. Sawan. Real-time hand-held ultrasound medical-imaging device based on a new digital quadrature demodulation processor. *IEEE Transactions on Ultrasonics, Ferroelectrics and Frequency Control*, 56(8):1654–1665, 2009. doi: 10.1109/tuffc.2009.1230.

- [266] Md. Omar Khyam, Shuzhi Sam Ge, Xinde Li, and Mark R. Pickering. Highly accurate time-of-flight measurement technique based on phase-correlation for ultrasonic ranging. *IEEE Sensors Journal*, 17(2):434–443, 2017. doi: 10.1109/jsen.2016.2631244.
- [267] Kavous Abbasi and Wissam M. Alobaidi. Estimation of time-of-flight based on threshold and peak analysis method for microwaves signals reflected from the crack. *Nondestructive Testing and Evaluation*, 33(4):393–404, 2018. doi: 10.1080/10589759.2018.1495204.
- [268] Stacey B. Plichta and Elizabeth A. Kelvin. *Munro's statistical methods for health care research*. Wolters Kluwer Health/Lippincott Williams & Wilkins, Philadelphia, PA, USA, 6 edition, 2012.
- [269] Eric D. Ryan, Joel T. Cramer, Terry J. Housh, Travis W. Beck, Trent J. Herda, and Michael J. Hartman. Inter-individual variability in the torque-related patterns of responses for mechanomyographic amplitude and mean power frequency. *Journal of Neuroscience Methods*, 161(2):212–219, 2007. doi: 10.1016/j.jneumeth.2006.11.007.
- [270] Edan Al-Zahrani, Chandrasekaran Gunasekaran, Michael Callaghan, Patrick Gaydecki, Diego Benitez, and Jackie Oldham. Within-day and between-days reliability of quadriceps isometric muscle fatigue using mechanomyography on healthy subjects. *Journal of Electromyography and Kinesiology*, 19(4):695–703, 2009. doi: 10.1016/j.jelekin.2007.12.007.
- [271] M S Stock, T W Beck, J M DeFreitas, and M A Dillon. Linearity and reliability of the mechanomyographic amplitude versus dynamic constant external resistance

- relationships for the biceps brachii. *Physiological Measurement*, 31(11):1487–1498, 2010. doi: 10.1088/0967-3334/31/11/006.
- [272] Xingchen Yang, Zhenfeng Chen, Nalinda Hettiarachchi, Jipeng Yan, and Honghai Liu. A Wearable Ultrasound System for Sensing Muscular Morphological Deformations. *IEEE Transactions on Systems, Man, and Cybernetics: Systems*, PP:1–10, 2019. doi: 10.1109/tsmc.2019.2924984.
- [273] Sungmee Park, Kyunghee Chung, and Sundaresan Jayaraman. Wearables. In Edward Sazonov and Michael R. Neuman, editors, *Wearable Sensors*, chapter 1.1, pages 1–23. Academic Press, 2014. doi: 10.1016/b978-0-12-418662-0.00001-5.
- [274] Andreas Demosthenous. Advances in microelectronics for implantable medical devices. *Advances in Electronics*, 2014:1–21, 2014. doi: 10.1155/2014/981295.
- [275] Xiayue Fan, Bin Liu, Jia Ding, Yida Deng, Xiaopeng Han, Wenbin Hu, and Cheng Zhong. Flexible and wearable power sources for next-generation wearable electronics. *Batteries & Supercaps*, 2020. doi: 10.1002/batt.202000115.
- [276] Chi-Kai Weng, Jeng-Wen Chen, and Chih-Chung Huang. A FPGA-based wearable ultrasound device for monitoring obstructive sleep apnea syndrome. In *2015 IEEE International Ultrasonics Symposium (IUS)*. IEEE, 2015. doi: 10.1109/ultsym.2015.0515.
- [277] Abhishek Basak, Vaishnavi Ranganathan, and Swarup Bhunia. A wearable ultrasonic assembly for point-of-care autonomous diagnostics of malignant growth. In *2013 IEEE Point-of-Care Healthcare Technologies (PHT)*. IEEE, 2013. doi: 10.1109/pht.2013.6461301.